Aerosol effects on microphysical processes and deep convective clouds

Thesis submitted for the degree of

Doctor of Philosophy

Max Heikenfeld

Linacre College

University of Oxford

Hillary 2019

Abstract

Aerosol–cloud interactions are an essential feature of the Earth's climate system. However, aerosol effects on deep convection are highly uncertain. Different conceptual models for the effects of aerosols on deep convective clouds have been proposed, and assessments based on both models and observations show a wide range of results. This thesis aims at unravelling the cloud microphysical pathways involved in these interactions using a hierarchy of different model simulations and novel analysis tools. A detailed pathway analysis based on microphysical process rates for individually tracked clouds is developed and applied to idealised supercell simulations with three different microphysics schemes in a cloud-resolving model (CRM). This reveals both consistent responses between the schemes, e.g. a suppression of warm rain formation and elevated freezing, and significant differences between the schemes due to the definition of hydrometeor classes and microphysical processes. The cloud tracking framework tobac is developed to provide a consistent way to perform analyses resolving the time evolution of individual clouds in a wide range of datasets. Its application is demonstrated for both CRM simulation results and geostationary satellite data. The cloud tracking and the pathway analysis are combined to investigate deep convective clouds in a large case study simulation and their aerosol response for two different CRMs. Separating the tracked clouds into different categories and compositing along a relative time axis allows for a detailed assessment of the cloud microphysics that resolves the time evolution of the clouds. Despite some similar aerosol responses like a suppression of warm-rain formation and surface precipitation, the analyses highlight significant differences in the cloud types and cloud evolution simulated by the two models, especially regarding the mixed- and ice-phase processes. The detailed investigation of the microphysical evolution of individually tracked clouds reveals important pathways for aerosol effects on deep convective clouds and substantial uncertainties that arise from the representation of microphysical processes in numerical models.

Acknowledgements

This thesis would not have been possible without the help, support and inspiration a number of people.

First, I want to thank my supervisor Philip Stier for his ideas, motivation, guidance and support. I really appreciated the freedom to explore my own research ideas but also knowing that I could count on you to combine the different approaches into a coherent research project.

Very special thanks go to my post-doctoral advisors Laurent Labbouz and Bethan White. Your ideas, feedback and all the motivation I got out of all the discussion were an invaluable input to this DPhil project. Thanks for the continued support and collaboration over negligible and seriously challenging time-zone differences in the more recent time. Thanks for also turning into great friends over the time spent on unravelling the mysteries of microphysics, convection and that truly particular island off the coast of Europe

I would like to thank the entire Climate Processes group that I have seen leaving and coming over all those years for a great time at our end of the corridor. I enjoyed all the inspiring insight from everyone's interesting work on all things clouds and aerosols, the great feedback and input to my own work, as well as all the good discussions over lunch and coffee breaks.

I want to thank Annica Ekman and Don Grainger, who examined this thesis, for the insightful feedback and an inspiring discussion during the viva.

I would like to thank everyone in AOPP for providing such a great working atmosphere. It was truly inspiring to hear about all the interesting research everyone is doing ranging from the depths of the oceans to far-away exoplanets.

I was fortunate to spend a summer at Colorado State University in Fort Collins as part of my DPhil project. I want to thank Sue van den Heever and everyone in the department for an inspiring time. I want to specifically thank Peter Marinescu for great collaboration on cloud tracking and the ACPC case study, both across the room and across an entire ocean.

I want to thank all the members of the scientific community that I interacted with at conferences, seminars and workshops over the last couple of years. A lot of the inspiration and ideas in this thesis came out of good discussions and feedback, even when things often just set a little spark of an idea that would only materialise in the work moths later. I would like to specifically thank Hugh Morrison and Greg Thompson for discussions about the details of microphysics schemes and Fabian Senf for important input on the cloud tracking.

The funding for this project was provided by the European Union as part of the research projects BACCHUS and RECAP, as well as the NERC Oxford Doctoral Training Programme in Environmental Research. I really enjoyed being part of the DTP and the community of students and researchers from the wide range of disciplines provided important input for my project, especially during the first couple of months.

I really appreciated being part of the great community of Linacre College during my time in Oxford. Inspiring discussions, football, Touch rugby, gardening and last but not least some great friendships I made there provided a nice balance to the work on the DPhil project.

I want to thank my sister and my parents for all the support over the last years and before. I really appreciated your regular visits to Oxford.

I can't thank Freya Hemsing enough for her the support during the last few years on this DPhil journey. All your input, questions, editing and proofreading have been invaluable for the work that went into this thesis. Thank you for keeping Eurostar and Lufthansa in business together with me over the last few years and joining me in Oxford for longer periods.

Contents

List of Figures

List of Tables

1. Introduction and motivation

Aerosols and clouds are key components of the Earth's climate system with strong impacts on the energy budget and the hydrological cycle of the atmosphere (Boucher et al., 2013). The interactions between aerosols and clouds, however, are highly complicated and not understood well. Consequently, aerosol–cloud interactions have been singled out as one of the primary sources of uncertainty in our ability to quantify the anthropogenic radiative forcing leading to global warming (IPCC, 2013a). The limited understanding affects both the conclusions that we draw from analyses of observational data from the last century and our understanding of future changes, e.g. due to the limited representation of crucial processes in global climate models that are essential to projections of the climate system on the scale of the coming decades.

Since aerosols play a crucial role in the formation of clouds by acting as cloud condensation nuclei or ice nuclei, indirect effects of changes in aerosols on the climate system through their interactions with clouds have been proposed and studied for decades. Much of the work based on seminal studies like Twomey (1977a) and Albrecht (1989) has focused on liquid clouds in the lower parts of the troposphere and has lead to an increased understanding of the physical processes involved, especially in the case of stratiform clouds (Boucher et al., 2013). Aerosol effects on convective clouds, however, remain highly uncertain, as highlighted in the last assessment report of the Intergovernmental Panel on Climate Change (IPCC) (IPCC, 2013a) and several recent review articles (Tao et al., 2012; Altaratz et al., 2014; Rosenfeld et al., 2014a; Fan et al., 2016). This can be mainly attributed to the poor understanding of mixed- and ice-phase cloud microphysics and the comparatively localised spatial scale on which the relevant physical processes occur and vary (Tao et al., 2012). Global climate models, as well as assessments based on satellite retrievals or field measurements, face severe problems in accurately repres-

enting aerosol-convection interactions and the resulting influence on the climate system (Boucher et al., 2013). High-resolution model simulations with cloud-resolving models (CRMs) allow for a more accurate representation of the physical processes by explicitly simulating the convection in individual clouds based on grid spacings of a few hundred meters to a few kilometres (Fan et al., 2016). However, significant uncertainties in the representation of cloud microphysical processes in numerical models and the complexity of deep convective clouds lead to a wide range of different results regarding the response of deep convective clouds to changes in aerosols in studies based on this kind of model, too. Recent review papers (Tao et al., 2012; Altaratz et al., 2014) have stressed the importance of assessing aerosol effects on convective clouds and microphysical processes at the spatial and temporal scale of individual convective clouds.

The role of a possible invigoration of deep convective clouds due to increases in aerosols has been discussed extensively based on different conceptual ideas (e.g. Rosenfeld et al., 2008) and observational evidence (e.g. Andreae et al., 2004; Koren et al., 2010a) over the recent decade without leading to a consensus on the relevance of aerosol effects on deep convective clouds for the global climate system (Fan et al., 2016).

This thesis aims to answer the following research questions:

- How does uncertainty in the representation of convective cloud microphysics in numerical models affect the assessment of aerosol effects on deep convective clouds?
- What are the main impact pathways of aerosol perturbations on the microphysical evolution of deep convective clouds?
- How does the effect of aerosols on individual deep convective clouds shape the response of an entire cloud field?

These questions are addressed based on several modelling studies with two different CRMs, WRF (Weather and Research Forecasting Model, Skamarock et al., 2008) and RAMS (Regional Atmospheric Modelling System, Saleeby and van den Heever, 2013).

This includes both idealised model simulations of individual clouds and large case study simulations of entire freely evolving cloud fields. Novel analysis methods are developed to assess the detailed microphysical processes at the spatial and temporal scale of individual clouds.

The following section will give a short overview of the individual chapters of the thesis.

1.1. Structure of the thesis

Chapter 2:

This chapter provides an overview of the relevant scientific concepts and the current state of the research on aerosol–cloud interactions and the effects of aerosols on deep convective clouds. The role of clouds and aerosols in the climate system is discussed with a specific focus on the implementation of the relevant physical processes in numerical models.

Chapter 3:

The propagation of aerosol-induced perturbations of the cloud liquid phase through the convective cloud microphysics in numerical models is investigated with a detailed microphysical pathway analysis. Simulations for two different idealised cases of supercell convection with WRF and are performed for three different microphysics schemes. The analysis focuses on individually tracked convective cells for a targeted assessment of the time evolution and morphology of the clouds. This includes detailed microphysical process rate diagnostics and the assessment of bulk cloud properties like cloud mass and cloud centre of gravity.

Chapter 4:

In this chapter, the cloud-tracking framework tobac developed as a new flexible tool that works on a large variety of different types of datasets. It is set up modularly to incorporate a range of different tracking algorithms. The application of tobac is demonstrated for

two example use cases based on high-resolution model output and geostationary satellite retrievals.

Chapter 5:

The microphysical pathway analysis developed in Chap. 3 and the tracking framework tobac presented in Chap. 4 are combined to analyse the effect of changes in aerosols on deep convective clouds in a freely evolving cloud field in a large case study simulation. This work has been carried out as part of a model intercomparison study with several CRMs simulating the aerosol response of isolated deep convection around Houston, Texas. Simulations using two of the models (WRF and RAMS) are investigated to reveal how the differences in the response to changes in aerosols can be related to the microphysical pathways in individual clouds and changes in the cloud types simulated by the models.

Chapter 6

The results from the individual chapters are summarised and combined into general conclusions. This includes an overview of new research questions that arise from the results of the thesis or that could be explored with the analysis methods developed as part of it.

2. Background

In this chapter, I introduce the most important background aspects of the research questions addressed in the individual chapters of the thesis. I first give an overview of the role of atmospheric aerosols (Sect. 2.1), clouds (Sect. 2.2) and their interactions (Sect. 2.3 and Sect. 2.3.1) in the climate system. As the thesis mostly relies on the analysis of simulations performed with cloud-resolving models (CRMs), I will introduce how the relevant physical processes are represented in numerical models using different conceptional approaches (Sect. 2.2.2). This includes how numerical models treat clouds and aerosols in general, and a specific focus on the representation of cloud microphysics and aerosol–cloud interactions in the models used in the following chapters of the thesis, WRF (Weather and Research Forecasting Model, Skamarock et al., 2008) and RAMS (Regional Atmospheric Modelling System, Saleeby and van den Heever, 2013). Sect. 2.3.1 gives a detailed overview of the current state of research in understanding the effects of aerosols on deep convective clouds and presents a comprehensive introduction to some theoretical concepts for these interactions that will be referred to in the individual chapters of the thesis.

2.1. Atmospheric aerosols

Atmospheric aerosols are defined as any type of solid or liquid particles suspended in the atmosphere. Suspended liquid and frozen water is not considered as part of this definition due to their importance and specific behaviour as cloud hydrometeors which is discussed in more detail in Sect. 2.2.2.

Aerosols are important in the natural state of the atmosphere (Boucher et al., 2013; Carslaw et al., 2013; Seinfeld and Pandis, 2016) both through their direct radiative effects

and in their role as cloud condensation nuclei (CCN). However, research on the role of aerosols in the climate system is of particular relevance as substantial amounts of aerosols are emitted due to human activity (Charlson et al., 1992; Lamarque et al., 2010). Due to their radiative effects and impacts on the evolution of clouds in the form of aerosol–cloud interactions, these additional aerosols impact the climate system by exerting a radiative forcing (RF), which is defined as a measure of the net change in the energy balance of the Earth system in response to the external perturbation (Charlson et al., 1992; Stocker et al., 2013). Aerosol emissions are the second-largest anthropogenic influence on the radiative balance of climate system after the well-known emission of greenhouse gases (predominantly carbon dioxide and methane) as evident from the assessment of anthropogenic radiative forcing from the last assessment report of the Intergovernmental Panel on Climate Change (IPCC)(IPCC, 2013a) shown in Fig. 2.1. The greenhouse gases have long lifetimes of years to centuries and are thus relatively well mixed within the atmosphere (IPCC, 2013a; Seinfeld and Pandis, 2016). In contrast, aerosols have a comparably short lifetime in the troposphere of no more than days to weeks due to effective removal by sedimentation and scavenging by clouds and precipitation (Seinfeld and Pandis, 2016). This leads to a substantial variation in both the spatial and temporal patterns of aerosols in the atmosphere (Schutgens et al., 2017), ranging from the scale of individual emission sources or individual weather systems to large-scale variations and transport (Anderson et al., 2003; Weigum et al., 2016). Furthermore, recent decades have shown a major shift of anthropogenic aerosol emissions from the traditional industrialised countries of Europe and North America to emerging economies, especially in Asia (Boucher et al., 2013; Klimont et al., 2013).

Natural emissions of aerosols include dust from deserts and arid regions, sea salt suspended at the ocean surface, carbonaceous particles from wildfires and secondary organic aerosols formed from biogenic emissions, especially from temperate and tropical forests (Andreae, 2007; Carslaw et al., 2013; Hamilton et al., 2018). Biogenic emissions such as organic carbon formed from gases emitted by tropical and boreal forests, bacteria and

fungi or dimethyl sulphate emissions from plankton in the ocean have become a strong focus of research in recent decades (Pöschl et al., 2010). Moreover, volcanic eruptions, such as the recent Icelandic eruption of 2014/15 (Gettelman et al., 2015; McCoy and Hartmann, 2015), emit aerosols and aerosol precursors into the atmosphere, particularly forming sulphate aerosols. Anthropogenic aerosol emissions primarily include sulphates and black carbon from the burning of fuels (Boucher et al., 2013; Hoesly et al., 2018). Furthermore, human activity affects other types of aerosols, e.g. through land-use change that impacts emissions of dust (Tegen et al., 2004) or through anthropogenic wildfires and agricultural burning (Werf et al., 2010). Nitrate aerosols are both impacted by natural and anthropogenic emissions and have become an important focus of research (Bouwman et al., 1997; Myhre et al., 2013a; Höpfner et al., 2019), especially since their role could become more important with an expected decrease in the emissions of other anthropogenic aerosols (Boucher et al., 2013; Hauglustaine et al., 2014).

The entanglement of natural and anthropogenic aerosol emissions and the related problem of estimating pre-industrial aerosol loading of the atmosphere is one of the main factors contributing to the uncertainty in estimates of the radiative forcing from anthropogenic aerosols (Carslaw et al., 2013; Hamilton et al., 2018). In combination with the limited scientific understanding of the indirect aerosol effects that will be discussed in more detail in Sect. 2.3, this leaves aerosol-induced anthropogenic forcing of the climate system as one of the main sources of uncertainty in the assessment of current and future anthropogenic climate change (see error bars in Fig. 2.1).

Aerosols play an important role in the radiative balance of the Earth's atmosphere. They affect the radiative fluxes by both scattering and absorption of radiation, depending on the size and composition of the particles and the wavelength of the light. This results in a combination of warming and cooling in the atmosphere as a complex superposition of different radiative effects in different regions and at different heights in the atmosphere (Boucher et al., 2013). Aerosol optical thickness (AOT) τ_a is related to the extinction of incoming irradiance I_0 by aerosol particles along a path through the atmosphere according

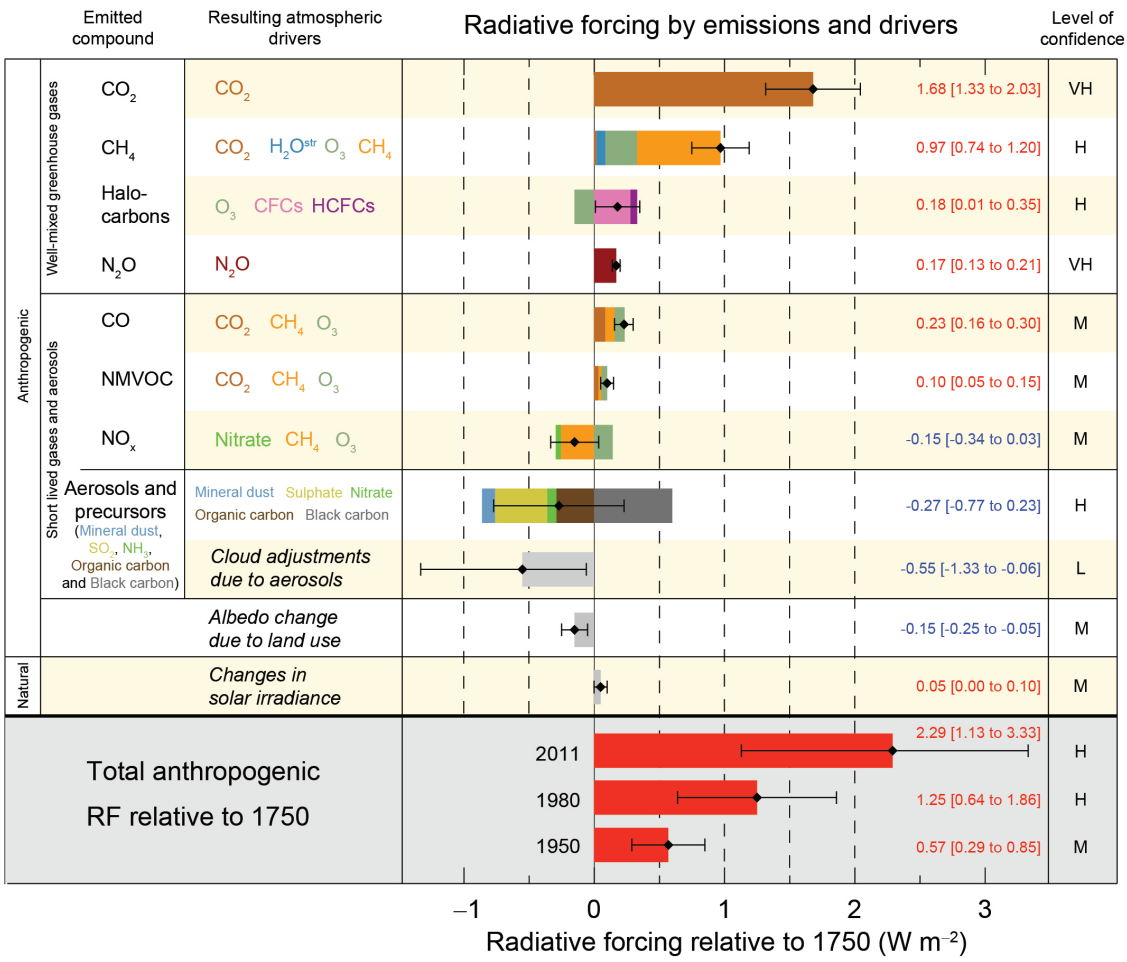

Figure 2.1: Major components of anthropogenic radiative forcing of the climate system over the period from 1750 to 2011. Error bars denote the uncertainty in the estimates and letters in the column on the right denote confidence level. The lack of understanding the two types of aerosol effects contributes strongly to the uncertainty of the total estimated anthropogenic forcing, with the forcing due to aerosol–cloud interactions pointed out as the only component with a low (L) confidence level (from IPCC, 2013b).

to

$$I = I_0 \, \mathrm{e}^{-\tau_\mathrm{a}} \tag{2.1}$$

$$\tau_a = \ln\left(\frac{I}{I_0}\right). \tag{2.2}$$

The aerosol optical depth (AOD) describes the AOT in a vertical column in the atmosphere from the surface to the top of the atmosphere. AOD is generally assumed to be representative of the aerosol mass concentrations in the atmosphere (Seinfeld and Pandis,

2016). However, it is also often used as a proxy for the CCN concentrations, e.g. in many satellite-based studies on aerosol–cloud interactions discussed in Sect. 2.3 (Koren et al., 2008; Boucher et al., 2013). It is important to note that this quantity is based purely on the radiative effect of the particles and does not provide any information on the vertical distribution of aerosols in the column.

The most important aerosol type that absorbs incoming shortwave radiation is black carbon (Bond et al., 2013). The absorption can be significantly enhanced due to the coating of particles with soluble species such as sulphate or organic matter (Schwarz et al., 2008; Boucher et al., 2013).

Scattering of incoming solar radiation is dominated by sulphates, sea salt, specific types of organic aerosols and mineral dust (Seinfeld and Pandis, 2016). The effect of aerosols on the radiative balance due to absorption of longwave radiation is considerably smaller than for shortwave radiation and restricted to large aerosol particles such as mineral dust or sea salt (Boucher et al., 2013). It generally leads to a warming of the atmosphere.

In this thesis, however, the focus is on the important indirect effect of aerosols on the radiative budget of the atmosphere through their impact on clouds as discussed in detail in Sect. 2.3. In the most recent IPCC report (Boucher et al., 2013; Myhre et al., 2013b), the direct and indirect effects of aerosols on clouds have been combined into the effective radiative forcing from aerosol–radiation interactions $\mathrm{ERF_{ari}}$ and from aerosol–cloud interactions $\mathrm{ERF_{aci}}$ (Fig.2.2). Estimates of the $\mathrm{ERF_{aci}}$ are highly uncertain, ranging from strongly negative forcing of up to $-1.6\,\mathrm{W\,m^{-2}}$ to almost no effective forcing at all (Boucher et al., 2013).

2.1.1. Representation of atmospheric aerosols in numerical models

The representation of aerosols in numerical models of the atmosphere varies significantly in complexity depending on the specific application. The approaches can be divided into three main groups, with the size distribution of the aerosol particles either described by sectional bins (bin schemes), individual modes represented by a size distribution function

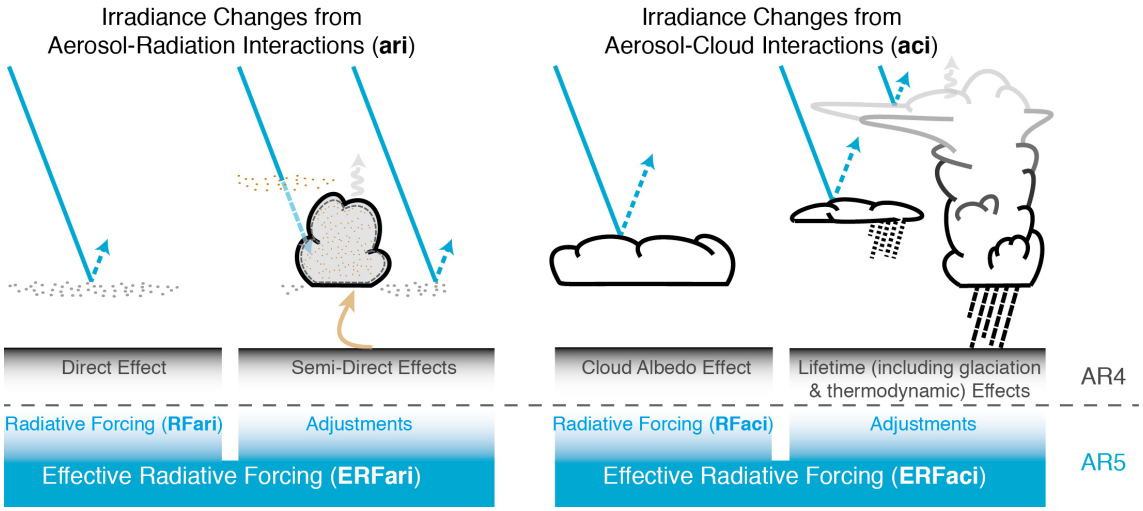

Figure 2.2: Contributions to aerosol radiative forcing from aerosol–radiation interactions (ERF_{ari}) and aerosol–cloud interactions (ERF_{aci}, discussed in Sect. 2.3) in the terminology of the last IPPC report (from Boucher et al., 2013).

(modal schemes) or predefined categories (bulk schemes) (Mann et al., 2012; Seinfeld and Pandis, 2016). Bin schemes allow for a more physically based description of the aerosol microphysics, but are computationally expensive, especially when taking into account a large number of different aerosol species (Mann et al., 2012). It has been shown that most aerosol size distributions can be well described by a superposition of modes following a log-normal distribution representing the number concentration of aerosols N as a function of the particle radius r (Whitby, 1978; Heintzenberg, 1994).

$$\frac{dN(r)}{d(\ln r)} = \sum_{i=1}^{I} \frac{N_i}{\sqrt{2\pi}\ln\sigma_i} \exp\left(-\frac{(\ln r - \ln \bar{r}_i)^2}{2\ln^2\sigma_i}\right) \tag{2.3}$$

Each mode i of the total modes I in the model is characterised by three moments: the number concentration N_i, the number median radius $\bar{r}_i$ and the standard deviation σ_i. The associated surface area, volume and mass distributions take a significantly different form due to the quadratic or cubic dependence of these quantities on the particle radius.

Typical aerosol distributions in the atmosphere can be separated into four distinct modes (Seinfeld and Pandis, 2016) as illustrated in Fig. 2.3. The nucleation mode with secondary aerosol particles below 10 nm diameters formed from nucleation in the atmosphere

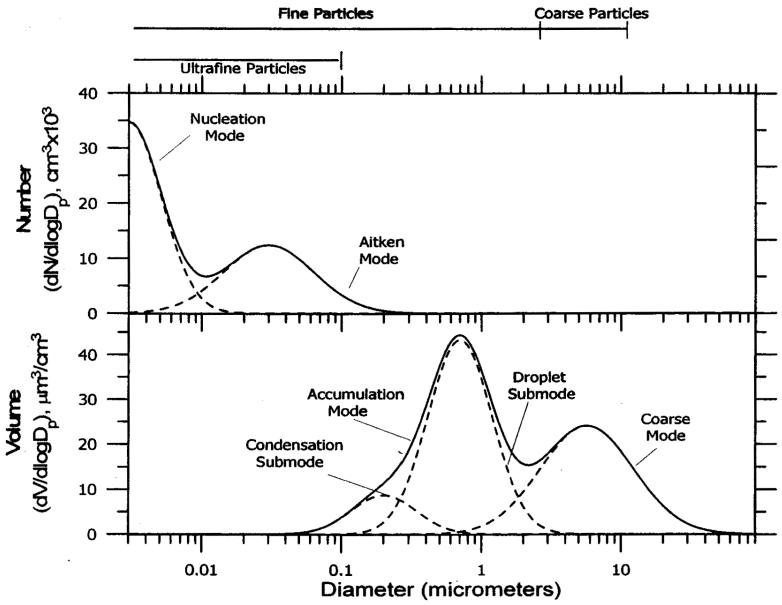

Figure 2.3: The four aerosol modes of a typical aerosol distribution represented through their number and volume size distributions. The contributions of the individual modes are shown with dashed lines and combine to the total distribution given by the solid line (from Seinfeld and Pandis, 2016).

and the Aitken mode with diameters of up to 100 nm dominate the number distribution of aerosols, but only contribute a small fraction to the total aerosol mass. The accumulation mode (100 nm to a few μm) is a significant sink for the smaller aerosol modes due to coagulation processes. The coarse mode with micron-sized aerosols consists mainly of mineral dust and sea salt (Porter and Clarke, 1997; Boucher et al., 2013).

The chemical composition of aerosols from different substances adds additional complexity to the models, as the contribution of individual species has to be prescribed for each mode or size bin. However, in this thesis, no fully interactive aerosol scheme including aerosol microphysics and chemical composition is used. In Chap.3, the effects of aerosols are represented through a variation of the cloud droplet number concentration (CDNC) in the microphysics scheme. In the simulations in Chap. 5, the aerosol distribution is represented by a single aerosol mode with a chemical composition represented through setting the κ value for the hygroscopicity (Sect. 2.1.2) and without including any of the direct radiative effects of aerosols.

2.1.2. Aerosols as cloud condensation nuclei (CCN)

Water vapour does not spontaneously condense into liquid cloud droplets in the atmosphere by homogeneous nucleation as condensation nuclei in the form of aerosol particles to are required to initiate this process. In contrast, ice clouds can form based on homogenous ice nucleation (Pruppacher and Klett, 2010). The processes leading to a formation of droplets in the presence of a soluble particle can be described by so-called Köhler theory (Köhler, 1936). It combines the two different physical effects of curvature and solute content on the vapour pressure over a forming cloud droplet.

The curvature of the droplet surface for a droplet diameter D affects the ratio of the vapour pressure over the droplet $e_s^{\mathrm{curv}}(D)$ to that over a flat surface $e_s(\infty)$

$$\frac{e_s^{\mathrm{curv}}(D)}{e_s(\infty)} = \exp\left(\frac{2\sigma}{DR_{\mathrm{v}}\rho_{\mathrm{w}}T}\right) = \exp\left(\frac{A}{D}\right), \tag{2.4}$$

with the curvature factor

$$A = \frac{2\sigma}{R_{\mathrm{v}}\rho_{\mathrm{w}}T}, \tag{2.5}$$

dependent on the surface tension of water σ, the temperature T, the density of water ρ_{w} and the universal gas constant R_{v}. Theoretically, this would allow for homogeneous nucleation of water droplets from random clustering of water molecules. However, this would require water supersaturation ratios that are orders of magnitude beyond the supersaturations of up to a few percent that actually occur in the Earth's atmosphere (Lohmann et al., 2016). Homogeneous droplet nucleation can thus be ruled out for droplet formation in clouds in the Earth's atmosphere.

However, if droplet formation takes place on an aerosol particle that includes some soluble material, the saturation vapour pressure over the curved water surface is lowered substantially. Raoult's Law describes this change in hygroscopicity due to the added solute from

the aerosol in the droplet with a diameter D on the saturation vapour pressure $e_s^{\mathrm{sol}}(D)$

$$\frac{e_s^{\mathrm{sol}}(D)}{e_s(D)} = 1 - \frac{B}{D^3}, \tag{2.6}$$

with the hygroscopicity parameter

$$B = \frac{nM_w}{\pi\rho_w}, \tag{2.7}$$

where n denotes the number of solute ions, while M_w is the mass of water in the droplet. The two effects can be combined to calculate the activation curve of a forming droplet

$$\frac{e_s^{\mathrm{sol}}(D)}{e_s(\infty)} = \frac{e_{\mathrm{s}}^{\mathrm{sol}}(D)}{e_{\mathrm{s}}^{\mathrm{curv}}(D)} \frac{e_{\mathrm{s}}^{\mathrm{curv}}(D)}{e_{\mathrm{s}}(\infty)} \tag{2.8}$$

$$= \left(1 - \frac{B}{D^3}\right) \exp\left(\frac{A}{D}\right). \tag{2.9}$$

A Taylor expansion of the exponential function leads to

$$\frac{e_s^{\mathrm{sol}}(D)}{e_s(\infty)} \overset{\text{Taylor}}{\approx} \left(1 - \frac{B}{D^3}\right)\left(1 + \frac{A}{D}\right) \tag{2.10}$$

$$= 1 + \frac{A}{D} - \frac{B}{D^3} - \frac{AB}{D^4}, \tag{2.11}$$

where the term featuring the inverse forth power in the diameter can be neglected based on the small diameters of forming droplets in the range of up to a few tens of microns, This leads to the Köhler equation

$$\frac{e_s^{\mathrm{sol}}(D)}{e_s(\infty)} \approx 1 + \frac{A}{D} - \frac{B}{D^3}, \tag{2.12}$$

The saturation ratio

$$S = \frac{e_s(D)}{e_s(\infty)} \approx \frac{A}{D} - \frac{B}{D^3} + 1, \tag{2.13}$$

follwing from this can be transformed into a supersaturation ratio

$$s = S - 1 \approx \frac{A}{D} - \frac{B}{D^3}. \tag{2.14}$$

Finding the maximum of this curve by setting the derivative to zero leads to the critical diameter D_c needed for a droplet to grow.

$$D_\mathrm{c} = \sqrt{\frac{3B}{A}} \tag{2.15}$$

Inserting this into equation (2.14) leads the critical supersaturation S_c

$$S_c = \frac{A}{D_\mathrm{c}} + \frac{B}{D_\mathrm{c}^3} = \frac{A}{\sqrt{\frac{3B}{A}}} + \frac{B}{\left(\sqrt{\frac{3B}{A}}\right)^3} = \left(1 - \frac{1}{3}\right)\sqrt{\frac{A^3}{3B}} \tag{2.16}$$

$$= \sqrt{\frac{4A^3}{27B}} \tag{2.17}$$

for the formation of cloud droplets on a CCN.

Fig. 2.4 illustrates the effect of the solute on the formation of a cloud droplet according to the Köhler equation (2.8) for three solute (ammonium sulphate) particles of different size.

This dependence of activation on the supersaturation shows that CCN are not a fixed range of particles, but a dynamically changing subset of the aerosol population depending on both the aerosol properties and the surrounding environment (vertical velocity, humidity, temperature) that determines the vapour pressure and the supersaturation S (Andreae and Rosenfeld, 2008). CCN concentrations are therefore measured or diagnosed in models as CCN at a specific supersaturation or a set of different supersaturation values to be meaningful (Miller and Bodhaine, 1982; Gryspeerdt et al., 2017; Schmale et al., 2017). The activation of CCN into cloud droplets does not only affect the cloud evolution but is also important for the development of the aerosol distribution itself. As activated particles are removed from the interstitial aerosol distribution and integrated into cloud droplets,

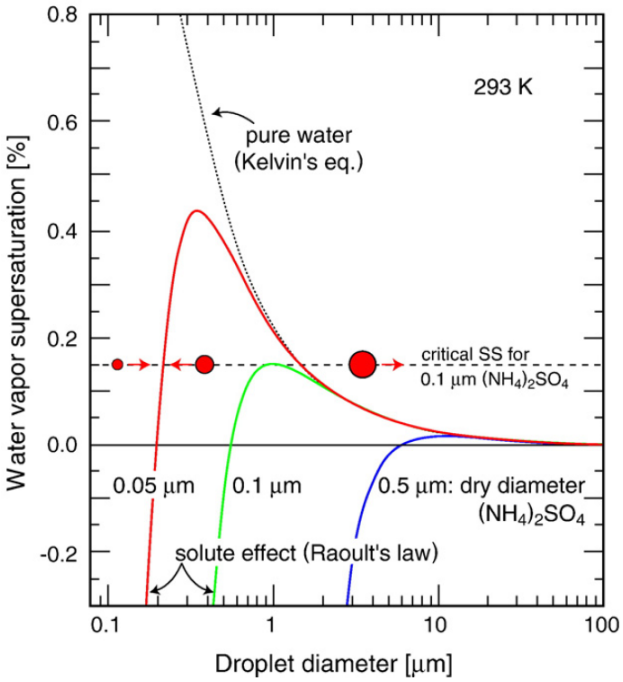

Figure 2.4: Vapour pressure equilibrium between a forming droplet and the environment due to the counteracting effects of Kelvin's equation and Raoult's law according to Köhler theory. The curves are shown for three different ammonium sulphate particles with different dry radii. The dashed black line shows the minimal supersaturation of 0.15 percent that has be exceeded to activate the 0.1 µm particle into a cloud droplet (from Andreae and Rosenfeld (2008) after Seinfeld and Pandis (2016)).

they are subject to cloud processing of aerosols. Subsequently, these particles can be re-released due to evaporation or sublimation of cloud hydrometeors leading to a changed size and chemical composition. Furthermore, the aerosol distribution is affected by the clouds due to the removal by wet scavenging (Seinfeld and Pandis, 2016) or convective transport of aerosols into higher atmospheric layers (Cui and Carslaw, 2006).

In addition to their role as CCN during the development of the cloud in the warm phase, certain aerosol types can also act as ice nuclei (IN) and facilitate the formation of ice particles within the cloud (Vali, 1996; Kanji et al., 2017). The ice-nucleating properties of aerosol particles are still poorly understood and have been related e.g. to a suitable lattice structure, specific crystal defects in dust particles or specific proteins in a range of biogenic particles (Kanji et al., 2017). IN can accelerate both the deposition of ice from the vapour phase and the freezing of cloud droplets upon contact with these particles or

with the particles immersed in existing droplets. In this thesis, however, I will solely focus on the effects of aerosols through their role as CCN and not assess any effects due to a variation of aerosols acting as IN. All model simulations are thus conducted with a constant impact of IN on the freezing and deposition processes based on different parametrisations described in Sect. 2.2.2.

2.1.3. Representation of droplet activation in numerical models

The activation of aerosols to cloud droplets is described in different ways in numerical models, which often depends on the horizontal and vertical grid spacing and the treatment of supersaturation in the microphysics scheme of the model (see Sect. 2.2.2). Ghan et al. (2011a) give an overview of several existing droplet activation parametrisations. In most of the parametrisations, the vertical velocity is used in combination with other environmental conditions to calculate the maximum supersaturation within the air parcel (Ghan et al., 2011b). In high-resolution simulations, the explicitly calculated vertical motion can be used in the calculation of droplet activation, while numerical simulations with larger horizontal grid spacings, e.g. for applications in general circulation models (GCMs), require assumptions about the subgrid-scale vertical velocity variation (Ghan et al., 2011a). Köhler theory (Sect. 2.3) and the dry aerosol properties can be used to derive the critical supersaturation and radii for the aerosol particles to determine the fraction of particles activated into cloud droplets. A typical parametrisation of this process in a numerical model assuming a distribution of the aerosols in log-normal modes for a single type of aerosol is described in Abdul-Razzak et al. (1998) and has been extended to multiple different concurrent aerosol species within the modes in Abdul-Razzak and Ghan (2000).

2.2. Clouds

Clouds are an ever-present feature of the Earth's atmosphere, covering about 70 percent of the Earth's Atmosphere at any given time (King et al., 2013; Warren et al., 2015). Des-

pite their common appearance, a formal definition of what actually constitutes a cloud has proven to be a challenging question. The International Cloud Atlas defined clouds as "a visible aggregate of minute particles of water or ice, or both, in the free air." (World Meteorological Organization, 1956), which captures the main aspect, but does not strictly determine, e.g. how much these particles have to be present to speak of a cloud or where the precise boundaries of individual clouds are located. This definition puts the focus on the individual cloud particles, hydrometeors, that make up the cloud. Aerosol effects on clouds are strongly linked to the evolution of these cloud hydrometeors occurring at the scale of the particles ranging from micrometres to a few centimetres, which are collectively described as *cloud microphysics* .

A slice through a deep convective cloud from the perspective of a numerical model is shown in Fig. 2.5 in visualisations that have been developed for a complete picture of the microphysical evolution in convective clouds as part of the analysis in this thesis. It shows a depiction of the individual cloud hydrometeors represented in the model microphysics and the microphysical processes transferring water mass and latent energy in the clouds as part of the microphysical evolution, which will be introduced in more detail in this chapter.

Clouds play a key role in the Earth system, controlling numerous important processes in the atmosphere. The distribution and composition of clouds have a strong impact on the radiation budget of the Earth. Clouds reflect incoming shortwave radiation from the Sun, resulting in a cooling effect of about $(45\text{–}50)\,\mathrm{W\,m^{-2}}$, and trapping longwave radiation from the Earth's surface which leads to a warming on the order of $(25\text{–}30)\,\mathrm{W\,m^{-2}}$ (Loeb et al., 2009; Trenberth et al., 2009; Stephens et al., 2012). Furthermore, cloud feedbacks to increasing atmospheric temperature (Bony et al., 2006; 2015) and aerosol–cloud interactions (Sect. 2.3) constitute two of the largest sources of uncertainty in our understanding of present and future anthropogenic radiative forcing (Boucher et al., 2013). Furthermore, clouds are a major element of the hydrological cycle in the atmosphere and thus hugely important in our understanding of the formation of precipitation and precipitation patterns

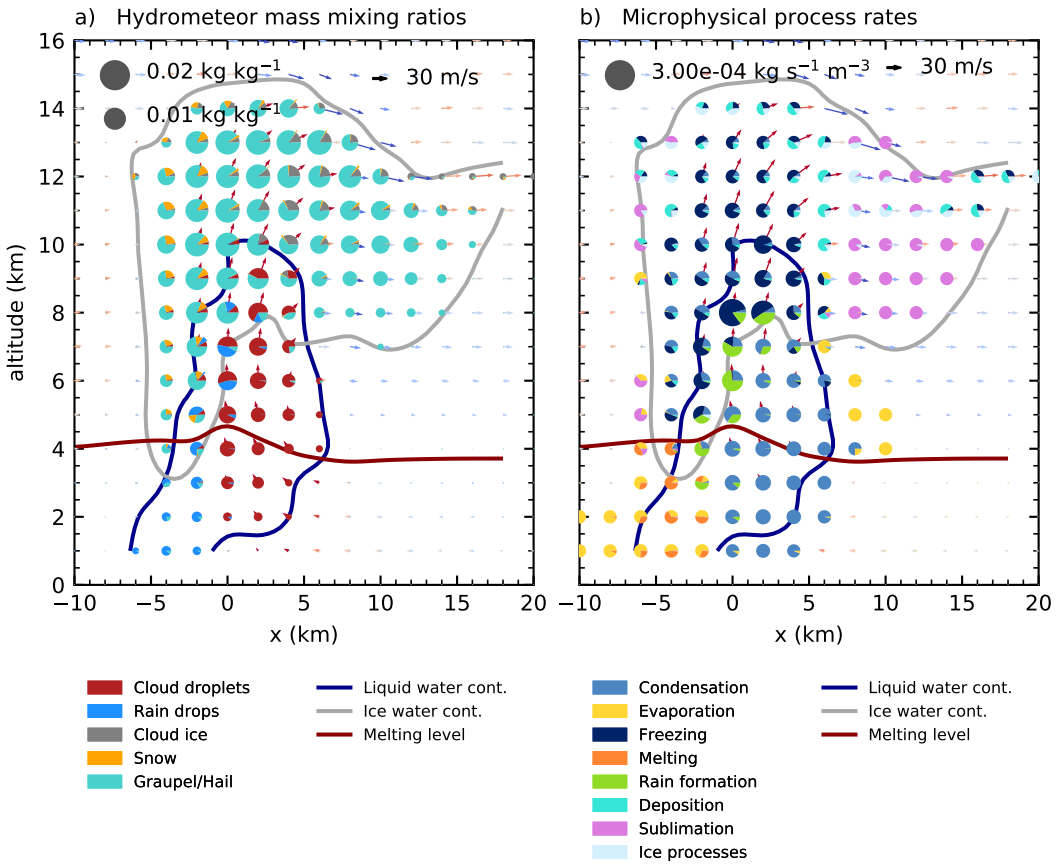

Figure 2.5: Hydrometeor mixing ratios (a) and grouped microphysical process rates (b) in a deep convective cloud. The area of each colour in the pie charts is proportional to the hydrometeor mixing ratio in (a). For the microphysical processes in (b), the area of each colour represents the mass water transfer in each group of processes. However, a non-proportional scaling has been used here to depict processes that differ by orders of magnitude. Mass mixing ratio contour lines at $1\,\mathrm{g\,kg^{-1}}$ are depicted as solid lines for liquid water (blue) and frozen water (grey), while the red line denotes the melting level in the cloud. Arrows depict the winds, featuring red colours for updrafts and blue colours for downdrafts.

on Earth (Yau and Rogers, 1989). Changes in precipitation due to anthropogenic climate change are highly uncertain (Collins et al., 2013), but will most certainly constitute the most substantial impact of global warming on humanity (IPCC, 2014). The understanding of clouds and cloud processes is also crucial to numerical weather forecasting, and deep convective clouds play an important role in different types of high-impact weather events such as storms, flooding or hail (Doswell, 2001; Gensini and Mote, 2014).

Since the early days of the scientific research on the nature of clouds (Lamarck, 1802; Howard, 1803), they have been roughly separated into three different categories, derived mainly from their visual appearance (Lohmann et al., 2016). Although these classifications have been extended over the last two centuries, as evident in the current edition of the International Cloud Atlas (World Meteorological Organization, 2017), a separation into these three main classes still holds for the most important aspects.

Different types of *stratiform clouds*, such as *stratus*, are characterised by a large horizontal extent compared to their vertical thickness, which means that they appear in the form of extended cloud layers often covering large areas (Houze, 2014). The vertical motions in these clouds are small, resulting in long lifetimes and limited precipitation (Wood, 2015). Although *stratocumulus* form due to convective processes, these types of clouds are capped under a strong inversion taking on a horizontally extended form that makes them similar to stratus clouds in many aspects (Wood, 2012; Lohmann et al., 2016). Extended stratocumulus decks cover large areas of the subtropical oceans (Wood, 2012). Due to their low altitude, they exhibit a strong cooling effect on the climate system and are extensively studied concerning aerosol–cloud–climate interactions (Stevens and Feingold, 2009; Boucher et al., 2013) as discussed in more detail in Sect. 2.3.

Cirrus clouds occur in the form of thin, wispy strands and are made up almost entirely of ice particles (Dowling and Radke, 1990). These clouds can form by deposition of water vapour due to synoptic or orographic forcing (Sassen et al., 2008). Cirrus are often directly interlinked with deep convective clouds, as they can form from the outflow of the anvils of deep convective clouds reaching the troposphere and spreading out laterally, especially in the tropics (Mace et al., 2006; Sassen et al., 2008) .

In contrast to the horizontally spread-out nature of the cirrus and stratus clouds, *convective clouds* are much more localised with a vertical extent of a similar order of magnitude to their horizontal extent. They are characterised by strong vertical motions and a rapid vertical evolution (Houze, 2014) leading to much shorter lifetimes than for the stratiform clouds. Convective clouds can be classified into different categories based on the evolu-

tion of their vertical extent. Updrafts are formed through the increase in buoyancy of air parcels that experience latent heat release due to condensation on activated cloud droplets. Shallow *cumulus* clouds are driven entirely by these warm-phase processes. These clouds generally have short lifetimes of a few tens of minutes (Isaac, 1986; Jiang et al., 2006). Apart from their appearance as typical "fair-weather clouds" in our temperate latitudes, they cover most of the trade wind regions over the subtropical oceans (Stevens and Feingold, 2009). *Cumulus congestus* are characterised by stronger vertical motions in the cloud and the development of individual towers reaching further up into higher levels or the lower troposphere but are still mainly consist of liquid water droplets (Rangno, 2015). If the buoyant air reaches the layers of the atmosphere with temperatures below 0°°C, further latent heat can be released due to the freezing of liquid water and the clouds can grow further into fully developed deep convective *cumulonimbus* clouds (Cotton et al., 2010; Rangno, 2015). As I focus on aerosol effects on these deep convective clouds in this thesis, I will describe the most important aspects of their structure and evolution in more detail in the following Sect. 2.2.1, before introducing the most important aspects of the detailed microphysical processes and their implementation in numerical models in Sect. 2.2.2.

2.2.1. Deep convective clouds

Deep convective clouds play a crucial role in the global climate system due to their effects on the vertical transport of moisture to the upper troposphere and into the stratosphere (Emanuel, 1994; Cotton et al., 2010). In the tropics, deep convection is crucial to the vertical structure of the atmosphere and influences globally important large scale atmospheric processes such as the formation of the Hadley cell (Emanuel, 1994). Furthermore, deep convective clouds have major importance to key features of the climate system such as the Madden-Julian Oscillation (MJO) or El Niño - Southern Oscillation (ENSO) dynamics, along with its crucial role in the formation of tropical cyclones (Tory et al., 2006). Deep convection also plays an important role in mid-latitude weather and

climate (Andrews, 2010) as the main cause of several types of severe weather events, such as tornadoes or flooding (Kunkel et al., 2012; Gensini and Mote, 2014). Large regions of the globe depend predominantly on precipitation from deep convective clouds for their supply of water (Yang and Smith, 2008). Due to their highly localised nature, cumulus clouds are not explicitly represented in numerical models at coarser scales, but can only be included in the form of convective parametrisations describing the overall effect of all convective clouds in a grid box on the large scale variables (Arakawa, 2004). The limitations in the representation of deep convection in current models used for both weather forecasting and climate research is seen as one of the main sources of uncertainty on modelling assessments on various important research questions (Boucher et al., 2013; Neumann et al., 2019).

In contrast to the moderate vertical wind speeds of up to a few metres per second in shallow cumulus clouds (Houze, 2014), the updrafts in severe deep convective clouds reach vertical velocities of several tens of metres per second (Heymsfield and Hjelmfelt, 1984; Miller et al., 1988). When the towering cumuli reach the tropopause at around 10 to 17 km (Gettelman et al., 2002), mainly depending on the geographic latitude, the airmass transported upwards in the updrafts cannot penetrate further up into the stratosphere. The cloudy air thus spreads out laterally and forms extensive anvils made up of ice-phase hydrometeors, that can cover areas much larger than the individual updraft towers feeding them. However, the inertia of the updraft can lead to an overshooting of the convective cloud tops, which plays an important role in the transport of water vapour into the lower stratosphere, especially in the tropics (Liu and Zipser, 2005; Dauhut et al., 2018).

During the mature stage of a deep convective cell, the upward motion in the updraft starts to get compensated by downdrafts that acquire negative buoyancy from condensate loading and latent cooling, e.g. due to melting processes. In the decaying stage of the cell, the updrafts weaken further and the vertical motion in the cell is dominated by the downdrafts, which terminates the active stage of the cell (Byers and Braham, 1948; Hobbs and Biswas, 1979).

When the negatively buoyant air in the downdrafts reaches the surface, it is forced to spread out horizontally and propagates as a gravity current. This forms *cold pools* made up of dense masses of air colder than the surrounding boundary layer, which spread out in a circular shape. The edges of these cold pools push up the unstable surrounding air, thus triggering the initiation of new cumulonimbus clouds, predominantly in the leading edge of storms (Thorpe et al., 1982; Tompkins, 2001).

The dominant structure of the individual confined updrafts in deep convective clouds means that they can be identified as individual characteristic cells (Byers and Braham, 1948; Lilly, 1975). Depending on the environmental conditions, the convective cells can either exist in an isolated fashion or organise into more complex entities. Isolated single-cell thunderstorms have lifetimes of up to a few tens of minutes (Lilly, 1975). However, thunderstorms also occur in clusters as multi-cell storms, e.g. arranged in a linear structure in so-called squall lines along or ahead of cold fronts (Hane, 1973). Deep convection can organise into even larger clusters of thunderstorms and form mesoscale convective systems (MCS) with a diameter of 100 km and more. These systems are more long-lived with lifetimes of several hours up to an entire day (Laing and Fritsch, 1997; Houze Jr., 2004; Houze, 2018). In this thesis, I mainly focus on isolated convective clouds in the form of supercell storms (Chap. 3) and scattered single-cell convection (Chap. 5).

Deep convective clouds generally occur as thunderstorms with intense lightning due to charge separation between the different hydrometeors, especially involving falling graupel and hail particles (Humphreys, 1914; Heymsfield and Hjelmfelt, 1984; Cotton et al., 2010). Detection of lightning through ground-based or space-borne instruments is an important tool in the identification of deep convection and can be used for the assessment of regional or global statistics of thunderstorms and deep convection (Orville et al., 2001; Steiger et al., 2002; Cecil et al., 2015). Radar observations, both from the operational networks in many industrialised countries and from dedicated research radars as part of measurement campaigns, have long been one of the most important techniques for our understanding of deep convective clouds (Hitschfeld, 1986; Stith et al., 2018).

In-situ measurements of cloud properties from aircraft are crucial for the understanding of the cloud microphysical processes (Heymsfield and Hjelmfelt, 1984). The danger to air traffic from the hazardous conditions in deep convective storms due to the strong vertical motions and the danger of aircraft icing (Cao et al., 2018) has been one of the main drivers for detailed research on the cloud microphysics, but also inherently limits the availability of this type if of in-situ measurements (Wendisch et al., 2016).

2.2.2. Cloud microphysical processes and their representation in numerical models

In this thesis, the evolution of deep convective clouds is primarily addressed from the perspective of the microphysical processes transferring mass and energy between the cloud hydrometeors and to the environmental air (Fig. 2.5b). This section thus provides a detailed overview of the most important cloud microphysical processes. This is focused on the processes in convective clouds and their representation in simulations with cloud-resolving models.

The microphysical processes in clouds consist of the transformation between water vapour and different types of hydrometeors, their transport and their evolution in the cloud. These processes act at length scales down to the size of the hydrometeors in the range of micrometres to centimetres. Therefore, they have to be parametrised in almost all practical applications of numerical models of the atmosphere, which ranges from high-resolution large eddy simulations (LES) with grid spacings of tens of metres to global model simulations with grid boxes of a few hundred kilometres in size (Khain et al., 2015). Fig. 2.6 visualises the most important microphysical processes discussed in more detail in this section. The cloud microphysical evolution is closely interlinked with other physical processes, which includes bidirectional influences from the microphysical developments on other processes and from these processes back on the microphysical evolution. These processes strongly depend on the thermodynamic and dynamical state of the atmosphere

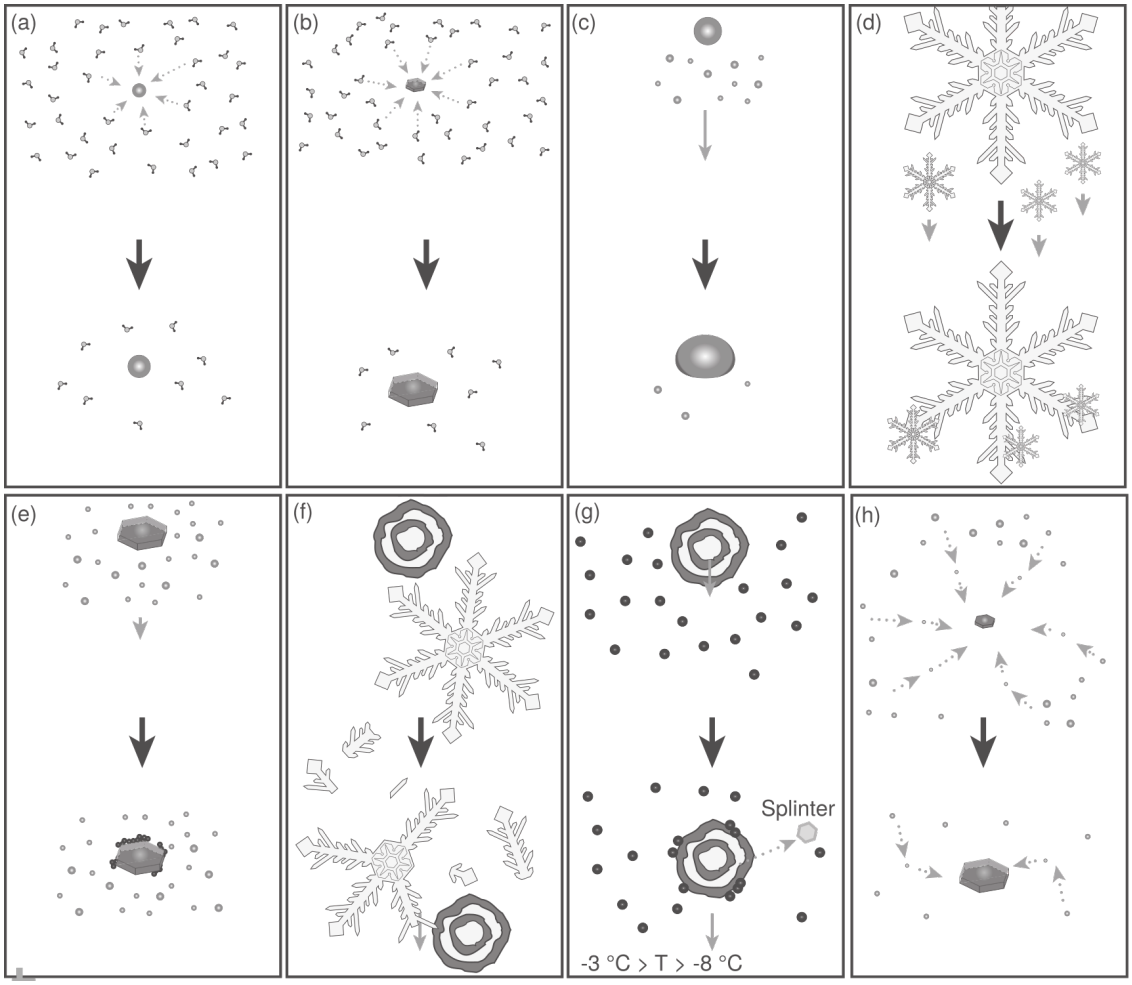

Figure 2.6: Some of the most important cloud microphysical processes described in this section: (a) condensational growth, (b) depositional growth, (c) collision–coalescence, (d) aggregation, (e) riming, ice multiplication due to (f) shattering by hailstones or (g) rime splintering (Hallett-Mossop process), (h) Wegener–Bergeron–Findeisen process (from Lohmann et al., 2016).

but also exhibit feedbacks to the dynamical evolution of the clouds through the release of latent heat and changes in cloud buoyancy (Cotton et al., 2010; Pruppacher and Klett, 2010; Khain et al., 2015). Furthermore, the resulting hydrometeor mixing ratios are passed to the model radiation scheme. The lack of information transfer about the hydrometeor sizes in model radiation schemes contributes to the uncertainty in the assessment of aerosol effects from modelling studies (White et al., 2017).

The calculations in almost all numerical microphysics schemes are based on a separation of the hydrometeors into different empirical classes such as cloud droplets, raindrops,

pristine ice, snow, graupel or hail. The separation of hydrometeors into fixed categories is necessary to take into account the strongly differing physical properties like density and shape, that affect important parameters and processes like fall speeds in the sedimentation or collision cross-sections. However, the slightly arbitrary semi-empirical nature of this separation into different classes, which can only map the complexity of the hydrometeor evolution in a limited way, is often criticised as a primary source of uncertainty (Khain et al., 2015; White et al., 2017). Several approaches towards partially overcoming those concerns will be touched upon in the more detailed descriptions of the individual implementations.

The main approaches to treat hydrometeors in model schemes can be divided into *bulk microphysics schemes* and *bin microphysics schemes* (Khain et al., 2015), similar to the approaches used for the representation of aerosols in numerical models (Sect. 2.1). Bulk microphysics schemes assume that the hydrometeors can be described by distinct classes (e.g. cloud droplets, rain, snow, cloud ice) each represented by a particle size distribution. Earlier modelling approaches used exponential size distributions for droplets or log-normal size distributions like the one shown for the aerosol particles in equation (2.3) (Pruppacher and Klett, 2010). Most current bulk schemes make use of a modified gamma function for the number of particles N dependent on the hydrometeor diameter D (Khain et al., 2015; Lohmann et al., 2016; Khain and Pinsky, 2018)

$$N(D) = N_0 D^{\mu} e^{-\lambda D}, \tag{2.18}$$

with the intercept N_0, the slope parameter λ, and a shape parameter μ.

Single-moment bulk microphysics schemes only take into account one moment of the hydrometeor distribution describing the mass mixing ratio of an individual hydrometeor class. Double-moment bulk schemes include a prognostic treatment of a second moment of the hydrometeor size distributions describing the number mixing ratio. This inclusion of the number concentrations of hydrometeors in the microphysical processes is crucial

for capturing the effects of aerosols acting as CCN or IN on the cloud microphysical evolution (Igel et al., 2014; Khain et al., 2015). Some bulk microphysics schemes include a third moment of the distribution that can include further information about the shape of the hydrometeors, e.g. describing the radar reflectivity (Milbrandt and Yau, 2005a; b). However, these triple-moment schemes have not entered widespread use in atmospheric models. Recent developments such as the Predicted Particle Properties (P3) microphysics scheme (Morrison and Milbrandt, 2014; Morrison et al., 2015) have focused on overcoming the strict, and sometimes slightly arbitrary classification of the different hydrometeors in bulk microphysics schemes by using one single ice class with smoothly varying parameters like density or riming fraction.The bulk microphysics schemes studied in more detail in this thesis (Thompson et al., 2008; Morrison et al., 2009; Saleeby and van den Heever, 2013) are all double-moment microphysics schemes prognostic in a different set of hydrometeor mass and number concentrations.

Bin microphysics schemes (e.g. Reisin et al., 1996a; b; Lynn et al., 2005a; b; Lebo and Seinfeld, 2011) represent the different hydrometeor classes by resolving the size distribution for a large number of discrete size bins, which leads to a more flexible representation of particle size distributions. This more detailed approach allows for a more realistic representation of numerous physical processes such as the variety of collection processes. The main advantages arise from the treatment of the liquid phase, which does not require the artificial separation into cloud droplets and raindrops necessary in bulk schemes. The ice-phase hydrometeors are generally separated into individual classes similar to the bulk schemes due to their complex shape and properties (Khain et al., 2015). However, the more detailed description of the size distributions makes these schemes computationally far more expensive than e.g. double-moment bulk schemes, because of the calculation of a large number of microphysical interactions and an increased number of advected prognostic variables. This limits the use of bin microphysics in most applications involving extensive model domains and long simulations as well as routine applications, e.g. for numerical weather forecasts (Khain et al., 2015).

The limitations of these two types of microphysics schemes can be partly overcome by using bin-emulating schemes such as the RAMS microphysics scheme (Walko et al., 1995; Saleeby and Cotton, 2004; Saleeby and van den Heever, 2013) used in Chap. 5. These schemes include a representation of the hydrometeor size distributions through individual size bins similar to a full bin microphysics scheme for some of the actual microphysical process rate calculations while reducing the size distribution back to a double- or triple-moment formulations for the advection of the variables.

Warm-phase microphysical processes

Although warm-phase processes are generally much better understood than the processes in the mixed and ice phase of clouds, there are several important challenges in the representation of warm-phase processes in numerical models (Pruppacher and Klett, 2010; Khain et al., 2015). This is especially important when studying aerosol–cloud interactions since several proposed effects of aerosols on clouds, including deep convective clouds, are based on the role of changes in CCN in clouds with a warm cloud base (Rosenfeld et al., 2008; Stevens and Feingold, 2009).

One major aspect in which current microphysics schemes differ strongly is the representation of *condensation* and *evaporation* of cloud droplets. Numerous models circumvent the explicit calculation of condensation and evaporation rates by assuming a thermodynamic equilibrium between cloud droplets and water vapour inside the clouds. This allows using a simple approximation called *saturation adjustment* (Lebo et al., 2012). For this approach, the supersaturation or subsaturation that has built up in a model time step is calculated as the difference between the vapour pressure and saturation vapour pressure over water. Subsequently, the amount of water vapour is adjusted to saturation with the difference in water mass transferred in the form of evaporation or condensation including the respective release of latent heat. Microphysics formulations that do not make use of saturation adjustment describe the condensation of cloud droplets explicitly through a solution of the diffusion equation (Khain et al., 2015). In bin-resolving or bin-emulating

microphysics schemes, these calculations take into account the number of cloud droplets in the individual size bins (Khain et al., 2015). For bulk schemes, different formulations have been presented, relying either on a bin-emulating formulation (Saleeby and van den Heever, 2013) or on approximate solutions of the diffusion equation (Morrison and Milbrandt, 2014).

Models prognostic supersaturation allow for the build-up of larger supersaturations in strong updrafts, where the adiabatic expansion of the air produces supersaturation faster than it can be depleted due to condensation of cloud droplets, notably where the number of droplets has significantly decreased due to collision-coalescence processes (Khain et al., 2012; 2015). Lebo et al. (2012) found that larger CDNC due to a higher number of aerosols acting as CCN can significantly increase condensational growth of droplets in supersaturated regions of the cloud and similarly lead to higher evaporation rates in sub-saturated parts of the clouds when using microphysics scheme with prognostic supersaturation. These two effects are not represented when using saturation adjustment, thus muting an essential aspect of aerosol effects on cloud microphysics (Lebo et al., 2012). Supersaturation adjustment often leads to an overestimation of condensation and hence latent heat release, especially in the lower parts of the clouds (Lebo et al., 2012; Khain et al., 2015).

In this thesis, the simulations with the two bulk microphysics schemes in WRF (Chap. 3, 4, 5) make use of saturation adjustment, while the WRF simulations with the spectral-bin microphysics scheme (Chap. 3) and the RAMS model (Chap. 5) feature a prognostic treatment of supersaturation as well as condensation and evaporation processes.

Evaporation of raindrops plays an essential role in determining the thermal state of the sub-cloud layer through evaporative cooling, which determines the formation of cold pools and strongly affects the subsequent evolution of a cloud or surrounding clouds. Thus, raindrop evaporation is parametrised explicitly in the two WRF bulk microphysics schemes used in this thesis. In contrast, condensation on raindrops is generally negligible due to the small relative surface area of the large raindrops compared to cloud droplets

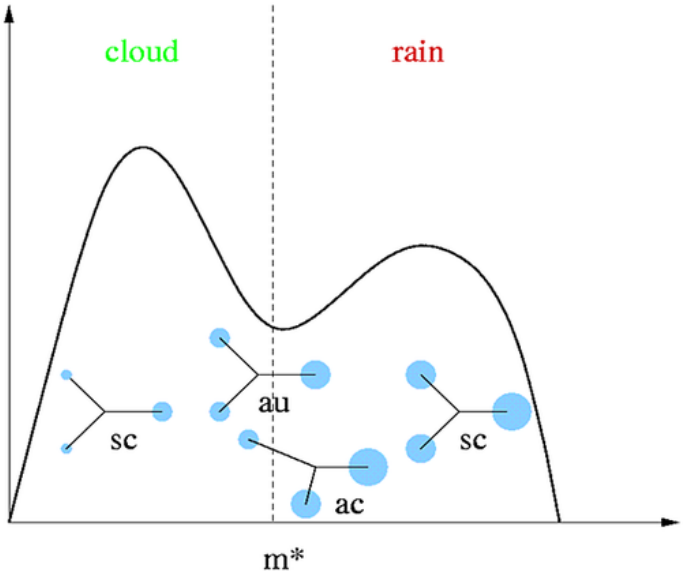

Figure 2.7: Schematic illustration of the collection processes in the warm phase parametrised as autoconversion of cloud droplets (au), accretion of cloud droplets by rain (ac) and self-collection of cloud droplets and raindrops (sc). The size distribution is shown related to the mass as f(m) with $m^{\star}$ denoting the mass separating cloud droplets from raindrops (from Khain et al. (2015) after Beheng (2012)).

(Cotton et al., 2010; Pruppacher and Klett, 2010).

The formation of raindrops due to *collision-coalescence* of cloud droplets is the essential processes for the formation of precipitation in liquid clouds (Kessler, 1969; Berry and Reinhardt, 1974b; Pruppacher and Klett, 2010). The description of the collision-coalescence in microphysics schemes is crucial for the representation of aerosol–cloud interactions in numerical models (Khain et al., 2015) due to the effect of aerosols on the CDNC. In bin schemes and bin-emulating schemes, these processes can be represented through numerical solutions to the collection equation (Khain et al., 2015) for the combinations of the different size bins. As opposed to the resolved treatment in bin schemes, collisions-coalescence processes between individual cloud droplets or between cloud droplets and raindrops have to be parametrised in bulk microphysics schemes, since cloud droplets and raindrops are represented by two individual size distributions (Fig. 2.7).

The parametrisation of so-called *autoconversion* describes collisions between cloud droplets to form raindrops (Pruppacher and Klett, 2010). Most current parametrisations in bulk

microphysics schemes are based on solutions to the collision-coalescence equation using a regression to simulation results from detailed bin-microphysics simulations to derive the respective parameters. In the Morrison scheme used in Chap. 3 and Chap. 5, a semi-empirical formulation based on a solution of the collection equation based on results from LES simulations with a bin microphysics formulation from (Khairoutdinov and Kogan, 2000) is used for the transfer of mass Q_{aut} and number N_{aut}, in the autoconversion parametrisation

$$Q_{\text{aut}} = 1350\, q_{\text{c}}^{2.47} N_{\text{c}}^{-1.79}, \tag{2.19}$$

with the cloud water mixing ratio q_{c} and CDNC denoted as N_{c}. The changes of droplet and rain number concentrations follow from the mean mass of cloud droplets and the mass of the smallest possible raindrop of radius r_{c}.

$$N_{\text{c,aut}} = \frac{Q_{\text{aut}}}{\frac{q_{\text{c}}}{N_{\text{c}}}} \tag{2.20}$$

$$N_{\text{r,aut}} = \frac{Q_{\text{aut}}}{\frac{4}{3}\pi\rho_w r_{\text{c}}^3} \tag{2.21}$$

In the Thompson microphysics scheme used in WRF model simulations in Chap. 3, autoconversion follows a relationship from Berry and Reinhardt (1974a,b) and another commonly used parametrisations has been derived in (Beheng, 1994) and (Seifert and Beheng, 2001). Although these parametrisations of the autoconversion process differ in their detailed form, they all lead to an increased transfer from droplets to rain with increased cloud water content, but a decrease with increased CDNC. These relationships represent the reduced probability of small cloud droplets colliding and forming a droplet large enough to represent a transfer to the hydrometeor class of raindrops. Differences in the autoconversion parametrisation constitute a significant factor of uncertainty in the representation of warm-phase microphysics in bulk schemes (White et al., 2017). Self-collection of cloud droplets, which describes the collision of two droplets to form a larger droplet still smal-

ler than the separation radius between cloud droplets and raindrops, is not represented in the two bulk microphysics schemes in WRF (Morrison and Thompson) used in this thesis. Once raindrops have formed, they can be very effective in collecting the smaller cloud droplets (Berry and Reinhardt, 1974c; Yau and Rogers, 1989; Pruppacher and Klett, 2010). This process is parameterised as *droplet accretion by rain* in most bulk microphysics schemes. The simulations with the Morrison microphysics scheme use the formulation from Khairoutdinov and Kogan (2000).

$$Q_{\text{acc}} = 67\,(q_{\text{c}} N_{\text{c}})^{1.15} \tag{2.22}$$

The Thompson microphysics scheme uses an accretion formulation based on Berry and Reinhardt (1974a,b). Accretion of cloud droplets by rain reduces the number concentration of cloud droplets but leaves the number of raindrops unchanged, while transferring water mass from droplet class to the rain class.

Once active, the process is much more effective at turning cloud water into rain than the autoconversion of droplets and contributes the majority of warm-rain formation in bulk microphysics schemes (Hill et al., 2015). However, the onset of this process is dependent on the existence of precipitation size droplets in the cloud, which can stem from either the autoconversion of cloud droplets described before or melting of ice-phase hydrometeors. This way the dependence of the autoconversion process on the droplet number concentration, and thus impacts from aerosol number concentrations, can significantly control the timing of the onset and the magnitude of surface precipitation from warm-phase processes in model simulations using bulk microphysics (Hill et al., 2015; White et al., 2017).

Bin microphysics schemes do not include the artificial split of liquid water drops into small cloud droplets and larger raindrops. Accretion of droplets of different size can thus be described directly through the stochastic collection equation for the different size bins of liquid water drops. The microphysics scheme used in RAMS in Chap. 5 makes use of a bin-emulating formulation for the warm-phase processes (Saleeby and Cotton, 2004).

Mixed- and ice-phase microphysics

As opposed to the cloud droplets and raindrops in the liquid phase, the frozen hydrometeors in clouds show a wide variety in shape and density. This leads to significant challenges in representing the different formation and evolution pathways in a numerical model (Pruppacher and Klett, 2010). In most microphysics schemes, the frozen hydrometeors are separated into several different categories, for example, pristine ice particles, snowflakes, graupel or hailstones.

The two bulk microphysics schemes in WRF used in this thesis include ice, snow and an additional dense hydrometeor category forming either graupel or hail. The RAMS microphysics scheme (Saleeby and Cotton, 2004; Saleeby and van den Heever, 2013) used in Chap. 5 stands out from most other bulk microphysics schemes by the number of different ice hydrometeor classes, which include pristine ice, snow, aggregates, graupel and hail. The spectral-bin microphysics scheme in WRF exists in two versions that differ in the number of hydrometeor classes in the ice phase apart from the number of size bins in each hydrometeor category. The simulations in this thesis make use of the full SBM scheme (Lynn et al., 2005a; Khain and Lynn, 2009) which includes three different categories of pristine ice particles (columns, dendrites and plates) along with snow, graupel and hail.

The *freezing* of liquid hydrometeors, cloud droplets and rain, can be separated into several different freezing mechanisms depending on temperature and the availability of suitable IN (Vali, 1996; Vali et al., 2015). *Homogeneous freezing* describes the freezing of cloud droplets without a specific nucleating particle which only occurs at very low temperatures. Typical temperatures used in microphysics schemes are -40 °C (Morrison et al., 2005) or -38 °C (Thompson et al., 2004). In the presence of ice-nucleating particles, *heterogeneous freezing* allows supercooled droplets and raindrops to freeze at significantly higher temperatures (Lohmann et al., 2016). In the case of *immersion freezing* the freezing is initiated due to the presence of an IN suspended in the liquid droplet, while *contact freezing* happens on the collision of a supercooled droplet with a suitable dry aerosol particle

such as dust. *Condensation freezing* describes the formation of an ice particle during the activation of an aerosol particle. Furthermore, water vapour can be directly deposited on the surface of IN in the form of *deposition nucleation*. In contrast to the relatively numerous aerosol particles acting as CCN, only a small number of aerosols can act as efficient IN. Generally only one in every 10^5 to 10^6 aerosol particles acts as an IN, mainly specific types of dust and biological particles such as bacteria or fungal spores (Kanji et al., 2017). The simulations in this thesis all focus on the role of aerosols acting as CCN, thus IN concentrations are not coupled to the aerosol variations, but described by parametrisations that are held fixed for all simulations.

Fracturing and shattering of existing ice particles in *secondary ice formation* (also called ice multiplications) can increase the initial number of ice particles by several orders of magnitude (Mossop et al., 1972; Choularton et al., 1978). These processes often occur during the formation of the ice particles, i.e. during freezing or due to sublimation processes or in collisions between different hydrometeors (Choularton et al., 1978; Pruppacher and Klett, 2010). An important component to the secondary ice production is the so-called *Hallett-Mossop process* in mixed-phase clouds (Hallett and Mossop, 1974), that describes the splintering of supercooled droplets or raindrops upon freezing in riming processes. The process mainly occurs in a temperature range between -3 °C and -8 °C and with substantial concentrations of large cloud droplets with larger frozen hydrometeor particles such as graupel. This provides a large number of additional small ice particles that can significantly affect the microphysical evolution of the cloud (Lohmann et al., 2016). This process is explicitly parametrised in most cloud microphysics schemes (see also Tab. 3.2 and Tab. 3.3 in Chap. 3).

Riming describes the accretion of supercooled cloud droplets and raindrops by frozen hydrometeors (Pruppacher and Klett, 2010). This can lead to a transfer of hydrometeors between frozen hydrometeor classes and plays an important role in the formation of graupel and hail from snow or pristine ice.

Melting of ice-phase hydrometeors plays an important role in the feedback of the micro-

physics on the cloud dynamics, especially in the formation of downdrafts (Knupp and Cotton, 1985; Srivastava, 1987). The melting of the different ice-phase hydrometeors is described with varying levels of complexity in microphysics models. The simplest approaches assume instantaneously melting of small hydrometeors such as pristine ice at temperatures exceeding 0 °C. More complex calculations take into account the diffusion of heat through a liquid layer surrounding the core of a larger frozen hydrometeor such as hail, shedding of water from melting particles or size-resolved melting in bin microphysics schemes (Fan et al., 2012; Khain et al., 2015). Collisions between raindrops and frozen hydrometeors can be separated into two different cases. Depending on the size of the particles involved and the ambient temperature either riming of rain similar to the cloud droplets results in frozen hydrometeors or subsequent melting of the resulting hydrometeors leads to larger raindrops.

Once formed in a cloud, ice-phase hydrometeors can gain or lose water mass due to *deposition* and *sublimation* processes, depending on the saturation vapour pressure over ice (Pruppacher and Klett, 2010). This leads to a relatively smoothly varying latent heating or cooling in the upper layers of the cloud (McGee and van den Heever, 2013). In contrast to the condensation/evaporation for the liquid phase, these diffusional growth processes of ice-phase hydrometeors are explicitly calculated in all microphysics schemes used in this thesis. The bin schemes allow for a size resolving evaluation of the diffusional growth equations, while bulk schemes use a specific parametrisation of these processes for each hydrometeor class (Khain et al., 2015). Thus, shifts in the prevalent ice hydrometeor class can strongly affect the deposition and sublimation processes in the cloud.

If the vapour pressure in mixed-phase clouds reaches a value in between the saturation vapour pressure over ice and water surfaces, the ice hydrometeors can grow rapidly through deposition transfer on the expense of supercooled droplets. This is known as the *Wegener-Bergeron-Findeisen* (WBF) process (Wegener, 1911; Findeisen, 1938; Findeisen et al., 2015; Storelvmo and Tan, 2015). In the case of a small number concentration of frozen hydrometeors, this can lead to rapid growth of relatively large particles that contribute

significantly to the cold-rain precipitation. However, recent studies have shown, that the WBF process as described here is not always active in mixed-phase clouds (Korolev, 2007).

2.2.3. High-resolution simulations of deep convection

In GCMs with grid sizes of a few tens to hundreds of kilometres, convective processes have to be parametrised due to their scale of only hundreds of metres to a few kilometres (Betts, 1997). Most global models make use of simple bulk mass flux schemes such as Tiedtke (1989). Additionally, the convective cloud microphysics in GCMs are often relatively basic, e.g. in the form of single-moment schemes with usually no representation of aerosol–cloud interactions, or in some recent parameterisations a limited representation of aerosol–cloud interactions (Zhang and Song, 2016). Therefore, the effects of aerosols on convective clouds are only represented in a limited way in most current climate models (Lohmann, 2008; Rosenfeld et al., 2014b; Fan et al., 2016). There are, however, parametrisation approaches for GCMs that aim at taking these effects into account, e.g. by simulating a spectrum of convective clouds instead of a single formulation for an average convective cloud (Wagner and Graf, 2010; Kipling et al., 2017; Labbouz et al., 2018), by representing probability density functions (PDF) for the subgrid variations of large-scale variables (Guo et al., 2015; Zhang et al., 2017) or in the form of superparametrisations resolving the subgrid-scale evolution in an embedded two-dimensional high-resolution model (Grabowski, 2001; Khairoutdinov and Randall, 2001; Khairoutdinov et al., 2005). Simulations with high-resolution limited-area models can be divided into so-called *convection-permitting* simulations with grid spacings of a few kilometres that allow for the resolution of the most important features of strong deep convective clouds and *cloud-resolving modelling* (CRM) that explicitly resolves the most important features of deep convective clouds (Langhans et al., 2012; Guichard and Couvreux, 2017). In recent years, convection-resolving models have started to be used for global simulations

(Satoh et al., 2017; Neumann et al., 2019) or long-term analyses on a continental scale (Ban et al., 2014). However, these simulations are characterised by extensive computational expenses, which will prevent their use in most research projects for many years to come (Neumann et al., 2019).

It has been shown that simulations with grid spacing of only tens to a few hundred metres (and thus effective resolutions well below the kilometre scale) are very beneficial in fully resolving the convective dynamics in cumulus clouds, especially when looking at secondary updrafts, smaller cumulus clouds, cold pool dynamics and entrainment of environmental air at the cloud edges (Bryan et al., 2003; Khairoutdinov et al., 2009; McGee and van den Heever, 2013). Simulations at these grid lengths are called *large eddy simulations* (LES) since the largest eddies of the boundary layer turbulence are explicitly resolved. The main difference in the parametrisations to CRM modelling is that the boundary layer turbulence is treated three-dimensionally in these simulations, compared to the separation in the boundary layer parametrisations used for convection resolving simulations at grid lengths of more than a few hundred metres. Nevertheless, these simulations still have to parametrise a wide range of sub-scale physical processes including the cloud microphysics (Khairoutdinov et al., 2009). (Mason, 1989; 1994). LES studies are usually performed on relatively small domains with idealised setups such as periodical domains, which does not allow for the evolution of structures on a larger scale or the interaction of the convective evolution with variations on a synoptic scale (Guichard and Couvreux, 2017). While most LES models have been used with a focus on warm-phase processes for a long time, there has been a dedicated focus on studying mixed-phase clouds with LES models in recent years (Khairoutdinov et al., 2009; Ovchinnikov et al., 2014; Savre et al., 2015; Heath et al., 2017).

In this thesis, simulation are performed at the CRM scale with horizontal grid spacings of 1 km in Chap. 3 and 500 m in Chap. 5.

2.2.4. Cloud tracking and time-resolved analyses of deep convection

The effects of aerosols over the life cycle of convective clouds have been pointed out to be of major importance for our understanding of aerosol-convection interactions (Tao et al., 2012; Altaratz et al., 2014; Fan et al., 2016). Assessing the time evolution of clouds and possible impacts of changes in aerosol conditions based on observational data or model simulations requires methods that identify and track individual clouds in the datasets and provide means to extract relevant quantities over the course of the cloud lifecycle. These types of analyses are generally addressed as *cloud tracking* and have played an important role in a wide range of applications in the atmospheric sciences based on different types of datasets over recent decades (Menzel, 2001). The algorithms developed for these analyses generally consist of a similar combination of the following individual analysis steps. First, relevant cloud features are identified in the dataset, e.g. based on specific threshold values or the identification of relative maxima or minima. Subsequently, these identified features are linked up into consistent cloud trajectories, which can be performed based on different types of algorithms, e.g. by using overlap assumptions or forecasting cloud motion from previous time steps. Quantitative analyses often require determining a representative area or volume of the individual clouds to derive representative statistical quantities from cloud properties in the input datasets.

Tracking of convective clouds in radar retrievals has been performed for decades (Crane, 1979; Rosenfeld, 1987), mainly with a focus on different types of severe weather implications, such as tornados, flash floods or hailstorms (Dixon and Wiener, 1993; Lakshmanan and Smith, 2009b). Geostationary satellite observations have been used extensively with cloud tracking analyses and object-based analyses, e.g. for understanding the initiation and evolution of different types of cumulus clouds (Mecikalski and Bedka, 2006; Mecikalski et al., 2011; Senf et al., 2015). By using a combination of different channels on geostationary satellite imagers, specific tracking algorithms have been developed to investigate deep convective clouds over their time evolution (Zinner et al., 2008; Autonès and Moisselin, 2013; Zinner et al., 2013). Tracking clouds and their horizontal motion

has also been used extensively in deriving horizontal wind fields from geostationary satellite retrievals for the use in numerical weather forecasting or the validation of forecasts (Menzel et al., 1983; Schmetz et al., 1993; Nieman et al., 1997).

Tracking of individual clouds in three-dimensional output of high-resolution model simulations at LES or CRM scale has often focussed on understanding shallow convective clouds. (Zhao and Austin, 2005a; b; Heus et al., 2009; Heus and Seifert, 2013; Heiblum et al., 2016a; b). Only a few studies have focussed on using these kinds of approaches to study deep convective clouds in the output of three-dimensional cloud-resolving model simulations (Terwey and Rozoff, 2014; Chen et al., 2017). Chap. 4 gives a more detailed overview of existing cloud tracking approaches for different applications and presents the development of the new tracking algorithm tobac that is applied for the analysis of CRM simulations in Chap. 5.

2.3. Aerosol–cloud interactions

Due to the important role of aerosols in cloud formation (Sect. 2.1.2), aerosol–cloud interactions play an important role in the climate system. Changes in cloud radiative properties and cloud cover due to anthropogenic changes in aerosols are of very important for the total anthropogenic radiative forcing of the climate system (Boucher et al., 2013) and generally referred to as *aerosol indirect effects* on climate (Lohmann and Feichter, 2005). The effects of changes in atmospheric aerosols on clouds are complex, since they involve an entire chain of different physical processes, such as the formation of suitable CCN or IN, droplet activation (Sect. 2.1.2) and the microphysical pathways of these changes through the cloud microphysical evolution (Sect. 2.2.2). Furthermore, the interactions between aerosols and clouds are strongly dependent on the cloud type and are entangled with the dynamical and thermodynamical evolution of the clouds (Fan et al., 2016). Assessments based on both satellite observations (Penner et al., 2011) and global model simulations (Lohmann and Feichter, 2005; Penner et al., 2006; Quaas et al., 2009;

Lohmann et al., 2010) have not been able to significantly narrow down the possible range of the effect of aerosol–cloud interactions on total radiative forcing. Thus, aerosol–cloud interactions have explicitly been pointed out as the aspect of anthropogenic radiative forcing with the most substantial uncertainty and the lowest level of confidence (Fig. 2.1 in the 5th assessment report of the IPCC (IPCC, 2013a; Myhre et al., 2013b).

The effects of aerosols on clouds have been most extensively studied based on pathways that are based on aerosols acting as CCN (Sect. 2.3) and subsequently changing the number of cloud droplets in liquid clouds (Rosenfeld et al., 2014b). Assuming no change in the total liquid water content in the clouds, this change in CDNC is associated with a change in the radius of cloud droplets, which has significant implications for the cloud evolution that are best understood for liquid clouds. The so-called *first aerosol indirect effect* on clouds and the climate system is based on the change of the cloud albedo due to the smaller and thus optically brighter cloud droplets, first investigated by Twomey (1974) and Twomey (1977b).

The same changes to CDNC and cloud droplet radius are also investigated for their impact on the cloud extent and cloud lifetime. These possible changes to the clouds constitute the so-called *second aerosol indirect effect* or cloud lifetime effect on the radiative balance of liquid clouds, which was first proposed by Albrecht (1989). Due to the smaller radius, the cloud droplets are less prone to grow into precipitation-size raindrops and rain out, which leads to a longer-lasting cloud and thus an effect on the overall cloud radiative balance. However, this effect is interlinked with a wide range of processes in the evolution of the cloud over time (Sect. 2.2.2). In mixed- and ice-phase clouds, cloud lifetimes can be affected by similar changes to the effective radius of ice particles due to aerosols acting as CCN or IN (Ekman et al., 2007; Fan et al., 2010). However, this effect involves a wider range of microphysical and dynamical processes as well as a different radiative forcing due to the longwave emission at higher altitude (Koren et al., 2010b) and will be discussed in more detail for deep convective clouds in the following section 2.3.1.

These two types of aerosol indirect effects have been studied extensively for specific

types of warm stratiform clouds, e.g. in the stratocumulus decks of the subtropical oceans (Wood, 2012). The effects of changes in aerosols on different types of convective clouds, however, are much harder to assess (Stevens and Feingold, 2009; Fan et al., 2016) and will be discussed in more detail in Sect. 2.3.1.

Several studies have shown that the relationships between of CCN concentrations, CDNC, cloud fraction, liquid water path and cloud albedo are strongly interconnected (Gryspeerdt et al., 2014; Feingold et al., 2016; Gryspeerdt et al., 2018), which leads to a much more complex picture of aerosol–cloud interactions from what is implied by simple composition into first and second aerosol indirect effect. Using AOD as a proxy for CCN to investigate the impact of aerosols on deep convective clouds by microphysical processes introduces challenges due to the effects of hygroscopic growth of aerosols (Altaratz et al., 2013). Furthermore, there are limitations in the scaling between the number of aerosols acting as CCN and the total radiative effect of the aerosol column (Shinozuka et al., 2015).

In addition to the microphysical effects on clouds through aerosols acting as CCN or IN, aerosol can also impact clouds through their direct influence on the radiative fluxes in the atmosphere (Sect. 2.1). These changes impact the environment in which clouds develop and thus affect the evolution and radiative effects forming the *semi-direct aerosol effect* on clouds (Hansen et al., 1997; Ackerman et al., 2000). This includes the radiative impact of both aerosol particles that are effective short-wave absorbers, e.g. black carbon, and short-wave scattering aerosols like sea salt or sulphate. Both can change the incoming solar radiation available for heating the surface layer of the atmosphere and alter the thermal profile in the atmosphere. The impact has been assessed based on satellite observations (Koren et al., 2004; 2008) and numerical models simulations at different scales (Lohmann and Feichter, 2001; Johnson et al., 2004, e.g.). Many studies find that increased absorption due to absorbing aerosols such as soot in the lower troposphere leads to weaker convection and decreased cloudiness (Koren et al., 2004; Feingold et al., 2005), which could act as one of the mechanisms that can effectively buffer the microphysical impacts of aerosols on clouds (Stevens and Feingold, 2009). There are also possible

pathways to an increase in cloud cover and thickness, e.g. in the case of aerosols above stratocumulus clouds (Johnson et al., 2004; Wilcox, 2010). The terminology of the last IPCC report (Boucher et al., 2013) includes the semi-direct effects as an adjustment in the effective radiative forcing from aerosol–radiation interactions ERF_{ari} (Fig. 2.2).

All aerosol–cloud interactions described until this point covered the effects of aerosols on clouds. However, there are also important feedbacks from clouds back on the aerosol distribution. The removal of aerosols from the atmosphere, especially for smaller particles, happens predominantly through activation scavenging in clouds and wet scavenging by precipitation (Seinfeld and Pandis, 2016). Therefore, cloud processes strongly determine the size distribution and chemical composition of atmospheric aerosols. This, in turn, affects the evolution of subsequent clouds through the processes describes before, which leads to a closely coupled system between atmospheric aerosols and clouds. These feedbacks have been included in many model simulations and can significantly impact assessments of aerosol–cloud interactions and their effects on the climate system (Ekman et al., 2011). In this thesis, however, simulations do not resolve such two-way feedbacks between aerosols and clouds in a fully coupled model setup.

2.3.1. Aerosol effects on deep convective clouds

Despite a dedicated focus of research on mixed- and ice-phase microphysics during the last decades, aerosol effects on deep convective clouds and a range of atmospheric processes involving convective clouds are still poorly understood (Boucher et al., 2013; Lohmann et al., 2016). This is mainly due to the wide range of competing and interacting processes involved in the development of deep convective clouds (Stevens and Feingold, 2009; Seifert et al., 2012; Lohmann et al., 2016). Furthermore, the relatively small spatial scale of tens or hundreds of metres to a few kilometres relevant in convective clouds and the evolution on comparatively short timescales of minutes (Cotton et al., 2010; Houze, 2014) pose significant challenges to the representation of these effects in different

types of numerical models and observational assessments (Boucher et al., 2013). Over recent years, several review articles (Tao et al., 2012; Altaratz et al., 2014; Rosenfeld et al., 2014a; Fan et al., 2016) have summarised the most important aspects of aerosol effects on clouds with a focus on deep convective clouds.

Different mechanisms leading to a strengthening of deep convective clouds, e.g. in the form of stronger updrafts and higher cloud tops, have been proposed over recent decades and are actively discussed as different pathways leading to a *convective invigoration* due to increases in atmospheric aerosols. (Rosenfeld et al., 2008; Stevens and Feingold, 2009; Lebo and Seinfeld, 2011). These concepts generally rely on the effect of an increased CDNC and thus smaller cloud droplet effective radius as discussed for the aerosol effects on liquid clouds in Sect. 2.3. The pathway to the invigoration of deep convective clouds through latent heating from additional freezing (Williams et al., 2002; Rosenfeld et al., 2008; 2014b) has been discussed extensively over the last decade and is shown schematically in Fig. 2.8. This conceptual idea is based on the delay or suppression of precipitation in the warm phase of the cloud due to increased CCN concentration, which allows for increased transport of condensate through the freezing level and subsequent increases in the latent heat release from freezing. This would lead to a more vigorous development of the ice phase of the cloud and increased surface precipitation due to the associated cold-rain processes. Rosenfeld et al. (2008) point out in their assessment that the subsequent off-loading of the additional ice-phase hydrometeors and latent cooling due to melting in lower layers contributes to the invigoration effect. This chain of effects is suggested to be strongest for clouds with a relatively warm cloud base, where the delay in the onset of precipitation allows for an accumulation of additional cloud water lifted to the freezing level (Li et al., 2011; Fan et al., 2012; Rosenfeld et al., 2014b).

However, the idea of convective invigoration does not strictly require the involvement of ice-phase processes. Stevens and Feingold (2009) postulate a pathway to the invigoration of warm cumulus clouds due to an increase in condensed water and smaller cloud droplets, which lead to increased evaporation at the cloud top. This further destabilises

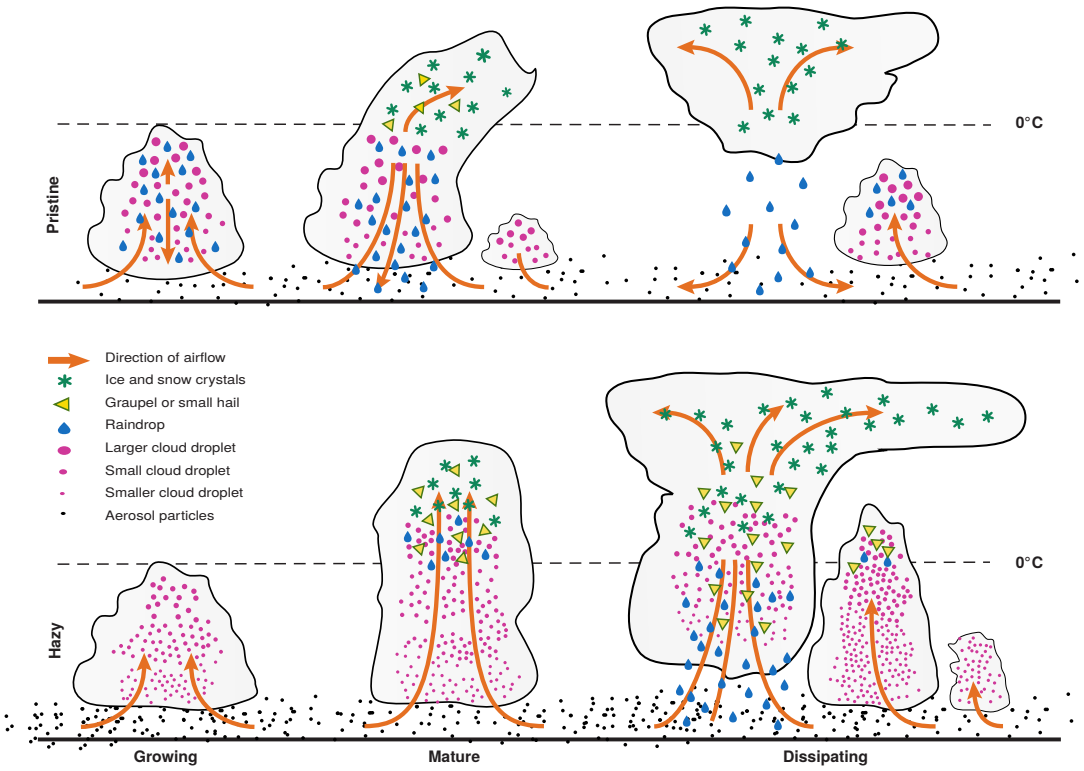

Figure 2.8: Convective invigoration through additional heat release from freezing has been proposed as a hypothesis for aerosol effect on deep convective clouds. The top panel shows the development of a deep convective cloud for a low CCN environment, the bottom panel for a high CCN environment. The increase in CDNC for the higher CCN concentrations leads to a suppression of the warm rain processes, which allows more condensate to be transported above the level of freezing. Additional freezing increases the latent heat release, leading to a stronger development of the deep convective cloud (adapted from Rosenfeld et al., 2008).

the cloud-top region and leads to an additional lifting of the cloud tops. Several studies have pointed out the strong role of warm-phase invigoration (Lebo, 2014; Sheffield et al., 2015; Lebo, 2018; Miltenberger et al., 2018a) based on increased condensation on smaller but more numerous cloud droplets, which can have a stronger effect than the cold-phase invigoration. The additional condensate loading from increased condensation and the decreased removal of hydrometeors due to precipitation can substantially reduce the buoyancy of the rising air parcels in the convective updrafts and has been pointed out (Grabowski and Morrison, 2016) as a major factor reducing the effective changes in the dynamical evolution of the cloud based on the invigoration mechanisms discussed before.

There have been several observational studies that indicate the presence of convective invigoration in deep convective clouds. Andreae et al. (2004) used in-situ aircraft measurements to show that intense pollution from biomass burning aerosols leads to an invigoration of deep convection over the Amazon rain forest in the form of higher cloud tops and increased precipitation. Similar results were obtained from satellite-based (Lin et al., 2006) and ground-based radar and lightning analyses in the same region (Williams et al., 2002). Studies using extensive ground-based measurements (Li et al., 2011; Yan et al., 2014) in the Southern Great Plains (SGP) of the United States reported clear signals of convective invigoration for clouds with warm cloud bases and cold cloud tops. Based on satellite observations across most of the globe. Koren et al. (2012) showed an increase in precipitation and cloud top height for increased AOD, both for continental and marine settings, and found results for specific regions of the tropical oceans in Koren et al. (2014). This was confirmed based on different satellite retrievals in Storer et al. (2014) for the tropical Atlantic.

There are, however, several recent studies that question some of the observed relationships or their interpretation as manifestations of the invigoration hypothesis in observations (Engström and Ekman, 2010; Wall et al., 2013; Nishant and Sherwood, 2017; Varble, 2018). Nishant and Sherwood (2017) revisited the analyses in Koren et al. (2014) with additional model simulations and showed that the observed relationship between aerosols and clouds could be explained by coexisting but independent variations between surface winds and both clouds and aerosols, while the apparent convective invigoration could be reproduced in the absence of any aerosol variations. Similar findings were reported in Engström and Ekman (2010). Boucher and Quaas (2013) argue that the relationship between AOD and precipitation found in Koren et al. (2012) could be explained by the direct impact of humidity on both variables. Varble (2018) scrutinised observations from the ARM SGP site in the Southern Great Plains used in Li et al. (2011) and Yan et al. (2014) and showed that most of the relationships interpreted as convective invigoration are either insignificant or can be put down to an increase in rainfall preceding the deep

convective events.

In the recent decade, there has been a wide range of previous studies using CRM simulations to investigate the impact of changes in aerosols acting as either CCN or IN on deep convection (Khain et al., 2004; 2005; Grabowski, 2006; Seifert et al., 2006; Fan et al., 2007; van den Heever and Cotton, 2007; Fan et al., 2009; Khain et al., 2009; Khain and Lynn, 2009; Grabowski and Morrison, 2011; Lebo and Seinfeld, 2011; Morrison and Grabowski, 2011; van den Heever et al., 2011; Khain et al., 2012; Lebo et al., 2012; Morrison, 2012; Fan et al., 2013; Grant and van den Heever, 2014; Kalina et al., 2014; Lebo and Morrison, 2014; Sheffield et al., 2015; White et al., 2017; Fan et al., 2018). Studies based on two-dimensional simulations include many of the earlier studies on aerosol effects on deep convection (Khain et al., 2005; Grabowski, 2006; Tao et al., 2007; Fan et al., 2009; Grabowski and Morrison, 2011), simulations run on extended domains for long time (van den Heever et al., 2011; Sheffield et al., 2015) and studies with large ensembles (Morrison and Grabowski, 2011). Numerous studies have simulated different three-dimensional idealised setups, such as squall lines (e.g. Lebo, 2014; Lebo and Morrison, 2014) or supercells (e.g. Seifert and Beheng, 2006; Khain and Lynn, 2009; Lebo and Seinfeld, 2011; Lebo et al., 2012; Morrison, 2012; Kalina et al., 2014; White et al., 2017). Recently, there have been more and more studies based on larger three-dimensional model domains simulating the effect of changes in aerosols on entire populations of deep convective clouds (Fan et al., 2013; White et al., 2017; Miltenberger et al., 2018a; b).

Many of these high-resolution modelling studies found indications for convective invigoration in the form of increased updrafts and mass transport (van den Heever et al., 2006; Storer and van den Heever, 2013; Miltenberger et al., 2018a) or precipitation (Khain et al., 2011; Storer and van den Heever, 2013; Miltenberger et al., 2018a). However, this manifestation of invigoration was often restricted to specific clouds types or environmental conditions (Khain et al., 2008; Fan et al., 2009; Kalina et al., 2014). There are also many studies that did not find significant responses in either convective updrafts

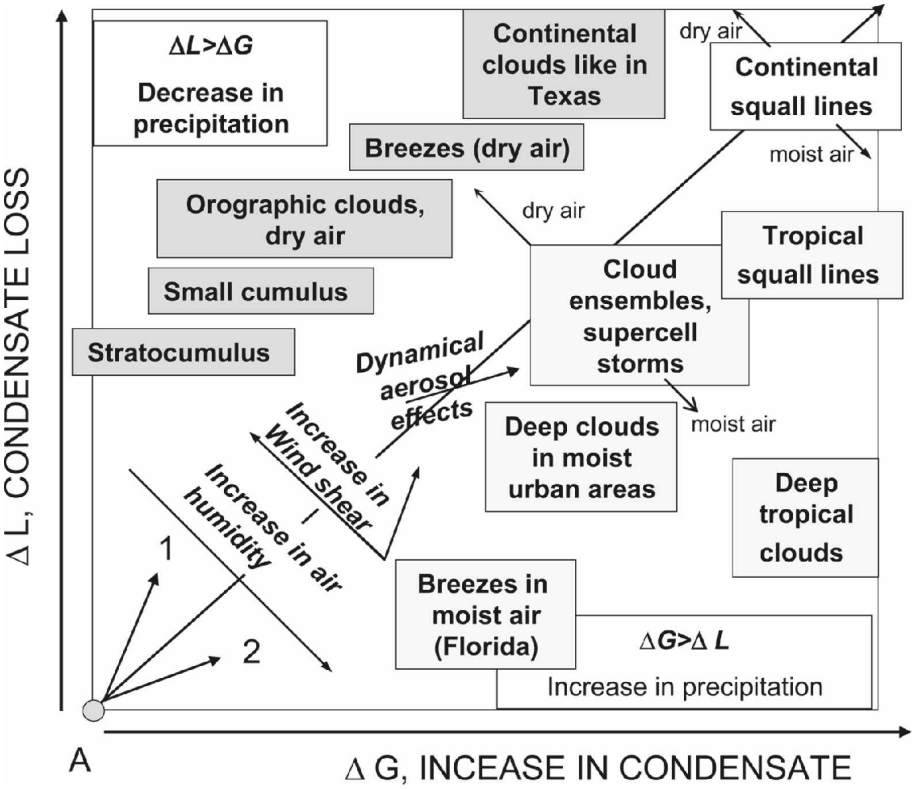

Figure 2.9: Aerosol effects on precipitation from deep convection under different environments compiled by Khain et al. (2008).

or precipitation that would correspond to a convective invigoration (Seifert and Beheng, 2001; Storer et al., 2010; White et al., 2017). The complex interactions between the cloud microphysical effects and dynamical changes in the clouds or cloud systems are pointed out as a complicating factor (Khain et al., 2005; van den Heever and Cotton, 2007; Storer et al., 2010; van den Heever et al., 2011) for example due to compensations between the aerosol effects on different modes of tropical convection (van den Heever et al., 2011) or due to role of cold pools in the mediation of aerosol effects (Kalina et al., 2014; Lebo and Morrison, 2014). Furthermore, there is a strong control on the effect of aerosols by the environmental conditions such as humidity (Khain et al., 2008; Kalina et al., 2014; Lebo and Morrison, 2014) or wind shear (Fan et al., 2009; Storer et al., 2010; Storer and van den Heever, 2013; Lebo and Morrison, 2014).Khain et al. (2008) provided an overview of the effects of increased aerosol concentrations on precipitation for different clouds types that is shown in Fig. 2.9. Fan et al. (2018) recently

pointed out how ultra-fine particles can affect the evolution of deep convection, which had been investigated before for marine deep convection in Khain et al. (2012). However, this study focused on the centre of the Amazon rainforest during the wet season, which is characterised by a very clean aerosol background sometimes described as the "green ocean" (Andreae et al., 2004). It is thus unclear, how representative this effects is for other places around the world with a higher background concentration in aerosol particles suitable to act as CCN. Grabowski and Morrison (2016) have not found a significant effect of additional small particles through thermodynamic changes in the cloud, with changes restricted to the number distribution of ice particles and a subsequent decrease in the strength of convection.

Several studies using CRMs have investigated the effect of different microphysics schemes on the aerosol effects on deep convection in the same modelling framework (Lebo and Seinfeld, 2011; Lebo et al., 2012; Wang et al., 2013; White et al., 2017) and found significant differences between the modelling schemes, often larger than the differences due to the variation in aerosols or aerosol proxies (White et al., 2017) as well as contrasting responses to aerosol perturbations (Lebo et al., 2012).

The effects of aerosol–radiation interactions on clouds in the form of semi-direct effects can possibly have an important impact on the evolution of deep convective clouds (Jiang et al., 2018). Particularly for strongly absorbing aerosols, the suppression of convection due to the change in the environmental temperature profile can counteract a possible invigoration due to increases in CCN (Koren et al., 2004; Rosenfeld et al., 2008). Several studies have found an optimal aerosol number concentration for which the effect of invigoration of aerosols due to microphysical effects has the strongest impact, before the suppression of convective activity takes over for very polluted aerosol conditions due to stabilisation of the environment and reduction in the triggering of convective activity (Rosenfeld et al., 2008). In most of these studies the strongest convective invigoration was found for aerosol number concentrations around 1000 cm^2 (Rosenfeld et al., 2008) and in a range of AOD around 0.25 (Koren et al., 2008; Rosenfeld et al., 2008).

Impacts of aerosols on the development of the ice phase in the cloud anvil can have particularly significant effects on the cloud radiative balance. Several studies (Storer et al., 2010; Morrison and Grabowski, 2011; van den Heever et al., 2011) found an increase in both the albedo and the height of the anvils of tropical convective clouds, which would have an impact on the total radiative budget of the Earth. Fan et al. (2013) showed that the effects of aerosols on the cloud microphysics can induce changes in the cloud anvils without leading to an invigoration of precipitation. Changes in the anvils can impact the cloud evolution and lead to a weakening of convection due to changes in the radiative profile of the atmosphere (Morrison and Grabowski, 2011). Koren et al. (2010b) found an increase in the altitude of tropical anvils in combination with an optical thinning in the shortwave associated with increased aerosol loading, which combines to a strong radiative warming effect on the climate.

The large discrepancies between the different assessment of a possible convective invigoration due to increases in aerosol loading is partially rooted in the variation of the choice of variables that are used to define the strengthening of the convective activity, which include updraft speeds, cloud top height, cloud fraction or surface precipitation (Lebo et al., 2012; Altaratz et al., 2014; Lebo, 2018). Furthermore, assessments based on changes in vertical velocity are significantly complicated by the large natural variability in cloud updraft speeds (Lebo, 2018).

The assessment of aerosol effects on deep convective clouds is inherently affected by the chaotic nature of the evolution of the atmospheric processes. This particularly affects studies that compare single realisations of a clean and a polluted case (Altaratz et al., 2014; Fan et al., 2016). Over recent years, different approaches were used to overcome this, e.g. based on model ensembles (Morrison and Grabowski, 2011; Miltenberger et al., 2018b). Another recent approach is the so-called ”piggybacking” method (Grabowski, 2015; Grabowski and Morrison, 2016), which allows for the realisation of the microphysical evolution in a simulation that is based on the dynamical realisation of a previous simulation and can be applied vice-versa for different aerosol conditions. However, this

method is limited in its representation of feedbacks between the microphysics and other physical processes in the simulation.

A recent review on aerosol effects on convective clouds (Altaratz et al., 2014) pointed out the particular importance of assessing the effects of aerosols on convective clouds in a way that takes into account the temporal evolutions of the cloud at time scales relevant for the evolution of deep convection. Chap. 4 and 5 present a way to disentangle the microphysical effects on clouds from the inherently chaotic evolution of a numerical model simulation based on analyses focused on the evolution of individually tracked clouds.

3. The propagation of aerosol effects through convective cloud microphysics

In this chapter, idealised simulations of deep convective supercells are used to investigate the propagation of perturbations in the cloud droplet number concentration (CDNC) due to changes in aerosols through the microphysical evolutions of the clouds. The microphysical pathway analysis is based on the implementation of detailed diagnostic output of the process rate of the individual microphysical process (Sect. 2.2.2) different model microphysics schemes in the Weather Research and Forecasting Model (WRF). The analysis is applied to individually tracked updrafts and cloud volumes in the simulation. This allows for an analysis that takes the time evolution of the microphysical evolution and bulk cloud properties into account, which is not the case for the usual approaches in the analysis of numerical model simulations as discussed in Sect. 2.3.1.

This chapter is based on an article published in *Atmospheric Chemistry and Physics (ACP)* with slight adaptions:

Heikenfeld, M., White, B., Labbouz, L. and Stier, P (2019). "Aerosol Effects on Deep Convection: The Propagation of Aerosol Perturbations through Convective Cloud Microphysics". Atmospheric Chemistry and Physics 19 (4): 2601–2627. https://doi.org/10.5194/acp-19-2601-2019.

I implemented the microphysical pathway diagnostics in WRF together with Bethan White and developed the pathway analysis based on that. I designed the study together with the co-authors. I performed the simulations and developed the data analysis including the tracking algorithm. I wrote the manuscript and completed the peer-review process with contributions and final approval by the other co-authors.

Abstract The impact of aerosols on ice- and mixed-phase processes in deep convective clouds remains highly uncertain, and the wide range of interacting microphysical processes is still poorly understood. To understand these processes, we analyse diagnostic output of all individual microphysical process rates for two bulk microphysics schemes in the Weather and Research Forecasting model (WRF). We investigate the response of individual processes to changes in aerosol conditions and the propagation of perturbations through the microphysics all the way to the macrophysical development of the convective clouds. We perform simulations for two different cases of idealised supercells using two double-moment bulk microphysics schemes and a bin microphysics scheme. The simulations cover a comprehensive range of values for cloud droplet number concentration (CDNC) and cloud condensation nuclei (CCN) concentration as a proxy for aerosol effects on convective clouds. We have developed a new cloud tracking algorithm to analyse the morphology and time evolution of individually tracked convective cells in the simulations and their response to the aerosol perturbations.
This analysis confirms an expected decrease in warm rain formation processes due to autoconversion and accretion for more polluted conditions. There is no evidence of a marked increase in the total amount of latent heat, as changes to the individual components of the integrated latent heating in the cloud compensate each other. The latent heating from freezing and riming processes is shifted to a higher altitude in the cloud, but there is no substantial change to the integrated latent heat from freezing. Different choices in the treatment of deposition and sublimation processes between the microphysics schemes lead to strong differences including feedbacks onto condensation and evaporation. These changes in the microphysical processes explain some of the response in cloud mass and the altitude of the cloud centre of gravity. However, there remain some contrasts in the development of the bulk cloud parameters between the microphysics schemes and the two simulated cases.

3.1. Introduction

Deep convective clouds are an important feature of the Earth's atmosphere, ranging from widespread convection dominating the atmosphere in the tropics to mid-latitude convective systems (Emanuel, 1994). The impact of aerosols on ice- and mixed-phase processes in convective clouds remains highly uncertain (Tao et al., 2012; Varble, 2018), which has implications for determining the role of aerosol–cloud interactions in the climate system. Representing these effects in global climate models poses additional challenges due to the relatively small length scales often less than a few kilometres at which convective clouds develop and because of limitations in the representations of microphysical processes in the convective parametrisations (Tao et al., 2012; Boucher et al., 2013; Sullivan et al., 2016) with only few models explicitly representing the effects of aerosols on deep convective clouds (e.g. Song and Zhang, 2011; Guo et al., 2015; Kipling et al., 2017; Zhang et al., 2017; Labbouz et al., 2018). The highly localised nature of convective processes also leads to major challenges in observations both from satellites and aircraft measurements (Rosenfeld et al., 2014b).

Over recent years numerous studies using cloud-resolving model simulations (CRM) have investigated aerosol–convection interactions in various setups, ranging from case study simulations to idealised simulations of squall lines or supercells like the cases used in this study (Seifert and Beheng, 2006; Storer et al., 2010; Morrison, 2012; Kalina et al., 2014). The results, however, vary strongly between many of these studies. The differences can be attributed to the simulation of different types of convection, different environmental conditions like humidity or wind shear, but are also related to differences between the models or modelling approaches used (Tao et al., 2012; Fan et al., 2016; White et al., 2017). These challenges in modelling are strongly related to numerous interacting physical processes (Fan et al., 2016) in cloud microphysics and to the interaction between clouds and other processes in the atmosphere on different scales (Tao et al., 2012). In addition to the analysis of process rates in numerical simulations, ana-

lytical evaluations of the microphysical rate equations of the microphysics schemes can give important insights into the propagation of aerosol effects in the cloud microphysics (Glassmeier and Lohmann, 2016). This kind of analytical approach works well for warm-phase clouds but is less conclusive for the response of mixed-phase clouds, especially deep convective clouds, due to many compensating effects and the complexity of the processes involving ice-phase hydrometeors (Glassmeier and Lohmann, 2016).

Convective invigoration (Andreae et al., 2004; Rosenfeld et al., 2008; Lebo and Seinfeld, 2011) has been proposed as a mechanism by which aerosols impact the development of deep convective clouds. A higher number concentration of aerosols suitable for acting as cloud condensation nuclei (CCN) can lead to more but smaller cloud droplets, which are less likely to be processed into rain and precipitated out of the cloud. This would lead to more water reaching the freezing level in the cloud where subsequent freezing leads to additional latent heating in the higher levels of the cloud, enhancing the strength of the convection with higher updraft speeds and cloud-top height. Other studies point out the additional impact of the larger number of aerosols, and subsequently cloud droplets, leading to smaller ice particles which then favours increased cloud fraction, cloud-top height, and cloud thickness (Fan et al., 2013) due to reduced fall speeds of the ice particles. This implies a significant radiative effect on the climate system through enhanced anvils (Koren et al., 2010b). Grabowski and Morrison (2016) argue that the effects can be purely attributed to the effects of smaller droplets and ice crystals with negligible effects of the thermodynamic enhancement proposed in Rosenfeld et al. (2008). Some of the differences in the assessments of convective invigoration due to aerosols are actually caused by the difference in the definition of both changes in aerosol and the quantification of the strength of convection based on different variables such as surface precipitation, updraft speeds or cloud-top heights (Lebo et al., 2012; Altaratz et al., 2014). Significant mechanisms buffering the impact of aerosols on clouds and precipitation, both with a focus on warm-phase processes (Stevens and Feingold, 2009) and for mixed-phase and ice clouds (Fan et al., 2016), have been proposed. However, recent studies question the attribution

of observed relationships between aerosol concentrations and cloud-top height to aerosol microphysical effects (Nishant and Sherwood, 2017; Varble, 2018). It is, therefore, one of the main goals of this paper to investigate whether and how these proposed mechanisms of convective invigoration, especially the proposed invigoration of convection due to additional latent heat release from freezing, manifest themselves in numerical simulations.

Many studies have pointed out the representation of cloud microphysics in models as one of the main sources of uncertainty in high-resolution model studies of aerosol–cloud interactions or cloud feedbacks to a warming climate, especially for mixed-phase and ice-phase clouds (Tao et al., 2012; Khain et al., 2015; White et al., 2017). This also holds for the role of the microphysics schemes in global model simulations of both convection and aerosol–cloud interactions (Lohmann and Feichter, 2005; Gettelman, 2015; Malavelle et al., 2017).

Most currently used cloud microphysics schemes can be separated into two approaches, bulk microphysics schemes and bin microphysics schemes (Khain et al., 2015). Bulk microphysics schemes assume a specific size distribution for a range of different hydrometeor classes and describe their evolution and interactions based on a certain number of moments of these distributions. Double-moment schemes with both prognostic mass and number concentrations of the hydrometeors are the current standard and necessary to meaningfully represent aerosol–cloud interactions (Igel et al., 2014; Khain et al., 2015). The separation of the hydrometeors into individual hydrometeor classes in microphysics schemes brings with it specific challenges in resolving the microphysical processes. In bulk schemes, liquid water in the cloud is separated into cloud droplets and raindrops. The collision-coalescence processes leading to the formation of rain from cloud droplets have to be parametrised through the artificial process of droplet autoconversion and a simplified treatment of accretion of droplets by raindrops. The semi-empirical nature of these parametrisations has been shown to be an important source of uncertainty in the assessment of aerosol–cloud interactions in numerical model simulations (Khain et al., 2015;

White et al., 2017). In the ice phase, most current microphysics schemes separate the hydrometeors into a number of different classes such as pristine ice, snow, hail or graupel. The equations and parameters for the calculation of the microphysical process rates as well as important physical properties of the hydrometeors, such as shape, density or the specific form of the size distribution are specified for each individual hydrometeor class. These choices additionally impact important physical processes such as the fall speeds of hydrometeors in the calculation of sedimentation or the radiative properties of the hydrometeors. This can lead to abrupt changes to the evolution of the cloud due to a change in the partition between the hydrometeor classes in the ice phase of the cloud (Morrison and Milbrandt, 2014). There have been developments towards overcoming the separation of ice hydrometeors into fixed individual classes (Harrington et al., 2013a; b; Morrison and Milbrandt, 2014; Morrison et al., 2015) by treating ice-phase hydrometeors as one single class with smoothly varying physical properties, which have been implemented in both cloud-resolving models and in global climate models. Nevertheless, most current applications rely on microphysics schemes performing the separation into different hydrometeor classes. Better understanding the possible effects and causes of shifts in the hydrometeor partitions through the comprehensive analysis of the microphysical pathways in the two bulk microphysics schemes is thus a main focus of this paper.

Bin microphysics schemes represent the different hydrometeors in the cloud through a number of individual size bins per hydrometeor class, thus allowing for more flexible representation of the actual size distribution and the interaction between the different size bins (Khain et al., 2015). Due to the large number of simulated variables, however, this approach results in high computational cost. One of the main benefits is avoiding the artificial separation between cloud droplets and raindrops that causes challenges in bulk microphysics schemes for example in the form of a parametrisation of the autoconversion processes (Khain et al., 2015). The representation of ice-phase hydrometeors in typical bin microphysics schemes, however, is based on separate hydrometeor classes as in the bulk schemes, each individually resolving their size distribution through a number of bins

(Khain et al., 2015). While many studies have proposed that bin-resolving microphysics schemes are necessary to reliably represent possible microphysical aerosol effects on convective clouds (Khain et al., 2004; Fan et al., 2012; 2016) in model simulations, a large range of studies and applications, e.g. routine numerical weather prediction (NWP), coupled simulations with complex aerosols and chemistry and global climate model simulations as well as a large number of CRM-based studies of aerosol–cloud interactions apply bulk microphysics schemes.

This study aims to unravel the underlying microphysical mechanisms responsible for the large diversity of simulated aerosol effects on convection through a comprehensive analysis of the propagation of aerosol perturbations through microphysical pathways in different microphysics schemes.

Tracking individual convective cells in the simulation makes it possible to draw direct conclusions about the behaviour of individual convective cells in the simulations, e.g. regarding their time evolution or the response to changes in simulation parameters that go beyond the bulk average over the simulation domain or the sum of all cloudy areas in the simulation. The analysis of tracked cumulus clouds has been applied in previous studies Dawe and Austin (e.g 2012), Heus and Seifert (2013) and Heiblum et al. (2016a,b) with a focus on various aspects of convective clouds including the effects of aerosol perturbations on deep convection (Terwey and Rozoff, 2014).

We have implemented detailed microphysical process-rate diagnostics for pathway analysis in the two double-moment microphysics schemes of Morrison et al. (2009) and Thompson et al. (2004). We analyse the cloud morphology and the spatial structure of the microphysical processes in individual tracked convective cells. We display the microphysical process rates in the form of scaled pie charts. This has been inspired by previous studies using this type of visualisation of the spatiotemporal development of physical processes for other applications. Schutgens and Stier (2014) performed a pathway analysis for the aerosol processes in a global climate model (ECHAM-HAM). Chang et al. (2015) applied a microphysical pathway analysis including a similar visualisation

of process rates to simulations of pyro-convective clouds, however, using a much simpler two-dimensional model for highly idealised individual clouds.

In addition to the detailed process-rate diagnostics, we derive important bulk cloud properties, such as the total cloud mass or the altitude of the centre of gravity and analyse their evolution over the life cycle of the tracked cells. Our approach goes beyond previous studies with a similar setup (Morrison et al., 2009; Kalina et al., 2014) that mainly focussed on domain average properties and only a specific subset of microphysical processes.

We use a well-documented idealised supercell setup based on Weisman and Klemp (1982) and Weisman and Klemp (1984), which was applied in previous studies (e.g. Khain and Lynn, 2009; Morrison et al., 2009; Kalina et al., 2014), to create a well-defined development of a strong convective cell, allowing us to focus on the microphysical evolution of individual convective cells. To test the representativeness of our results from this first case, we include simulations for a second idealised supercell case based on the measurements and model setups from Kumjian et al. (2010), Naylor and Gilmore (2012) and Dawson et al. (2013).

We represent idealised aerosol perturbations through changes to a fixed cloud droplet number concentration (CDNC) in each simulation with the two bulk microphysics schemes. This allows us to isolate the actual cloud microphysical pathways from uncertainties in the representation of the activation of CCN in numerical models (Ghan et al., 2011b; Simpson et al., 2014; Rothenberg et al., 2018). Simulations are performed for a comprehensive range of CDNC for each microphysics scheme ranging from values representative of very clean, maritime conditions (CDNC=50 cm^{-3}) to very polluted situations (CDNC=2500 cm^{-3}).

We compare the results to simulations performed with a bin microphysics scheme (HUJI spectral-bin scheme) for a subset of the analyses to investigate whether the effects investigated in more detail through the microphysical pathway analysis for the two bulk microphysics schemes agree with the response of a bin microphysics scheme to perturbations of aerosol proxies.

3.2. Methods

3.2.1. Model setup

The simulations are performed with the Weather and Research Forecasting model (WRF) version 3.7.1 (Skamarock et al., 2008). We use the two-moment microphysics schemes from Thompson et al. (2004, 2008), denoted as THOM, and from Morrison et al. (2005, 2009), called MORR in our figures and tables. To isolate the role of cloud microphysics for aerosol effects on deep convection from additional uncertainties in model-simulated aerosol fields, we apply a fixed cloud droplet number concentration (CDNC) in the two bulk microphysics schemes for each simulation. In each of the schemes, the CDNC is reset to the chosen value at the end of each model time step in all cloudy grid points. We vary this CDNC value between different simulations as a proxy for aerosol number concentration. There are versions of both bulk microphysics schemes that include the activation of a fixed CCN spectrum or even interactive aerosols (Wang et al., 2013; Thompson and Eidhammer, 2014). However, the implementation of both the cloud droplet activation and the representation of the aerosol distributions is very different between the two microphysics schemes, which would add additional differences between the schemes compared to representing the perturbations in the form of a varying CDNC.

The detailed analyses of the process rates in this paper are carried out for simulations using the two bulk microphysics schemes. To investigate how the results obtained from the detailed analysis of the two bulk microphysics schemes hold for a bin cloud microphysics scheme, we also include additional simulations with the Hebrew University cloud model (HUCM) spectral-bin microphysics scheme (Khain et al., 2004; Lynn et al., 2005a; b), called SBM in the rest of the paper. We perform a subset of the analyses for this microphysical scheme, excluding the detailed microphysical process-rate analysis but including the analysis of changes to the hydrometeor mixing ratios and the bulk cloud properties. We use the full version of the spectral-bin microphysics scheme in WRF (Khain et al., 2012) and perform a variation of CCN number concentration.

Both bulk microphysics schemes make use of saturation adjustment, removing all water vapour exceeding the saturation vapour pressure in each time step and instantaneously condensing it to cloud water at each time step. This prevents a build-up of supersaturation in strong updrafts and can thus impact the effects of perturbations in the microphysics (Lebo et al., 2012). The bin microphysics scheme (SBM) includes an explicit calculation of supersaturation in the microphysics at each time step and allows for a build-up of supersaturation in strong updrafts over several time steps.

We simulate two different idealised supercell cases. The first set of simulations (CASE1) is based on the default WRF quarter-circle shear supercell case representative of a supercell case over the southern Great Plains of the United States (Khain and Lynn, 2009; Lebo and Seinfeld, 2011). This case uses an initial sounding described in Weisman and Klemp (1982) with a surface temperature of 300 K and a surface vapour mixing ratio of $14\,\mathrm{g\,kg^{-1}}$. The wind profile is taken from Weisman and Rotunno (2000) and features a wind shear of $40\,\mathrm{m\,s^{-1}}$ made up of a quarter-circle shear up to a height of 2 km and a linear shear further up to 7 km height. The initiation of convection is triggered by a warm bubble with a magnitude of 3 K in potential temperature centred at 1.5 km height in the centre of the domain with a radius of 10 km horizontally and 1.5 km vertically in which the perturbation decays with the square of the cosine towards the edge of the bubble (Morrison, 2012). This type of setup has been used for a number of similar studies in the past (Morrison and Milbrandt, 2010; Storer et al., 2010; Morrison, 2012; Kalina et al., 2014). To test the representativeness of the results for different cases of idealised deep convection, a set of simulations for a second supercell case (CASE2) is based on an observed supercell storm over Oklahoma in 2008 (Kumjian et al., 2010). In contrast to the first case, the initial profiles are from observations used in the model experiments in Dawson et al. (2013). This case features a drier initial profile with a surface temperature of 308 K and a surface water vapour mixing ratio of $16\,\mathrm{g\,kg^{-1}}$ along with wind shear of similar magnitude to CASE1. The initiation of convection in this case is created by forced convergence near the surface based on nudging the vertical velocity over the same volume

that is used for the warm bubble in CASE1. The methodology is described in detail in Naylor and Gilmore (2012) and we use an updraft speed peaking at 5 $\mathrm{m\,s^{-1}}$ at the centre of the volume.

All simulations are performed without an explicit boundary layer scheme. Furthermore, the simulation does not include any calculations of surface fluxes or radiation fluxes. The horizontal grid spacing of the simulations is 1 km to sufficiently resolve the main features of the simulated supercell. We use a model domain size of 84 grid cells in each horizontal dimension and open boundary conditions on each side of the modelling domain. The vertical resolution of the 96 model layers varies from about 50 m at the surface to 300 m at the top of the model. Simulations are performed with a time step of 5 seconds. The standard model diagnostics and the microphysical pathway diagnostics (Section 3.2.3) are output every 5 minutes to sufficiently resolve the development of the microphysical processes during the life cycle of the deep convective clouds.

3.2.2. Variation of aerosol proxies: CDNC or CCN

We analyse the effects of varying the CDNC in the two bulk microphysics schemes to isolate the impact of microphysical pathways. We use a CDNC of 250 $\mathrm{cm^{-3}}$ as a baseline simulation. Simulations are performed for two CDNC values corresponding to a cleaner environment than the baseline simulation (50 $\mathrm{cm^{-3}}$ and 100 $\mathrm{cm^{-3}}$) and five values representing more polluted conditions (500 $\mathrm{cm^{-3}}$, 1000 $\mathrm{cm^{-3}}$, 1500 $\mathrm{cm^{-3}}$, 2000 $\mathrm{cm^{-3}}$and 2500 $\mathrm{cm^{-3}}$).

For the simulations with the spectral-bin microphysics scheme, activation of aerosols to cloud droplets is calculated from a CCN spectrum following the equation $N_C = N_0 \cdot S^k$, with the prognostic supersaturation S, the particle number concentration N_0 and an exponent k. The exponent is $k = 0.5$ in all simulations, while N_0 is set to a fixed value in the range from 75 $\mathrm{cm^{-3}}$ to 6750 $\mathrm{cm^{-3}}$ for each simulation and held constant over the simulation period. This yields cloud droplet number concentrations with median values spanning a similar range to those chosen for the two bulk microphysics schemes (Table 3.1).

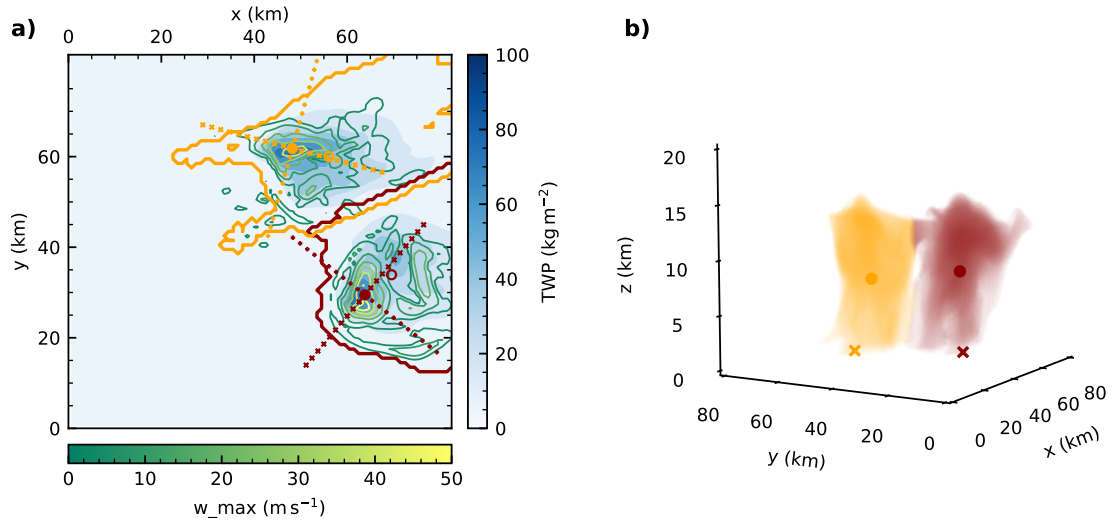

Figure 3.1: a) Illustration of the result of the tracking and watershedding methodology after 90 minutes of simulation time with the total water path field in blues and contours of column maximum vertical velocities in greens. The filled circles represent the tracked updraft cores, while the empty circles show the position of the centre of gravity determined by the watershedding algorithm. Crosses denote the slices along/across the line of travel of the cell that are used for the analysis of the cloud morphology. The coloured contour lines represent the projection of the respective cloud mask for each cell to the surface. b) Three-dimensional rendering of the 1 g kg^{-1} condensate mixing ratio threshold of the two tracked cells in the simulation at the same point in time including the horizontal location of the tracked updraft (cross) and centre of gravity (dot).

3.2.3. Pathway analysis

We have extended two double-moment bulk microphysics schemes, the Morrison scheme (Morrison et al., 2005; 2009) and the Thomson scheme (Thompson et al., 2004; 2008) in WRF 3.7.1, by writing detailed microphysical pathway diagnostics at each output time step. This includes all individual process rates for both hydrometeor mass and hydrometeor number mixing ratio as well as individual latent heating rates for the three phase transitions (liquid–vapour, liquid–ice, ice–vapour) and the hydrometeor mass and number tendencies for the individual hydrometeor classes (cloud water, rain, cloud ice, graupel, snow) are diagnosed at every output time step.

For most analyses in this study, the individual microphysical processes are grouped into a consistent set of classes according to their contribution to the hydrometeor mass transfer in the model. This includes the six different phase transitions between frozen hydromet-

Table 3.1: Overview of the 52 simulations performed in this study, including the two cases simulated and the different CDNC/CCN values for each of the microphysics schemes. The CDNCs for the SBM simulations are the median values for grid points with a cloud water mixing ratio larger than $10\,\mathrm{g\,kg^{-1}}$.

Case	**Microphysics**	**CDNC** ($\mathrm{cm^{-3}}$)	**CCN** ($\mathrm{cm^{-3}}$)
CASE1 Weisman and Klemp (1982) Weisman and Klemp (1984)	**MORR** Morrison et al. (2005, 2009)	**50, 100, 250, 500, 1000, 1500, 2000, 2500**	–
	THOM Thompson et al. (2004, 2008)	**50, 100, 250, 500, 1000, 1500, 2000, 2500**	–
	SBM Khain et al. (2004) Lynn et al. (2005a,b)	12, 28, 5 128, 419, 648, 870, 1310, 1753, 2194	**67.5, 135, 270, 540, 1350, 2025, 2700, 4050, 5400, 6750**
CASE2 Naylor and Gilmore (2012) Dawson et al. (2013) Kumjian et al. (2010)	**MORR** Morrison et al. (2005, 2009)	**50, 100, 250, 500, 1000, 1500, 2000, 2500**	–
	THOM Thompson et al. (2004, 2008)	**50, 100, 250, 500, 1000, 1500, 2000, 2500**	–
	SBM Khain et al. (2004) Lynn et al. (2005a,b)	12, 25, 47, 171, 393, 603, 819, 1239, 1657, 2078	**67.5, 135, 270, 540, 1350, 2025, 2700, 4050, 5400, 6750**

eors, water drops and water vapour (*condensation*, *evaporation*, *freezing* including riming, *melting*, *deposition* and *sublimation*) as well as the warm *rain formation* due to autoconversion and accretion of cloud droplets and all processes that transfer mass between the different frozen hydrometeors as *ice processes*. For some of the more detailed analyses, this grouping is performed in a more detailed way, e.g. separating freezing and riming processes or splitting them up by the specific hydrometeor class involved in the transfer. A collection of all the individual microphysical process rates represented in the two bulk microphysics schemes including the grouping discussed here is given in the Appendix (Table 3.2 for the Morrison microphysics scheme and in Table 3.3 for the Thompson microphysics scheme).

3.2.4. Convective cell tracking

We have developed a tracking algorithm focussed on the tracking of individual deep convective cells in CRM simulations, but flexible enough to be extended to other applications, e.g. simulations of shallow convection or based on geostationary satellite observations using brightness temperature data. The initial tracking of features is performed on the column maximum vertical velocity at each output time step using the Python tracking library trackpy (Allan et al., 2016). These features are then filtered and linked to consistent trajectories. The trajectories are extrapolated to two additional output time steps at the start and at the end to allow for the inclusion of both the initiation of the cell and the decaying later stages of the cell development.

Based on these trajectories, a three-dimensional watershedding algorithm given by *morphology.watershed* from the Python image processing package scikit-image (Walt et al., 2014), is applied to the total condensed water content field (mass mixing ratio of all hydrometeors) at each output time step to infer the volume of the cloud associated with the tracked updraft. We use a threshold of $1\,\mathrm{g\,kg^{-3}}$ to define the core cloudy grid points in the simulations. A variation of this threshold by up to an order of magnitude to $0.1\,\mathrm{g\,m^{-3}}$ only showed minor changes to the results of the study.

A separate watershedding is performed for both liquid water content (cloud droplets and rain drops) and ice water content (all ice hydrometeors). This allows for the determination of the centre of gravity and the mass, for the entire cloud as well as for the in-cloud liquid and frozen phases, respectively. The evolution of the centre of gravity has been studied mainly for warm convective clouds (e.g. Koren et al., 2009; Dagan et al., 2015; Dagan et al., 2017; 2018) and with a focus on the warm phase of deep convective clouds (Chen et al., 2017).

The tracking algorithm does not explicitly treat splitting and merging of convective cells. In all simulated cases in this study, the initial convective cell splits into two separate counter-rotating cells early into the simulations. In CASE1 this leads to a relatively symmetric situation with similarly strong individual cells. In both cases, one of the cells de-

velops more directly out of the initial cell, in CASE1 this is the right-moving cell, while in CASE2 this is the stronger left-moving cell. In each simulation, this stronger cell gets picked up as a continuation of the initial cell by the tracking algorithm. The second cell has been analysed following the same methodology and showed very similar results in all major aspects. We have thus decided to focus on the analysis of the first cell in this paper and to not discuss the results from the second cell in more detail.

Microphysical process rates, latent heating rates and other cloud microphysical parameters such as hydrometeor mixing ratios are summed up for regularly spaced altitude intervals in the volume of the individual cells to get representative profiles for each cloud. We interpolate the microphysical process rates and other variables used in the analysis to slices along and perpendicular to the line of travel of the cell (Fig. 3.1) to visualise and analyse the morphology of the cells for different simulation setups and at different stages of the cloud life cycle.

3.3. Results

3.3.1. Baseline simulations

The simulations with CDNC = 250 cm^{-3} for both bulk microphysics schemes (Fig. 3.2 and Fig. 3.3) are used as a baseline simulation representative of intermediate aerosol loading. As for all the following figures for CASE1, these analyses are based on a combination of the initial stage of the cell and the right-moving cell after the cell split. We use three different points in time (15 minutes, 25 minutes and 60 minutes) to illustrate the microphysical evolution of the cell in simulations with the two different microphysics schemes. During the initial phase of the formation of the convective cloud in the simulation using the Morrison bulk microphysics scheme (Fig. 3.2a,d,g), the two major microphysical processes are condensation to form cloud droplets and rain formation from these droplets, while the top of the cloud at around 7.5 km is already influenced by freezing and riming processes. The simulation with the Thompson microphysics scheme shows a similar

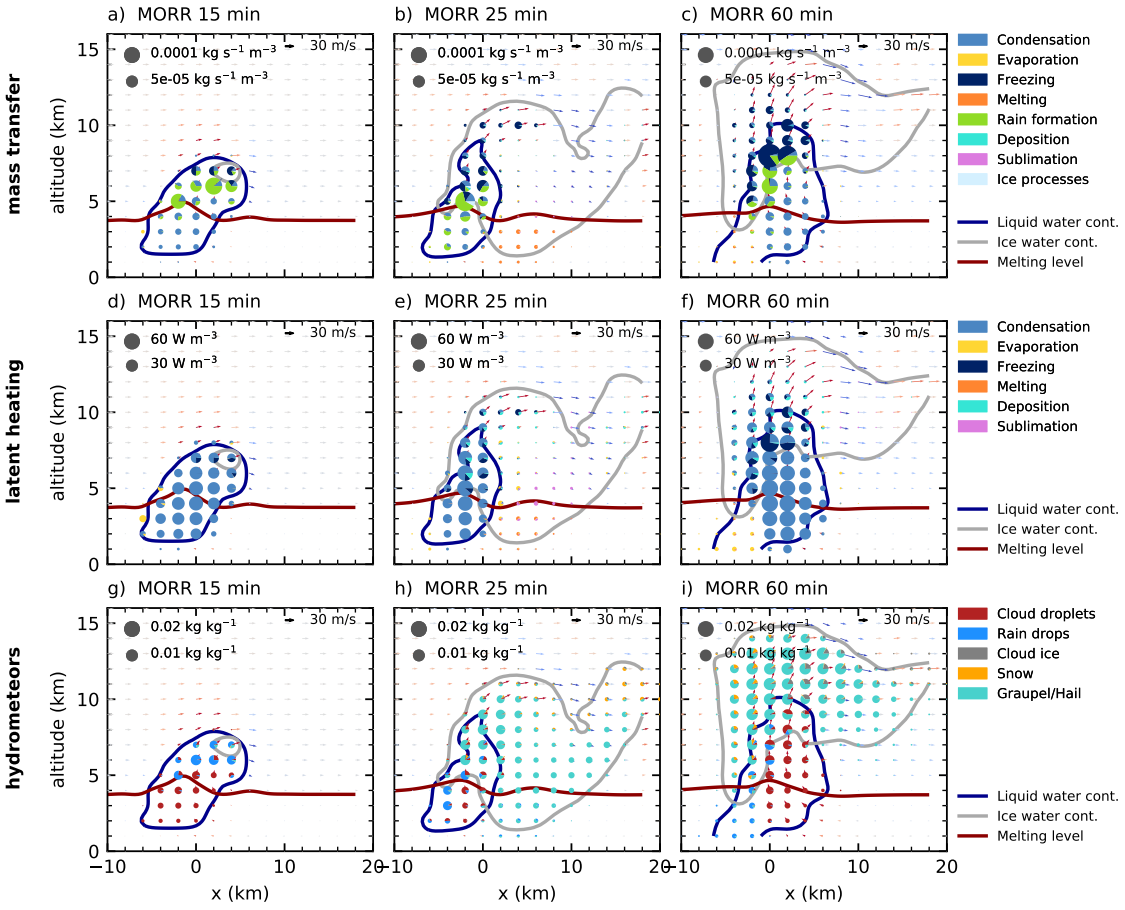

Figure 3.2: Cloud microphysical morphology along a slice parallel to the cell track for a cloud droplet number concentration of 250 cm^{-3} for the Morrison microphysics scheme. The area of each specific colour in the pie charts is proportional to the water turnover (a-c) in $kg\,m^{-3}\,s^{-3}$ and latent heating (d-f) in $W\,m^{-3}$ for the process rates and to the mass mixing ratio for the hydrometeors (g-i). Contour lines denote the mixing ratio threshold of 1 g/kg for liquid (blue) and frozen (grey) water content as well as the melting level (0°C isotherm). Arrows denote the wind field with updrafts in red and downdrafts in blue.

development during the initial cloud stage (Fig. 3.3a,d,g). The initiation of freezing at the top of the cloud is slightly delayed in comparison to the simulation with the Morrison scheme. During the next 10 minutes, the cell quickly intensifies, dominated by the development of rain formation (autoconversion of cloud droplets and accretion of cloud droplets by rain) between 4 and 7 km. Freezing occurs at a height of about 7-8 km. After an hour of simulation, the cell has developed into a mature supercell with hail dominating the mass mixing ratio in the ice phase. A substantial amount of cloud droplets extends

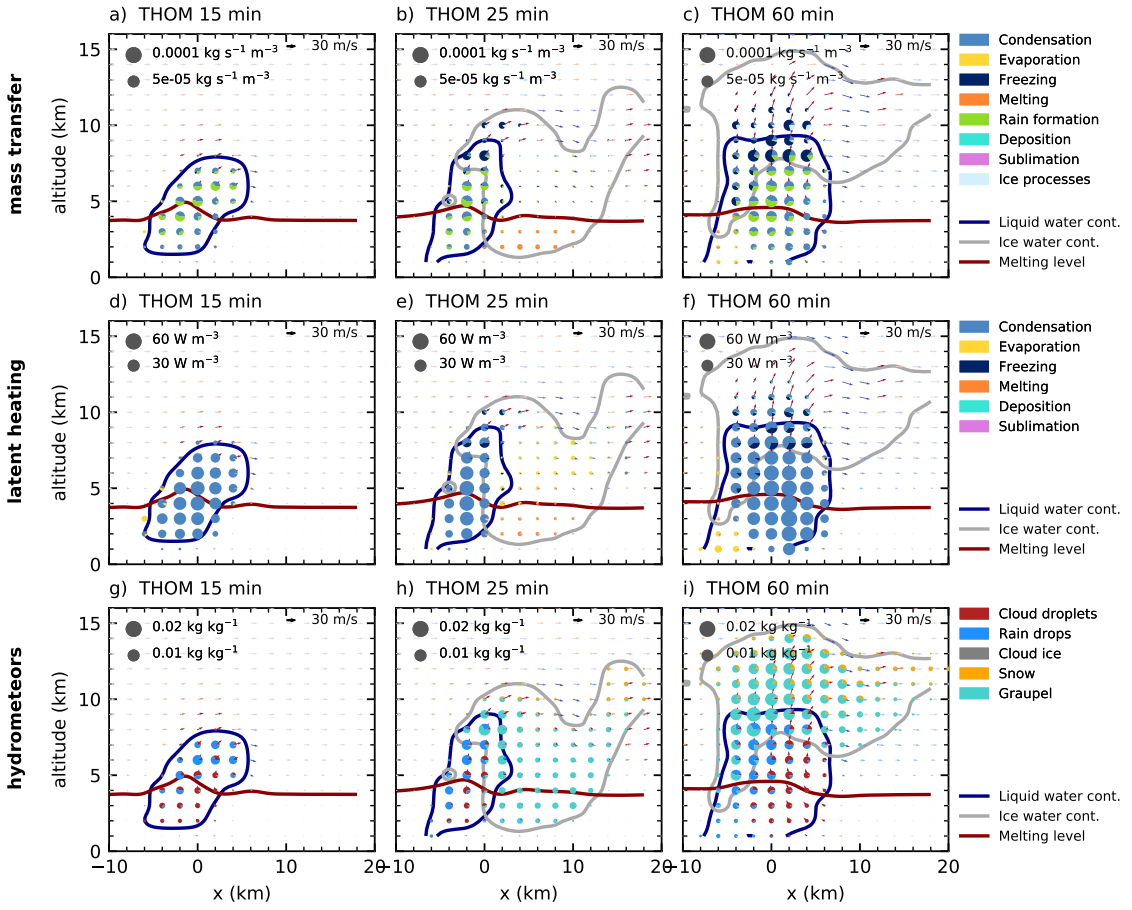

Figure 3.3: Cloud microphysical morphology along a slice parallel to the cell track for a cloud droplet number concentration of 250 cm^{-3} for the Thompson microphysics scheme as in Fig. 3.2.

up to 10 km height. Rain formation and freezing occur in the region of the strongest updraft with a width of about 5 km for both microphysics schemes. During the later stage, the freezing in the simulation using the Morrison microphysics scheme takes place over a substantial vertical range and is strongest at both edges of the mixed-phase region of the cloud at around 8 km and 10 km altitude (Fig. 3.2c). The Thompson scheme instead shows a more confined region of freezing. In both bulk microphysics schemes, condensation processes dominate the latent heat release in the cloud for all stages of the cloud development (Fig. 3.2d-f, Fig. 3.3d-f). In the mature stage of the cell, the main difference in the hydrometeor classes between the two microphysics schemes is an enhanced pres-

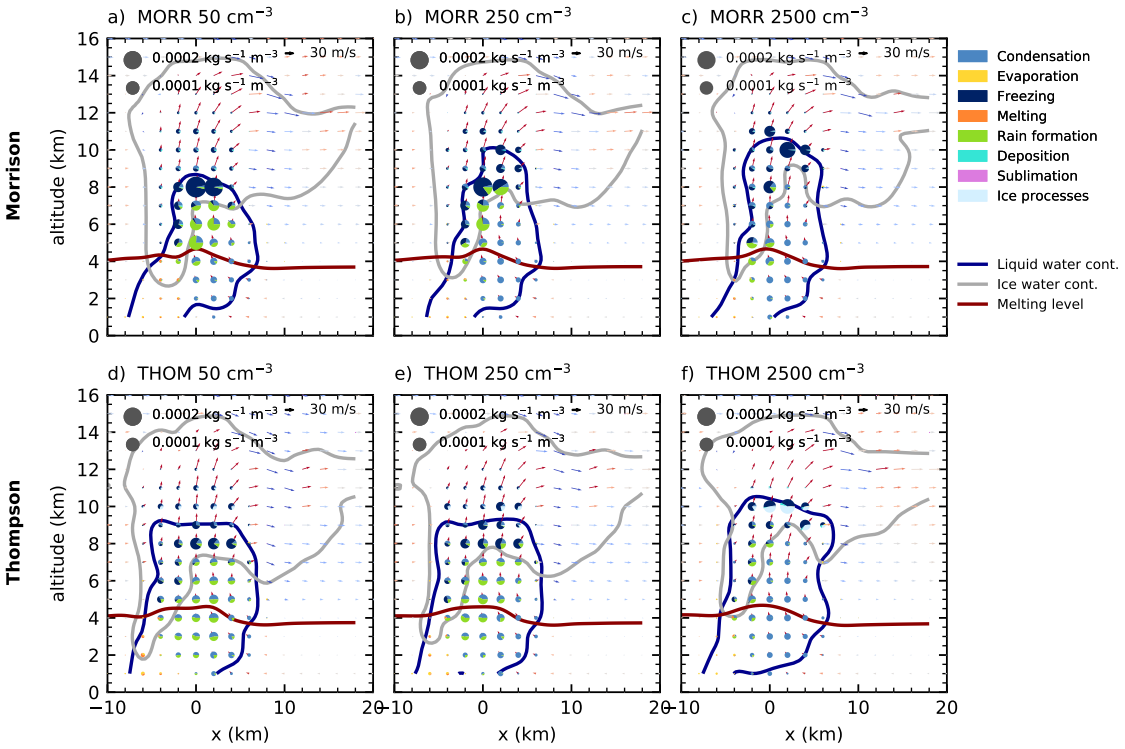

Figure 3.4: Cloud microphysical morphology along a slice through the cloud parallel to the track of the cell for simulations with three different CDNC values (left: 50 cm^{-3}, middle: 2500 cm^{-3},right: 2500 cm^{-3}) after 60 minutes of simulation using the two bulk microphysics schemes (top: Morrison, bottom: Thompson).

ence of snow both in the core and in the anvil for the Thompson microphysics scheme (Fig. 3.2i and Fig. 3.3i).

3.3.2. Effects on cloud morphology and microphysical process rates

We first investigate changes to the right-moving cell in CASE1 due to a variation of CDNC. We focus on three different CDNC values (clean, baseline, polluted; see Fig. 3.4) after 60 minutes of simulations using the two bulk microphysics schemes. In the microphysical process rates, a decrease in rain formation from droplets (autoconversion and accretion) with increasing CDNC is evident in the core of the cell for both bulk microphysics schemes. For both bulk schemes, the freezing and riming processes are shifted upwards with increasing CDNC. The mixed-phase region of the cloud, indicated by the liquid water mixing ratio contour in Fig. 3.4, extends about 1-2 km higher in the polluted

case for each bulk scheme.

In the hydrometeor mass mixing ratios (Fig. 3.5), an increase in cloud droplet mass at the expense of raindrops for increasing CDNC is evident in both bulk microphysics schemes and the spectral-bin microphysics scheme, particularly in the mixed-phase region of the cloud at around 6-8 km). In the Thompson scheme, most of the ice-phase hydrometeor mass is present in the form of snow for the high CDNC simulation (Fig. 3.5d), especially towards the cloud top and in the anvil region, while graupel dominates except in the anvil for the cleanest case (Fig. 3.5c). In contrast, the ice phase in the Morrison scheme shows a high hail mixing ratio for low and high CDNC values (Fig. 3.5a,b) and additional ice particles, but only small amounts of snow in the simulation with the highest CDNC value. The simulations using the spectral-bin microphysics scheme (Fig. 3.5e,f) show a stronger increase in cloud droplet mass mixing ratio than the two bulk schemes for increased CCN. Graupel and hail, the predominant ice-phase hydrometeors in the cleanest simulation, get replaced by cloud-ice particles for the highest CCN value. However, it has to be taken into account that the definition of the hydrometeor classes differs between the three different microphysics schemes.

Fig. 3.6 provides a vertically resolved view of the time evolution of the microphysical process rates over the life cycle of the right-moving cell for the two bulk microphysics schemes under the cleanest and most polluted conditions. For both schemes, a strong decrease in the warm rain formation processes (autoconversion of cloud droplets and accretion of cloud droplets by rain) with increased CDNC can be observed. This even leads to a complete shut-down of warm rain production in the Thompson scheme, which is also evident in the absence of rain hydrometeors in Fig. 3.5. As a result, evaporation in the lowest model levels decreases strongly for the high CDNC value in the simulations with the Thompson scheme. Both microphysics schemes show a substantial decrease in the total amount of melting of frozen hydrometeors below the melting line at about 4 km height. The strong cooling due to evaporation and melting in the cleanest cases for the simulations with the Thompson scheme (Fig. 3.6c) can explain that the lifetime of the

cell is about 10 to 20 minutes shorter than for the more polluted cases and the other bulk scheme. The dominant region of freezing processes is lifted from around 8 km height in the low CDNC case to around 10 km for the high CDNC case height in both schemes. While deposition on ice hydrometeors is an important process for all values of CDNC for the Morrison scheme, it becomes more enhanced for the most polluted simulation using the Thompson scheme, related to the change in the dominant ice-phase hydrometeor class to snow (Fig. 3.5). Condensation onto cloud droplets is present in all simulations up to 10 km height in comparable amounts and dominates the latent heating due to the large energy transfer involved. Deposition processes onto ice hydrometeors are important for both the cleanest and the most polluted simulation in the Morrison scheme, while the Thompson scheme shows much more deposition in the most polluted case, which can be related to the changes in the hydrometeor composition (Fig. 3.5). The decrease in the total amount of microphysical mass transfer in all simulations around 55 minutes into the simulations is caused by the splitting of the tracked cell into two individual cells. However, no clear change to the relative proportions of the different processes can be observed at this stage.

A more detailed analysis of the processes involved in the formation of rain over the lifetime of the cell in the different cases (Fig. 3.7) reveals that autoconversion of cloud droplets to rain for the highest CDNC values in both bulk schemes is almost negligible, with only very little autoconversion in the Morrison scheme, even for the smallest CDNC value. Accretion of cloud droplets by rain is strongly depressed for high CDNC in both microphysics schemes. Melting of ice hydrometeors contributes substantially to the production of rain in both bulk schemes and is reduced for the high CDNC case, especially in the Thompson scheme.

The processes transforming liquid to frozen water can be further broken down into processes representing the freezing of individual cloud droplets or raindrops and riming processes, in which existing ice-phase hydrometeors accrete liquid water (Fig. 3.8). For both bulk microphysics schemes, freezing of raindrops and cloud droplets occurs in two separ-

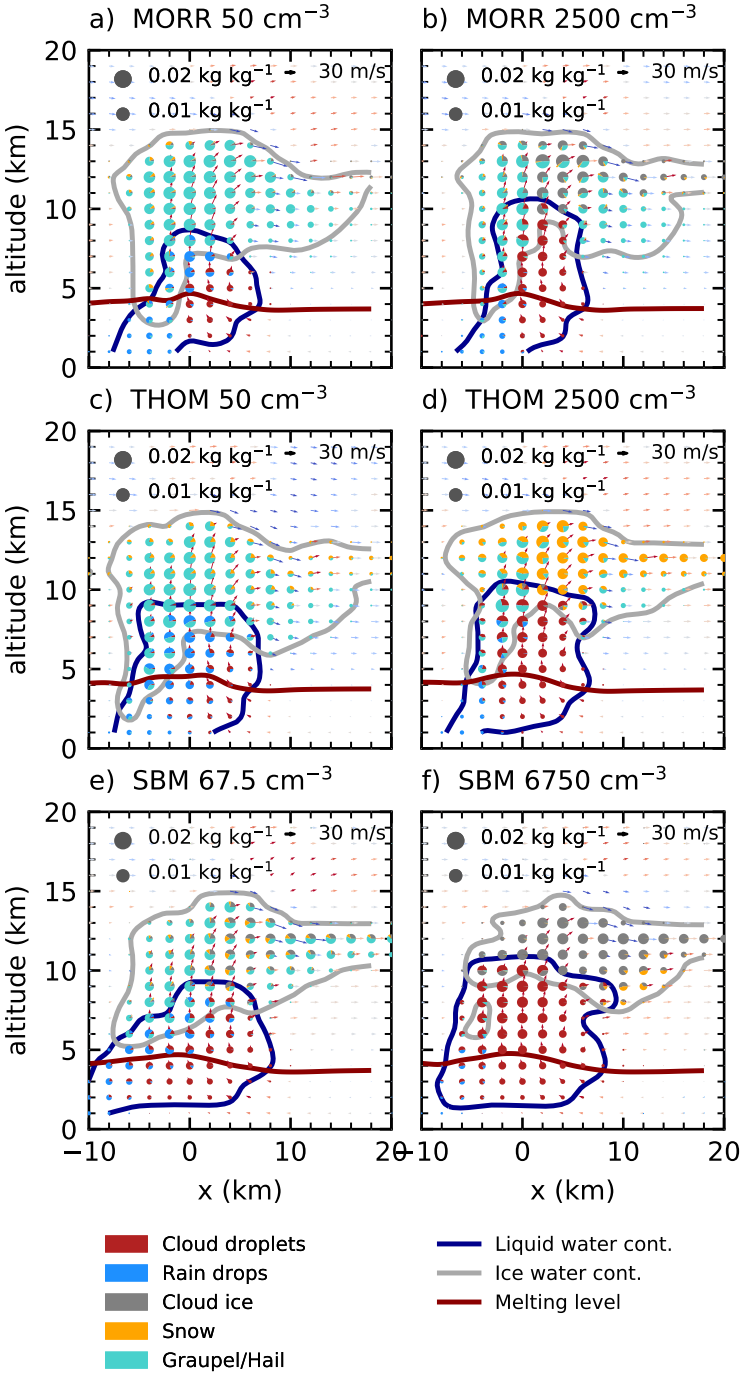

Figure 3.5: Hydrometeor mass mixing ratios in a slice along the line of travel of the cell for the cleanest (left) and most polluted (right) simulations after 60 minutes of simulation for the three microphysics schemes in CASE1.

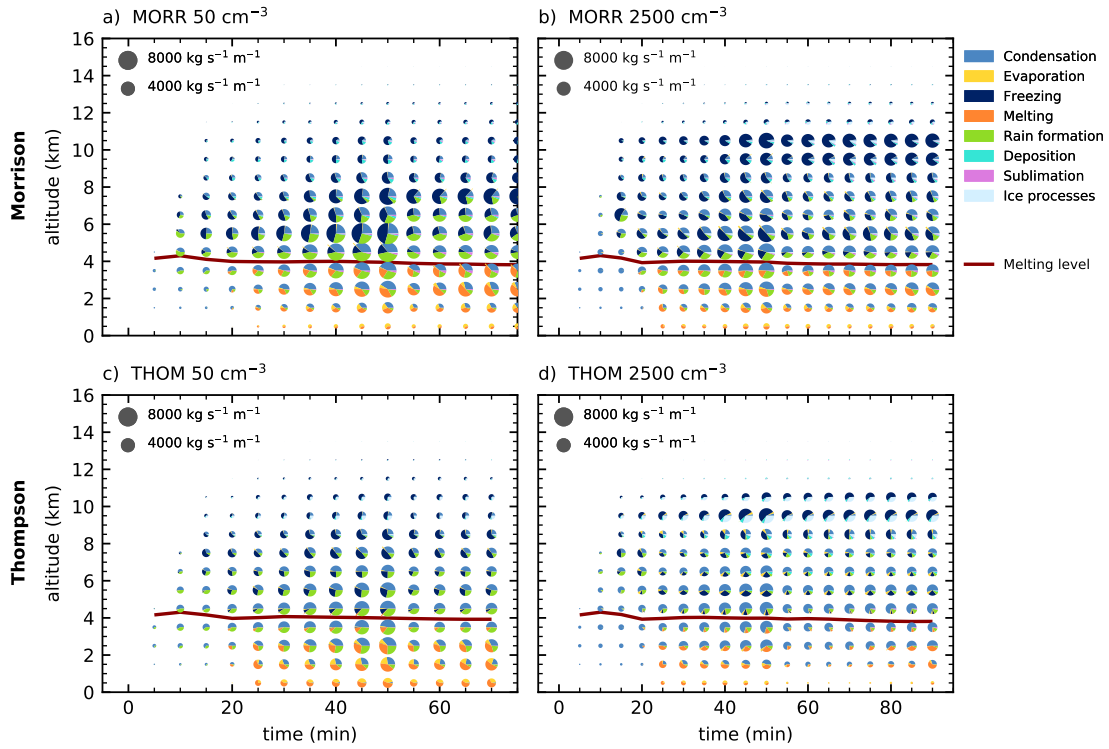

Figure 3.6: Time evolution of the microphysical process rates for the cleanest (left) and most polluted (right) simulations and the two bulk microphysics schemes (Morrison: top, Thompson: bottom) in CASE1. The pie charts denote mass transfer summed up over the volume of the cloud in each altitude interval for the different groups of microphysical process rates with the area of each colour proportional to the mass transfer. The red line shows the height of the 0°C isotherm.

ate layers, with freezing of raindrops at around 8 km and freezing of cloud droplets above a height of 10 km up to 14 km. In both microphysics schemes, freezing of raindrops is strongly decreased for increased CDNC (Fig. 3.8b,d), while freezing of cloud droplets is increased by about a factor of 3. This is not related to the parametrisation of the freezing processes (described in more detail in Appendix 3.B), which does not include any information about cloud droplet effective radius and raindrop effective radius through the number concentrations. Instead, these changes are purely a result of the shift in the abundance of cloud droplets and raindrops (Fig. 3.5).

The riming processes are spread out over a much larger altitude range in the cloud, between the melting level at about 4 km and about 11 km height for riming of cloud droplets and below 9 km for the riming of raindrops. Riming is markedly stronger at

all CDNC values in the simulations with the Morrison scheme (Fig. 3.8a,b). In the Morrison scheme, riming of rain droplets is strongly decreased for higher CDNC and mainly restricted to around 5 km height. In the Thompson microphysics scheme (Fig. 3.8c,d), raindrop riming is also strongly decreased for high CDNC, but still occurs over the same height range as in the low CDNC case. Both microphysics schemes show a slight increase in droplet riming with higher CDNC over the entire altitude range. We can thus explain the shift in freezing and riming processes observed in Fig. 3.6 by a decreased riming of rain droplets at lower altitudes and a shift from the freezing of raindrops to the freezing of cloud droplets occurring at higher altitudes.

The evolution of the deposition and sublimation processes (Fig. 3.9) shows substantial differences between the two bulk microphysics schemes and a strong response to a variation of CDNC. The calculation of deposition and sublimation in the microphysics scheme is explicitly parametrised for each hydrometeor class, taking into account detailed information on the size distribution of the hydrometeors (Thompson et al., 2004; Morrison et al., 2005). In the Morrison scheme (Fig. 3.9a,b), the increase in CDNC leads to a decrease in both deposition and sublimation over the entire height of the cloud. These processes dominantly occur on hail for the cleanest case and are more distributed over hail, snow and pristine ice in the polluted case, which agrees with the shifts in the hydrometeor mixing ratios (Fig. 3.5a,b).

In the simulations with the Thompson microphysics scheme (Fig. 3.9c,d), deposition and sublimation processes show a very different behaviour. The strong increase in snow in the cloud with increasing CDNC (Fig. 3.5c,d) leads to a strong increase in both deposition and sublimation on snow. Deposition on ice is of the same order of magnitude for the cleanest case, but is not strongly affected by a change in CDNC. Sublimation of graupel only occurs around and below the melting layer and is substantially reduced by increasing CDNC. As deposition on graupel is prohibited in this microphysics scheme, there is no decrease in deposition on graupel associated with the changes in the hydrometeor ratio compensating the increase in deposition on snow. This leads to a strong increase in total

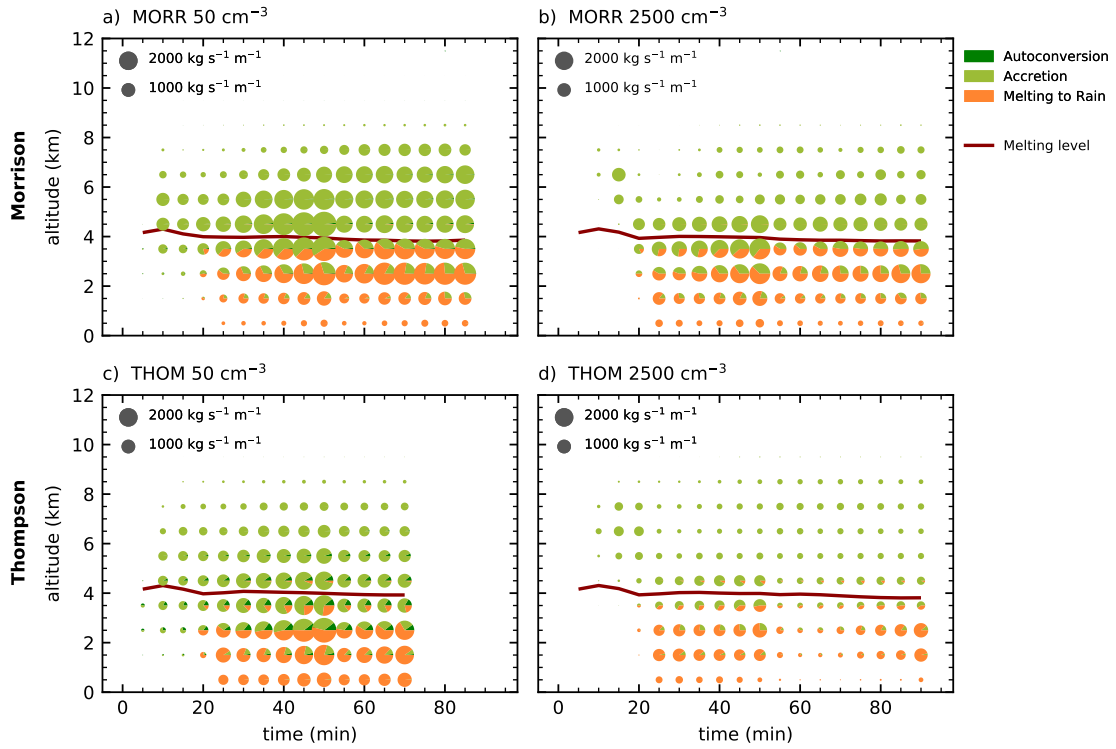

Figure 3.7: Time evolution of the microphysical process rates relevant for rain formation processes (autoconversion, accretion of cloud droplets by rain and melting of ice hydrometeors) as in Fig. 3.6.

deposition with increased CDNC as the main response in the Thompson scheme.

Latent heating constitutes a key feedback of the microphysics scheme onto the model dynamics along with changes to the buoyancy due to changes in condensate loading. The vertically resolved latent heating over the lifetime of the tracked cell in CASE1 is shown in Fig. 3.10 for all three microphysics schemes and split up into the individual phase changes for the two bulk microphysics schemes in Fig. 3.11.

Latent heat release from condensation is the dominant contribution to the latent heating and about a magnitude stronger than the other contributions, thus determining the general shape of the latent heating profile (Fig. 3.10 and Fig. 3.11a,g). The changes to condensation due to changes in CDNC in the two bulk microphysics schemes are comparatively small, which can be explained by the use of saturation adjustment in the calculation of the condensation, which does not include an effect of changes in droplet radius on the condensation.

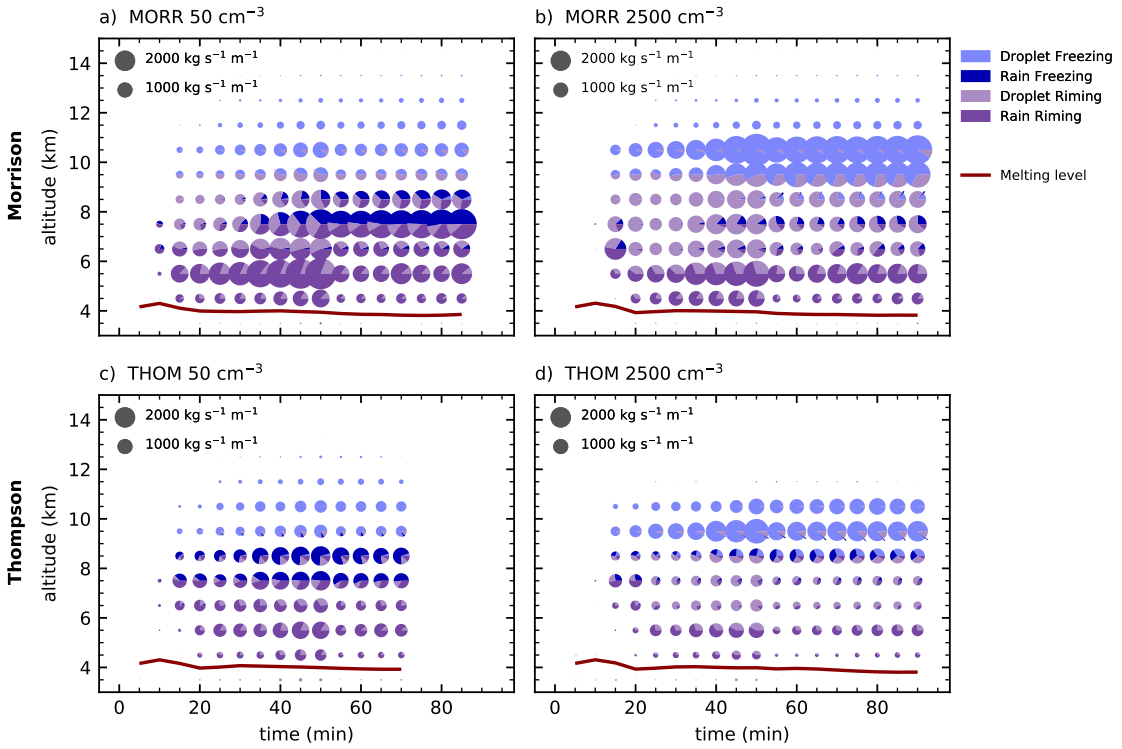

Figure 3.8: Time evolution of the microphysical process rates of freezing and riming processes as in Fig. 3.6.

The same limitation applies to the evaporation of cloud droplets, which also cannot show any direct effect from changes in CDNC due to the use of saturation adjustment. However, the evaporation shows much stronger differences between the two microphysics schemes and also a stronger effect of a variation in CDNC (Fig. 3.11b,h). The strong changes in the evaporation at higher levels in the mixed-phase region of the cloud, especially for the Thompson scheme, can be explained with the changes in deposition on frozen hydrometeors (Fig. 3.11e,k). The increased deposition with increasing CDNC through the changes to the frozen hydrometeors could lead to a further decrease in the saturation vapour pressure over water in the water-subsaturated regions of the cloud and thus additional evaporation. There is also a noticeable decrease in condensation in the higher layers of the mixed-phase region of the cloud at around 10 km for the Thompson scheme (Fig. 3.11g), which could be similarly related to the increase in deposition. The evaporation in the lower layers is associated with the evaporation of raindrops. The differences between the

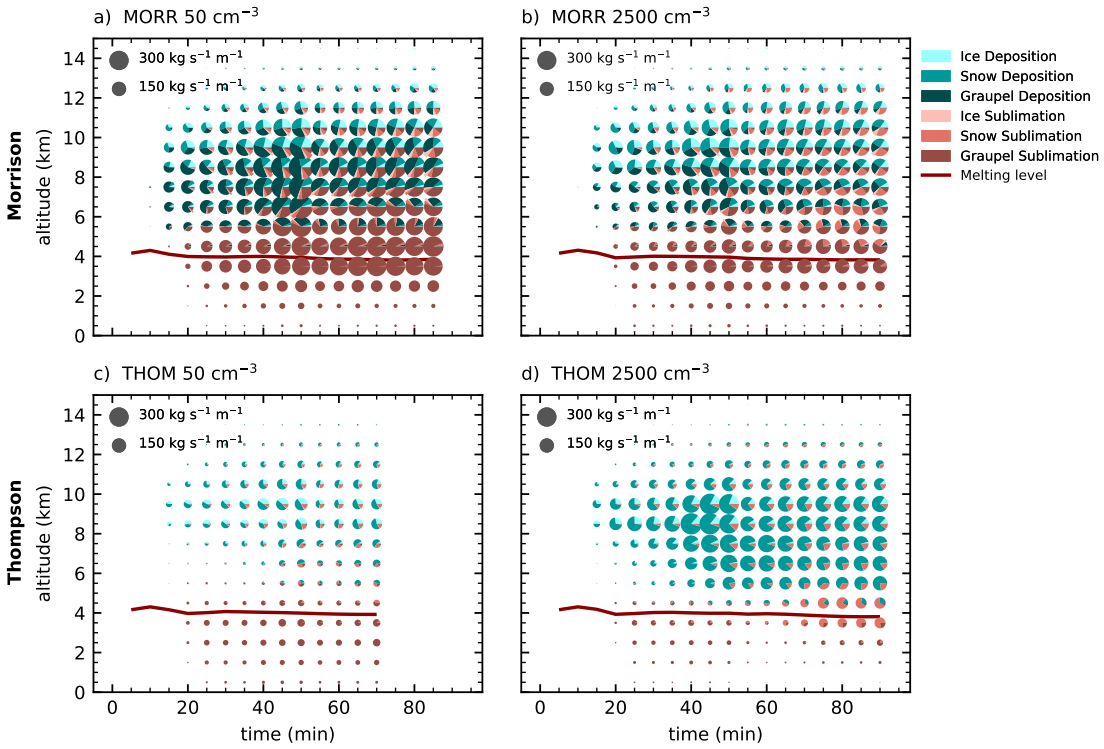

Figure 3.9: Time evolution of the microphysical process rates of deposition and sublimation as in Fig. 3.6.

two schemes and the variation with changes in CDNC can be directly related to the differences in the amount of rain, which is both higher and more strongly decreasing with increasing CDNC in the Thompson scheme than in the Morrison scheme.

All three microphysics schemes show a small shift of latent heating to higher altitudes superimposed on that in the range between 7 km and about 10 km for increasing CDNC (Fig. 3.10), which can be associated with the shifts in freezing and riming (Fig. 3.11d,i), described in more detail in Fig. 3.8. The decrease in latent cooling from melting processes in the lowest layers is stronger in the Thompson scheme than in the Morrison scheme (Fig. 3.11b,h).

There are large differences between the microphysics schemes in the latent heating and cooling from sublimation and deposition and their response to changes in CDNC. The Morrison scheme shows a clear decrease in both sublimation and deposition with increased CDNC (Fig. 3.11e,f). Apart from changes due to the shift in hydrometeors from

hail to snow and cloud ice (Fig. 3.5 and Fig.3.9), these decreases can be related to the lower amount of ice hydrometeors in the mixed-phase region of the cloud. Although these two changes cancel each other to a large extent in the integrated latent heating, the two processes occur at different heights, which results in a shift of latent heating to lower levels, opposing the changes to the freezing and riming processes (Fig. 3.11c). Furthermore, this strong decrease in sublimation leads to a decrease in water vapour near the cloud base, which could cause the consistent decrease in condensation at around 5 km altitude in the Morrison scheme (Fig. 3.11a).

In the Thompson scheme, sublimation of ice hydrometeors is weak and barely affected by changes in CDNC (Fig. 3.11l). However, increases in CDNC lead to an increase in deposition in the higher parts of the cloud (Fig. 3.11k). This effect can be explained by the observed shift in hydrometeors from graupel to cloud ice and snow since deposition on graupel is turned off in the Thompson microphysics scheme, while it occurs on both snow and cloud ice. This increase in deposition could be the main reason for the changes observed in evaporation of cloud droplets as it increases the sub-saturation over water in the mixed phase in regions that are supersaturated with respect to ice. This can be interpreted as a manifestation of the Wegener–Bergeron–Findeisen process (Wegener, 1911; Findeisen, 1938; Findeisen et al., 2015; Storelvmo and Tan, 2015), transferring water mass from liquid hydrometeors to the frozen hydrometeors. This constitutes an additional feedback from the changes in the ice phase back on the liquid-phase hydrometeors.

In contrast to the increased latent heating from freezing or melting, changes in condensation and evaporation, as well as in sublimation and deposition, are linked to a change in condensate loading, which affects the buoyancy of the cloud and thus at least partially buffers the impact of latent heating and cooling on the dynamics of the clouds.

The changes to the vertically integrated latent heating in the cloud for all three microphysics schemes do not show a clear trend with increasing CDNC (Fig. 3.10d,e,f). The Thompson scheme shows slightly higher integrated latent heating for the two simulations with the highest CDNC content, but no consistent trend over the rest of the simulations

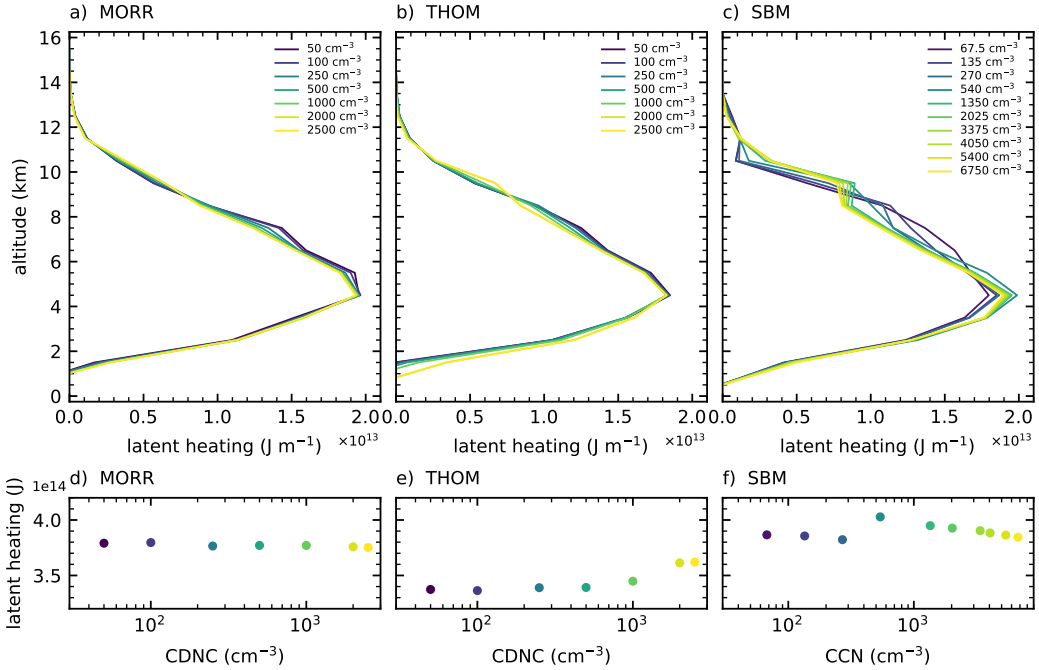

Figure 3.10: Profiles of the sum of latent heating over the lifetime of the dominant tracked cell for the three microphysics schemes in CASE1.

(Fig. 3.10e). The SBM simulations show a slightly decreasing trend of integrated latent heating for the highest CDNC values above 1000 cm^{-3} but no consistent trend over the entire range of values (Fig. 3.10f) . Despite the change to the altitude of freezing there is no systematic change in the integrated latent heat release from freezing for both bulk microphysics schemes that would contribute to an invigoration of the cloud. In the Morrison scheme, the strong changes in deposition and sublimation almost entirely cancel out when integrated vertically. In the Thompson microphysics scheme, the increase in the integrated latent heat release from deposition cancels out the decrease in the integrated evaporation of cloud droplets and rain.

3.3.3. Effects on cloud mass and centre of gravity

The tracking and watershedding allow for a determination of the cloud mass inside the identified cloud volumes and the centre of gravity of the hydrometeors in the cloud. These

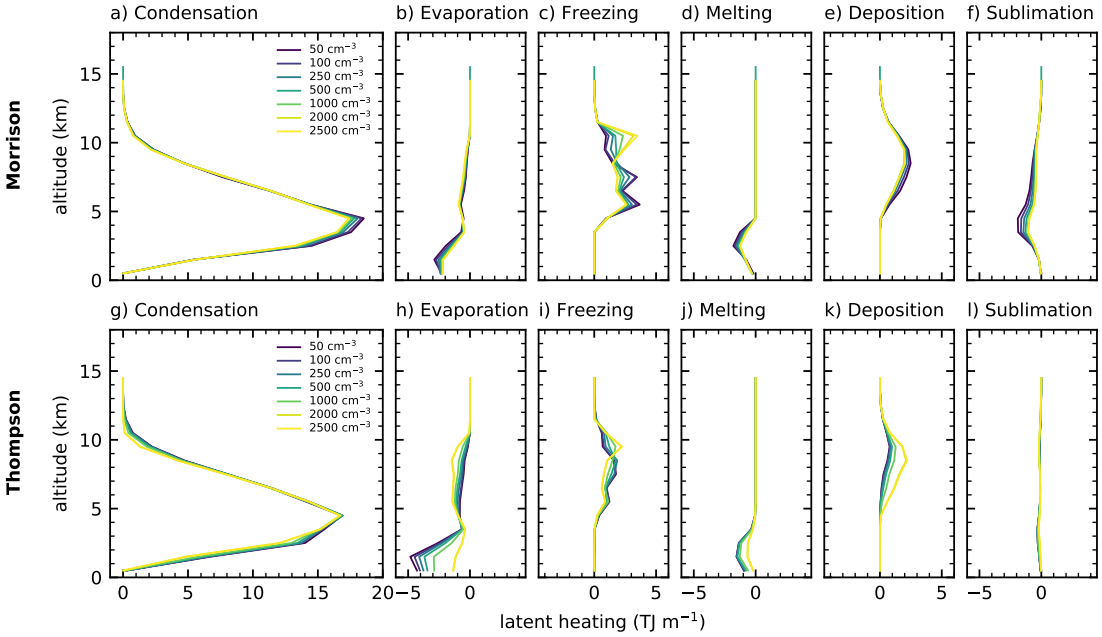

Figure 3.11: Profiles of the components of the latent heating and cooling over the lifetime of the tracked cell for the two bulk microphysics schemes in CASE1.

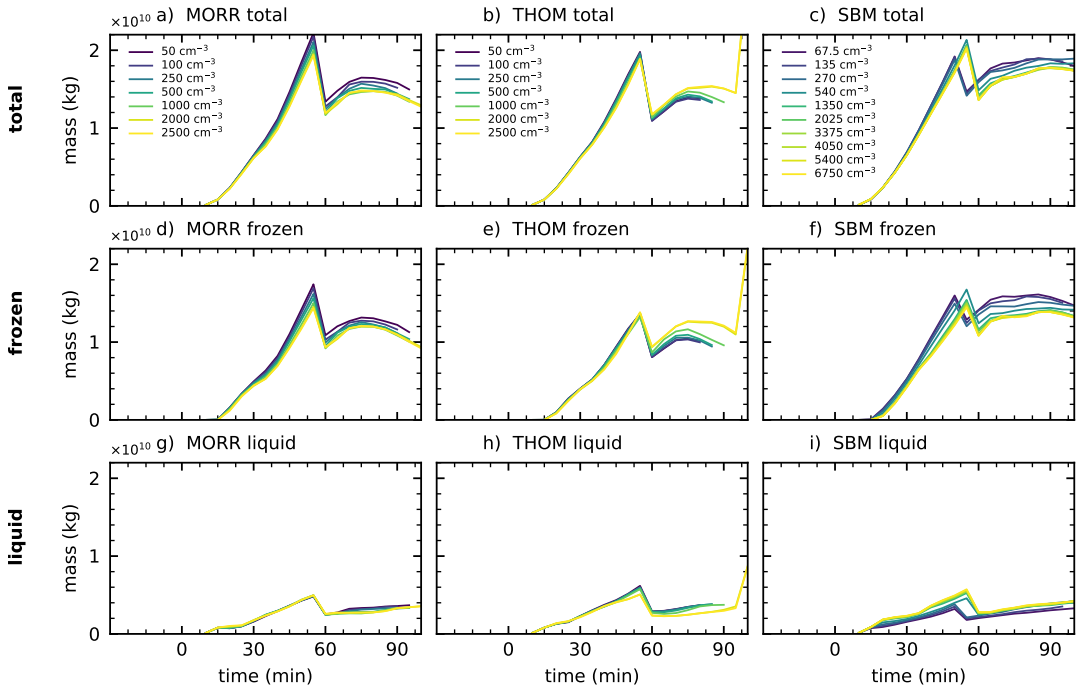

Figure 3.12: Total water mass, liquid water mass and frozen water mass in the analysed right-moving cell for the three different microphysics schemes (Morrison: left, Thompson: middle, SBM: right) in CASE1. The jump in the curves occurs at the point where the cell splits into two individual cells.

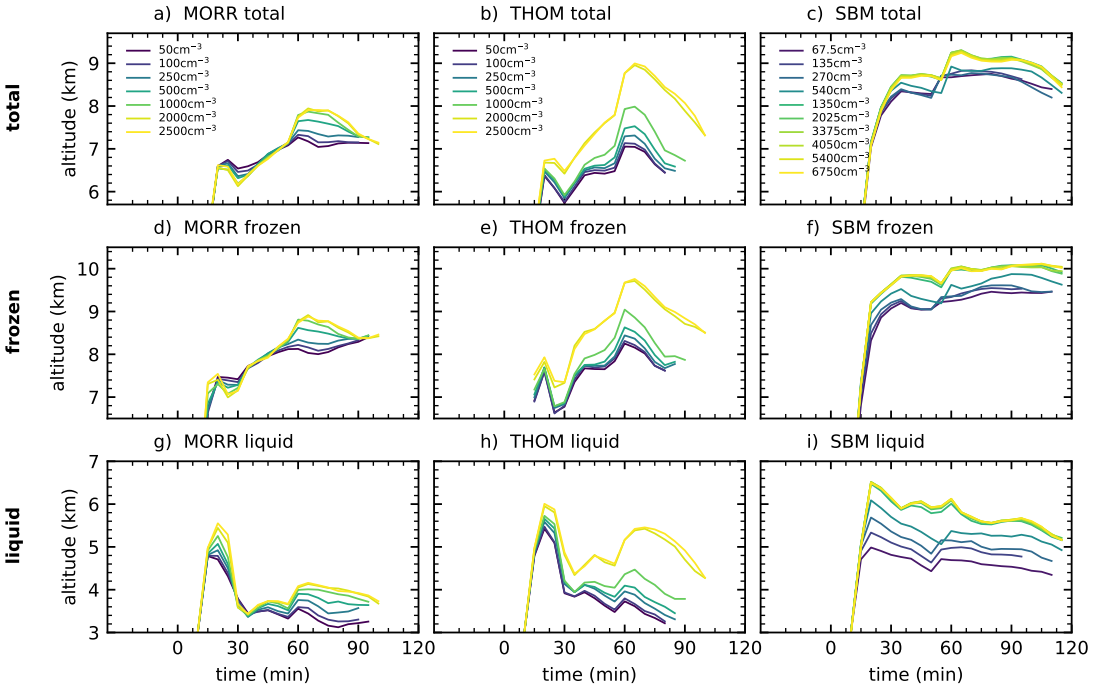

Figure 3.13: Altitude of the centre of gravity of the cloud and the individual phases in the analysed right-moving cell for the three different microphysics schemes (Morrison: left, Thompson: middle, SBM: right) in CASE1.

analyses are also performed separately for the liquid-phase and ice-phase hydrometeors in the cloud, which allows us to relate the changes in the properties for the entire cloud to changes in the individual phases.

The evolution of the cloud mass and the mass of the two water phases in the cloud (Fig. 3.12) in the three microphysics schemes is similar, with a maximum cloud mass of about $2{\cdot}10^{10}$ kg for all microphysics schemes before the splitting of the cell and then about $1.5{\cdot}10^{10}$ kg for the two bulk microphysics schemes (Fig. 3.12a,b) and slightly higher cloud masses of up to $1.8{\cdot}10^{10}$ kg in the spectral-bin microphysics scheme (Fig. 3.12c). The cloud mass and also the difference between the bulk schemes and the bin scheme are dominated by the ice-phase hydrometeors, while the liquid-phase mass is very similar in all three different microphysics schemes, making up about 20-25% of the total cloud mass.

There are, however, marked differences in the response to changes of the aerosol proxy between the microphysics schemes. The Morrison scheme shows a decrease in total cloud

mass and ice-phase mass by about 10-15% over the range in which we increase the CDNC and no substantial changes in the liquid phase. This decrease in ice-phase mass can be directly linked to the changes in the microphysical process rates analysed in Sec. 3.3.2. The shift of freezing to higher altitudes leads to a reduction in frozen hydrometeors in the mixed phase of the cloud and thus less growth of the ice phase through vapour deposition. In the Thompson scheme, however, increased CDNC leads to an increase in ice-phase and total mass and a small increase in cloud liquid mass. This increase agrees well with the increased deposition due to the changes in the ice hydrometeor partition in the cloud discussed in Sec. 3.3.2. In the simulations using the SBM scheme, the two phases show a differing response to the aerosol proxy with increased liquid hydrometeor mass and a decrease in ice-phase mass for increasing CCN.

The altitude of the centre of gravity is affected by the choice of microphysics scheme, with an overall higher centre of gravity for the SBM scheme (Fig. 3.13c) compared to the two bulk microphysics schemes (Fig. 3.13a,b).

There is a consistent response in the cloud heights for all three microphysics schemes. The microphysics schemes show an increase in the height of the centre of gravity of the entire cloud, which is more pronounced using the Thompson scheme (about 1.5 km) than in the Morrison scheme(about 0.5-1 km). This includes an upward shift in both the liquid and frozen water in the cloud. The increased height of the liquid phase can be directly related to the decrease in the formation of warm rain (Fig. 3.6) and the more numerous cloud droplets reaching higher up in the cloud in the polluted case compared to the dominating raindrops in the cleanest case (Fig.3.5). The increase in the altitude of the ice phase in the cloud with increased CDNC can be related to the changes in the altitude of the freezing processes. However, it can also be a result of the lower fall speeds of the ice and snow hydrometeors dominating in the polluted case instead of graupel and hail in the cleanest cases. As for the bulk microphysics schemes, there is an increase in the height for both phases in the simulations using the SBM scheme, which is more pronounced in the liquid phase of the cloud.

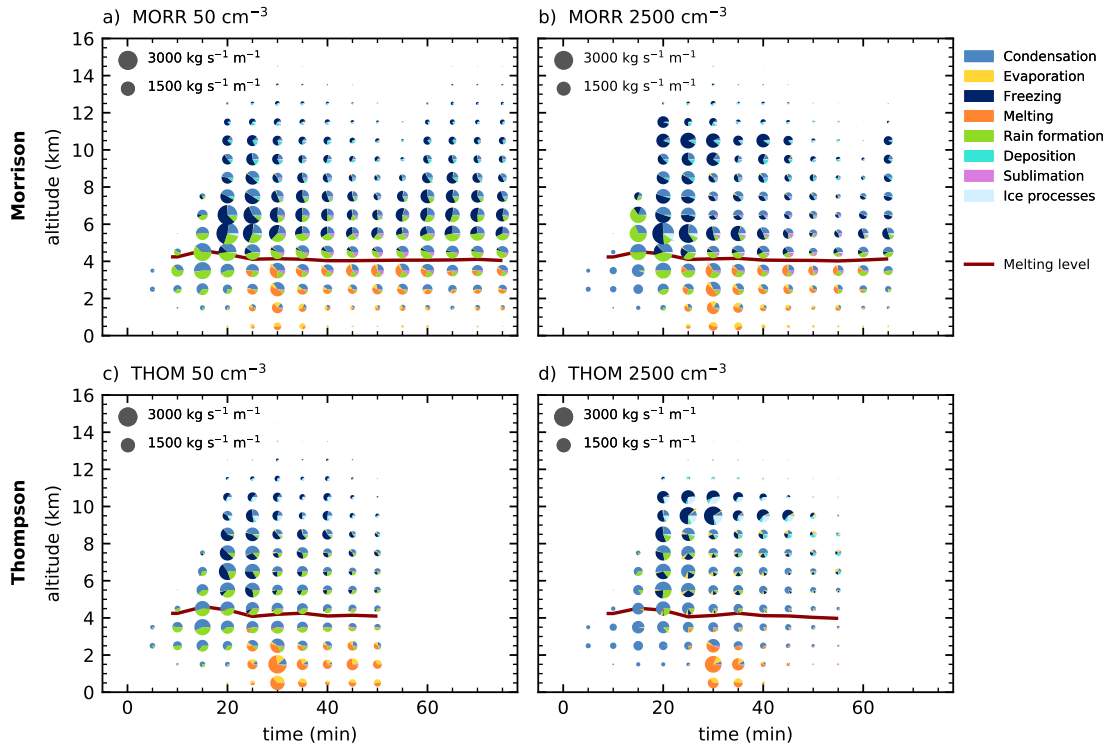

Figure 3.14: Temporal evolution of the microphysical process rates in CASE2 for the cleanest (left) and most polluted (right) simulations and the two bulk microphysics schemes (Morrison: top, Thompson: bottom). The pie charts denote the different groups of microphysical process rates with the area proportional to the sum of the microphysical process rates in the specific altitude interval inside the cloud volume.

All three microphysics schemes show a clear saturation in the effect of changes in the CDNC/CCN concentration. Variations above 2000 cm^{-3} in the bulk schemes and above 1350 cm^{-3} in the SBM simulations only lead to small effects on both the cloud mass and the altitude of the centre of gravity of the different phases.

3.3.4. Sensitivity test: a second idealised supercell case (CASE2)

To investigate the representativeness of the results and the response of the deep convective clouds to the variation of aerosol proxies CDNC and CCN, the same set of simulations and analyses have been performed for a second idealised supercell case (CASE2) with different forcing and initial conditions (Section 3.2.1).

The time evolution of the cloud-averaged process rates for the two bulk microphysics

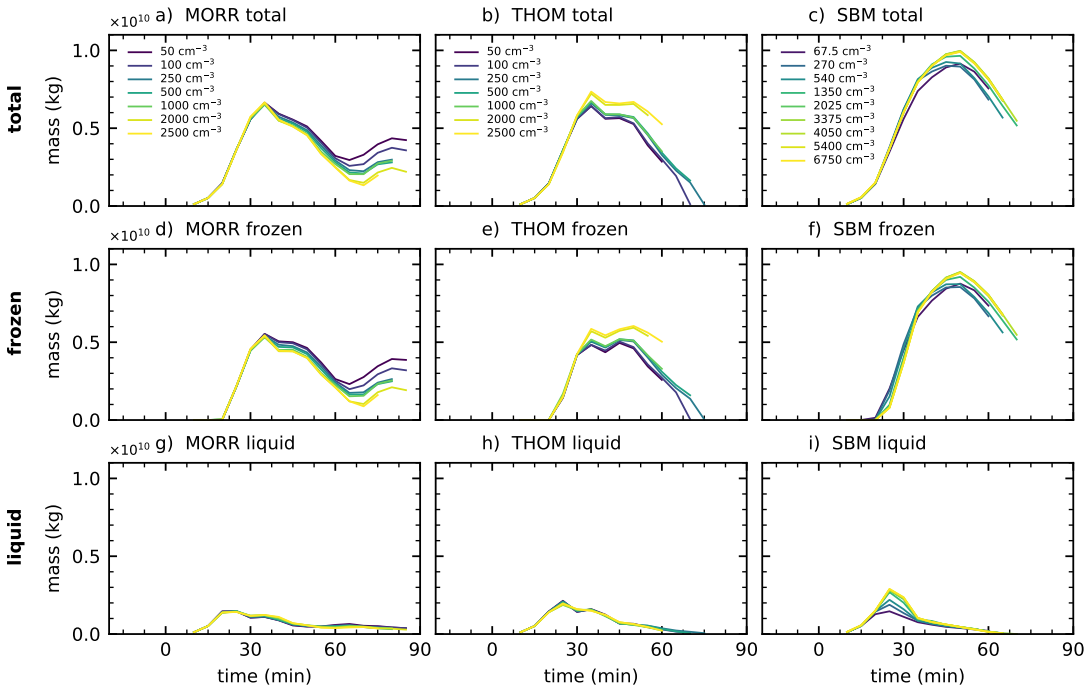

Figure 3.15: Total water mass, liquid water mass and frozen water mass in the analysed left-moving cell for the three different microphysics schemes (Morrison: left, Thompson: middle, SBM: right) in CASE2.

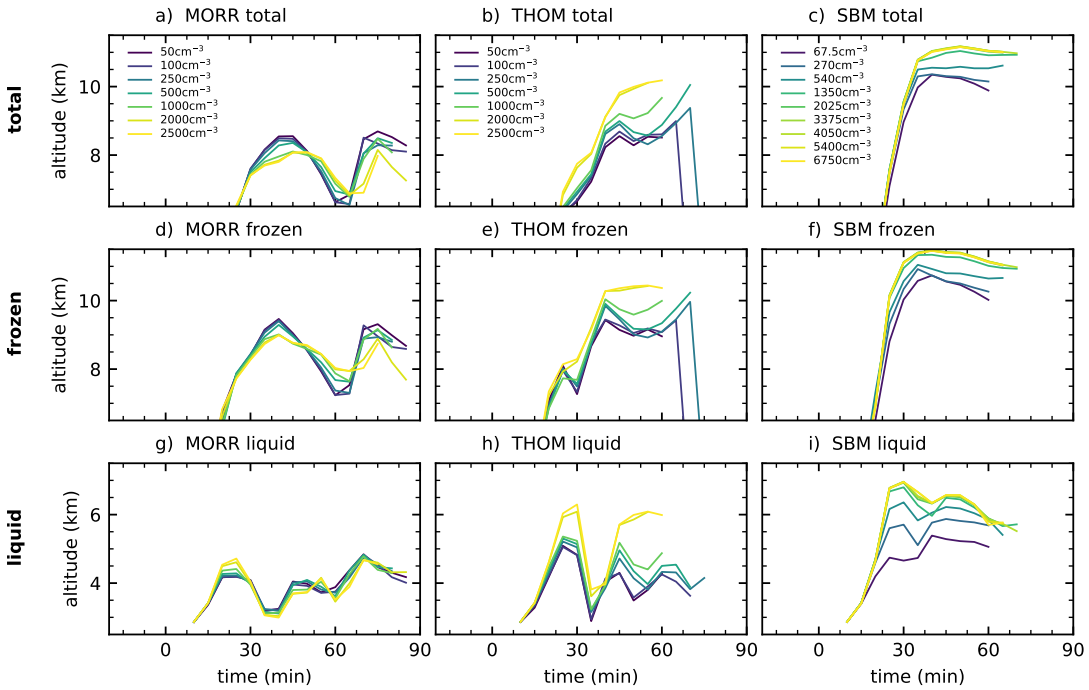

Figure 3.16: Altitude of the centre of gravity of the cloud and the individual phases in the analysed left-moving cell for the three different microphysics schemes (Morrison: left, Thompson: middle, SBM: right)in CASE2.

schemes (Fig. 3.14) shows that the total microphysical water transfer is much weaker in CASE2 than in CASE1, with process rates about a factor of 3 smaller. This case shows much stronger differences between the two bulk microphysics schemes in the general evolution of convection. For the Morrison microphysics scheme, a development of the convective cloud in two stages occurs. After an initial maximum in the microphysical processes after around 30 minutes of simulation time, the convective activity becomes weaker before picking up again after about an hour of simulation time. For the Thompson microphysics scheme, this second episode of development in the tracked cell is completely absent for all simulations, with the cloud dissipating after about 60 minutes of simulation time, which is about 25 minutes earlier than using the other two microphysics schemes. This is potentially related to the substantially higher cooling at and below cloud base due to the evaporation of rain and the melting of frozen hydrometeors. The cooling can substantially weaken the convective updraft and thus prevent the further development of the cell that takes place in the simulations using the two other microphysics schemes. This finding agrees with a shorter lifetime of the cleanest case for the simulations with the Thompson scheme in CASE1 (Fig. 3.6).

Despite these differences in the evolution, CASE2 shows very similar changes in the microphysical processes due to a variation of CDNC to CASE1 for both microphysics schemes. The formation of rain due to autoconversion of cloud droplets and accretion by rain is smaller and restricted to lower heights in the polluted case using the Morrison microphysics scheme. For the Thompson microphysics scheme, the formation of rain is decreased and shifted to higher levels in the model under polluted conditions. Furthermore, the freezing and riming processes predominantly occur at higher altitudes than in the clean case for both bulk microphysics schemes.

In line with these changes to the microphysical process rates, the evolution of the cloud mass in CASE2 (Fig. 3.15) is smaller than in CASE1 for the two bulk microphysics schemes, with about half as much hydrometeor mass in the cloud up to about $5{\cdot}10^9$ kg. The ice phase is more dominant, with the liquid phase of the cloud only accounting for

less than a quarter of the total cloud mass. The simulation with the spectral-bin microphysics scheme shows a larger cloud mass than the two bulk schemes for this case, only about 30% smaller than in CASE1 (Fig. 3.15a,b,c), which includes much more frozen hydrometeor mass than the two bulk microphysics schemes (Fig. 3.15d,e,f), while liquid-phase mass is similar between the three microphysics schemes (Fig. 3.15g,h,i).

The effects of a variation of CDNC are quite similar to the ones seen in CASE1 for the two bulk microphysics schemes (Fig. 3.15a,b). The simulations with the Morrison scheme show a relatively small decrease in cloud mass, while cloud mass increased by about 15% for the Thompson microphysics scheme. These changes are almost entirely due to changes in the ice phase of the clouds with no marked effects of a variation in the liquid phase (Fig. 3.15g,h) for both bulk schemes. The simulations with the spectral-bin microphysics scheme, however, show an opposite response compared to CASE1, with an increase in cloud mass of a similar magnitude to the variation in the two bulk microphysics schemes (Fig. 3.15c), which is dominated by changes in the ice phase (Fig. 3.15f). There is an increase of almost 50% in cloud liquid mass in the earlier stages of the cloud evolution (Fig. 3.15i) at around 25 minutes of simulation time between the cleanest and the most polluted simulations with the SBM scheme. This coincides with a delayed evolution of the ice phase during that period of the developing cloud.

The changes in the altitude of the centre of gravity show less clear relationships with changes in the aerosol proxies CDNC/CCN in this case for the two bulk microphysics schemes. The Morrison scheme (Fig. 3.16a,d,g) has the strongest variation in the time evolution of the altitude of the centre of gravity but generally shows a decrease in the altitude for both the liquid and ice phases in the cloud. In the Thompson scheme (Fig. 3.16b,e,h) increased CDNC leads to an increase in the height of the centre of gravity of the entire cloud and of both phases of water in the cloud. Similarly, increasing CCN in the spectral-bin microphysics scheme (Fig. 3.16c,f,i) leads to a strong increase in the altitude of the cloud mass and the individual phases, with the COG of total mass about 1.5 km higher in the most polluted case (6750 cm^{-3}) compared to the clean case (67.5 cm^{-3}) and

an even stronger shift of up to 2 km in the liquid phase. All the SBM simulations with a higher CCN value than about 1500 cm^{-3} lead to relatively similar results, which means that the aerosol effects saturate at this value.

3.4. Conclusions and outlook

We investigated the effects of changes in cloud droplet number concentration (CDNC) and cloud condensation nuclei (CCN) concentrations on the development of idealised simulations of deep convection to test proposed aerosol effects. This includes different mechanisms of convective invigoration (Rosenfeld et al., 2008; Lebo and Seinfeld, 2011; Fan et al., 2013; Grabowski and Morrison, 2016). A combination of cell tracking and detailed process-rate diagnostics was used to investigate the evolution and structure of the microphysical processes in individual deep convective cells. We used three different cloud microphysics schemes (two bulk schemes and one bin scheme) to investigate how the choice of microphysics scheme affects these results. By covering a wide range of values of CDNC/CCN representative of conditions from very clean to very polluted, we were able to look for consistent responses of the clouds to changes in these aerosol proxies and thus go beyond a simple comparison of just clean and polluted conditions.

An increase in cloud droplet number concentration from values representing clean conditions (CDNC=50 cm^{-3}) to strongly polluted conditions (CDNC=2500 cm^{-3}) leads to a shift of freezing processes to higher levels in both bulk microphysics schemes. Detailed analyses of the individual process rates confirmed that this is indeed related to a shift from freezing of rain to freezing of cloud droplets and a decrease in riming of raindrops due to larger amounts of liquid water in the form of cloud droplets instead of rain. This, in turn, can be related to the changes in autoconversion and accretion in the warm-phase region of the cloud. This is in line with the first step of the mechanisms proposed for convective invigoration of deep convection due to an increase in aerosols acting as CCN (e.g. Rosenfeld et al., 2008; Lebo and Seinfeld, 2011; Fan et al., 2013; Altaratz et al., 2014).

These changes are concurrent and linked to changes in the prevailing hydrometeors in the different parts of the clouds. Both bulk microphysics schemes showed a strong increase in cloud droplet mass mixing ratio at the expense of raindrops for increased CDNC. This shift leads to an increase in the height of freezing and riming processes, which shifts the latent heat release from freezing upwards by about 2 km. This response is consistent between the different microphysics schemes and confirms earlier studies that stated the importance of changes in the partition between rain and cloud droplets in determining the evolution of freezing and riming (Seifert and Beheng, 2006; Kalina et al., 2014). The simulations with the SBM scheme show an upward shift in latent heating that is very similar to the one observed for the two bulk schemes and associated with the lifting of the freezing and riming processes. This confirms that the effect is not just an artefact of the separate treatment of raindrops and cloud droplets in the bulk microphysics schemes or the application of saturation adjustment. In the ice phase of the clouds, there is a clear shift from mainly graupel or hail in the low-CDNC simulations to larger fractions of snow and ice crystals in the high-CDNC simulation.

A more detailed analysis of the different components of the latent heating for the two bulk microphysics schemes shows a complex superposition of changes to the different phase changes in the tracked cells. This confirms results from previous studies on the effects of aerosols on supercells (Khain et al., 2008; Morrison, 2012; Kalina et al., 2014) and other deep convective clouds (Ekman et al., 2011) that pointed out a range of compensating processes limiting convective invigoration and a strong dependency on the environmental conditions in which the cloud develops. Condensation and evaporation are the largest contributions to latent heating and cooling in the cloud. The relative changes in these two processes due to changes in the aerosol proxies are comparatively small, except for the changes in the evaporation of rain due to the strong decrease in the formation of rain. This is to be expected, as condensation and evaporation of cloud droplets in the two bulk microphysics schemes are represented using saturation adjustment, which does not include the effect of changes in cloud drop radius on the condensation and evaporation processes.

Saturation adjustment has the potential to mask the effects of aerosols in highly supersaturated strong convective updrafts as described, e.g. in Lebo et al. (2012) and Fan et al. (2018). Lebo et al. (2012) argue that saturation adjustment, as used in both bulk microphysics schemes in this study, leads to an artificial increase in condensation in the lower levels of the clouds, which would limit the effects of aerosol concentrations on buoyancy in mid and high levels.

There are marked differences between the two bulk schemes in the profiles of sublimation and deposition as well as in the response of these processes to changes in CDNC. This can be attributed to different parameter choices in the schemes. The strongest differences result from the fact that deposition onto graupel hydrometeors is not allowed to occur in the Thompson microphysics scheme, which leads to a strong increase in deposition due to the replacement of graupel by the other ice-phase hydrometeors on which deposition occurs. This strong increase in deposition additionally drives changes in condensation and evaporation in the mixed-phase region of the cloud via the Wegener–Bergeron–Findeisen process. By effectively removing water vapour, this leads to a noticeable feedback on the evaporation and condensation on cloud droplets that are intrinsically not affected by changes in CDNC because of the use of saturation adjustment. It was also shown that the melting of frozen hydrometeors contributes substantially to the formation of raindrops, especially under high CDNC conditions, which forms an additional important feedback of changes in the ice-phase on the warm-phase processes.

The changes to the individual components of integrated latent heating in the cloud due to a variation of CDNC compensate each other in the two bulk microphysics schemes. Hence, there is no clear change in the total integrated latent heating in the cloud with changes in CDNC/CCN and no thermodynamic invigoration from changes in the microphysics due to the change in the aerosol proxies. This result is confirmed in the SBM simulations, that also do not show any substantial changes in vertically integrated latent heating for a variation of CCN. Therefore, the absence of convective invigoration in the bulk microphysics schemes cannot be solely attributed to the application of saturation adjustment.

The analysis of the clouds with respect to the total cloud mass and the altitude of the centre of gravity showed some contrasting results between the different microphysics schemes. There is a clear signal of a lifting of all parts of the clouds to higher altitude under polluted conditions, probably associated with the changes in the ice-phase hydrometeor partition. This agrees with findings from, e.g. Fan et al. (2013), reporting substantial changes to cloud height and even in the absence of convective invigoration in the form of increased total latent heating in the cloud. However, the analysis of cloud mass revealed opposing trends in the response between the three microphysics schemes. There is no clear pattern in the different responses to CDNC/CCN with regard to these bulk cloud properties, with variations between the two bulk microphysics schemes often as large as between the bulk schemes and the spectral-bin microphysics scheme, which confirms the strong differences between microphysics schemes found in previous studies (Lebo et al., 2012; Khain et al., 2015; White et al., 2017).

The results for the first case (CASE1), based on Weisman and Klemp (1982), are supported by the analysis of a second idealised supercell case (CASE2), based on Kumjian et al. (2010) and Dawson et al. (2013). The microphysical process-rate diagnostics revealed similar changes in rain formation and the altitude of freezing and riming processes for the two bulk microphysics schemes in this second case. All three microphysics schemes showed that the effects of a variation of CDNC or CCN saturate above a threshold value in both simulated cases. Variations above a CDNC of around 2000 cm^{-3} in the bulk schemes and above a CCN concentration of 1500 cm^{-3} in the bin microphysics scheme do not lead to any further changes in the convective clouds with regard to cloud condensate mass or altitude. This confirms results from previous studies such as Kalina et al. (2014) that reported saturation of the aerosol effects at similar values.

The pathway analysis developed for this study also includes the process rates for the number concentrations of the different hydrometeors. This includes processes like ice multiplication that could play an important role to better understand some of the possible pathways of aerosol effects on convective clouds (Fan et al., 2013; 2016).

This work focused on the analysis of microphysical pathways of aerosol effects on deep convective clouds in an idealised framework. To test the robustness of the results under realistic scenarios, including potential buffering mechanisms, we are currently applying our analysis framework to large case study simulations of isolated convection over the area around Houston, Texas, as part of the ACPC initiative (Aerosol, Cloud, Precipitation, and Climate Working Group, http://www.acpcinitiative.org) . We apply the cell tracking algorithm and the analysis of the detailed process-rate output developed in this study for a range of different cloud-resolving models and contrasting aerosol conditions. In these simulations, the individual deep convective clouds in the cloud field evolve and interact freely, which allows for a thorough analysis of important aspects such as the impact of aerosol conditions on the cell lifetimes or the statistics of the cloud size spectrum. The introduction of parameters describing the entire convective cell such as cloud mass and the position of the centre of gravity can contribute to a meaningful analysis of cloud-field simulations with a large number of individual clouds.

The understanding of the detailed structure of microphysical processes in individually tracked deep convective clouds and the analysis of the pathways through which aerosol perturbations affect the deep convective clouds advance our understanding of aerosol–cloud interactions. This can be used to inform the parametrisation of microphysical processes and aerosol-convection interactions in global climate models. Recent developments in the use of global cloud-resolving models in climate research (e.g. Ban et al., 2014; Seiki et al., 2014; Sato et al., 2018) further motivate a detailed understanding of the pathways of aerosol effects on convective clouds and the uncertainties in their representation in numerical models.

3.A. Convective cell tracking and cell-based analysis

The tracking algorithm tracks individual convective cells and their volume based on the model output fields of vertical velocity and total condensate mixing ratio. The tracking

of maxima in the column vertical velocity field is performed using trackpy (Allan et al., 2016). The algorithm from trackpy that is used to identify the updraft features requires an initial assumption for the size of the tracked object. We chose a diameter of 15 km to represent the large convective updrafts in the supercell cases. Tracked updrafts are required to exist for six output time steps, i.e. 30 minutes, to be included in the analysis, which helps to exclude spurious features in vertical velocity and thus focus on the analysis of properly developed deep convective cells. We extrapolate by two time steps at the beginning and at the end of each tracked trajectory to include a representation of the initial development of the convective clouds and the evolution after the weakening of the central updraft.

The volume of the convective clouds is determined by a watershedding algorithm using a fixed threshold to determine the extent of the individual clouds based on the tracked updrafts. We use a threshold of $1\,\mathrm{g\,cm^{-3}}$ for the total water content in this study and a variation of this threshold by an order of magnitude to $0.1\,\mathrm{g\,cm^{-3}}$ showed that choosing a lower threshold did not have a strong impact on the cloud volume and cloud mass or any of the more detailed process analyses.

3.B. Microphysics schemes and process-rate diagnostics

Table 3.2 and Table 3.3 give an overview of the microphysical process rates for the hydrometeor masses as they are implemented in the two bulk microphysics schemes (Thompson et al., 2008; Morrison et al., 2009) studied in this paper.

In the Thompson scheme, some of the process rates are defined as signed variables representing two opposed processes. In these cases, we have used the process-rate variable with the positive sign for the respective process and ignored the values with the negative sign, which are covered by the opposing process (e.g. PRG_RCG for riming of rain on graupel and PRR_RCG for melting of graupel due to the collection by rain). Condensation/evaporation processes and deposition/sublimation processes are only defined through

one combined process-rate variable in the code. We have thus added the process rates with a negative sign as a variable in our diagnostics (e.g. E_PRW_VCD for the evaporation of droplets in addition to PRW_VCD for condensation) to allow for independent analyses of these, e.g. when aggregating the variables in space or time.

Ice multiplication according to the Hallet–Mossop process is implemented differently in the two bulk microphysics schemes. In the Morrison scheme, this is implemented as a direct transfer of water mass from the liquid phase to ice particles and considered to be contributing to riming. In the Thompson scheme, however, it forms a transfer from the frozen hydrometeor to new ice particles and is thus part of the ”ice processes”. Hence, these processes are found in different categories in the two tables presenting the process rates. As the actual mass transfer is negligibly small this difference between the schemes is not relevant for the analyses performed in this study.

In the Morrison microphysics scheme as used in this study, the autoconversion of cloud droplets and accretion by rain are parametrised based on Khairoutdinov and Kogan (2000) and ice nucleation is based on Cooper (1986) and (Rasmussen et al., 2002). The Thompson scheme applies an autoconversion parametrisation based on Berry and Reinhardt (1974a), while the different freezing modes follow Bigg (1953), Cooper (1986) and Koop et al. (2000).

The two bulk microphysics schemes differ in important parameters regarding the different hydrometeor classes. The Morrison microphysics scheme is used in its configuration that treats the dense frozen hydrometeors as hail with a density of $900\,\mathrm{kg\,m^{-3}}$, while the simulations with the Thompson microphysics used graupel with a density of $500\,\mathrm{kg\,m^{-3}}$. The density of cloud ice, however, is higher in the simulations with the Thompson scheme $890\,\mathrm{kg\,m^{-3}}$ compared to the Morrison scheme ($500\,\mathrm{kg\,m^{-3}}$), while snow density is set to $100\,\mathrm{kg\,m^{-3}}$ for both schemes. The Thompson scheme has a more complex treatment of the snow hydrometeor class compared to the Morrison scheme, making use of a combination of two size distributions and thus allowing for a variation of the density over its evolution (Field et al., 2005; Thompson et al., 2008). The fall speed calculations

are based on different equations in the two microphysics schemes, all parameters for the hydrometeor classes are left at their default values.

Table 3.2: Mass transfer process rates for the Morrison microphysics scheme (Morrison et al., 2009).

Variable	Description	from	to	Grouping
PCC	Condensation on droplets	vapour	droplets	Condensation
EPCC	Evaporation of droplets	droplets	vapour	Evaporation
PRE	Evaporation of rain	rain	vapour	
PRC	Autoconversion	droplets	rain	Rain formation
PRA	Accretion	droplets	rain	
MNUCCC	Contact freezing of droplets	droplets	ice	Freezing
MNUCCD	Primary ice nucleation	droplets	ice	
QICF	Homogeneous freezing of droplets	droplets	ice	
MNUCCR	Contact freezing of rain	rain	ice	
QGRF	Homogeneous freezing of rain	rain	graupel	
QNIRF	Homogeneous freezing of rain	rain	snow	
PSACWS	Riming on snow	droplets	snow	Riming
PSACWI	Riming on ice	droplets	ice	
PSACWG	Collection of droplets by graupel	droplets	graupel	
PGSACW	Collection of droplets by snow	droplets	graupel	
PRACS	Rain-snow collection	rain	snow	
PIACR	Ice-rain collision	rain	graupel	
PIACRS	Ice-rain collision	rain	snow	
PRACG	Collection of rain by graupel	rain	graupel	
PGRACS	Collection of rain by snow	rain	graupel	
QMULTG	Ice multiplication droplets and graupel	droplets	ice	
QMULTS	Ice multiplication droplets and snow	droplets	ice	
QMULTRG	Ice multiplication rain and graupel	rain	ice	
QMULTR	Ice multiplication rain and snow	rain	ice	
PGMLT	Melting of graupel	graupel	rain	Melting
QIIM	Melting of ice	ice	droplets	
PSMLT	Melting of snow	snow	rain	
PRD	Deposition on ice	vapour	ice	Deposition
PRDS	Deposition on snow	vapour	snow	
PRDG	Deposition on graupel	vapour	graupel	
EPRDG	Sublimation of graupel	graupel	vapour	Sublimation
EVPMG	Graupel melting and evaporating	graupel	vapour	
EPRD	Sublimation of ice	ice	vapour	
EPRDS	Sublimation of snow	snow	vapour	
EVPMS	Snow melting and evaporating	snow	vapour	
PRAI	Accretion of cloud ice by snow	ice	snow	Ice processes
PRCI	Autoconversion of cloud ice to snow	ice	snow	
PRACI	Ice–rain collection (ice to graupel)	ice	graupel	
PRACIS	Ice–rain collision (ice to snow)	ice	snow	
PSACR	Collection of snow by rain	snow	graupel	

Table 3.3: Mass transfer process rates for the Thompson microphysics scheme (Thompson et al., 2008).
* denotes processes that are implemented but disabled in the microphysics scheme.

Variable	Description	from	to	Grouping
PRW_VCD	Condensation	vapour	droplets	Condensation
PRV_REV	Evaporation of rain	vapour	droplets	Evaporation
E_PRW_VCD	Evaporation of cloud droplets	droplets	vapour	
PRR_WAU	Autoconversion	droplets	rain	Rain formation
PRR_RCW	Accretion	droplets	rain	
PRI_WFZ	Freezing of cloud droplets	droplets	ice	Freezing
PRI_RFZ	Freezing of rain to ice	rain	ice	
PRG_RFZ	Freezing of rain to graupel	rain	graupel	
PRS_SCW	Collection of droplets by snow	droplets	snow	Riming
PRG_SCW	Collection of droplets by snow	droplets	snow	
PRG_GCW	Collection of droplets by graupel	droplets	graupel	
PRG_RCG	Collection of rain by graupel	rain	graupel	
PRR_RCS	Collection of rain by snow	rain	snow	
PRR_RCS	Collection of rain by snow	rain	graupel	
PRR_RCI	Collection of ice by rain	rain	graupel	
PRW_IMI	Melting of ice	ice	rain	Melting
PRR_GML	Melting of graupel	graupel	rain	
PRR_RCS	Collection of snow by rain	snow	rain	
PRR_RCG	Collection of graupel by rain	graupel	rain	
PRS_SDE	Deposition on snow	vapour	snow	Deposition
PRS_IDE	Deposition on ice to snow	vapour	snow	
PRI_IDE	Deposition on ice	vapour	ice	
PRG_GDE *	Deposition on graupel	vapour	graupel	
PRI_INU	Ice nucleation	vapour	ice	
PRI_IHA *	Freezing of aqueous aerosols	vapour	ice	
E_PRS_SDE	Sublimation of snow	snow	vapour	Sublimation
E_PRI_IDE	Sublimation of ice	ice	vapour	
E_PRG_GDE	Sublimation of graupel	graupel	vapour	
PRS_SCI	Collection of ice by snow to graupel	ice	graupel	Ice processes
PRS_IHM	Hallet–Mossop process	snow	ice	
PRS_IAU	Autoconversion of ice to snow	ice	snow	
E_PRS_RCS	Collection of snow by rain	snow	graupel	
PRI_RCI	Collection of ice by rain	ice	graupel	
PRG_IHM	Hallet–Mossop process	graupel	ice	

4. tobac: A flexible framework for tracking clouds in diverse datasets

The analysis of individually tracked clouds for their microphysical evolution and bulk cloud properties presented in Chap. 3 enabled a detailed analysis of the evolution of microphysical process rates and bulk cloud properties over the life-cycle of individual deep convective clouds. However, this analysis was developed for the use with a specific numerical model for a specific scientific application. The same limitation applies to most of the previously developed tracking analyses for clouds in high-resolution model simulations (Dawe and Austin, 2012; Heus and Seifert, 2013), which restricts the applicability to other applications and the ability to compare different approaches for the same datasets. An important application of a more flexible approach is the simultaneous analysis of model simulations and observational data for the evaluation of model performance or intercomparison studies comparing different numerical models for the same simulation case. The relatively small and short idealised cases simulated in Chap. 3 did not pose significant challenges to the computational performance of the analysis. However, memory usage and processing time are crucial once large datasets, e.g.from numerical model simulations with extended domains or retrievals from geostationary satellite retrievals, are analysed for extended periods of time.

To overcome these limitations, the tracking approach developed in Chap. 3 is extended into the tracking and analysis framework *tobac* (Tracking and Object-Based Analysis of Clouds) in this chapter. The application of *tobac* is presented using two different examples including both high-resolution model results and geostationary satellite retrievals. The framework is applied based on two different physical quantities to show the flexibility of the software that can be used with every spatially resolved time-evolving dataset.

This chapter is based on a journal article in discussion for *Geoscientific Model Development (GMD)* as:

Heikenfeld, M., Marinescu, P.J.,Christensen, M., Watson-Parris, D., Senf, F., van den Heever, S. C. and Stier, P., "tobac v1.0: towards a flexible framework for tracking and analysis of clouds in diverse datasets". 2019. Geoscientific Model Development Discussions, May, 1–31. https://doi.org/10.5194/gmd-2019-105.

I have conceptualised and developed tobac as a lead developer with input and contributions from the other co-authors. Matt Christensen has downloaded and processed the GOES-13 satellite data for use in the second example application. I have conceptualised and performed the data analysis. I have written the manuscript with input and final approval from all coauthors. *tobac* is currently extended by additional tracking and analysis routines by Fabian Senf (TROPOS Leipzig, Germany) and Will Jones (University of Oxford, UK). The software package is publicly available in a GitHub repository at https://github.com/climate-processes/tobac.

Abstract We introduce tobac (Tracking and Object-Based Analysis of Clouds), a newly developed framework for tracking and analysing individual clouds in different types of datasets, such as cloud-resolving model simulations and geostationary satellite retrievals. The software has been designed to be used flexibly with any two- or three-dimensional time-varying input. The application of high-level data formats, such as iris cubes or xarray arrays, for input and output allows for convenient use of metadata in the tracking analysis and visualisation. Comprehensive analysis routines are provided to derive properties like cloud lifetimes or statistics of cloud properties along with tools to visualise the results in a convenient way. The application of tobac is presented in two examples. We first track and analyse scattered deep convective cells based on maximum vertical velocity and the three-dimensional condensate mixing ratio field in cloud-resolving model simulations. We also investigate the performance of the tracking algorithm for different choices of time resolution of the model output. In the second application, we show how the framework can be used to effectively combine information from two different types of datasets by simultaneously tracking convective clouds in model simulations and in geostationary satellite images based on outgoing longwave radiation. tobac provides a flexible new way to include the evolution of the characteristics of individual clouds in a range of important analyses like model intercomparison studies or model assessment based on observational data.

4.1. Introduction

Clouds are a major feature of the Earth's atmosphere and control many critical processes in the Earth's energy and water budgets (Trenberth et al., 2009). Different types of convective clouds play important but distinct roles in many regions of the globe. Shallow cumulus clouds are widespread over the subtropical trade-wind latitudes and have a strong impact on the radiative balance of the atmosphere, including a potential for strong feedbacks from anthropogenic perturbations of the climate system (Stevens and Feingold, 2009). Deep convective clouds are a defining element of the atmosphere over most of the tropics (Nesbitt et al., 2006), driving both local weather dynamics and larger scale circulation patterns, which has impacts on the entire climate system (Emanuel, 1994). Furthermore, deep convective clouds play a major role in extreme weather events all over the globe (Doswell, 2001; Gensini and Mote, 2014). Therefore, clouds and their interactions with other aspects of the climate system are an essential aspect of many important challenges in our understanding of the Earth's atmosphere and current changes due to anthropogenic influences (IPCC, 2013a). The nature of convective clouds is highly localised. Individual convective cells undergo rapid dynamic development over relatively short timescales of minutes to hours (Orlanski, 1975), while organised convective features, such as mesoscale convective systems (MCS), can persist for many hours or even days (Orlanski, 1975; Laing and Fritsch, 1997; Fritsch and Forbes, 2001; Feng et al., 2018). Further advances in understanding the physical processes underlying the development of these clouds require analysis techniques that go beyond the usual approaches, which are often based on bulk statistical properties over larger regions in space and time, such as entire modelling or observational domains. Model intercomparison studies with cloud-resolving model (CRM) simulations have mostly relied on the comparison of domain and time-averaged quantities or similar statistics (Varble et al., 2011; 2014a; b; Fan et al., 2017). This generally limits the investigation of differences between the models on the scale of individual convective cells or analyses that take the temporal evolution

of individual clouds into account.

Any analysis focused on the properties of individual clouds in larger databases containing numerous cloud elements and aimed at including the time evolution over their development cycle requires some form of cloud tracking technique. A large body of work exists on tracking individual clouds in different types of data, ranging from ground-based radar and geostationary satellite retrievals to model simulations at a range of different resolutions. We now present a short but certainly not exhaustive overview of existing approaches. This will be used to show the capabilities of the existing software and to discuss drawbacks or limitations which motivated the development of the more flexible software framework tobac (Tracking and Object-Based Analysis of Clouds) presented here.

Tracking of individual convective clouds in radar data has been performed for decades (Crane, 1979; Rosenfeld, 1987). These efforts were often motivated by their use in nowcasting of severe weather warnings, e.g. for flooding due to convective precipitation, damage from hail or impacts of high wind speeds such as tornadoes (Dixon and Wiener, 1993; Lakshmanan and Smith, 2009a). Satellite-based tracking of convective clouds has been performed both with a similar focus on nowcasting convection and for long-term analysis in climate research (Menzel, 2001; Sieglaff et al., 2012). Special tracking algorithms that combine information from different wavelength bands of imagers on geostationary satellites, such as Cb-TRAM (Zinner et al., 2008; 2013) and RTD (Autonès and Moisselin, 2013) have been developed as tools to identify and track deep convective clouds throughout their development cycle, including the initial stage of rising cumulus towers. However, both products have been developed for a specific application that strongly limits a more general adaption of the software by the user. Several other studies have used geostationary satellite data to investigate the growing phase and glaciation of deep convective clouds (Mecikalski and Bedka, 2006; Mecikalski et al., 2011; Senf et al., 2015; Senf and Deneke, 2017). Other applications have specifically focused on the analysis of long-lived MCSs over different regions of the globe (Machado et al., 1998; Feng et al., 2012; Hagos et al., 2013; Feng et al., 2018).

Tracking of individual cloud objects in high-resolution CRM simulations and large-eddy simulation models (LES) has been developed alongside the evolution of these simulations in recent decades. Earlier studies on tracking shallow convection in high-resolution model simulations (Zhao and Austin, 2005a; b; Heus et al., 2009) strongly relied on manual detection techniques. Subsequently, Dawe and Austin (2012) and Heus and Seifert (2013) presented automated methods of tracking shallow convection that rely on a continuous release of a decaying tracer from the model as described in Couvreux et al. (2010). However, the functionality of the tracer release and advection must be specifically implemented in each model and restricts the use of this technique to output of high-resolution models. Cloud tracking algorithms applied online during the actual model simulations (Plant, 2009) have the advantage of direct access to the relevant model fields at the model time step and thus the highest possible time resolution. However, these online algorithms must also be implemented separately in a specific model.

Moseley et al. (2013, 2016) tracked precipitation patterns for investigations of deep convective clouds and convective invigoration. Davis et al. (2006) and Davis et al. (2009) presented an object-based analysis of rainfall patches, including tracking capabilities, which was applied to precipitation on a relatively large regional scale. Heiblum et al. (2016a,b) developed and applied a tracking algorithm for warm convective clouds that determines cloud volumes from the condensate mixing ratio field and then propagates the clouds based on the velocity of the cloud centre of mass. This algorithm allows for cloud splits and merges to form complex cloud entities possibly involving numerous individual clouds. Only a few studies have focused on tracking individual deep convective clouds in model simulations in a way that takes into account the actual cloud volumes (Chen et al., 2017). Terwey and Rozoff (2014) developed a tracking algorithm for individual convective updrafts and applied it to CRM simulations of hurricane cases with two different models. However, this effort has not been provided to the community as a generalised software package aimed at more widespread use cases. Several other approaches that included the tracking of individual updrafts in different types of cumulus clouds in a very

detailed manner (Sherwood et al., 2013; Hernandez-Deckers and Sherwood, 2016) would not be easily transferable to data with a lower temporal and spatial resolution.

Despite these advances in developing detailed cloud tracking approaches for use in highly resolved model simulations, most current studies are performed with model grid spacings of several hundreds of metres to a few kilometres, especially when using larger domains or simulations for longer time periods. Providing adequate ways of performing tracking and object-based analyses for different types of clouds, including deep convection, in these kinds of simulations provides a key pathway to better understanding the underlying physical processes.

This overview clearly shows the wide range of extensive efforts that went into the development of elaborate software and analysis tools to track clouds in different types of datasets. However, it also highlights the problem of limited compatibility between the different existing approaches and implementations, especially regarding the intended use of tracking clouds based on different data sources using the same algorithms and analysis tools.

To address some of these limitations of existing approaches and provide a more functional tool with increased flexibility for different applications, we have developed tobac as a new flexible software tool for the identification, tracking and analysis of clouds. This approach certainly does not intend to replace the existing tools in their specific applications, but is rather aims to provide a flexible framework that can be used for a wide range of different datasets and also allows the future integration of some of the existing approaches discussed here.

tobac is designed in a modular way that includes the following basic steps, which are described in detail in the following sections 4.2.1–4.2.5:

1. Data input and output

2. Feature detection

3. Segmentation of cloud areas/volumes

4. Trajectory linking

5. Object-based analysis and visualisation

tobac provides a framework that allows for a convenient application to output from a wide range of model simulations and observational products, as long as it is provided with sufficient temporal and spatial resolution and contains output variables that can be used to identify individual clouds. Therefore, the software package can be used for a range of important applications like model intercomparison studies, which generally rely on simpler analysis methods that do not capture the evolution of individual clouds. These capabilities also allow for comparative studies between model simulations and observational datasets, e.g. from satellite retrievals, using the same underlying statistical methods. Due to the modular structure, tobac is set up for the integration of existing or newly developed algorithms for the different steps in the analysis chain. The implementation in Python provides tobac with access to numerous more specialised existing software libraries for different aspects of the software, such as data input/output, memory usage and the existing functionality from the field of image processing. We also show how we can leverage an existing Python library from an entirely different field of the physical sciences to perform integral parts of the linking step in our application. Furthermore, the choice of Python for tobac makes the package more easily accessible to users as it allows for easier integration into existing analysis workflows and also stimulates the integration of additional components in the modular workflow of the package.

To show the advantages of tobac in practical applications, we present two different examples of using the framework in tracking and analysing deep convective clouds. In the first application, the detection of features is performed on the column-maximum vertical velocity at each output time interval from a CRM simulation. A three-dimensional watershedding algorithm is applied to the updraft field and to the total condensed water content field (mass mixing ratio of all hydrometeors) at each step in time to infer both the volume of the individual updrafts and the clouds associated with the tracked updrafts. These fea-

tures are then filtered and linked into consistent trajectories. We use the tracking results to assess the distribution of cloud lifetimes and the requirements for the model output temporal resolution. In the second application, we perform a simultaneous analysis for model and satellite data. Similar vertically resolved data as used in the other example are usually not available from satellite imagers. The information in most satellite retrievals of cloud properties is limited to two-dimensions. With a multi-spectral selection of channels from the satellite instrument, cloud-top height and radiative properties can be retrieved (McGarragh et al., 2018). An analysis of model-simulated and satellite-retrieved fields of outgoing longwave radiation is presented to demonstrate the flexibility of the tobac approach. By making use of the framework consistently across different datasets like this, we can compare the tracked clouds in both data sources by examining the statistical properties of the resulting population of convective clouds, thereby facilitating model-observation comparisons.

4.2. Software description

In this section, we describe the general design and workflow of the software package as illustrated in Fig. 4.1 for the two example applications presented in Sect. 4.3 and Sect. 4.4. The implementation of the individual analysis steps described here reflects an example combination of analysis steps currently implemented in tobac. Due to the modular setup of the package, different parts of the workflow can be combined in a different way or replaced by future additions to the framework.

4.2.1. Data input and output

The input data for the framework are provided in a high-level format of either Iris cubes (Met Office, 2018) or xarray DataArrays (Hoyer and Hamman, 2017), which include detailed metadata for each data variable, such as units and coordinates. The algorithm

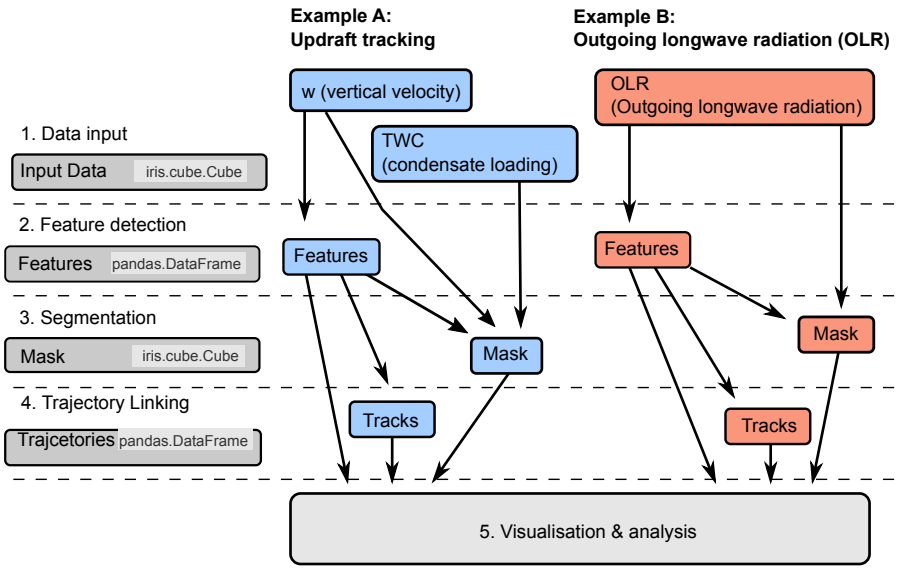

Figure 4.1: Schematic overview of the general workflow of the tobac tracking analysis framework and of the two examples presented in this manuscript.

can thus automatically use these metadata, and the tracking setup can be controlled independently of the temporal resolution, spatial resolution or dimensions of the input data. Tracking parameters representing physical properties like distances or time periods can be set in physical units and are automatically converted to pixel-based values needed for the underlying calculations. Scientific data are provided in a vast variety of different file formats and data structures. Implementing a way of loading the data into the right format for an application often proves to be a significant limitation to the use of new datasets and generally consumes an unjustifiable amount of time and effort, apart from providing an important source of implementation errors. The Python library Community intercomparison Suite (CIS) (Watson-Parris et al., 2016) overcomes this challenge and provides a convenient way to automatically load a vast array of observational datasets into Iris-compatible objects for direct use in tobac.

Both Iris and xarray make use of so-called ”lazy loading” based on the dask package (Rocklin, 2015; Dask Development Team, 2016) for efficient memory usage. The initial loading of data from a file only creates a place-holder. Then, individual operations on the data are combined and evaluated once the final result is to be saved, printed or plotted.

Only at this stage are data actually loaded from disk into the physical memory of the computing machine and individual calculations performed. Based on these capabilities, the entire tobac framework is written with a focus on limiting instantaneous memory usage by splitting up calculations into chunks, e.g. along the time dimension. Hence, even large datasets with individual fields much larger than the memory available on the computing system can be conveniently processed without special adaptation by the user.
The output of the tracking analysis is given in commonly used high-level Python data format as pandas DataFrames (McKinney, 2010) for a table containing the tracked cell centres and trajectories and as Iris cubes or xarray DataArrays for the masks of cloud volumes or areas. This output is automatically amended with the same metadata as the input data like coordinates (e.g. time, longitude, latitude), along with additional information from the tracking process, e.g. a time coordinate relative to the initiation of an individual convective cell. This allows for the convenient and direct use of the output for visualisation and further analyses.

4.2.2. Feature detection

The feature detection can work with any two-dimensional field either present or derived from the input data. In the first example, we use maxima in the maximum vertical velocity in each column of the three-dimensional high-resolution model output to identify individual updrafts (see Sect. 4.3). In the second example, minima in outgoing longwave radiation from satellite retrievals and model output are used in the feature detection (see Sect. 4.4).
To identify the features, contiguous regions above or below a threshold are determined and labelled individually. Smoothing the input data, e.g. with a Gaussian filter, makes this step much more reliable. Erosion of the labelled regions by a specified length or number of pixels leads to more robust detection of individual features as described in Senf et al. (2018).

To describe the specific location of the feature at a specific point in time, we have investigated the use of different spatial properties describing the identified region. The geometric centre can be strongly affected by changes in the shape of the boundary, which is determined based on the selected threshold value. Instead, we have found that a weighted mean

$$\vec{x}_{\text{mean}} = \sum_{\text{i}} w_{\text{i}} \vec{x}_{\text{i}} \tag{4.1}$$

with weights w_{i} given by the difference between the values of the chosen field at the individual points V_{i} and the threshold value V_{feature}

$$w_{\text{i}} = \frac{V_i - V_{\text{feature}}}{\sum_{\text{i}} V_{\text{i}} - V_{\text{feature}}} \tag{4.2}$$

has proven to perform best in determining a robust feature position. We can interpret this position as the centre of mass of the component of the field exceeding the chosen threshold value.

Using a single threshold to identify features can lead to problematic results in two different ways. A very restrictive threshold means that clouds with weak vertical velocities or clouds during their initial and decaying stage will not be captured. On the other hand, a weakly restrictive threshold can lead to spurious results as it might lead to large unconfined regions around deep convection being selected, or to an unwanted merging of several distinct cloud features into one. To resolve these conflicting requirements arising in the case of a single threshold value, we have developed a step-wise approach with a range of threshold values (Fig. 4.2). These threshold values have to be chosen specifically for each application of tobac. The choice can be based on a detailed analysis of the data used for tracking to determine where the features separate from the background, e.g. based on histograms as shown in Sect. 4.4, or using empirical values from previous studies of the specific phenomena. The feature identification starts with labelling the regions for the least restrictive threshold. For each threshold value, features are identified in the

same way (Fig. 4.2b,d,f) and replace existing features that were found based on a less restrictive threshold value in the surrounding region (Fig. 4.2e,g).

This combination of different thresholds allows tobac to detect lower intensity features representing weaker convective clouds or clouds in their initial or decay stage but identify localised features with stronger updrafts or colder cloud tops within the weaker-threshold areas. In the first example application (Sect. 4.3), consecutive maximum updraft threshold values of 3, 5 and 10 $\mathrm{m\,s^{-1}}$ were used, while tracking based on OLR in the second example (Sect. 4.4) was performed with consecutively smaller threshold values (250, 225, 200, 175 and 150 $\mathrm{W\,m^{-2}}$).

4.2.3. Segmentation

Once features and feature centres are identified, segmentation techniques are used to associate areas or volumes to each identified feature. In the current version of the tobac framework, we have implemented segmentation using watershedding techniques from the field of image processing (skimage.morphology.watershed from the scikit-image library (Soille and Ansoult, 1990; Walt et al., 2014) with a fixed threshold value $V_{\mathrm{segmentation}}$. This value has to be set specifically for every type of input data and application, as explained in more detail for the two example applications in Sect. 4.3 and Sect. 4.4. Watershedding segmentation treats the input field as a topographic map and separates the input into individual regions similar to individual watersheds or catchment basins along a dividing ridge in a geological context (Meyer, 1994). These techniques are widely used in several existing cloud tracking and analysis algorithms described in Sect. 4.1, such as Heiblum et al. (2016b), Fiolleau and Roca (2013) and Senf et al. (2018).

This segmentation routine can be performed for both two-dimensional and three-dimensional data. At each time step, a marker is set at the position (weighted mean centre) of each feature identified in the detection step in an array otherwise filled with zeros. In the case of the three-dimensional watershedding, all cells in the column above the weighted mean centre position of the identified features fulfilling the threshold condition $V_{\mathrm{segmentation}}$ are

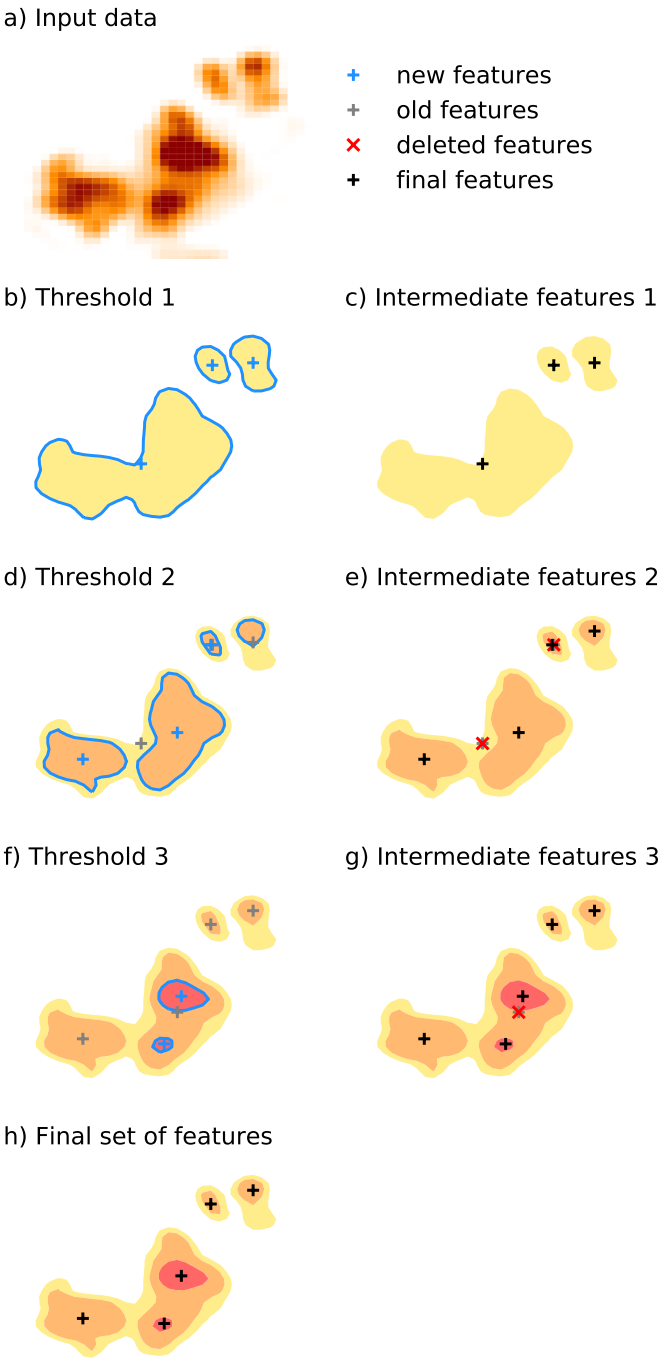

Figure 4.2: Schematic illustration of the multi-threshold feature detection approach using three different threshold values.

set to the respective marker. The algorithm then fills the area (2D) or volume (3D) based on the input field starting from these markers until reaching the threshold $V_{\text{segmentation}}$. If two or more cloud objects are directly connected, the border runs along the watershed line between the two regions. This procedure creates a mask of the same shape as the input data, with zeros at all grid points where there is no cloud or updraft and the integer number of the associated feature at all gridpoints belonging to that specific cloud/updraft. This mask can be conveniently and efficiently used to select the volume of each cloud object at a specific time step for further analysis or visualisation.

The structure of tobac allows for the future implementation of other algorithms for the segmentation step, e.g. replacing the watershedding approach by random walk techniques (Grady, 2006; Wang et al., 2019) or other image processing tools.

4.2.4. Trajectory linking

The individual features and associated area/volumes identified in each time step have to be linked into cloud trajectories to analyse the time evolution of cloud properties for a better understanding of the underlying physical processes. For this step, we have implemented a linking method that makes use of trackpy (Allan et al., 2016), a Python library originally developed for tracking particles and cells in microscopic images. The linking determines which of the features detected in a specific time step (see Sect. 4.2.2) is identical to an existing feature in the previous time step. For each existing feature, the movement within a time step is extrapolated based on the velocities in a number of previous time steps. The algorithm then breaks the search process down to a few candidate features by restricting the search to a circular search region centred around the predicted position of the feature in the next time step. For newly initialised trajectories, where no velocity from previous time steps is available, the algorithm resorts to the average velocity of the nearest tracked objects.

The parameter v_{max} restricts how much the future position of a feature is allowed to de-

viate from a linear extrapolation of the trajectory over time. It thus has the units of a velocity and describes the dependency of the circular search range d on the output time step Δt in the data used for the tracking

$$d = v_{\max} \Delta t. \tag{4.3}$$

In the applications (Sect. 4.3 and 4.4), we set this value to $v_{\max}$=10 m s^{-1}, which results in a search range of 600 m around the projected position for 1 minute data input and 3 km for 5 minute data input. Variations in the shape of the regions used to determine the positions of the features can lead to quasi-instantaneous shifts of the position of the feature by one or two grid cells even for a very high temporal resolution of the input data, potentially jeopardising the tracking procedure. To prevent this, tobac uses an additional minimum radius of the search range $d_{\min}$ (2 km, equivalent to four times the grid spacing in Sect. 4.3) that specifies a lower limit for the size of the search region. Both these parameters are given as physical quantities and then converted into pixel-based values used in trackpy. This allows for cloud tracking that is controlled by physically-based parameters that are independent of the temporal and spatial resolution of the input data. We make use of this for cloud tracking with different model output frequencies for the same simulations in the example application in Sect. 4.3.

Features can be allowed to be missed for a certain number of time steps (*memory*) and still get linked into a trajectory. However, this option should be used with caution, as it can lead to erroneous trajectory linking, especially for data with low time resolution. For example, convective clouds can produce outflow boundaries that initiate new convective clouds nearby, and the newly-formed clouds are more likely to be linked to the original clouds with this option. The trajectories can also be extrapolated to additional output time steps at the start and at the end of the tracked path. This allows for the inclusion of both the initiation of the cell and the decaying later stages of the cell development that may have been unidentified based on the chosen thresholds. Furthermore, a threshold for the

minimum lifetime of the tracked objects can be used to exclude the analysis of clouds that have only been tracked for a very short period and are likely to be spurious features. Such tracked objects can contaminate analyses focusing on the cloud lifetime and associated quantities.

The trajectories are recorded in a pandas DataFrames. This enables filtering the resulting trajectories, e.g. to reject trajectories that are only partially captured at the boundaries of the input field both in space and time.

The current version of the linking step does not include an explicit treatment of the splitting and merging of clouds, as implemented in several of the cloud tracking algorithms reviewed earlier (Dawe and Austin, 2012; Heus and Seifert, 2013; Heiblum et al., 2016b). Instead, the algorithm creates a continuous track for the cloud that most directly follows the direction of travel of the preceding or following cell path. However, we have structured the implementation of tobac in a way that allows for the future addition of more complex tracking methods recording a more complex network of relationships between cloud objects at different points in time.

4.2.5. Object-based analysis and visualisation

To make use of the results of the previous steps, we provide detailed tools to analyse and visualise the tracked objects. We provide a set of routines that enable performing analyses and deriving statistics for individual clouds, such as the time series of integrated properties and vertical profiles. We also provide routines to calculate summary statistics of the entire population of tracked clouds in the cloud field like histograms of cloud areas/volumes or cloud mass and a detailed cell lifetime analysis (see Fig. 4.5 and Fig. 4.9).

These analysis routines are all built in a modular manner. Thus, users can reuse the most basic methods for interacting with the data structure of the package in their own analysis procedures in Python. This includes functions performing simple tasks like looping over all identified objects or cloud trajectories and masking arrays for the analysis of individual

cloud objects. Plotting routines include both visualisations of the entire cloud field and detailed visualisations for individual convective cells and their properties.

4.2.6. Advantages of the implementation in Python

While the majority of the existing tracking approaches reviewed in Sect. 4.1 are implemented either in Fortran, C and C++ or in proprietary programming languages like MATLAB, we have chosen to use Python for our tracking framework for several practical reasons. Python has become the go-to standard for data analysis in many fields of scientific research, including the atmospheric sciences in recent years (Lin, 2012; Perkel, 2015). This makes it possible to develop software that is accessible and modular, which allows for the successful addition of user-contributed algorithms or the adoption or application of the workflow for cases beyond those presented here. The use of libraries in the scientific Python ecosystem including NumPy, SciPy, and matplotlib (Hunter, 2007; Walt et al., 2011), along with a large stack of existing and optimised libraries providing image processing features (Walt et al., 2014), means that the package is based on actively developed open-source projects. This ensures an accurate, effective and tested implementation of the individual calculations as well as the continuous integration of new developments and improvements. Most of these Python libraries use Fortran or C for the actual underlying calculations, which means that many of the individual operations within tobac make use of the increased computational speed of these languages. The use of Python also means that even users without extensive programming experience will be able to easily adapt existing procedures into the workflow or contribute additional algorithms to the modular structure of the tobac tracking framework.

The implementation in Python also enables the use of Jupyter notebooks (Perez and Granger, 2007; Kluyver et al., 2016) as an innovative way of developing, visualising and sharing scientific data analyses. We provide examples of the analyses presented here as Jupyter notebooks provided in the software package.

Memory limitations have been cited as a significant challenge for the application of many

of the presented algorithms (Dawe and Austin, 2012; Heus and Seifert, 2013). The use of modern memory management techniques such as ”lazy data loading” in the underlying Python libraries Iris (Met Office, 2018) or xarray (Hoyer and Hamman, 2017), which both rely on the dask data types (Rocklin, 2015), allows for clear and concise source code while sparing the users of having to deal with memory-related considerations themselves.

4.3. Example A: tracking of convective cells in high-resolution model simulations based on updraft velocities and condensate mixing ratios

In the first example, we apply the tracking framework to CRM simulations of scattered deep convection. Deep convective clouds are characterised by regions of strong vertical motions which are concentrated in relatively confined updraft cores that dominate the dynamics of the cloud evolution (Cotton et al., 2010). Hence, the updraft cores are well suited to be used for identifying and tracking individual convective cells. We use the total condensate mixing ratio, i.e. the total amount of liquid and frozen water per mass of dry air, to associate the identified updraft cores with the respective cloud volume at each time. We make use of simulations that were performed as part of a larger model intercomparison case study in the deep convection working group of the Aerosol, Clouds and Precipitation (ACPC) initiative (van den Heever et al., 2017) aimed at understanding the response of scattered convection over the region around Houston, Texas to changes in aerosol number concentrations. The tracking algorithm presented here will be used as part of the analysis for the model intercomparison study using several different three-dimensional CRMs. Here we use model results from simulations with the Weather Research and Forecasting (WRF) model (Skamarock et al., 2005) with a horizontal grid spacing of 500 m and vertical grid spacing of 50–300 m. The model time stepping is 2 s for the outmost domain and 1.5 s for the two inner domains. The simulations use the Morrison microphysics scheme (Morrison et al., 2005; 2009) and the Rapid Radiative Transfer Model (RRTMG) short and longwave radiation scheme (Iacono et al., 2008). The simulations are performed in

a nested setup with three domains using grid spacings of 4.5 km, 1.5 km and 500 m. Initial conditions for all domains and boundary conditions for the outermost domain were provided by the GDAS-FNL reanalysis NCEP (2015). The simulations have been performed for 24 hours from 12:00 UTC on the 19 June 2013 to 12:00 UTC on the 20 June 2013. The simulations setup is described in more detail in Chap. 5 and in van den Heever et al. (2017). In this example, we use data from the innermost domain with a 500 m grid spacing and 500 grid cells in each horizontal direction. The simulation results are output at a frequency of 1 minute for an extended part of the simulation period (3 hours, 21:00 UTC – midnight) and at a frequency of 5 minutes for 12 hours of the simulations (16:00 UTC – 04:00 UTC). The outermost domain of the same nested simulation setup is used for the comparison with satellite data presented in Sec. 4.4.

We use a combination of the three-dimensional fields of vertical velocity and total condensate mixing ratio in this application to track individual convective clouds. The individual steps of the analysis are visualised for a specific point in time and a subset of the model domain in Fig. 4.3. The three-dimensional vertical velocity field is reduced to the maximum updraft velocity in each model column over a mid-tropospheric range of geopotential height (3000 m to 8000 m) (Fig. 4.3a). This avoids the impact of strong vertical motions both in the lower troposphere, that may be associated with outflow boundaries, and also gravity waves in the upper troposphere. A Gaussian filter with a variance of $\sigma = 1\,\mathrm{km}$ is used to filter the input in the feature detection step (Fig. 4.3b) to create a smoother field that assists in the feature detection. This two-dimensional field is then used to identify individual deep convective updrafts in the simulation. The feature identification following Sect. 4.2.2 is performed with a set of three updraft velocity thresholds of $3\,\mathrm{m\,s^{-1}}$, $5\,\mathrm{m\,s^{-1}}$ and $10\,\mathrm{m\,s^{-1}}$ (Fig. 4.3c) and yields the individual features marked in Fig. 4.3d. Segmentation is performed on the condensate mixing ratio using the watershedding technique (see Sect. 4.2.3) with a threshold of $0.5\,\mathrm{g\,kg^{-1}}$ to identify the cloud volumes corresponding to the individual identified updrafts. The cloud volumes derived with watershedding from the condensate mixing ratio field of each of the identified up-

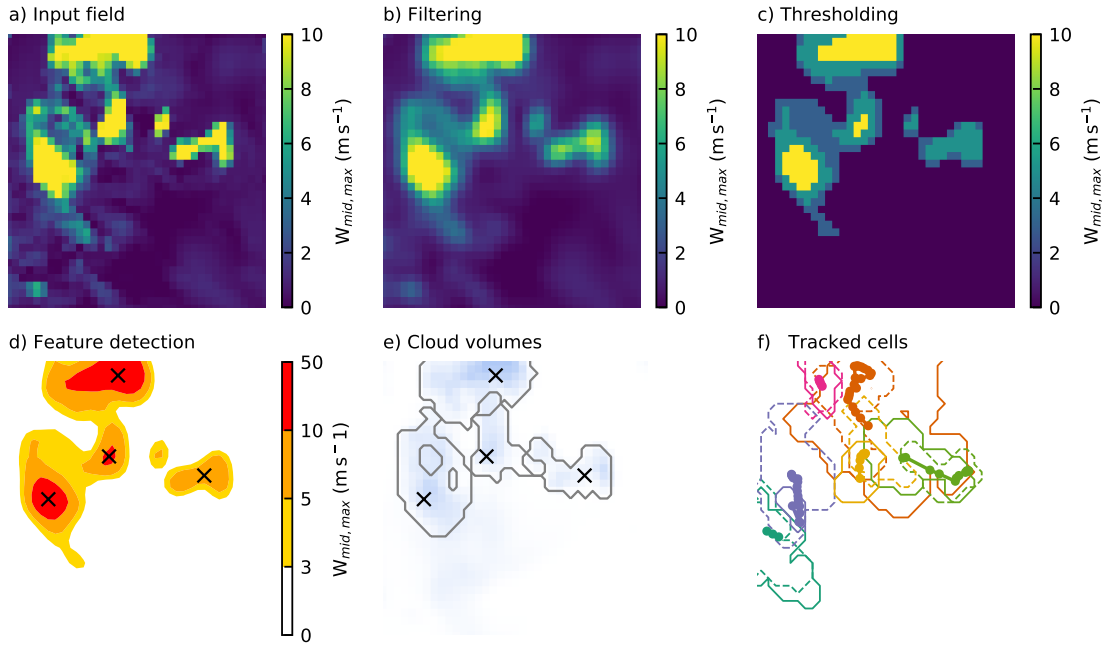

Figure 4.3: Schematic overview of the individual steps of the tracking algorithm for an example subset of the domain used in example A including the input mid-tropospheric velocity field. The input data (a) are smoothed with a filter (b) before regions above or below a set of thresholds are determined (c) to identify the individual features (d). (e) shows the surface projection of the associated cloud volumes determined in the segmentation set and (f) shows the entire trajectories of the cells present at this time step, including the surface projection of the cell volume at the start (dashed) and at the end (solid) of the trajectory.

drafts is represented by the surface projection of the 3D volumes (Fig. 4.3e). Note that the intersecting lines in Fig. 4.3e represent instances where cloud volumes associated with different updraft cores may be present in the same column but at different altitudes. Trajectories are formed by linking up the individual features and are shown including the surface projection of the cloud volumes at the initial and final time step of each tracked cell (Fig. 4.3f). A smaller subset of the data and analysis for this example including the tracking analysis and visualisation is available as a Jupyter notebook as part of the package source code.

4.3.1. Time resolution requirements for cloud tracking

The cloud tracking framework presented here can be applied to model output from any atmospheric model simulation with sufficient resolution to resolve the features intended to be studied. However, successful tracking of individual clouds in the simulation output requires sufficiently high spatial and temporal resolution. However, writing output data at high frequency from numerical model simulations drastically increases the computational expense of the simulations and the size of the output datasets. For observational data, such as geostationary satellite data, the available time resolution might be limited by technical restrictions such as scanning time or data transmission. It is thus important to determine the necessary input frequency for the successful tracking of a specific type of dataset.

The tracking step (Sect. 4.2.4) uses trackpy, which is based on the tracking methods developed for in Crocker and Grier (1996). The algorithm has been originally developed for microscopic particles; however, all considerations apply equally to the tracked features we regard here in tobac. In their development of the algorithm, the authors state that successfully linking objects into trajectories is only feasible if the typical displacement of a particle during one time step is smaller than the typical inter-particle spacing. To assess how valid these assumptions are for our application, we investigated the nearest-neighbour distances for individual cells and the typical displacement of the tracked objects within one time step. Distances between cloudy updrafts (Fig. 4.4a) were most frequently around 5 km with a substantial tail of up to 30 km representing more isolated cells. This distribution is independent of the chosen output time step as it represents an instantaneous relationship between cells at individual points in time. The updraft propagation velocities derived for tracking with a 1 minute output time step (Fig. 4.4b) were most frequently at around $4\,\mathrm{m\,s^{-1}}$ with more than 90 % of the velocities below $10\,\mathrm{m\,s^{-1}}$.

Using the output time step and these velocities, we can calculate the displacement of the clouds within one tracking time step and compare that to the nearest-neighbour distances (Fig 4.4c). In addition to the time step of 1 minute, the displacements that would result from lower output frequencies of 5, 10, 15 and 30 minutes based on these velocities were

calculated (Fig 4.4c). While there is no clear overlap between the nearest-neighbour distance distribution and the displacement distribution for an output time step of 1 minute, the tails of the distributions start overlapping for 5-minute input data, although the peaks are still distinctly separate. For lower output frequencies of 15 minutes and 30 minutes, however, there is a clear overlap between the nearest-neighbour distance distribution and the distributions of displacement within one time step. Therefore, these frequencies would be outside the range postulated for the successful application of the tracking algorithm used by trackpy. Hence, when applying this tracking algorithm, it is important to understand both the spatial distribution of the desired tracked features and their propagation velocities to ensure that the output time step is sufficiently frequent. For the simulations assessed here, both 1-minute and 5-minute output frequencies would be acceptable for tracking cloudy updrafts, with 1-minute output likely to provide more successful and accurate tracks.

The cloud lifetimes (Fig. 4.5) are analysed for the same 3-hour period using the two different time resolutions (1 minute and 5 minutes) and agree well for clouds with lifetimes larger than about 15 to 20 minutes. For shorter lifetimes, the 1-minute input data yield substantially more tracked cells. It is obvious that we can only properly represent and analyse cloud lifetimes for clouds that exist over a certain number of output time steps in this framework. An individual cloud that is tracked for 5 to 10 minutes based on 1-minute output allows for robust conclusions about the evolution of the cloud in that period. The same time would merely lead to two or three individually identified objects for 5-minute data output, which would be the minimum to draw any useful conclusions about the lifetimes or time evolution of the clouds.

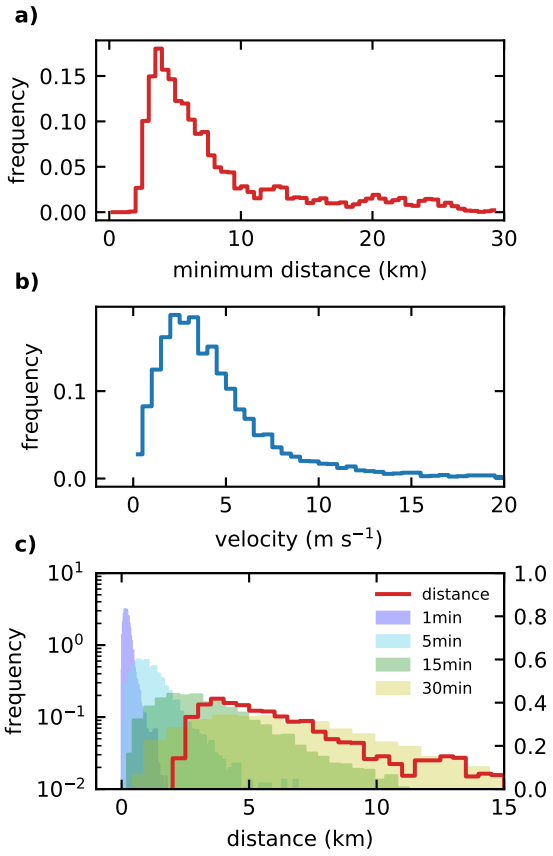

Figure 4.4: (a) Distributions of the distance to the next identified object for all identified objects and (b) velocities for tracked cloud objects at each time step of the trajectories. (c) The distribution of derived travel distances of individual clouds during one output time step (shaded colours) resulting from these velocities in (b) is shown together with the distribution of the minimal distance to the nearest-neighbour for individual objects as shown in (a).

4.4. Example B: tracking of deep convective clouds in model simulations and geostationary satellite data based on outgoing longwave radiation (OLR)

Satellite retrievals are an important tool in climate and weather research as they are an effective way of obtaining observation-based quantities over greater spatial scales in the atmosphere. Specifically, geostationary satellites offer continuous coverage in space and time for a specific region and can, therefore, be used for understanding the temporal evolution of atmospheric phenomena. Direct comparisons of model simulations with satellite

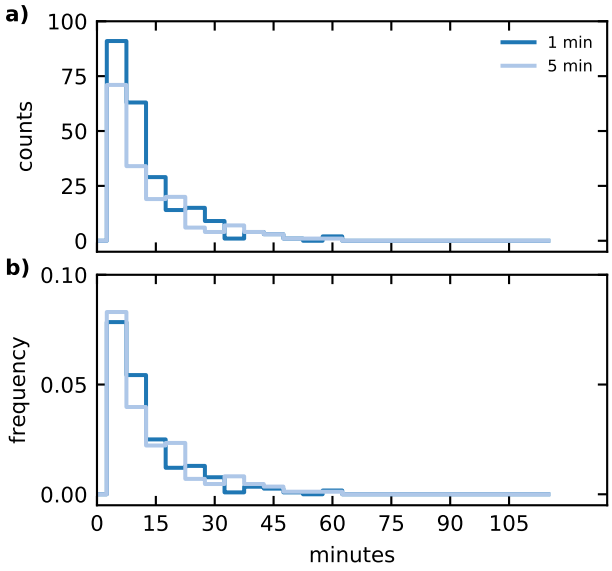

Figure 4.5: Cell lifetimes for tracking and analysis using two different output time steps (1 minute and 5 minutes) showing both total counts (a) and the PDF (b).

retrievals for the same area and time period are an important means of assessing the models' capabilities to successfully represent atmospheric processes in the real world. Using a tracking framework for the analysis allows us to investigate the representation of clouds in the model in a way that takes the development of individual clouds within the population of clouds into account as opposed to relying on temporal and spatial statistics of the cloud field. Using the same tracking framework for both model and observation data allows for a more robust comparison between them.

Here, we use satellite data from the Geostationary Operational Environmental Satellite (GOES) system, specifically GOES-13 (Hillger and Schmit, 2007), and WRF model simulation results from the ACPC deep convection case study (van den Heever et al., 2017). The satellite data were downloaded from the NOAA Comprehensive Large Array-data Stewardship System (CLASS) (NOAA, 2019) for the Continental United States (CONUS) area in NetCDF format. The NOAA Weather and Climate Toolkit (WCT) (National Climatic Data Center, NESDIS, NOAA, 2019) was used to convert pixel counts to radiances and brightness temperatures for the two channels used in the analysis here. The satellite data used in this example has an average horizontal spacing of about 4 km.

The model simulation comprises the outermost nested grid of the nested WRF simulation setup described in Sect. 4.3 as well as in Chap. 5. This outer domain covers a much larger area, encompassing most of Texas and the surrounding states of the southern USA, as well as neighbouring areas of northeastern Mexico. It features a grid spacing of 4.5 km and a width of 400 grid cells, equivalent to 1800 km in each horizontal direction. The simulation results were output at a time resolution of 15 minutes for the entire 24-hour simulation period from 12:00 UTC on 19 June 2013 to 12:00 UTC on 20 June 2013.

Although the temporal and spatial resolution of the input data can be arbitrary for the use in tobac, a meaningful comparison of the two datasets requires that the analysis covers the same region at a similar temporal and spatial resolution. The spatial resolution of the two datasets is reasonably similar (around 4 km for the satellite data and 4.5 km for the model output) and both datasets use a regular 15-minute interval, with a difference of up to a minute due to the scan time of the satellite data. The satellite data were restricted to the same temporal and spatial extent as the model output.

Top of the atmosphere outgoing longwave radiation (OLR) is used to track individual deep convective clouds in both model simulations and satellite retrievals. OLR is a standard model output for most high-resolution simulations and is often used as a diagnostic for simulated deep convection (Pearson et al., 2010; Russo et al., 2011). OLR retrievals also have the benefit that they do not depend on other aspects of a complicated radiative transfer model, which require, amongst other assumptions, that pixels are assigned as either cloud or cloud-free for the radiative retrieval of several optical (effective radius and optical depth) and thermal (cloud top temperature and height) cloud properties (McGarragh et al., 2018). For the satellite data, we use an empirical conversion derived in Singh et al. (2007) to convert the radiances L from two channels in the GOES-13 measurements, the water vapour channel (WV, 5.8 to 7.30 μm) and a channel in the infrared window (WIN,

10.2 to 11.2 μm), to OLR.

$$OLR = 11.44\,L_{\mathrm{WIN}} + 9.04\,L_{\mathrm{WV}} + \frac{9.11\,L_{\mathrm{WV}}}{L_{\mathrm{WIN}}} - \frac{86.36}{L_{\mathrm{WIN}}} - 0.14\,L_{\mathrm{WV}}^2 + 111.12\,. \tag{4.4}$$

Singh et al. (2007) report an uncertainty from these conversions within 2.5 $\mathrm{W\,m^{-2}}$.

The distribution of OLR for the model simulations and the satellite retrievals show a very similar shape (Fig. 4.6). The satellite-retrieved OLR features a larger number of pixels characterised by lower OLR values in the range between 100 and 250 $\mathrm{W\,m^{-2}}$ corresponding to deep cloud tops. The range covered and the peak position of OLR, corresponding to cloud-free and low cloud regions around 290 $\mathrm{W\,m^{-2}}$, agree well between the model simulation and the satellite retrieval.

We use these histograms to choose the threshold values for the feature detection and the segmentation steps in the tobac routine. The threshold for the outline of the convective clouds in the segmentation step (250 $\mathrm{W\,m^{-2}}$) reflects the lower tail of the peak of OLR in both the model simulations and the satellite retrievals. The additional thresholds used in the feature detection algorithm (250, 225, 200, 175 and 150 $\mathrm{W\,m^{-2}}$) are distributed over the range of OLR values in the part of the distribution representing the deeper clouds.

The individual steps of the tracking analysis for the model data are shown in Fig. 4.7, but the same steps are applied equally to the satellite-retrieved data. The outgoing longwave radiation field (Fig. 4.7a) is filtered with a Gaussian filter with a standard deviation of $\sigma = 4.5\,\mathrm{km}$, equivalent to the grid spacing of the model data (Fig. 4.7b). The feature identification following Sect. 4.2.2 is performed with the set of five OLR thresholds of 250, 225, 200, 175 and 150 $\mathrm{W\,m^{-2}}$(Fig. 4.7c,d). The segmentation is performed using the watershedding technique (Sect. 4.2.3) with an OLR threshold of 250 $\mathrm{W\,m^{-2}}$ to identify the area of the individual clouds leading to the cloud areas shown in 4.7e. The complete linked trajectories of all clouds present at the specific time step, as illustrated in the other sub-figures, are shown in Fig. 4.7f with the cloud extent at the start (dashed)

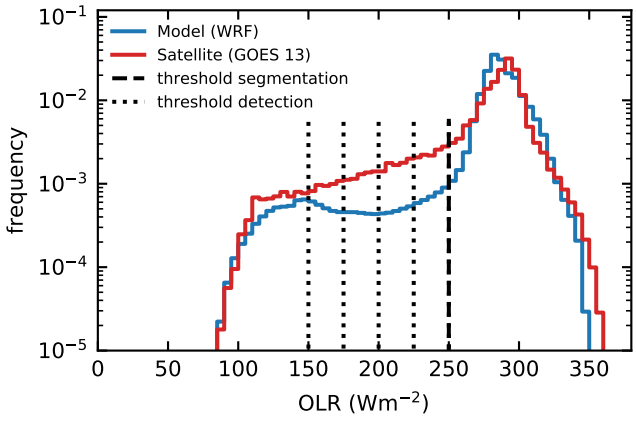

Figure 4.6: Probability density function of OLR for the model simulation and the satellite retrievals including the thresholds (vertical dashed and dotted lines) set for feature detection and segmentation.

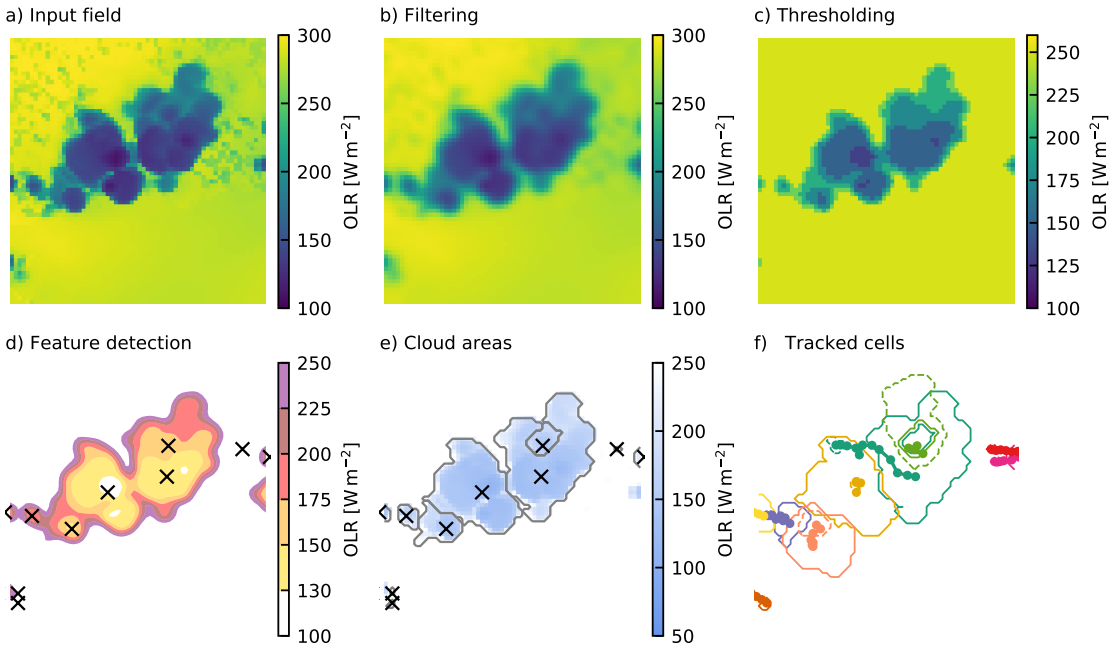

Figure 4.7: Schematic overview of the individual steps of the tracking algorithm for an example subset of the domain used in example B based on outgoing longwave radiation. The input data (a) are smoothed with a filter (b) before regions above or below a set of thresholds are determined (c) to identify the individual features (d). (e) shows the associated cloud areas determined in the segmentation step and (f) shows all individual clouds present at the time step over their entire life cycle, including outline the cloud area at the start (dashed) and at the end (solid) of the trajectory.

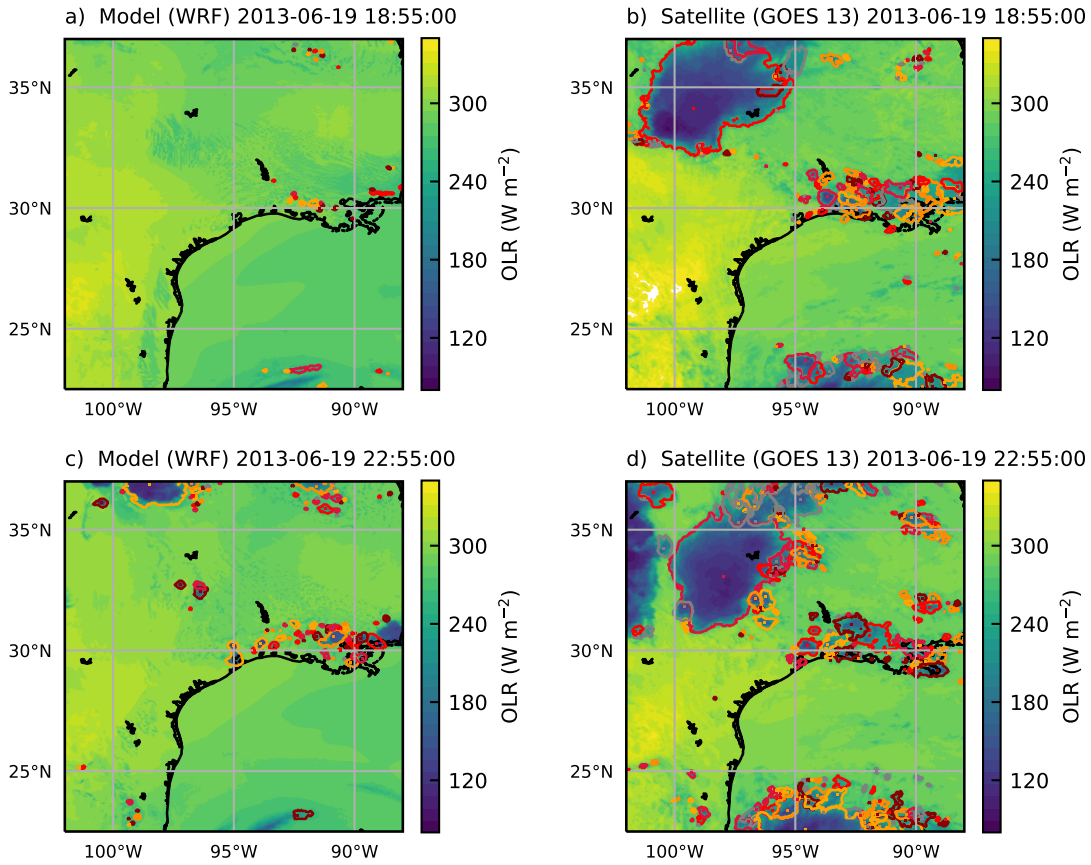

Figure 4.8: Identified and tracked objects at two specific points in time (19/06/2013 18:55 UTC and 22:55 UTC) based on outgoing longwave radiation for the WRF simulations with 4.5 km grid spacing on the left (a, c) and the outgoing longwave radiation derived from the combination of two GOES-13 channels following Singh et al. (2007) on the right (b, d).

and end (solid) of the lifetime of the cloud. A smaller subset of the data and analysis for this example including the tracking analysis and visualisation is available as a Jupyter notebook as part of the package source code. The tracked clouds for both the model simulation and the satellite retrieval are visualised for two different times in Fig. 4.8. Both the model simulations and the satellite retrieval show many individual convective clouds in a region north of the coastline, especially towards the east of the analysed domain around the Mississippi River Delta and further inland in Texas. In addition, larger connected regions of clouds occur both towards the southern end of the analysed domain over the

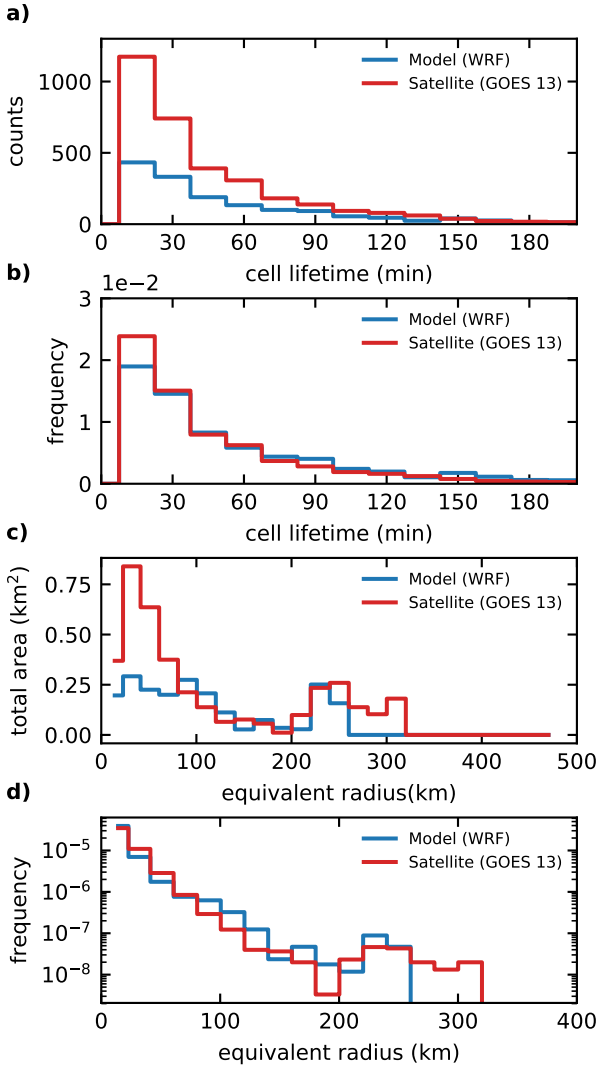

Figure 4.9: Distributions of cloud lifetimes obtained from the tracking of model data and satellite retrievals, shown as total counts (a) and frequency (b). The distribution of cloud areas is shown as the distribution of total area resulting from the sum in each area bin (d) and as a pdf of cloud area (c). Both these distributions are plotted against the equivalent radius of a circular cloud of the same area.

Gulf of Mexico and in the form of a large organised storm system entering the domain from the north-west. The propagation of this large system is not represented accurately in the model simulation, as it shows a lag of several hours and is smaller in magnitude than in the satellite retrievals. The lifetime distribution of the clouds identified and tracked from the model simulations and from the satellite retrievals show a similar distribution (see Fig. 4.9a). However, more clouds are identified in the satellite data than in the model

data. When normalised for total number, the lifetime distributions agree better between the two different data inputs (Fig. 4.9b). Most cloud objects are tracked for periods of up to an hour, but in both the model simulations and the satellite retrievals there are numerous cloud objects tracked for up to several hours. The distributions of the cloud areas (Fig. 4.9c,d) show that the total cloud area for both model and satellite data is made up of two types of identified objects, smaller tracked clouds with a radius of up to 100 km and large tracked features with a radius of a few hundred kilometres. Due to the larger number of tracked clouds, there is more total cloud area in the tracked clouds in the satellite data. The distribution of cloud sizes is relatively similar between the two datasets. The satellite data show more small clouds below 100 km equivalent radius. Furthermore, the size of the largest tracked objects is larger in the satellite data than in the model data, which corresponds to the large MCS propagating through the domain of interest (Fig. 4.8), and which is not represented properly in the model simulations with respect to both timing and total size.

An analysis of the cloud velocities and nearest-neighbour distances as described in Sect. 4.3.1 is presented in Fig. 4.10. The distribution of both the nearest-neighbour distances (Fig. 4.10a) and the cloud displacement velocities (Fig. 4.10b) agree well between the model simulations and the satellite retrieval. The peak of the nearest-neighbour distances appears around 20 km. The propagation velocities peak at around $8\,\mathrm{m\,s^{-1}}$, with most of the velocities below $20\,\mathrm{m\,s^{-1}}$. A comparison of the nearest-neighbour distances and the displacements per input time step that would result for different temporal resolution (1, 5, 15 and 30 minutes) shows that the 15-minute time step used here already shows some overlap in the distributions. Longer time steps of 30 minutes or more would probably lead to problems in the tracking, while shorter time steps of a few minutes would be expected to improve the tracking further. However, output at similarly high temporal frequencies is not always feasible or simply not available for a lot of data sources, e.g. for the GOES-13 geostationary satellite retrievals used in this study. The newest generation of geostationary satellite imagers such as the GOES-R series (GOES 16/17) that has

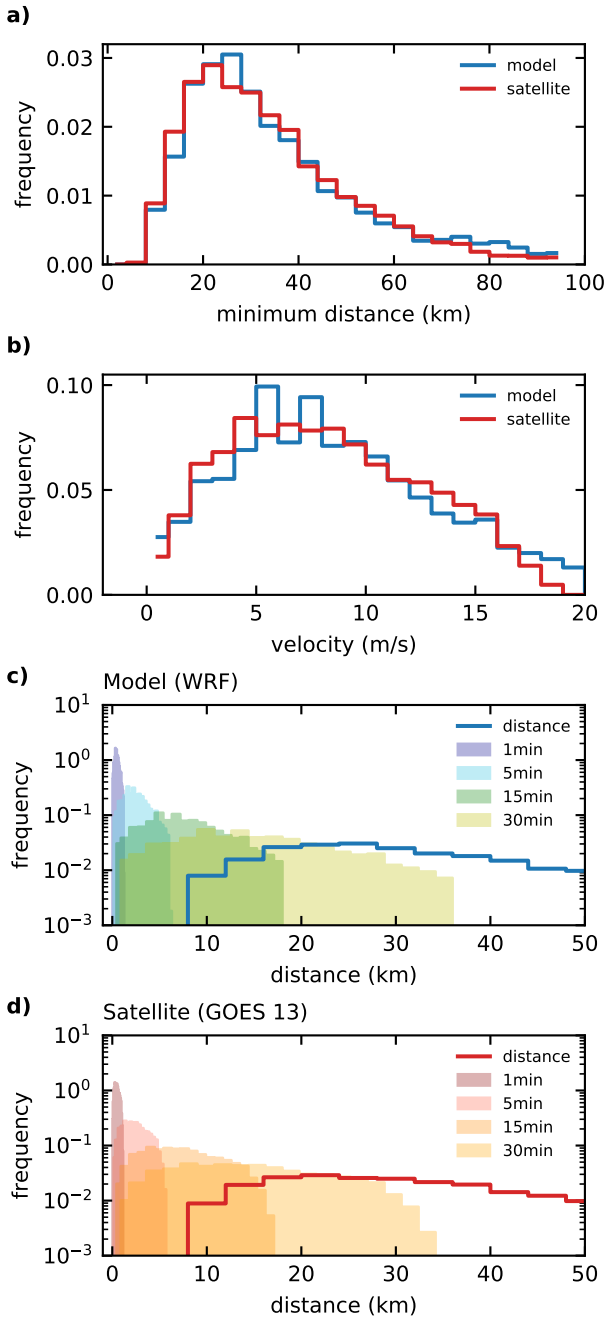

Figure 4.10: (a) Distributions of the distance to the next identified object for all identified objects and (b) velocities for tracked cloud objects at each time step of the trajectories for both the model simulations and the satellite data. (d) The travel distance per input interval resulting from different time resolution of the input based on these velocities (b) is shown together with the distribution of the minimal distance to the nearest-neighbour in (a) for the model data in (c) and for the satellite data.

replaced the GOES-13 satellite used here, as well as Himawari-8 (Bessho et al., 2016) and the future Meteosat Third Generation (MTG) satellites (Stuhlmann et al., 2005) all feature substantially higher temporal and spatial resolution.

The scattered convective cells of differing depths over the area of Houston that were the focus of the analysis in the first application example (Sect. 4.3) are not clearly resolved in these two datasets. The lower spatial resolution of the simulations and satellite retrieval (around 4 km compared to 500 m in the high-resolution simulations used in Sect. 4.3) limit the spatial scale of cloud features that can be resolved to more than a few tens of kilometres in radius. The use of outgoing longwave radiation as a variable for feature identification does not include as much information as the three-dimensional model output fields used in Sect. 4.3, however, it provides complementary information to compare model simulations with satellite retrievals.

4.5. Conclusions

We have presented tobac, a new framework for object-based analysis and tracking individual convective clouds in different types of input data. The workflow of the software package consists of the detection of suitable features, segmentation of the areas or volumes representative of an individual cloud object and subsequent linking of objects at individual time steps into trajectories. All individual steps are implemented in a modular way, thereby allowing for the implementation of different algorithms for each of the steps, should the need arise.

We have developed a feature detection algorithm based on identifying regions above/-below a defined sequence of thresholds in two-dimensional input fields. Cloud volumes or cloud areas are associated based on a watershedding technique featuring a single specific threshold value on two- or three-dimensional input fields.

We have shown how we can leverage another open-source Python package trackpy, ini-

tially developed for application in microscopy, in the tobac framework to link up cloud objects at individual time steps into consistent cloud trajectories. These cloud trajectories allow for an analysis of cloud lifetimes and the time evolution of cloud properties and physical processes in the clouds over the lifetime of the cloud. The analysis routines provided as part of the package can be applied to derive cloud properties and statistics for individual clouds over their life-cycle as well as for the entire population of clouds in the analysed cloud field. The built-in visualisation routines allow for a convenient way to assess the performance of the analysis and evaluate the choice of parameters for the different steps of the analysis framework. The automatically created animated visualisations of individual tracked cells can guide users in the development of further detailed analyses based on the analysis tools provided in the framework.

The implementation of the tracking framework in Python enables the use of extensive and actively developed open source libraries for scientific computing. We have shown that this provides numerous advantages, e.g. for memory management, data structures and visualisation. The rapid development of the underlying libraries means that tobac can profit from future advances without any further development of tobac and any requirements on the side of the user. The modular structure of the framework allows for the inclusion of other existing or newly developed methods for the individual steps of feature detection, object segmentation and tracking into the software package in the future. These capabilities enable the use of different tracking algorithms in parallel for evaluation and comparisons as well as tracking based on different types of input data in a single analysis framework.

We have presented two application examples of the use of tobac for the study of deep convective clouds. In the first application (example A), we have tracked scattered deep convective cells based on a combination of the vertical velocity and total condensate mixing ratio fields from CRM simulations with WRF over the area around Houston, Texas. The simulations were performed with a grid spacing of 500 m, and thus represent a typical application of a CRM. The tracking framework is currently being applied to other CRMs

for the same case study as part of the ACPC deep convection case study (van den Heever et al., 2017) to investigate the response of deep convective clouds in models to changes in aerosols. We have performed the tracking for different output frequencies to evaluate the dependency of the tracking performance on the time resolution of the input data. The output resolutions of 1 minute and 5 minutes lead to comparable tracking results for scattered convective cells. This result can be confirmed using an analysis of typical displacement velocities of the clouds and nearest-neighbour distances between the individual identified cloud objects.

In a second application (example B), we have presented a simultaneous tracking of deep convective cloud features and larger convective systems based on outgoing longwave radiation output from model simulations with convection-permitting grid spacing (4.5 km) and outgoing longwave radiation derived from geostationary satellite retrievals (GOES-13) in the same region. The 15-minute time resolution available from the satellite retrieval is shown to be sufficient for successful tracking performance. The analysis also demonstrated that the model simulations and the satellite retrieval feature clouds with a similar lifetime distribution. The distribution of cloud areas in model and satellite data shows a similar combination of smaller convective cells and larger systems. The main differences occur for the largest tracked systems, which are stronger in the satellite retrievals. This can be explained by the limited representation of the propagation of two large organised storms within the model domain. This would have been more challenging to assess from a bulk analysis of the domain-wide averaged properties.

The newest generation of geostationary satellites, such as Himawari-8 or GOES-16/17, provide substantially higher spatial and temporal resolution (Bessho et al., 2016; Schmit et al., 2016). These advances will strongly improve the applicability of this type of satellite data for use in object-based tracking and analyses with tobac, and also allows for a wider range of applications, e.g. by capturing smaller scattered cells such as the ones investigated in Sect. 4.3.

The ability of tobac to be used for both models and observations as shown in these ex-

amples helps to compare models with observations more directly, and therefore, better understand the differences between the two types of data.

Although we have focused on tracking and analysing deep convection here, there are numerous other applications that tobac can be used for without much additional work. There are a large number of existing data products, such as high-resolution radar data, e.g. from NEXRAD over the United States or similar networks in several other regions of the world (Reed et al., 2017), that would be most suited for the use with tobac. Furthermore, the application of tobac is not strictly limited to the analysis of clouds, and it can also be applied to study other features of the Earth system that can be identified as well-defined time evolving regions, such as distinct aerosol plumes in the atmosphere or plankton in the surface layer of the ocean.

We are currently working on implementing additional algorithms for the modular steps of the framework, e.g. based on the analyses developed in Senf et al. (2018). Additionally, we are implementing a more flexible representation of the links between cloud objects at specific points in time, which will allow for a proper treatment of more complex splitting and merging of cells. We invite the community to contribute to the future development of tobac both through the implementation of existing algorithms into the common framework and by using the framework as a basis for new developments.

5. A Lagrangian view of microphysics and aerosol effects on deep convection

The microphysical pathway analysis developed in Chap. 3 allowed to infer a detailed understanding of the propagation of aerosol-induced changes to cloud droplet number concentration (CDNC) through the microphysics of deep convective clouds. This analysis revealed important mechanisms that control the differences in the response for different microphysics schemes in a single cloud-resolving model (CRM). These simulations have been performed for a particular type of deep convective clouds in the form of supercells. The idealised simulation setup only allowed for limited interaction between the cloud and its environment compared to an entire cloud field in reality. The tracking analysis used for these simulations in Chap. 3 has been extended into the complete tracking and analysis framework tobac in Chap. 4. This allows for effective use of the analyses focused on individual clouds in different types of datasets including large numbers of convective clouds. Its application has been demonstrated for both high-resolution model simulations and geostationary satellite retrievals.

In this chapter, the analyses developed in the two previous chapters are combined to analyse the response of deep convective clouds in a large, freely developing cloud field in a case study simulation. The analysis is performed for two different CRMs to extend the investigation of the role of numerical model representation in the assessment of aerosol–convection interaction from Chap. 3 beyond the effect of different microphysics schemes.

The text of this chapter is based on a manuscript in preparation for submission to a peer-reviewed journal with several co-authors as:

Heikenfeld, M., Marinescu, P. J., White, B., van den Heever, S. C. and Stier, P. "A Lagrangian view of microphysics and aerosol effects on scattered deep convection"

The simulations with the two CRMs were performed as part of the model intercomparison study in the framework of the Aerosol, Cloud, Precipitation, and Climate (ACPC) Working Group. I was strongly involved in the development of the case study setup for the intercomparison study together with Peter J. Marinescu, Susan C. van den Heever (both Colorado State University), Bethan White (Monash University), Ann M. Fridlind (NASA Goddard Institute for Space Studies) and Philip Stier (University of Oxford), which has been documented in (van den Heever et al., 2017). I have performed the simulation with WRF and Peter J. Marinescu performed the simulations with the RAMS model as part of the ACPC intercomparison. I have created of domain-wide precipitation assessment of all CRMs in the intercomparison for a more general publication about the entire model intercomparison study that is currently in preparation. I have designed the analysis based on the analysis methods developed in the two other chapters of the thesis (Chap. 3 and 4). I have written the manuscript with input and feedback from the other co-authors.

Abstract Aerosol–cloud interactions remain one of the main uncertainties in our understanding of the Earth's climate system. Aerosol effects on deep convective clouds are particularly uncertain due to large uncertainties in the representation of mixed- and ice-phase microphysics in model microphysics schemes. Simulations of scattered convective cells have been performed with the two cloud-resolving models WRF and RAMS as part of the ACPC deep convection intercomparison study over the area around Houston, Texas. The simulations for a clean and a polluted case were used to assess the impact of changes in aerosols on the cloud microphysics and the evolution of the convective cloud field. Domain-wide average analyses of surface precipitation and cloud properties show large differences between the two models including more surface precipitation and a more vigorous development of the ice phase in the clouds in RAMS compared to WRF. However, the response of the two models to an increase in aerosols is consistent, both showing suppression of warm rain formation and surface precipitation. We extend the analysis based on tracking individual updraft cells in the simulations and performing analyses that take the time evolution of the cells into account. Classification into different categories of convective clouds enables a separation of the model response into contributions from different cloud types. This reveals differences in the total number of cells, cell lifetimes and also the partition between shallow warm-phase cumulus clouds and mixed-phase deep convective clouds between the two models. Analyses of the hydrometeor composition and microphysical process rates for composites of the tracked clouds showed that there is good agreement between the two models for warm-phase processes and the response of shallow convective clouds. However, the two models exhibit substantial differences in the strength of the deep convective clouds and the evolution of the mixed- and ice-phase processes between the two models.

5.1. Introduction

Deep convective clouds are an essential feature of the Earth's atmosphere. However, the impact of aerosols on mixed- and ice-phase microphysical processes in convective clouds remains highly uncertain (Tao et al., 2012; Varble, 2018). This has important implications for determining the role of aerosol–cloud interactions in the climate system (Fan et al., 2016). The highly localised nature of convective processes leads to significant challenges in observational assessments and in the representation in models at different scales (Rosenfeld et al., 2014b). Modelling studies have found a wide range of responses of convective clouds to changes in aerosol conditions, from suppression of convective strength and precipitation to invigoration of convective activity (Khain et al., 2008; Tao et al., 2012; Altaratz et al., 2014; Fan et al., 2016). These differences in the aerosol response of the clouds have been related to the simulation of different types of convection and differences in the environmental conditions like humidity or wind shear (Khain et al., 2008; Tao et al., 2012). However, differences between the models or modelling approaches used in the individual studies play an important role in the results (Tao et al., 2012; Fan et al., 2016; White et al., 2017). The challenges in modelling the effects of aerosols on deep convection are strongly related to the large number of interacting physical processes (Fan et al., 2016) in the cloud microphysics. Furthermore, there are complex interactions between the cloud microphysics and other physical processes at different scales, such as cloud dynamics or large scale circulations (Tao et al., 2012).

Convective invigoration due to increased aerosols (Andreae et al., 2004; Rosenfeld et al., 2008; Lebo and Seinfeld, 2011) has been suggested in the form of a number of related effects that would cause a strengthening of convective activity as a result of higher aerosol number concentrations, e.g. based on an increase of the latent heat release from freezing. However, several recent studies question the attribution of observed relationships between aerosol concentrations and convective strength to aerosol microphysical effects (Nishant and Sherwood, 2017; Varble, 2018) due to the existence of multiple con-

founding factors. A larger number of aerosols and subsequently smaller effective droplet radii can also lead to smaller ice particles. This causes a reduction in fall speeds, which favours increased cloud fraction, cloud top height, and cloud thickness (Fan et al., 2013). This results in a potential radiative effect on the climate system through enhanced anvils (Koren et al., 2010b; Storelvmo et al., 2011) along with changes in the cloud albedo (Storelvmo et al., 2011). Different mechanisms that could significantly buffer the impact of aerosols on cloud development and precipitation have been proposed, originating from both warm-phase processes (Stevens and Feingold, 2009) and mixed- and ice-phase processes (Fan et al., 2016). Large differences between different microphysics schemes and different cloud-resolving models (CRM) have been found in several previous intercomparison studies (Fridlind et al., 2012; Varble et al., 2014a; b; Wang et al., 2015; White et al., 2017). It has been pointed out that it is particularly challenging to decide whether a specific model or microphysics scheme performs better than others based on limited observational data or to determine whether the agreement between a specific model simulation and observations is actually based on the correct reasons (Fridlind et al., 2012; Varble et al., 2014a; b; Fridlind et al., 2019).

The Aerosol, Cloud, Precipitation, and Climate initiative (ACPC, http://acpcinitiative.org/) has designed a model intercomparison study to investigate the response of scattered deep convective clouds to changes in aerosols for different CRMs. The case study domain around Houston is characterised by a large source of aerosols both from urban emissions and the large concentration of petrochemical industries, while the coastal location also allows periods with relatively clean air masses advected from the Gulf of Mexico. This creates a natural laboratory where, depending on the prevailing inflow direction, contrasting aerosol conditions representative either of mildly polluted conditions or strongly polluted air masses occur. These conditions are represented in the models by simulating a clean case (CLN) and a polluted case (POL). Preliminary analyses we performed for the ACPC model intercomparison show large differences in the simulations with the different CRMs, e.g. in domain-averaged accumulated precipitation (Fig. 5.1) that differs by

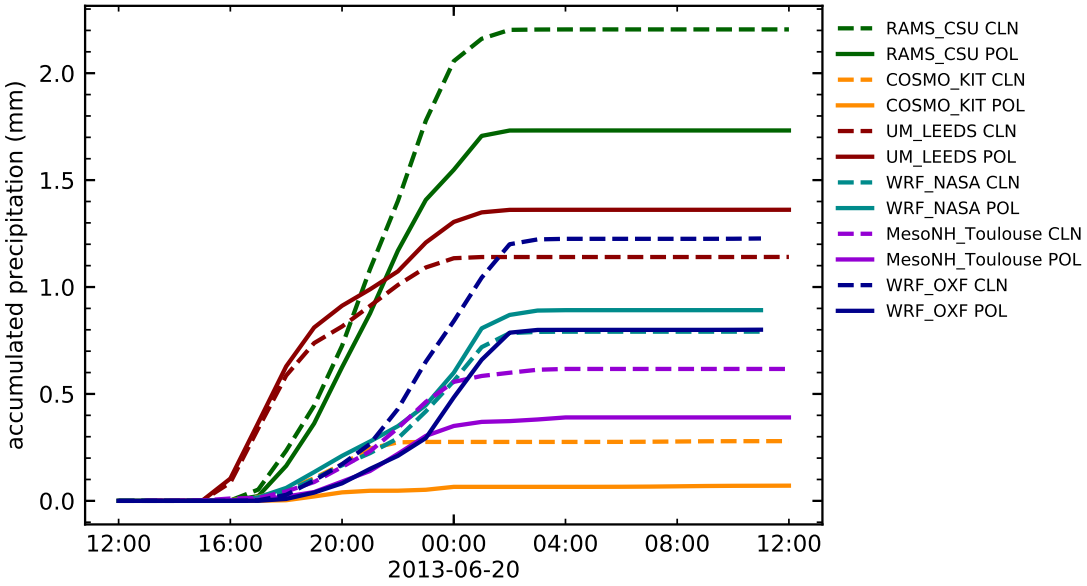

Figure 5.1: Domain-averaged accumulated precipitation over the entire simulation period for all ACPC CRMs for the clean and polluted cases.

almost an order of magnitude between the individual models. Furthermore, the models do not agree on the response to changes in aerosols, both in sign (suppression or invigoration) and in magnitude. Further analyses have shown similar differences for several other variables such as updraft speeds or condensate loading (not shown). The domain-wide differences between the individual models are more pronounced than the effects of changes in the aerosol conditions in individual models.

The case study area around Houston has been in the focus of several previous studies on clouds and aerosol–cloud interactions. Enhancement of convection above and downwind of the urban area of Houston has been observed in the form of both precipitation (Shepherd and Burian, 2003; Shepherd, 2005; Tao et al., 2012) and an enhancement of lightning strikes (Orville et al., 2001; Steiger et al., 2002). This response is attributed to the combination of a microphysical impact through aerosols from urban pollution and the additional surface heating due to the built-up areas of the urban area (Orville et al., 2001; Shepherd and Burian, 2003). Fan et al. (2007) and Fan et al. (2008) used a two-dimensional CRM to investigate the effects of aerosol chemical and optical properties on

deep convective events over Houston. They found an increase in convective activity and surface precipitation due to aerosol indirect effects, but a suppression due to semi-direct effects of absorbing aerosols through the radiative heating of the lower troposphere. Li et al. (2008) performed three-dimensional simulations for a summertime convective event in the same region, however, using a comparatively small domain and grid spacing of 2 km. The response to increases in CCN was an increase in surface precipitation over the range of clean to reasonably polluted conditions but suppression of surface precipitation for highly polluted conditions beyond CCN concentrations of 5000 cm^{-3}. Carrió et al. (2010) and Carrió and Cotton (2011) used RAMS, one of the two CRMs used in this study, to simulate the effect of the growth of the Houston urban area on convection in a similar modelling domain to the one used here. Their results suggest convective invigoration due to increased latent heat release from freezing, but a non-monotonic response of surface precipitation due to the interaction of different processes.

Most previous CRM intercomparison studies (Fridlind et al., 2012; Varble et al., 2014a; b) have focused on the analysis of spatially-averaged properties in order to be representative of a given area or a specific type of ground-based observation. This allows representing the time evolution of cloud properties at the scale of, e.g. the diurnal cycle or changes over several hours. However, these approaches preclude an investigation of the time evolution of individual clouds in more detail, which limits the understanding of specific aerosol effects, e.g. on the lifetime of the clouds. Altaratz et al. (2014) concluded in their review on aerosol–cloud interactions that assessing the time evolution of convective clouds is crucial in understanding aerosol effects on convective clouds.

In this study, we focus on two of the models in the ACPC intercomparison study, the Weather Research and Forecasting (WRF) model (Skamarock et al., 2008) and the Regional Atmospheric Modelling System (RAMS, Saleeby and van den Heever, 2013). The ACPC deep convection model intercomparison was specifically set up to allow for a detailed investigation of the microphysical effects of aerosols and the evolution of the scattered convective cells in the domain. In Chap. 3 (Heikenfeld et al., 2019b), the

propagation of changes in cloud droplet number concentration (CDNC) due to aerosol perturbations through the model microphysics was investigated in idealised simulations of supercell storms. This analysis revealed shifts in microphysical process rates and hydrometeor composition associated with changes to CDNC and major differences due to the use of different microphysics schemes. However, it is important to go beyond idealised cases for single clouds to investigate the response of entire cloud fields to changes in aerosols. Therefore, we extend this type of analysis for tracked convective clouds in an interactively developing cloud field in a large simulation domain. The tracking and analysis framework tobac (tracking and object-based analysis of clouds) established in Chap. 4 (Heikenfeld et al., 2019a) is used in this study to identify individual convective updrafts and associate cloud volumes based on the total condensate mixing ratio. This allows us to derive numerous temporally and spatially resolved quantities over the evolution of the individually tracked clouds. Using a categorisation into different types of clouds, e.g. liquid-phase shallow convection or clouds that undergo the entire evolution of a developing deep convective thunderstorm, allows us to separate the domain-wide response into the contributions from different types of convective clouds. Cloud composites allow for a temporally and vertically resolved evaluation of time evolution cloud microphysical development, which helps to reveal differences between the models or the detailed pathways of aerosol effects. This establishes a framework for future analyses of the model results from the different CRMs in the ACPC deep convection intercomparison study.

5.2. Methodology

5.2.1. Model setup

We perform simulations with two CRMs, WRF and RAMS, which are contributions to the ACPC model intercomparison study focusing on scattered deep convection around Houston, Texas (van den Heever et al., 2017). The model setups are kept as similar as

possible in terms of the domain setup, initial, boundary and aerosol conditions, while differences in the parametrisation of physical processes between the models are retained to investigate the uncertainty due to the spread of responses in two state-of-the-art CRMs. The simulation setup includes periods with high-frequency output (5-minute output for 12 hours and 1-minute output for 3 hours) and detailed microphysical process output from all participating models. This enables a detailed focus of the analyses of the microphysical pathways in the convective clouds and their time evolution. The most important aspects of the model setup are summarised in Table 5.1 and Table 5.2.

WRF is used in version 3.7.1 (Skamarock et al., 2008). The simulations use the RRTMG scheme (Iacono et al., 2008) for both short and longwave radiation. The YSU scheme (Hong et al., 2006) is used for the boundary layer parametrisation. The cloud microphysics in the WRF simulation is based on the Morrison scheme (Morrison et al., 2005; 2009), which makes use of saturation adjustment for the calculation of condensation and evaporation of cloud droplets. The activation of aerosols is not explicitly represented in the microphysics in these simulations, but instead represented by a variation of the CDNC held fixed for each model simulations (see also Sec. 5.2.2) .

RAMS (Saleeby and van den Heever, 2013) is used in version 6.1. The model makes use of a bin-emulating double-moment bulk microphysics scheme (Walko et al., 1995; Meyers et al., 1997; Saleeby and Cotton, 2004; 2005; Saleeby and van den Heever, 2013) that includes a prognostic treatment of supersaturation. Saleeby and van den Heever (2013) give a detailed overview of the model version used in this study, including the details of the aerosol treatment. RAMS utilises an interactive aerosol model with activation scavenging, but no other sinks or sources of aerosols. The radiation scheme is the two-stream formulation presented in Harrington (1997) and Harrington et al. (1999).

The model simulations are performed with three nested grids of 4500 m (D1), 1500 m (D2) and 500 m (D3) horizontal grid spacing. Both models simulate convection explicitly in each of the model domains without applying any cumulus parametrisation. All three domains are centred around the KHGX NEXRAD radar (29.471 ° N, 95.0792 ° W) south-

Table 5.1: Model setup and physical parametrisations for the two CRMs WRF and RAMS used in this study.

	WRF	RAMS
Radiation SW	RRTMG (Iacono et al., 2008)	Harrington (1997), Harrington et al. (1999)
Radiation LW	RRTMG (Iacono et al., 2008)	Harrington (1997), Harrington et al. (1999)
Boundary layer scheme	YSU (Hong et al., 2006)	–
Microphysics	Morrison scheme (Morrison et al., 2005; 2009)	RAMS microphysics (Walko et al., 1995), (Saleeby and Cotton, 2004), (Saleeby and van den Heever, 2013)
Hydrometeor categories	2 liquid (cloud, rain) 3 frozen (ice, snow, hail)	3 liquid (cloud, drizzle, rain) 5 frozen (ice, snow, aggregates, graupel, hail)
Aerosol activation	– (direct variation of CDNC)	Lognormal aerosol mode and lookup tables based on parcel bin model (Saleeby and van den Heever, 2013)
Aerosol removal	–	activation scavenging, precipitation scavenging
Aerosol regeneration	–	no
Saturation adjustment	yes	no
Freezing	Cooper (1986), Rasmussen et al. (2002)	DeMott et al. (2010), Walko et al. (1995), Saleeby and van den Heever (2013)
Droplet autoconversion and accretion	Khairoutdinov and Kogan (2000)	– (bin-emulating scheme)
Land surface	NOAH LSM (Chen and Dudhia, 2001)	LEAF3 (Walko et al., 2000)

east of Houston. In WRF, the nested model grid cell numbers must align to be multiples of each other, which leads to slight differences in the WRF domain sizes compared to the RAMS setup (Table 5.2). The initial meteorological state for all domains and the boundary conditions for the outermost domain are based on 6-hourly data from the GDAS FNL analysis (NCEP, 2015). The inner two domains are each influenced continuously by their surrounding domain using a one-way nesting. Therefore, there is no feedback from the inner domains towards the simulation in the surrounding domains. The innermost of these

Table 5.2: Domain and simulation setup for the three model domains used in the simulations with RAMS and WRF.

Domain	D1	D2	D3
model time step Δt	2 s	1.5 s	1.5 s
radiation time step Δt_{rad}	60 s	60 s	60 s
horizontal cell number n_x, n_y	400	550 (WRF: 546)	500 (WRF: 498)
horizontal grid spacing Δx Δy	4500 m	1500 m	500 m
vertical levels n_z	95	95	95
vertical spacingΔz	50 m–300 m	50 m–300 m	50 m–300 m
domain centre position	29.4719 ° N, -95.0792 ° E	29.4719 ° N, -95.0792 ° E	29.4719 ° N, -95.0792 ° E
hourly output (UTC)	19 June 12:00 – 20 June 12:00	19 June 12:00 – 20 June 12:00	19 June 12:00 – 20 June 12:00
5-minute output (UTC)	–	–	19 June 16:00 – 20 June 04:00
1-minute output (UTC)	–	–	19 June 21:00 – 20 June 00:00

three domains D3 is the primary focus of the analyses presented in this study.

5.2.2. Aerosol perturbations

We perform simulations for two different aerosol conditions; a clean case (CLN) representative of maritime air masses with low aerosol number concentration and a polluted case (POL) representing highly polluted air masses affected by urban emissions from the Houston area and other sources of aerosols such as long-range transport of forest fire emissions. Aircraft measurements performed during the DiscoverAQ measurement campaign over Texas in September 2013 (NASA, 2013) and satellite CDNC retrievals following Rosenfeld et al. (2016) for the actual date of the case study simulations are used to create representative aerosol conditions for these two scenarios.

The aerosols are represented as a single log-normal aerosol mode with a mean geometric diameter of 100 nm and a standard deviation of σ_{g} of 1.8 for both the clean and the pol-

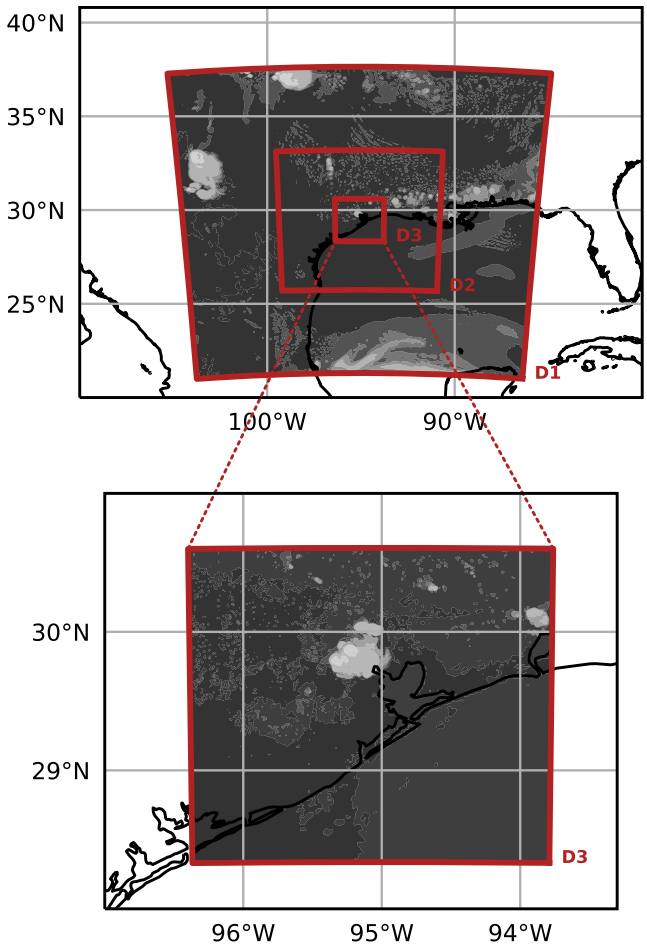

Figure 5.2: Domain setup for the case study simulations with the three different nested domains (a) and a detailed view of the innermost domain D3 that is the primary focus of the analyses (b).

luted case. In the polluted case, aerosol number concentrations near the surface are 4000 cm^{-3}, while the clean case has a number concentration of 500 cm^{-3}. This value is held constant throughout the boundary layer up to a height of 3 km after which a linear decrease follows up to a constant value of 100 cm^{-3} above 5 km height for both the polluted and the clean case. The chemical properties of the aerosols are given by the hygroscopicity parameter κ (Petters and Kreidenweis, 2007), which is set to 0.2 based on data from the DiscoverAQ aircraft measurements (van den Heever et al., 2017). The simulations with the WRF model use a variation of CDNC to represent the effects of changes in aerosols

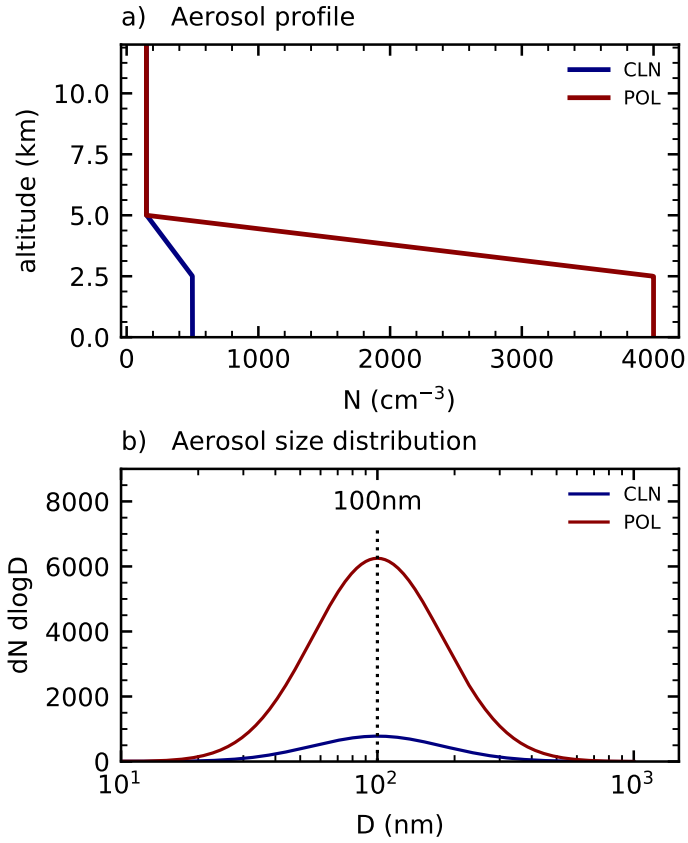

Figure 5.3: Aerosol setup for case study simulations showing (a) the vertical profiles of aerosol number concentration and (b) the size distributions for the two cases CLN and POL.

on the cloud droplets, similar to the procedure chosen in Chap. 3. The intended implementation of a prognostic CDNC in the microphysics scheme has encountered significant problems with the stability of the code due to the interaction of different physical parametrisations in the model. The simulations with WRF are performed for eight different values of CDNC as in Chap. 3, which allows for additional investigations regarding the robustness of the observed response to changes in aerosols compared to the simulations based on a single clean and polluted simulation. We have chosen the two simulations with CDNC values of 250 cm^{-3} (CLN) and 2500 cm^{-3} (POL) for the rest of the analyses along with the two simulations with RAMS, as they are most similar to the CDNC values in the two RAMS simulations.

5.2.3. Convective cell tracking

We extended and improved the tracking algorithm used for the cell-based analysis in Chap. 3 (Heikenfeld et al., 2019b) into the tracking and analysis framework tobac in Chap. 4 (Heikenfeld et al., 2019a). The tracking is applied to the four simulations (CLN and POL for each of the two models WRF and RAMS) for the 3-hour period with 1-minute output frequency from 21:00 UTC to midnight on 19 June 2013.

The tracking setup used for this study is very similar to the example described in detail in Sec. 4.3. In the first step, individual updrafts are identified based on a set of thresholds for upward vertical velocities of 3, 5 and 10 $\mathrm{m\,s^{-1}}$. We restrict the analysis of the column maximum vertical velocity to a mid-level layer ranging from the top of the boundary layer at 3.5 km to a height of 8 km. This excludes high vertical velocities in the boundary layer, e.g. from cold pool dynamics, and effects of gravity waves in the higher atmosphere from the identification of the individual updrafts (Cotton et al., 2010).

At each output time step, the total condensate field, i.e. the sum of all hydrometeor mass mixing ratios, is used to derive a cloud volume associated with each updraft feature based on a watershedding algorithm and a threshold value of 0.1 $\mathrm{g\,kg^{-1}}$. To avoid capturing extensively interconnected anvils, the cloud region associated with an updraft is limited to a distance of 10 km around the updraft centre. The identified updraft features are linked into consistent trajectories based on a linking algorithm from the trackpy package (Allan et al., 2016) as described in Chap. 4. The tracking algorithm does not explicitly treat splitting and merging of convective cells. Therefore, isolated cells are expected to be captured for the entire life cycle, while many cells that interact directly with other clouds will generally only be tracked for part of their entire life cycle. This aspect is assessed in more detail in Sec. 5.3.4.

5.3. Results

5.3.1. Domain-averaged analysis of model differences

In this section, we present the differences between the two models from the perspective of domain-wide sums and averages of surface precipitation, condensate loading of the different hydrometeor classes and microphysical process rates. This assessment is based on the hourly data output from the innermost domain D3 for the entire simulation period of 24 hours. In Sec. 5.3.3, we will introduce a more detailed analysis based on the tracking of individual cells to relate the changes and differences observed in the entire domain to the evolution and response of individual clouds.

The domain-averaged accumulated precipitation over the entire 24-hour simulation period (Fig. 5.5a) shows a strong difference between the two models. The simulation with RAMS produces about twice as much precipitation in the domain as the WRF simulations. In both models, the precipitation sets in after around 5 hours of simulation time, corresponding to noon local time (17:00 UTC). The accumulation of surface precipitation continues until around 15h into the simulation, corresponding to 22:00 local time (03:00 UTC). There is no substantial surface precipitation in the inner domain D3 after this time until the end of the simulations at 12:00 UTC on the next day. The timing of precipitation differs markedly between the models, showing weaker surface precipitation for the first couple of hours in both WRF simulations. The domain-averaged profiles of hydrometeor concentrations and microphysical process rates (Fig. 5.4) show strong differences between the two model simulations. RAMS produces substantially more total hydrometeor mass in the domain, both in the form of liquid water (cloud droplets and raindrops) and for the different types of frozen hydrometeors. In the liquid phase, both models show similar amounts of liquid water content at altitudes of up to 5 km. However, the cloud droplets extend much further up into the mixed-phase altitudes in RAMS with more supercooled water up to about 8.5 km than in WRF. The differences between the two models are much stronger in the domain-averaged liquid water content contributed by rain. Although rain

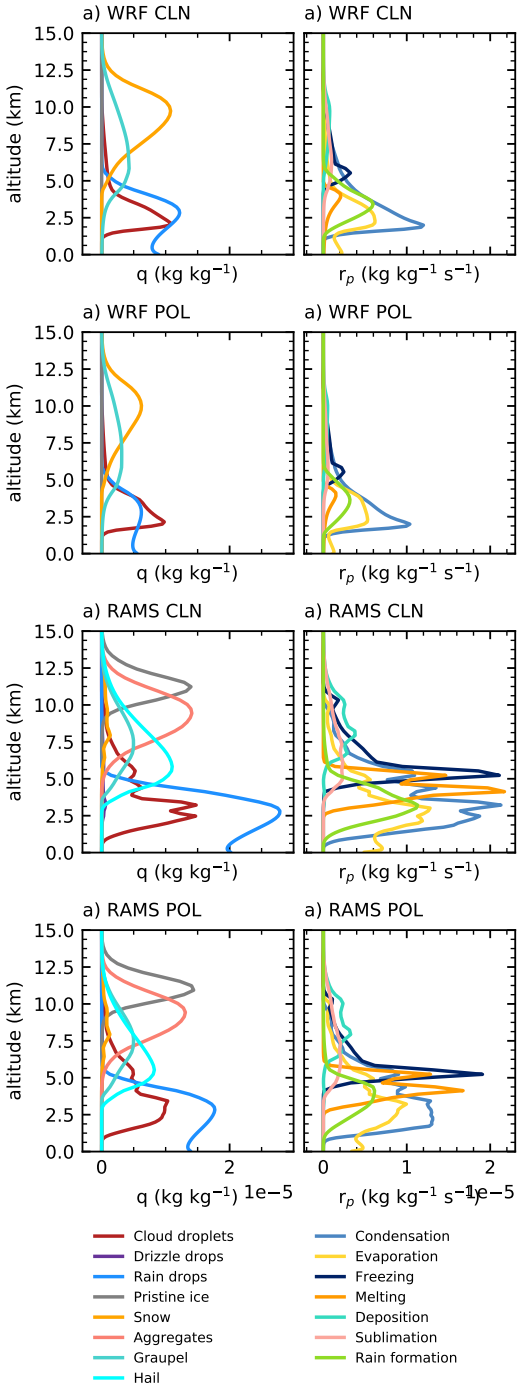

Figure 5.4: Domain- and time-averaged process rate and hydrometeor mass mixing ratio profiles for the two models in the clean and polluted case based on the 3-hour target period used in the tracking analysis.

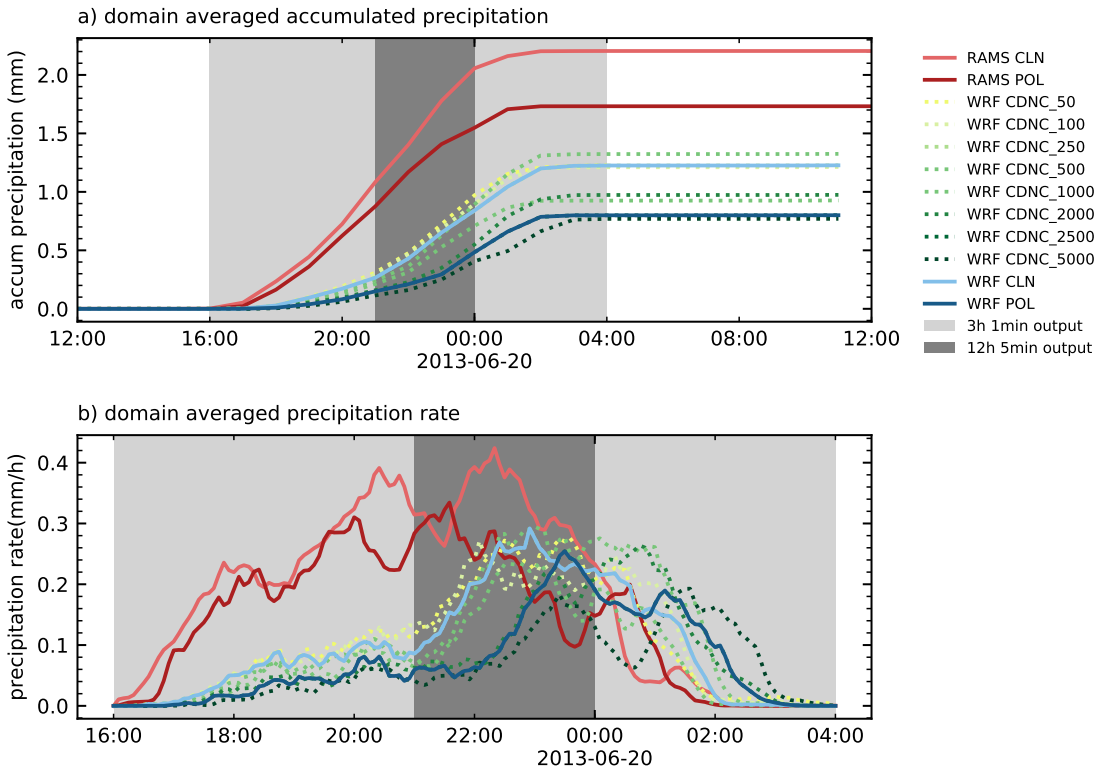

Figure 5.5: Domain-averaged accumulated precipitation (a) and domain-averaged precipitation rate (b) for the different model simulations with RAMS and WRF used in the main analysis of this chapter, as well as for additional simulations with different CDNC values with WRF. Darker coloured lines represent more polluted conditions for each model. The WRF simulations with CDNC values of 250 cm^{-3} and 2500 cm^{-3} are used as CLN and POL in the analysis here, thus describing the same data in this figure. Two shades of grey mark the two periods of high-resolution output.

occurs in the same altitude range from the surface up to 5 km height, there is about twice as much rain mass in the simulations with RAMS. The two models differ strongly in the mixed- and ice-phase processes and subsequently in the vertical profile of frozen hydrometeors. Both freezing and melting processes are almost an order of magnitude stronger in the RAMS simulations than in the WRF simulations, which agrees with the larger mass of frozen water in the RAMS simulations. The two models show a maximum of the denser ice hydrometeors (hail and graupel in RAMS and hail in WRF) at a height of around 6 km. The lower density ice hydrometeors (snow, pristine ice and aggregates) show strong differences between the two models. In WRF, the ice water content at higher altitudes of

around 7 to 12 km is dominated by snow with only minimal amounts of pristine cloud ice. In the simulations with RAMS, there is about twice as much frozen water at these altitudes, in the form of pristine ice and aggregates, while the snow category is only present with a small amount at a lower altitude. For RAMS, the aggregate content peaks at around 9 km height, while most of the pristine ice is present between 10 and 12.5 km height.

5.3.2. Domain-average analysis of the aerosol response

Based on this discussion of differences between the models, we can investigate the effects a change in aerosol conditions with on both domain-average surface precipitation and domain averages profiles of the microphysical variables.

The response of precipitation to changes in aerosols is consistent between the two models with a decrease in domain-wide precipitation for increased aerosols. This decrease is of a similar order of magnitude of about 0.45 mm for both model simulations. The aerosol response of the domain-wide surface precipitation disagrees with previous studies over the study region that reported increased precipitation due to invigorated convection (Fan et al., 2007; Li et al., 2008) or suppression only for extremely polluted conditions beyond the range of aerosol conditions assessed here (Li et al., 2008). However, both these studies have focused on a single strong convective event with either two-dimensional model setups (Fan et al., 2007) or in a relatively small modelling domain with coarser resolution (Li et al., 2008). This leads to limited comparability to the complex cloud field simulated here.

The additional simulations performed with WRF for 6 other CDNC values in the range between 50 cm^{-3} and 5000 cm^{-3} show that the suppression of surface precipitation with increases in aerosols is indeed relatively monotonic and not just a random effect between the two simulation cases. However, this analysis also highlights that there are considerable differences in the timing of the convective activity on the scale of a few hours, which will be discussed further in the could-resolving analysis in Sect. 5.3.3.

The domain-mean response to changes in aerosol conditions in the domain-averages profiles of hydrometeor mass mixing ratios and microphysical models is much smaller than the differences between the two models in both aerosol cases. Both models show a decrease in rain water mixing ratio by about 45 % in WRF and by about 25 % in RAMS. Furthermore, there is a decrease in the drizzle category in RAMS, which only constitutes a small fraction of the hydrometeor mass in both cases. These changes can be linked to the decrease in warm rain formation in the two models by 36 % in WRF and by 25 % in RAMS. Both models show a slight decrease in domain-wide condensation by about 5 % along with an increase in evaporation. In the frozen hydrometeors, there is a marked difference between the two models in the response to the changes in aerosol conditions. In the WRF model, the increase in CDNC leads to a decrease in the total mass of frozen hydrometeors, which includes a decrease in both snow and hail. In RAMS, the increase in aerosol leads to an increase in pristine ice and only small changes in both snow and aggregates. This increase is associated with a slight decrease in the dense hydrometeor categories graupel and hail. Both models show changes to deposition and sublimation that agree with the observed changes in hydrometeor mass mixing ratios, with a 20 % decrease in both processes in WRF and a slight increase of a few percent in RAMS. However, these changes compensate each other for the total latent heating.

5.3.3. Lagrangian analysis of the cloud field using cell tracking

The domain-wide analysis of microphysical cloud properties allows for a representative assessment of the total amount of clouds present in the domain as well as the total energetic turnover due to microphysical processes. This is important for the total effect of clouds on important physical processes such as radiation or the thermal structure of the atmosphere. However, when trying to explain these differences, the spatially and temporally averaged perspective has significant limitations as it does not represent the life cycle of individual convective cells in the population of clouds. To overcome the limitations of

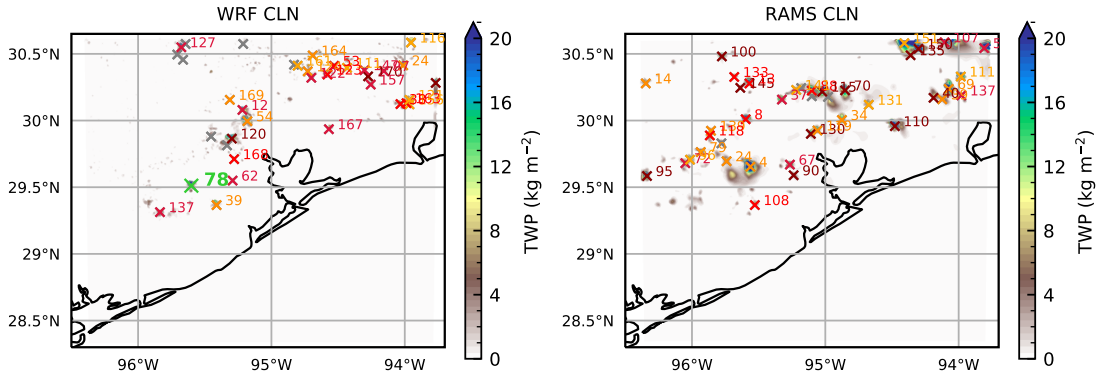

Figure 5.6: Cloud field represented by the total water path (TWP) with tracked cells for (a) WRF and (b) RAMS during the time of maximum convective activity (21:30 UTC, 16:30 local time). A green marker identifies the cell visualised in detail in Fig. 5.7 in the map for WRF (a).

an analysis based on domain-wide statistics (Sect. 5.3.1) we analyse individual clouds in the cloud field. This allows us to assess whether there are substantial differences, both between the two different models and due to changes in the aerosol conditions. Furthermore, the detailed microphysical pathway analysis that was developed in Chap. 3 can be used to assess both the time evolution of the microphysical processes in the clouds and the morphology of the individual cloud hydrometeors and the microphysical process rates.

The individually tracked convective cells are depicted for a single point in time in Fig. 5.6 for both models. Figure 5.7 shows the evolution of a typical tracked cell (cell no. 120 in the WRF CLN case, as highlighted in Fig. 5.6a) as an example of the analyses that are extended to the entire cloud field based on cloud composites (Sect. 5.3.6). We identify characteristic points in time for the evolution of the cloud based on integrated quantities such as microphysical process rates or hydrometeor mass. We have chosen to investigate the following characteristic points in time to break up the time evolution of individual cells into different stages. The initiation is defined as the first point in time at which the tracking algorithm identifies a specific updraft. The onset of freezing characterises the first point in time when freezing and riming processes set in. Furthermore, the timing of maximum latent heat release, maximum cloud hydrometeor mass and maximum warm

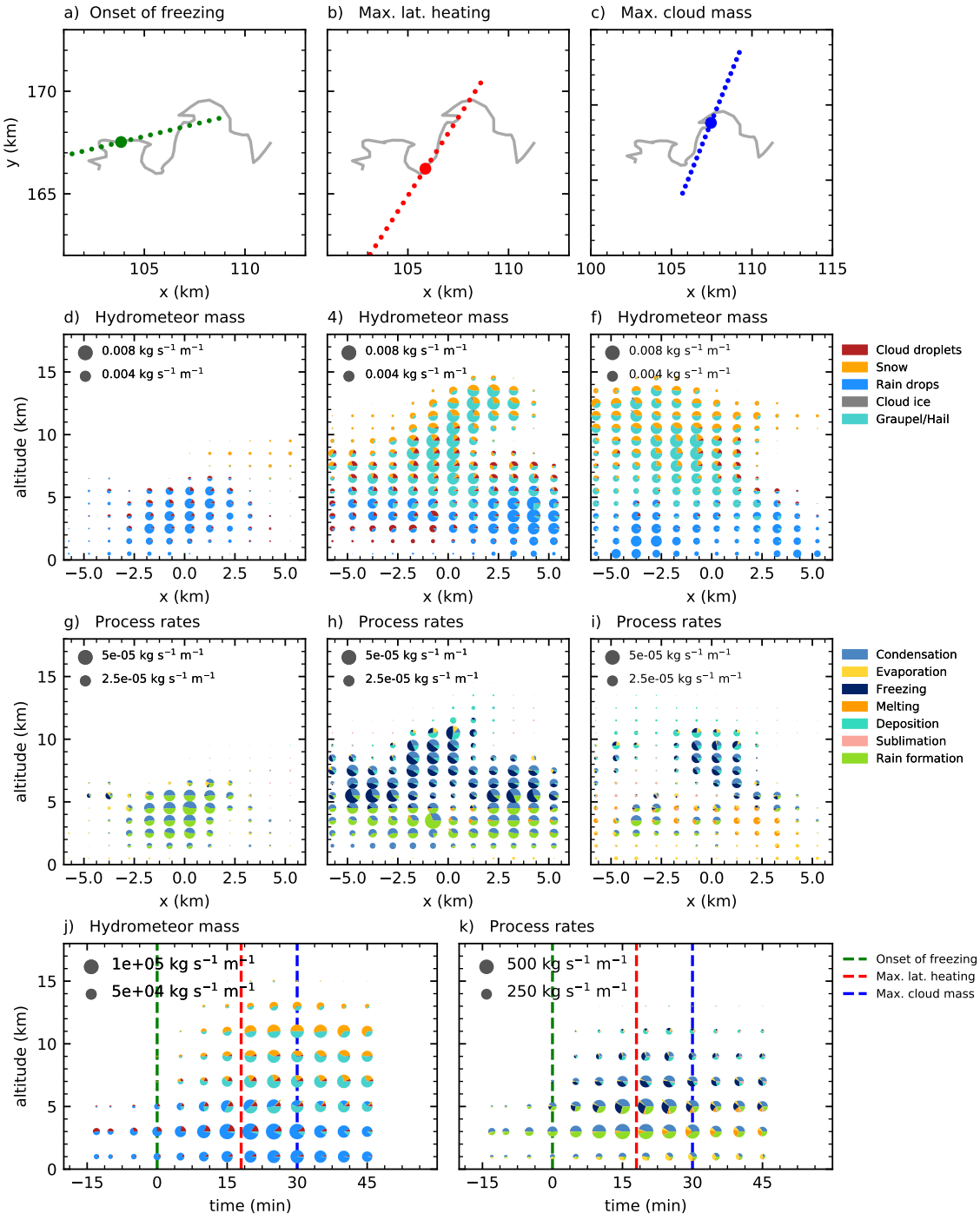

Figure 5.7: Conceptual overview of the cell tracking and the microphysical analysis. The trajectory of the cell (grey line) is depicted with the individual points in the time evolution, onset of freezing processes (a), timing of maximum latent heat release (b) and maximum cloud hydrometeor mass (c). These panels also show the surface projection of the vertical slices through the cloud along which the hydrometeor mass mixing ratios (d,e,f) and microphysical process rates (g,h,i) are visualised in the two following rows. The time evolution of the horizontally accumulated hydrometeor mass (j) and process rates (k) is depicted along with vertical lines that show the specific points in time in the panels above.

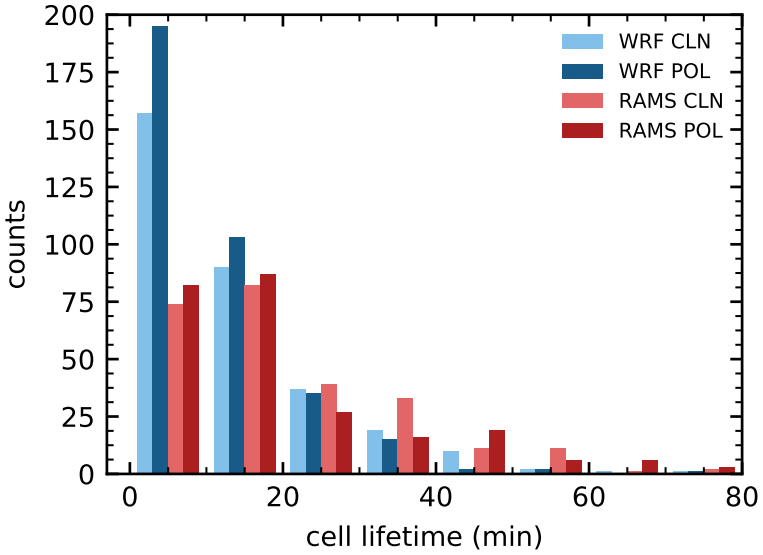

Figure 5.8: Histogram of cloud lifetimes detected by the tracking algorithm for both CRMs (WRF in blues, RAMS in reds) and the two cases CLN and POL.

rain formation are all based on integrated quantities and give additional reference points in the time evolution of the individual cells. These points in the evolution of the example cell are shown as vertical lines in Fig. 5.7j and Fig. 5.7k. The assessment of the morphology of the hydrometeor mass mixing ratios (Fig. 5.7d,e,f) and microphysical process rates (Fig. 5.7g,h,i) is performed for the same points in time for slices through the cloud along the lines in the equivalent panel in Fig. 5.7a,b,c. The condensate content in the different hydrometeor classes and the microphysical process rates are summed up over specific layers within the cloud at each individual output time step to produce the time evolution of the hydrometeor content (Fig. 5.7j) and microphysical process rates (Fig. 5.7k).

5.3.4. Updraft lifetimes

The analysis of the lifetimes of the individual tracked convective clouds (Fig. 5.8) shows that the lifetimes of the tracked updrafts agree well between the two models WRF and RAMS for lifetimes between 10 and about 40 minutes. WRF shows more updrafts that were only tracked for a short period of less than 10 minutes, which includes cells that were only tracked for a part of their lifetime and smaller updrafts near larger convective

cells. In contrast to WRF, RAMS shows a substantial number of cells that were tracked for more extended periods longer than 40 minutes. There is, however, no clear effect of the changes in aerosol between the CLN and POL case in either of the two models.

5.3.5. Classification of tracked clouds

The scattered convection in the simulation domain can be separated into different types of clouds. The evolution of the cloud phase in the individual tracked cells (Fig. 5.9a,b) shows that there is a clear separation between different tracked updrafts. Many clouds are entirely dominated by warm phase hydrometeors, especially in simulations with WRF (Fig. 5.9a). Other tracked cells show the transition into deep convection featuring a dominance of ice-phase hydrometeors. Some individually tracked updrafts split off existing deep convective clouds and thus feature ice-phase hydrometeors and mixed- and ice-phase processes over their entire existence. The differences between the partition of the cloud field into these types of clouds could be contributing substantially to the differences between the two models observed in the domain-wide analyses (Sect. 5.3.1) and also impact the response to changes in aerosol conditions. Therefore, the tracked cloud objects are separated into the following categories to perform separate analyses for each subset of the cloud field:

warm Clouds that never show substantial freezing or frozen hydrometeors

warm-cold Clouds that initially show only warm-phase processes and then transition into deeper clouds with the evolution of mixed- and ice-phase processes.

cold Clouds that are already showing ice-phase processes at the initial point of their tracked evolution. These clouds are missing the initial warm-phase development of the cell, either because it was not tracked properly or because they have been formed by splitting off from an existing deep convective cell

Table 5.3: Number of tracked cells in each category for the four different simulations.

	RAMS		WRF	
	CLN	POL	CLN	POL
all	203	198	317	353
warm-cold	68	62	48	26
warm	44	59	156	227
cold	38	26	15	9
rest	53	51	98	91

rest Tracked updrafts that do not fit into any of the specific categories, e.g. as they are only tracked for a subfraction of a cell lifetime.

The total number of tracked cells, as well as the numbers in the different categories of clouds in the four different simulations, are summarised in Table 5.3 and visualised in Fig. 5.9b. There are more individually tracked updrafts in the two simulations with WRF than with RAMS. However, these are mainly contributed by additional updrafts tracked for a relatively short period (see Fig. 5.8).

The separation into the different cloud categories shows differences between the two models. There are about three times as many warm clouds in both cases for WRF as for RAMS. The clouds that are tracked through the transition from warm-phase dominated to mixed-phase dominated processes (warm-cold) show a similar number between both cases (CLN and POL) with RAMS and the CLN case in WRF, but a lower number of tracked cells is observed in the WRF POL case. This can be related to the suppression of precipitation, hydrometeors and mixed-phase processes that was observed in the domain-wide analysis (Sect. 5.3.1). RAMS has more clouds that fall into the cold category of tracked cells that already show a substantial ice phase at initiation, while simulations with WRF feature about twice as many updrafts in the category rest than the two simulations with RAMS.

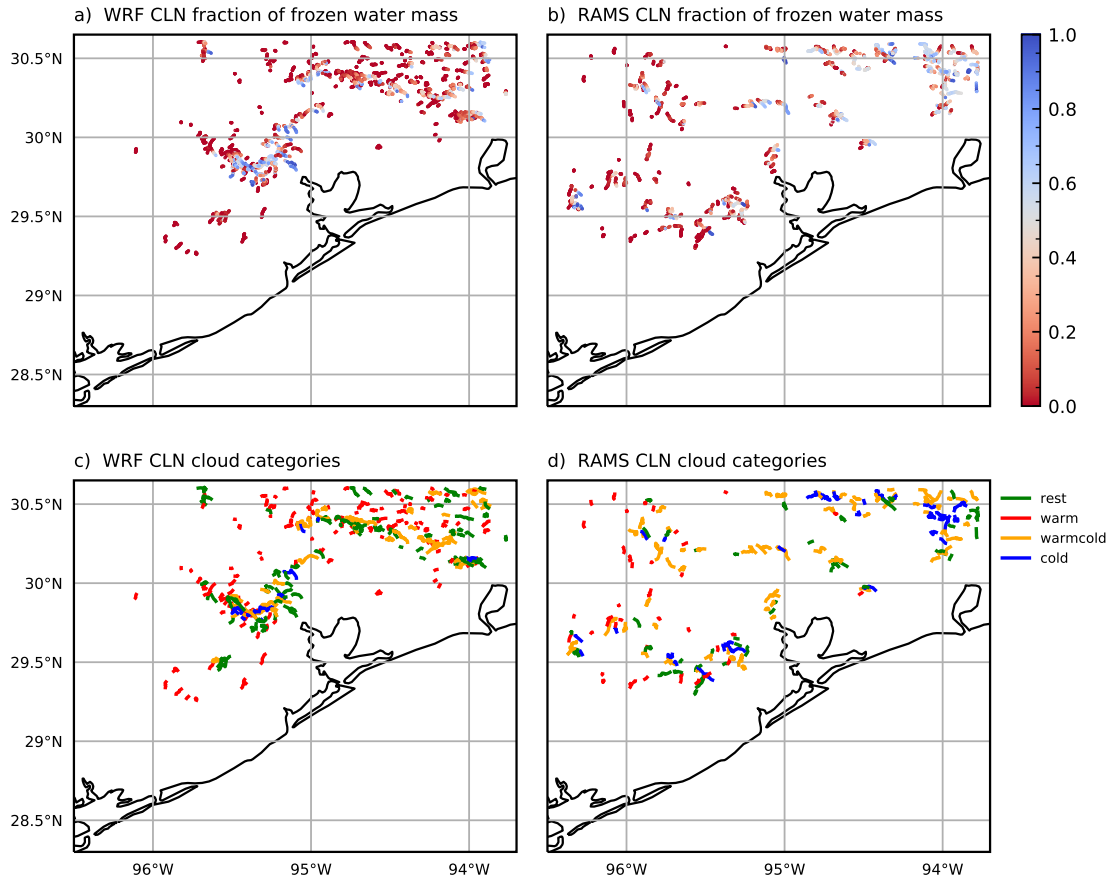

Figure 5.9: All tracked cells with the fraction of frozen water mass (a, b) and the categorisation (c, d) for the 3-hour period used in the tracking analysis.

5.3.6. Cloud composites and assessment of the "average" cloud

The tracking of the individual clouds in the cloud field allows for an analysis of the time evolution of individual clouds. To go beyond the analysis for an individual cell as shown in Fig. 5.7, the clouds are combined into cloud composites. Different clouds, however, develop at a different rate, with different lifetimes and different periods covering the specific phases of cloud evolution. Furthermore, the updrafts might not be tracked perfectly for the entire cloud life-cycle, e.g. by missing the initial initiation stage or the final decay of the convective cloud. Therefore, an absolute time axis based on initiation and dissipation is not the right way to assess the clouds' time evolution. Furthermore, the different types of clouds present in the simulation results (Sect. 5.3.5) can be treated differently to investigate their main characteristics separately. Due to the detailed output of a large

range of model diagnostics at high temporal resolution (1 minute), we can use the specific points in time that are identified for every individual cloud (Sect. 5.3.3) to composite the time evolution of the individual clouds around these characteristic points in time.

To assess the time evolution of all tracked clouds, we create cloud composites for all tracked cells and for subsets of clouds in the different categories discussed in Sect. 5.3.5. This is based on shifting the time evolution of the clouds (Fig. 5.7j,k) for a specific characteristic point in their evolution align for all clouds. The timing of maximum latent heat release is used to create a composite for all tracked clouds, thus creating a manifestation of the average convective cloud in the model simulations. These composites are shown for the hydrometeor mass in Fig. 5.10 (WRF) and Fig. 5.11 (RAMS), and for the microphysical process rates in Fig. 5.12 (WRF) and Fig. 5.13 (RAMS). The simulations with WRF show a strong difference in the structure of the average tracked cloud in the two cases CLN and POL, especially regarding the mixed- and ice-phase processes. While the total liquid water content in the form of cloud droplets is not affected by the change in aerosol conditions, there is a strong decrease of the rain water mixing ratio by about a factor of three (Fig. 5.10), which can be related to the decrease in warm rain formation of a similar order (Fig 5.12). The ice-phase of the average tracked cloud is strongly suppressed in the POL case (Fig. 5.10) along with the respective mixed- and ice-phase processes, such as freezing or melting (Fig. 5.12).

RAMS shows a much more similar picture for the composite clouds of all tracked cells between the two cases CLN and POL. The hydrometeor masses (Fig. 5.11) reveal a marked decrease in the total amount of rain water in the lowest 4 km from CLN to POL, while the total liquid water in the form of cloud droplets is not strongly affected. There is a strong decrease in hail mixing ratio and a smaller decrease in both aggregates and pristine ice in the higher region of the cloud. The microphysical process rates show a general weakening of all microphysical processes along with a decrease in warm rain formation in the polluted case which is directly associated with the effects of the changes in aerosols.

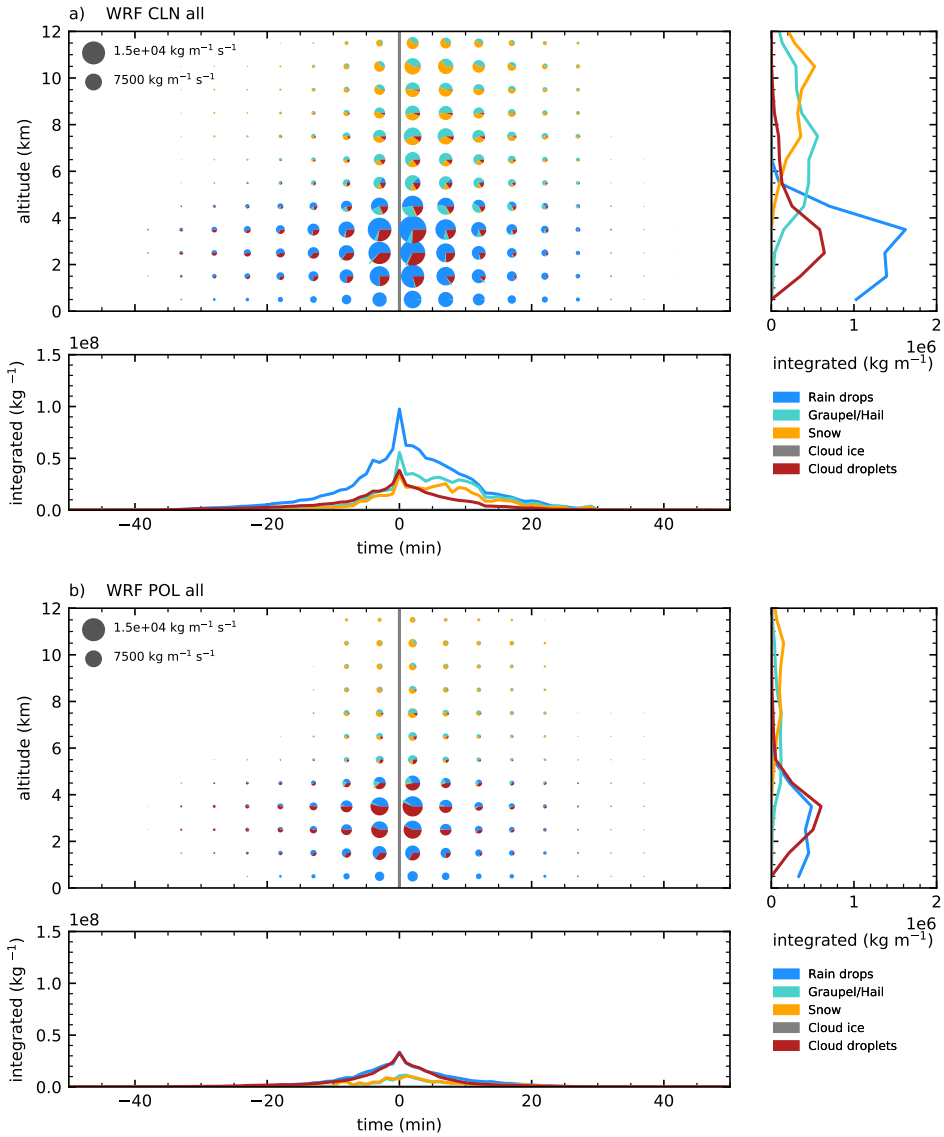

Figure 5.10: Hydrometeor mass mixing ratios for a composite of all tracked cells aligned around the timing of maximum latent heat release for WRF in the CLN and POL case.

However, these composites of all tracked cells include very different types of clouds and are thus strongly affected by the differences in the number of clouds of each type (Table 5.3). Therefore, two more specific subsamples of clouds are discussed in detail, namely clouds that are tracked throughout their entire transition from the warm-phase development into deep convection (warm-cold) and warm clouds that only feature liquid phase hydrometeors and liquid-phase microphysics (warm).

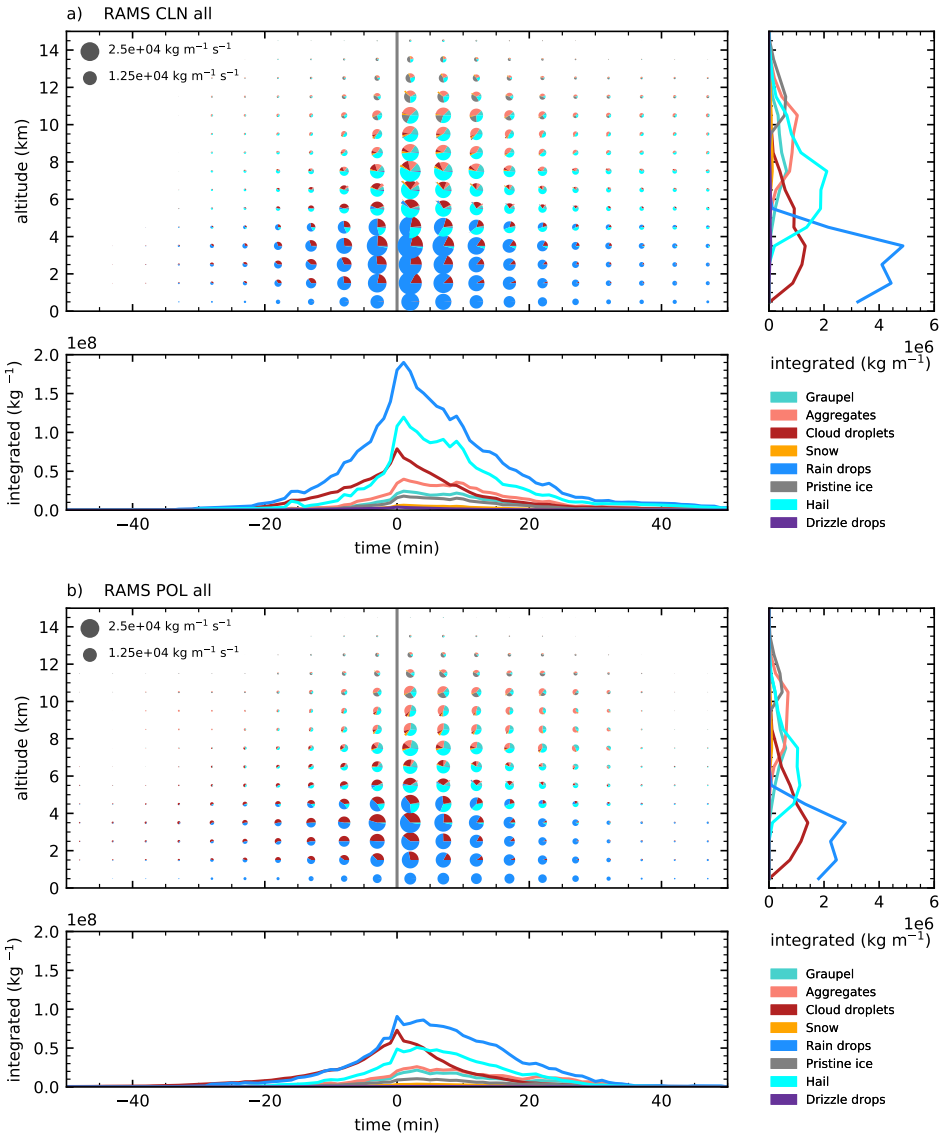

Figure 5.11: Hydrometeor mass mixing ratios for a composite of all tracked cells aligned around the timing of maximum latent heat release for RAMS in the CLN and POL case.

5.3.7. Aerosol effects on the transition of clouds to deep convection

We composite the clouds that show the transition from warm-phase cumulus to deep convective cumulonimbus around the time of the onset of freezing. This allows separating effects of the changes in aerosols on the evolution of the cloud in different phases of its lifetime, e.g. in the initial warm phase, during transition and then for fully developed deep convection. These composites are shown for the hydrometeor mass in Fig. 5.14 (WRF) and Fig. 5.15 (RAMS) and for the microphysical process rates in Fig. 5.16 (WRF) and

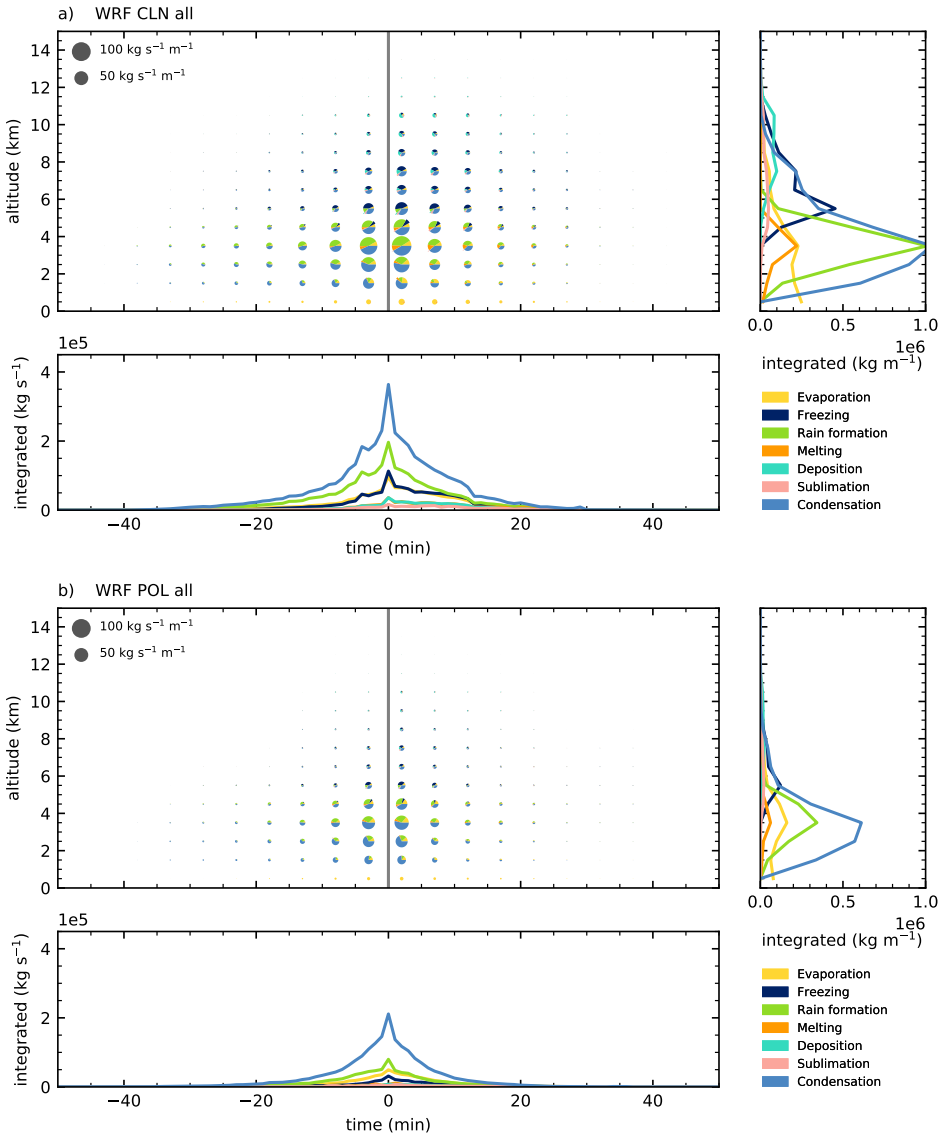

Figure 5.12: Microphysical process rates for a composite of all tracked cells aligned around the timing of maximum latent heat release for WRF in the CLN and POL case.

Fig. 5.17 (RAMS).

The assessment of this type of clouds confirms the suppression of the ice-phase hydrometeors in the POL case in the WRF simulations (Fig. 5.14). However, the assessment of the microphysical process rates (Fig. 5.16) shows smaller differences in the total microphysical process rates between the two cases. These are mainly based on a different cell lifetime in the CLN case compared to the POL case, while the vertical structure and the magnitude of the microphysical processes around the time of the onset of the ice phase

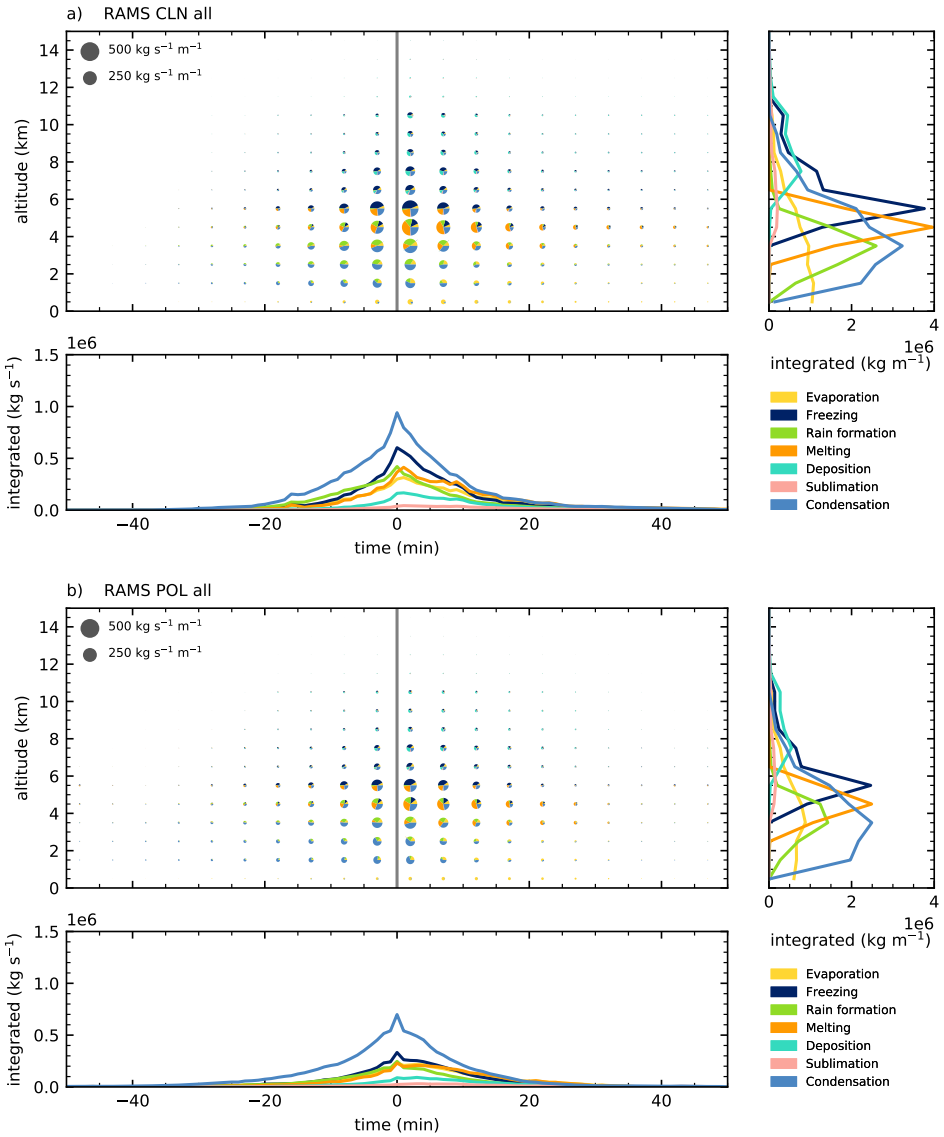

Figure 5.13: Microphysical process for a composite of all tracked cells rates aligned around the timing of maximum latent heat release for RAMS in the CLN and POL case.

in the clouds are very similar for the two cases. The tracked cells of this category in the RAMS simulations show a similar vertical structure and time evolution between the two cases for both hydrometeors (Fig. 5.15) and microphysical processes (Fig. 5.17), except for the differences in the warm-phase processes. The differences in the partition of the liquid phase only extend to a few minutes after the onset of freezing. This can be related to the rapid increase in melting processes after the onset of mixed-phase processes (Fig. 5.17) in both cases. The melting of frozen hydrometeors provides large amounts of

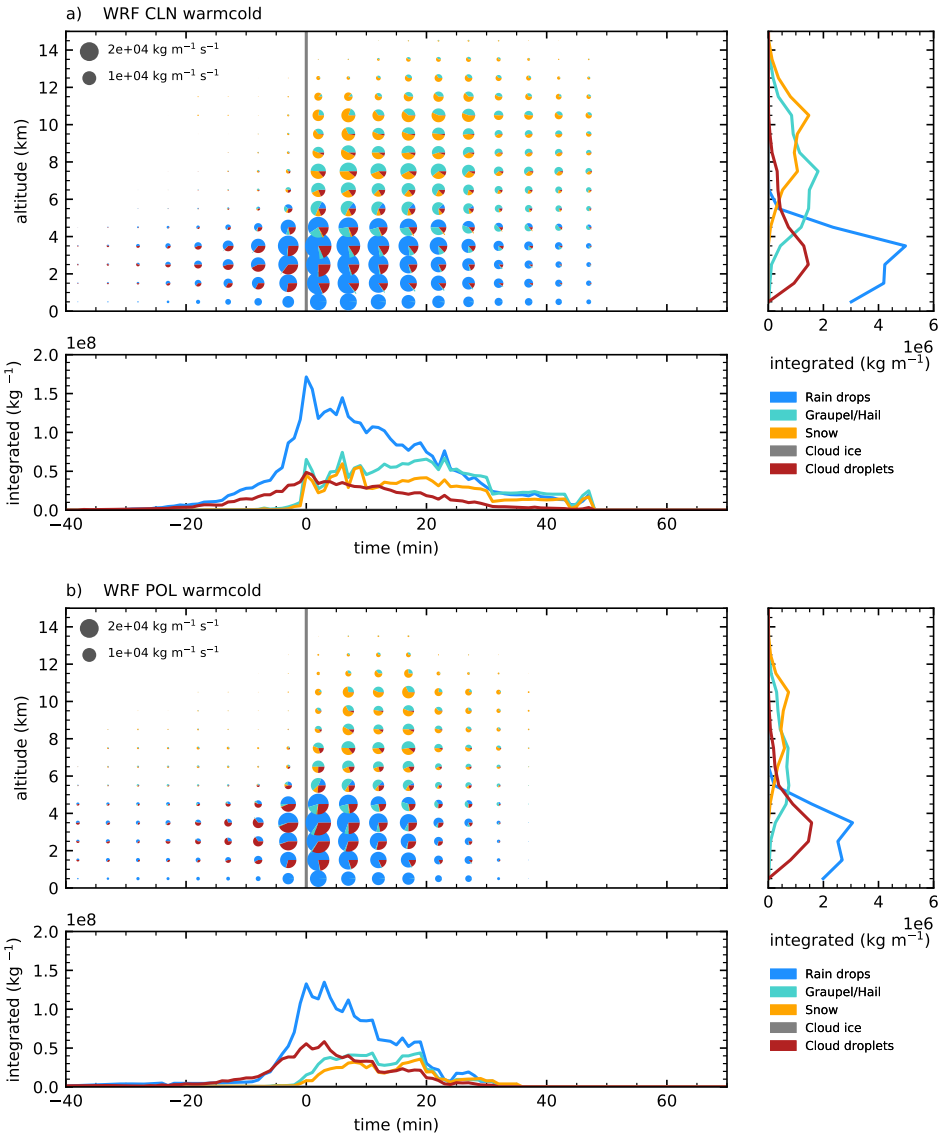

Figure 5.14: Hydrometeor mass mixing ratios aligned around the onset of freezing for WRF in the CLN and POL case for clouds making the transition from warm- to cold-phase processes.

raindrops that contribute to a strong increase in warm rain formation due to the effective accretion of cloud droplets by raindrops. The two models show a discrepancy in the role of these melting processes. In RAMS, the melting of frozen hydrometeors coincides almost entirely with freezing and riming both in magnitude and timing but shifted to a lower altitude by about 1 km. There is no clear effect of the change in aerosol conditions on the freezing and melting processes in RAMS. In WRF, even those clouds that eventually glaciate, do so much less vigorously with smaller total amounts of freezing and

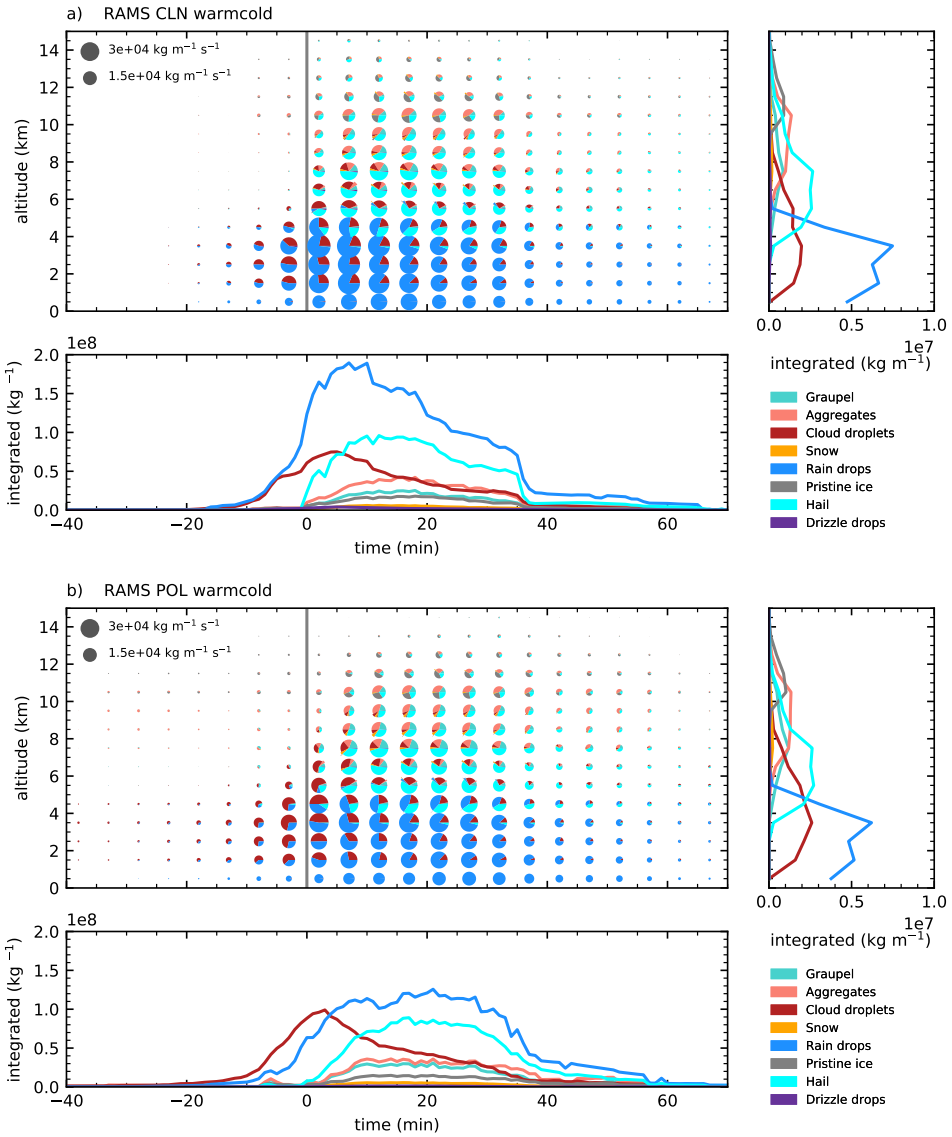

Figure 5.15: Hydrometeor mass mixing ratios aligned around the onset of freezing for RAMS in the CLN and POL case for clouds making the transition from warm- to cold-phase processes.

riming (Fig. 5.16). In contrast to RAMS, only a small fraction of the frozen hydrometeors melt to form additional rain. Instead, a larger fraction of the frozen water is lost from the ice phase through sublimation processes (Fig. 5.4). However, this sublimation in the cloud anvils is not entirely captured by the analysis here, as cloud volumes based on a condensate threshold (Sect. 5.2.3) do not fully capture the cloud anvils.

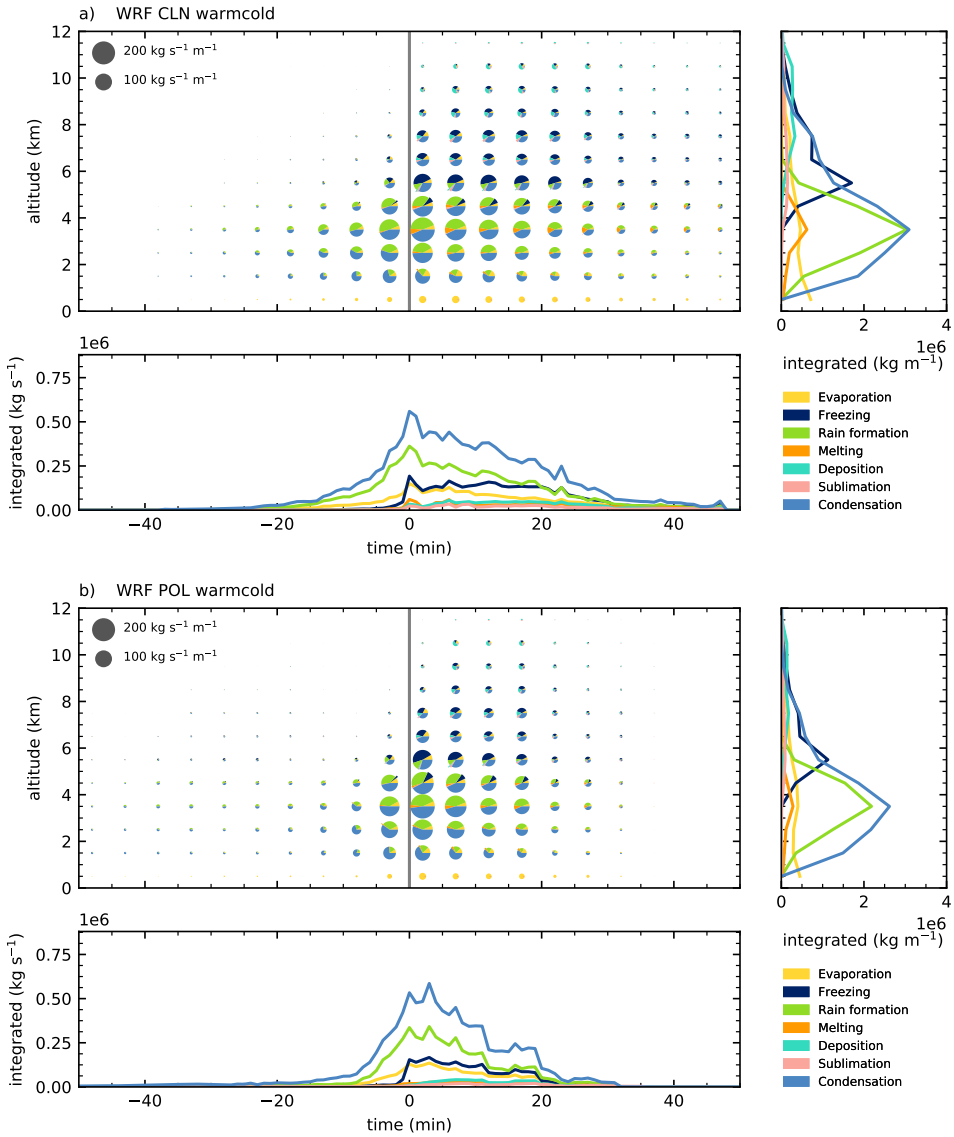

Figure 5.16: Microphysical process rates aligned around the onset of freezing for the WRF model in the CLN and POL case for clouds making the transition from warm- to cold-phase processes.

5.3.8. Aerosol effects on warm clouds

The subset of tracked clouds that are completely characterised by warm-phase processes and only contain liquid water in the form of cloud droplets and raindrops occur in both models and for both cases (Fig. 5.9a, b). However, they are more numerous in the WRF simulations (Table 5.3), while the average warm cloud is larger in RAMS, both in terms of total liquid water mass (Fig. 5.19) and microphysical processes (Fig. 5.21), than in the

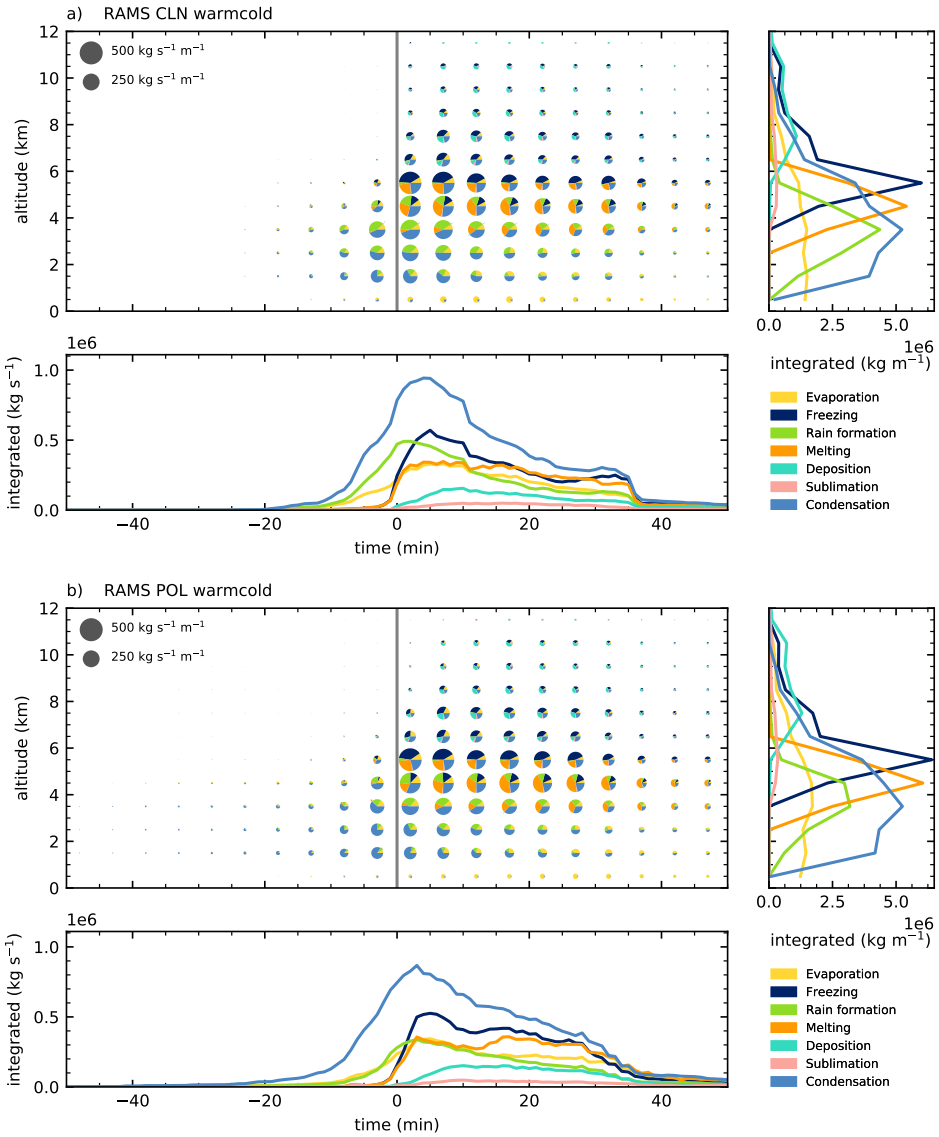

Figure 5.17: Microphysical process rates aligned around the onset of freezing for the RAMS model in the CLN and POL case for clouds making the transition from warm- to cold-phase processes

WRF simulations (Fig. 5.18 and Fig. 5.20). Apart from that difference, both models show a very similar structure of these clouds, both concerning hydrometeor composition and process rates. The total condensate content in the clouds decreases slightly from clean to polluted conditions, with a strong decrease in the total mass of rain, but a slight increase in the mass of cloud droplets (Fig. 5.18 and Fig. 5.19). This is caused by the strongly decreased warm rain formation (Fig. 5.20 and Fig. 5.21). However, there is no obvious change in the lifetime of the tracked warm convective clouds, that could be expected to

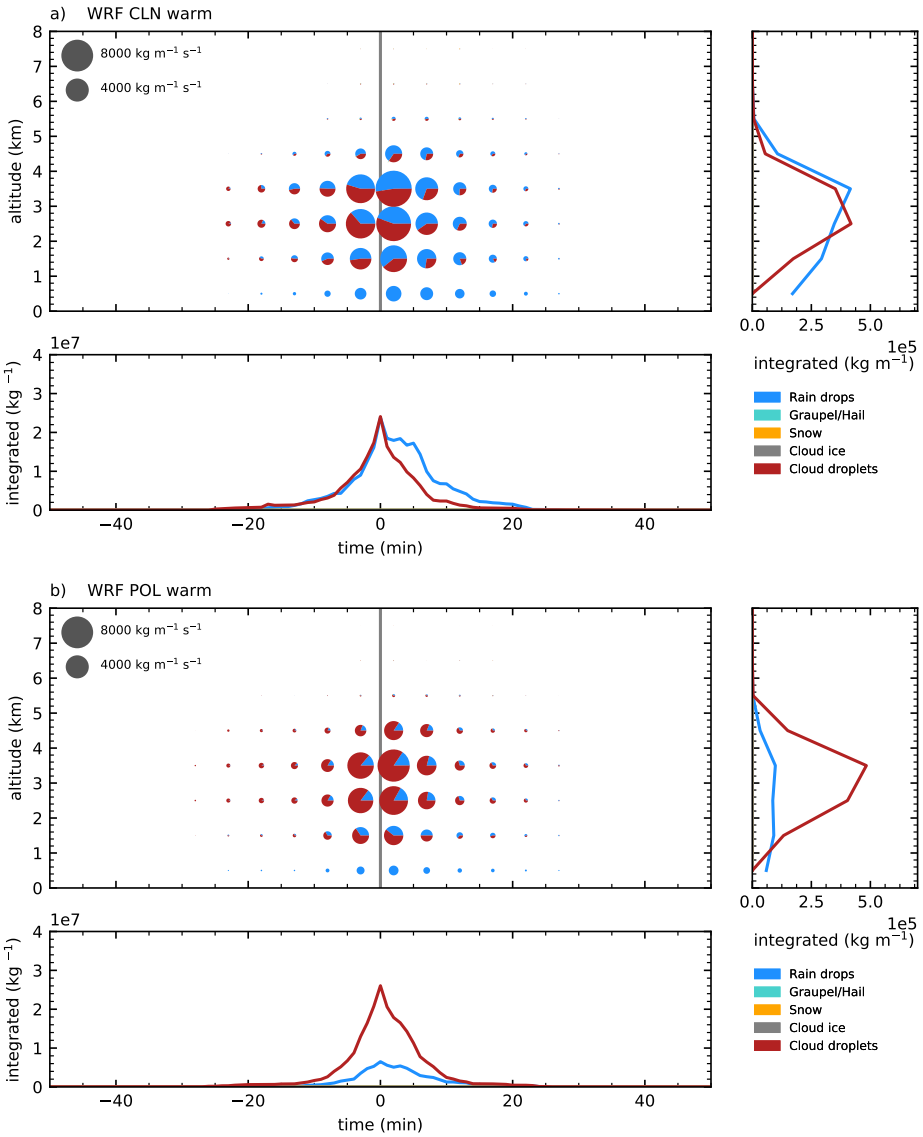

Figure 5.18: Hydrometeor mass mixing ratios aligned around the timing of maximum latent heat release for WRF in the CLN and POL case for clouds that only show warm-phase processes.

result from the decrease in precipitation formation. Both models show no differences to the evaporation and condensation processes due to the change in aerosol conditions at altitudes above cloud base. However, there is a decrease in evaporation near the surface for the POL case, which can be associated with a decrease in the evaporation of rain due to the decrease in warm rain formation and subsequent lower rain mass mixing ratio.

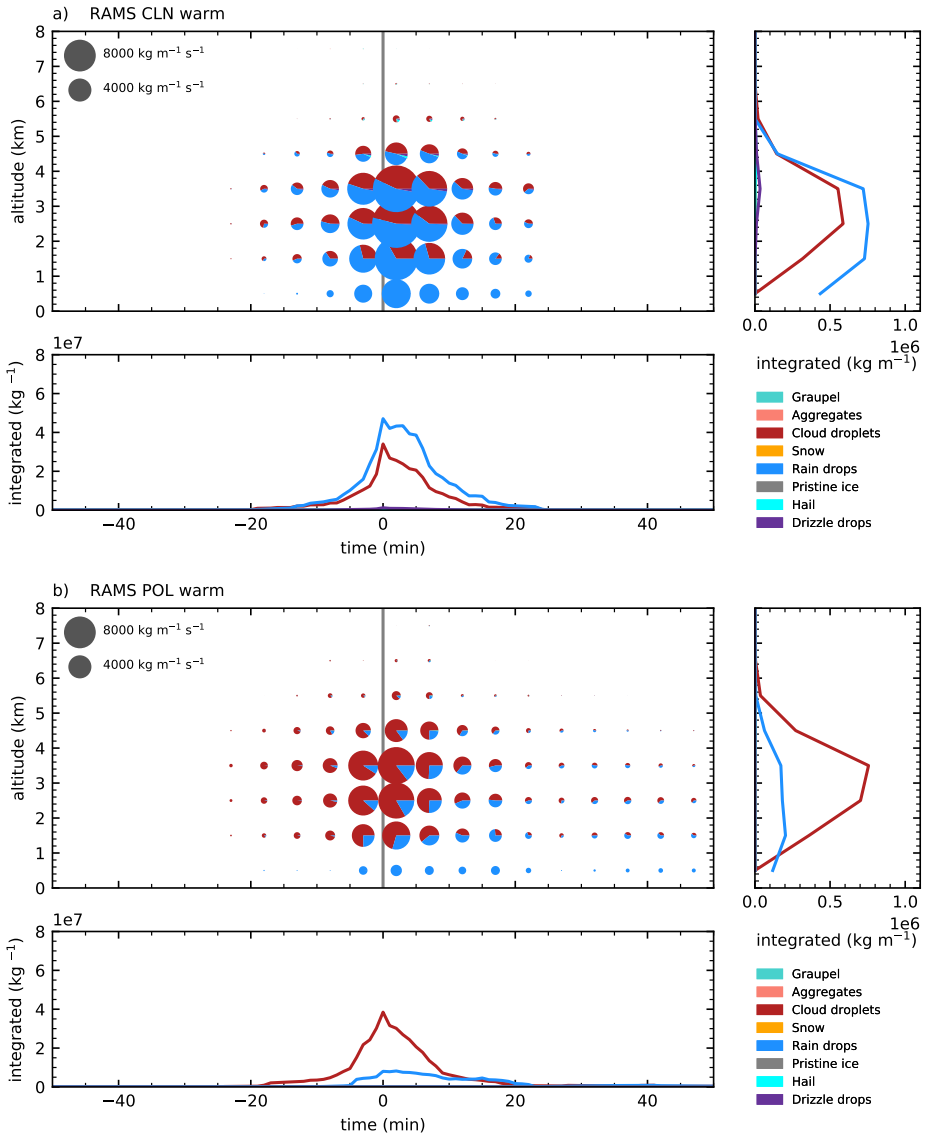

Figure 5.19: Hydrometeor mass mixing ratios aligned around the timing of maximum latent heat release for RAMS in the CLN and POL case for clouds that only show warm-phase processes.

5.3.9. Surface precipitation from tracked clouds

In addition to the vertically resolved analysis of microphysical cloud properties, such as hydrometeor masses or process rates, we can use the cloud tracking and compositing approach to investigate the time evolution of the surface precipitation further for both the strong differences between the models and the response to changes in aerosols between the clean and polluted case. Figure 5.22 shows the time evolution for a composite of all

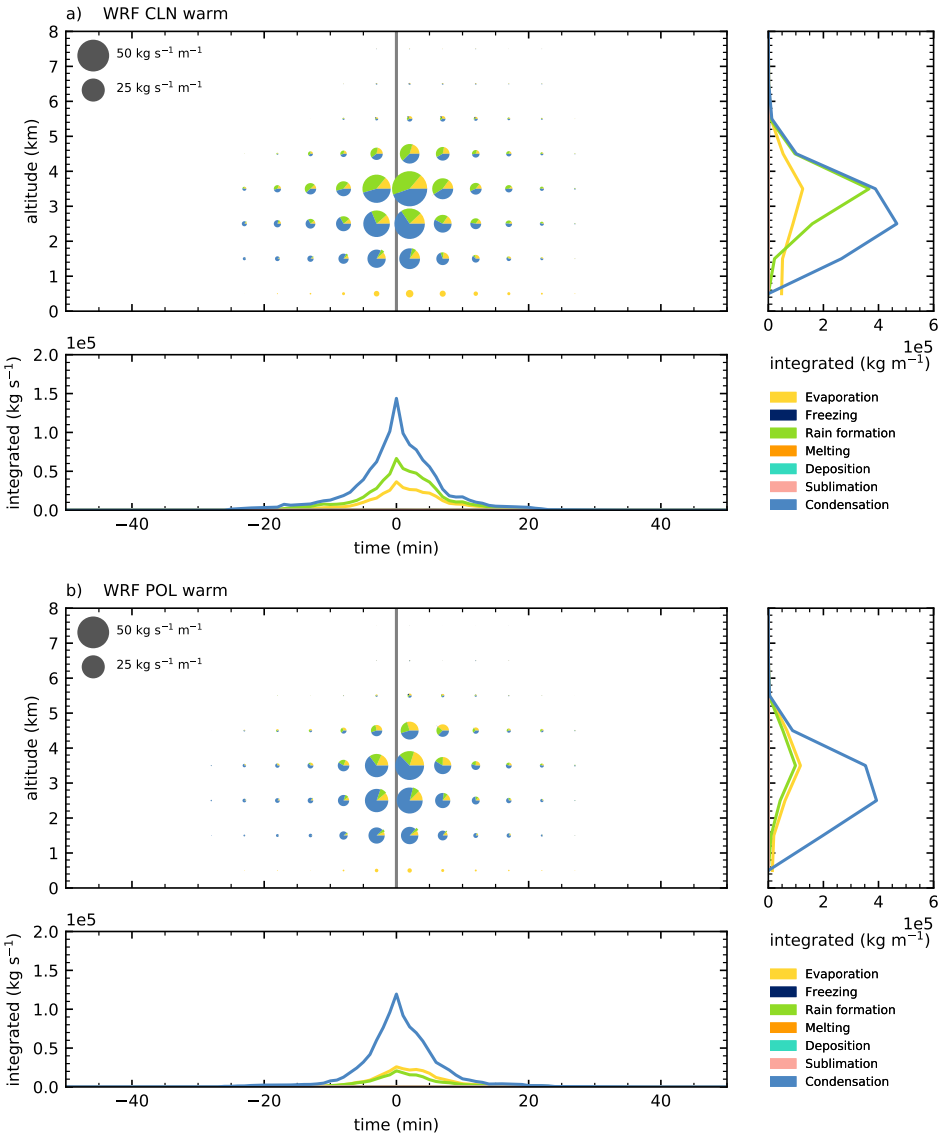

Figure 5.20: Microphysical process rates aligned around the timing of maximum latent heat release for WRF in the CLN and POL case for clouds that only show warm-phase processes.

cells (Fig. 5.22a) and for the different categories of tracked cells (Fig. 5.22b-e).

In both models, the decrease in precipitation in the domain-wide analysis (Fig. 5.5a) can be related to a decrease over the entire life cycle of the clouds. Both models show very similar accumulated precipitation for the initial phase of the clouds until the time of maximum latent heat release, while RAMS has substantially more precipitation in the later stages of the clouds of for longer-lived clouds for both cases.

Precipitation from the glaciating cells (Sect. 5.3.7) contributes about half of the total sur-

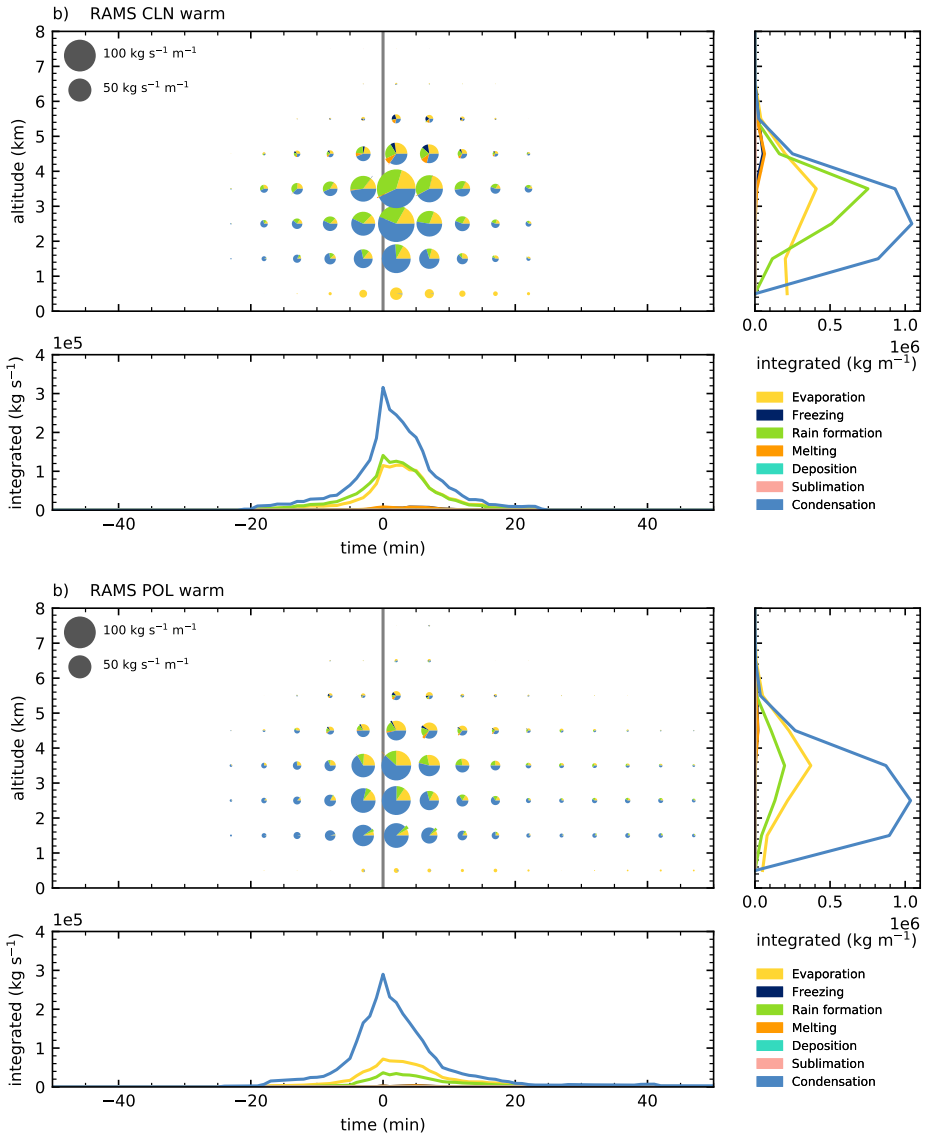

Figure 5.21: Microphysical process rates aligned around the timing of maximum latent heat release for RAMS in the CLN and POL case for clouds that only show warm-phase processes.

face precipitation for both models (Fig. 5.22b). The response in precipitation shows some differences between the two models for this type of cells. In RAMS, the decreased precipitation with increased aerosols for these cells can be traced back to the suppression of precipitation in the first 20 minutes after the onset of freezing. In contrast, the total surface precipitation slightly increases for the last stages of the clouds with the longest lifetimes.

Warm clouds contribute more to the total surface precipitation in WRF than in RAMS

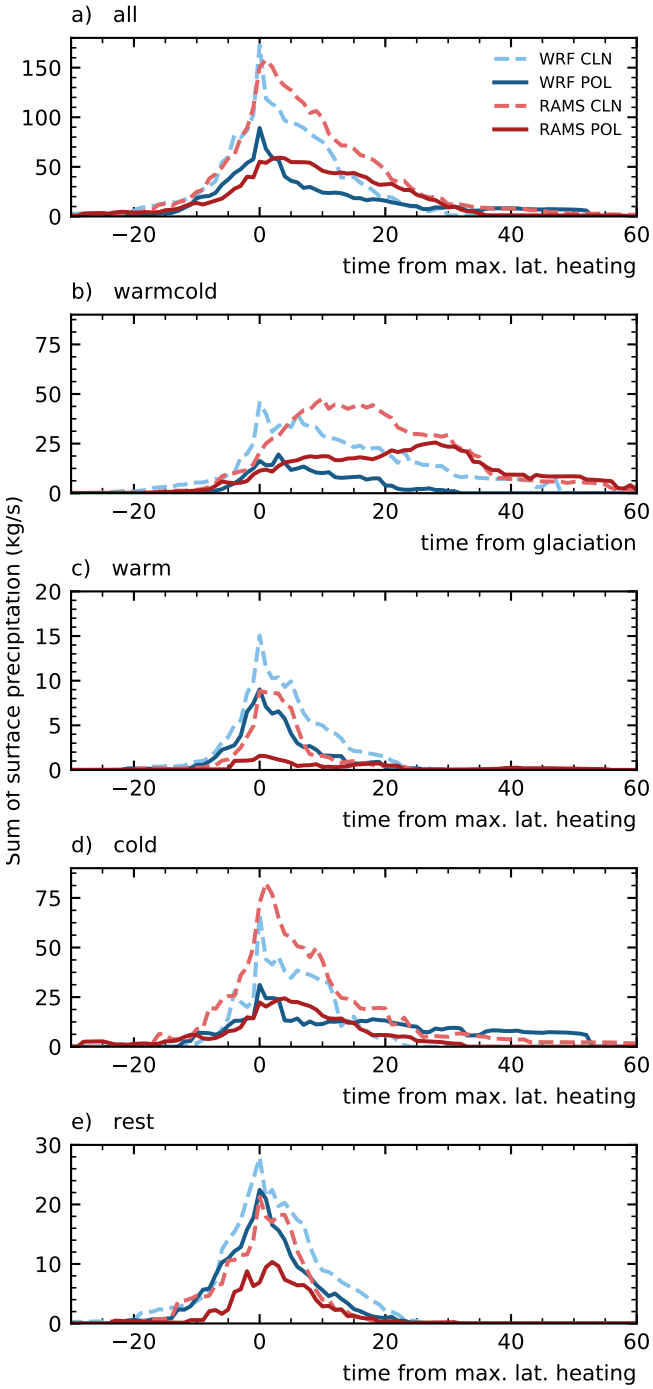

Figure 5.22: Summed up precipitation over the time evolution of all cells (a) and the individual categories (b, c, d, e) centred around the time of maximum integrated latent heat release (a, c, d, e) and the onset of freezing (b) for the two cases CLN and POL in WRF and RAMS.

(Fig. 5.22c). However, the response to a change in aerosols is much stronger in RAMS, with almost complete suppression of precipitation from these clouds for the POL case. Cloud classified as cold, i.e. those that already show frozen water at the initial timing of the tracked updraft, contribute substantially to the surface precipitation in the domain (Fig. 5.22d). These clouds show a very similar decrease in total contribution to the surface precipitation for both models, except for the large contribution from a few long-lived cells in the WRF POL simulation. The final category collecting those tracked updrafts that could not be identified as one of the other types of clouds for a more detailed study shows a considerable decrease in precipitation with increased aerosols in both models (Fig. 5.22e). The timing of precipitations is relatively symmetric around the time of maximum latent heat release, which can be explained as these updrafts probably represent random samples from the entire life cycles of individual cells.

5.4. Conclusions and outlook

We have simulated scattered convection over the region around Houston in the southern United States with two different CRMs, WRF and RAMS, under clean and polluted aerosol conditions. The analysis of domain-averaged cloud properties and specifically domain-averaged surface precipitation for the entire simulation period revealed a consistent response to increased aerosols. Both models show a suppression of warm rain formation and surface precipitation. The consistent response in surface precipitation was further confirmed by additional simulations with the WRF model, covering a wide range of different CDNC values, which exhibit a relatively monotonic decrease in domain-averaged accumulated surface precipitation. However, domain-averaged profiles of hydrometeor mass mixing ratios and microphysical process rates show large differences between the two models, especially concerning the extent of the ice phase of the cloud. These differences between the models are larger than the response to changes in aerosols in each model.

Individual convective cells were identified, tracked and analysed based on the tracking framework developed in Chap. 4. To introduce a relative time axis, characteristic points in the tracked cloud evolution, such as maximum latent heat release, the onset of freezing or maximum cloud mass, were used to align different clouds. This allowed creating composites representing an average cloud in the population of tracked clouds, both for the time evolution of the clouds and for the cloud morphology along slices at specific stages of their development. The composites of all tracked cells confirmed the assessments from the domain-wide analysis. However, the interpretation of these composites is challenging as they convolute the time evolution of different types of convective clouds in the simulations.

Therefore, vertically integrated cloud properties and this assessment of the timing of specific microphysical processes in the clouds were used to subset the population of tracked convective cells into four different categories of clouds. This revealed considerable differences between the models with substantially more entirely liquid clouds in WRF and more clouds that show a substantial evolution of ice-phase processes in RAMS. We first focused on the subset of tracked cells that undergo the transition from an initial warm-phase evolution to deep convection involving mixed-phase and ice-phase processes (warm-cold). In the simulations with WRF, the analysis of these clouds confirms the suppressed deep convection in the polluted case that was deduced from the analysis based on domain-wide averages of surface precipitation and microphysical process rates. This includes both a strong decrease in the number of clouds in this category and a much weaker evolution of the individual cells. In RAMS, the differences between the two cases for this category of clouds is minimal and mainly restricted to suppression of rain formation and surface precipitation in the earlier stages of the cloud around the time of the onset of freezing. The time evolution of the microphysical process rates shows that the suppressed response in the later stages of the clouds can be related to the feedback of the mixed-phase processes onto the warm phase. Melting ice hydrometeors provide large amounts of raindrops, which allows the warm rain formation to increase to a similar level as in the clean case

due to effective accretion of cloud droplets. The assessment of the warm clouds reveals a much more similar behaviour between the two models. Both models show a strong decrease in precipitation formation from warm rain processes but only a small increase in cloud water content and no changes to cloud lifetimes.

Previous observational studies (Orville et al., 2001; Steiger et al., 2002; Shepherd and Burian, 2003; Shepherd, 2005) reported an increase in precipitation and lightning activity with increased aerosols downwind of the urban areas around Houston, which would support the idea of convective invigoration. This relationship between increases in aerosols and the evolution of the convective clouds could not be confirmed by the model simulations in this study, as both models show suppressed rather than invigorated convective activity and precipitation for the polluted case in comparison to the clean case. The observed suppression of surface precipitation also disagrees with previous modelling studies over the study region that found an increase in precipitation (Fan et al., 2007; Khain et al., 2008; Li et al., 2008) over the range of aerosol conditions studied here, and related it to convective invigoration.

The microphysical evolution of the clouds studied here is strongly interlinked with the dynamical evolution of the clouds and convective updrafts due to the release of latent heating from the microphysical transformations and the impact of vertical motions on the microphysical processes. Future work will combine the results obtained here with a detailed analysis of the vertical momentum budget for the same set of individually tracked clouds. These combined analyses will allow us to relate the differences and responses in microphysical processes and surface precipitation to changes in updraft strength for individual clouds and the role that these interactions play in shaping the evolution of the entire cloud field. The microphysical process rate output from the two models includes more detailed process rates than used here, i.e. riming or freezing separated into the different hydrometeors and freezing modes. Extending the analysis, similar to the analyses presented in Chap. 3, could lead to additional insights, e.g. regarding important influences of changes in the riming processes on the vertical structure of the cloud response

to changes in aerosols as discussed in Chap. 3 and previous studies (Seifert and Beheng, 2006; Kalina et al., 2014).

The simulations with the WRF model have been performed using a variation of CDNC, similar to the approach in Chap. 3 instead of the full ACPC aerosol setup including lognormal aerosol modes and activation (van den Heever et al., 2017). These simulations will be repeated with a version of the microphysics scheme including activation and a prognostic cloud droplet number to allow for a consistent analysis with the other simulations in the ACPC intercomparison.

The convective activity and precipitation in the different cases simulated for the two models showed substantial differences in their timing, which has been explored further based on the eight simulations performed with different CDNC values in WRF. This particularly affects the 3-hour window of 1-minute high-frequency output that has been chosen for the analysis based on tracking. The 5-minute data available form the model simulations for a more extended period of 12 hours covers the entire life cycle of the daily convective activity in the modelling domain and could thus be used for more representative extension of the analyses presented here. This will have to include an assessment of the performance of the tracking and the composite analyses for the lower output frequency of 5 minutes.

We have only focused on the innermost domain with a grid spacing of 500 m in this study. Extending the assessment of representation of convection in the models to the two outer nests (4.5 km and 1.5 km grid spacing) will allow investigating how much of the difference between the modelled convection is affected by differences propagating into the inner domain from a different evolution at coarser resolution in the outer domains. This can be combined with the assessment of convective activity in the satellite retrievals based on the workflow presented in Chap. 4.

Additional comparisons to observational data from satellite and radar retrievals will help scrutinise the large differences between the different CRMs. The comparison between convective clouds in a subset of the model simulations discussed here and geostationary satellite observations presented in Chap. 4 could be extended to the entire range of mod-

els in the ACPC deep convection case. This will help to put the differences between the models in the context of observational constraints. The new generation of geostationary satellites (GOES-16 and GOES-17) that is now operational over the case study area (Schmit et al., 2016) allows for much more useful constraints on the model representation of scattered deep convection due to improved spatial and temporal resolution. The combination of these analyses with both radar observations such as the ones presented in Fridlind et al. (2019) and forward-simulated radar fields from the CRM simulations will provide additional observational constraints to the model representation of the convective clouds. These comparisons will be important in the preparation of the TRACER field campaign over the study area in the summer of 2021 (https://www.arm.gov/research/campaigns/amf2021trace, ARM, 2019). It will investigate convective clouds and convective initiation with extensive ground-based facilities such as research radars, radiosondes and aerosol measurements. This research campaign will provide detailed and focused observation of many convective cells, which will have to be complemented with targeted model data analyses such as the one presented here.

6. Conclusions and outlook

The importance of aerosol–cloud interactions for the climate system has been investigated for decades (Twomey, 1977b; Albrecht, 1989) and is still one of the primary sources of uncertainty in our ability to quantify and project the anthropogenic influence on the current and future climate (IPCC, 2013a). The impact of changes in aerosols on deep convective clouds and the role of these interactions in the climate system remain particularly uncertain. This includes both impacts on the radiative forcing and potential influences of aerosols on the hydrological cycle at a variety of scales (Tao et al., 2012; Boucher et al., 2013). The large uncertainties can be attributed to the complexity of the physical processes involved and limitations in their assessment based on both observations and numerical model simulations (Boucher et al., 2013; Rosenfeld et al., 2014a; Fan et al., 2016). Different conceptual ideas for possible aerosol effects on convective clouds have been proposed (Rosenfeld et al., 2008; Stevens and Feingold, 2009) over recent decades, and assessments based on both modelling studies and observations have revealed a wide range of different, and often contrasting, responses of deep convective clouds to changes in aerosol conditions (Tao et al., 2012; Altaratz et al., 2014; Fan et al., 2016).

The work presented in this thesis was conducted to improve our understanding of aerosol–convection interactions through a detailed focus on the microphysical pathways involved in the cloud response and the temporal evolution of the cloud microphysics. A hierarchy of different cloud-resolving model (CRM) simulations and novel analysis techniques were combined to investigate both individual aspects in the chain of microphysical processes and their complex interaction with other aspects of the clouds and the surrounding atmosphere.

In Chap. 3, idealised model simulations of supercell thunderstorms were analysed to investigate the propagation of changes in cloud droplet number (CDNC) through the microphysical evolution of individual convective cells. Model simulations with the Weather and Forecasting model (WRF) were performed with two bulk microphysics schemes, the Morrison scheme (Morrison et al., 2005; Morrison and Grabowski, 2008) and the Thompson scheme (Thompson et al., 2004; 2008), as well as with the Hebrew University Cloud Model spectral-bin microphysics scheme (HUCM SBM) (Lynn et al., 2005a; b). WRF was extended by detailed output of all individual microphysical process rates calculated within the different microphysics schemes to allow for an assessment of the pathways and their representation in the model microphysics schemes. Furthermore, a method for identifying and tracking individual convective updrafts in the simulation was developed. It enables analyses at the spatial and temporal scale of individual clouds that explicitly resolve the time evolution of the individual microphysical processes and associated bulk cloud properties. These analyses showed some similar microphysical changes with increased CDNC for the two bulk microphysics schemes in two simulated cases. The increase in CDNC leads to a substantial decrease in warm rain formation and a shift of latent heat release from freezing and riming processes to higher altitudes. This could be related to a transition from processes involving raindrops to processes involving cloud droplets and a dominant role of riming processes in the response. Changes in the dominant ice-phase hydrometeors for the variation of the aerosol proxy were observed in all three microphysics schemes, as graupel and hail are replaced by snow and cloud ice particles for more polluted conditions. Differences in the definition of the hydrometeor classes and the associated processes for individual hydrometeor types, such as the different treatment of deposition on graupel, can explain part of the discrepancies in the response between the microphysics schemes. It was shown that this chain of processes includes important feedbacks from the ice-phase processes back onto the liquid phase of the cloud, for example in the form of impacts of changes in sublimation and deposition on condensation or evaporation as a manifestation of the Wegener–Bergeron–Findeisen process. The re-

sponse of the bulk cloud properties such as cloud mass or the altitude of the centre of gravity of the cloud shows marked differences between the microphysics schemes in the two cases. Despite the differences in the response of the bulk cloud properties to changes in the aerosol proxies, the simulations with all three microphysics schemes and for both cases each showed a monotonic response to changes in CDNC and cloud condensation nuclei (CCN) concentration. Furthermore, the effects of changes in the aerosol proxies reach saturation for CDNC/CCN values above $1000\,\mathrm{cm}^{-3}$ in all simulations, which confirms previous studies (Kalina et al., 2014).

To make this type of analysis available for a more general application, the tracking algorithm developed for the analysis of the idealised cases in Chap. 3 was evolved into the tracking and analysis framework tobac presented in Chap. 4. tobac was designed with an accessible structure and offers flexibility to be used with a wide range of different types of input data, thus overcoming limitations of most existing tracking software. The package is set up in a modular way with individual steps for feature detection, segmentation to determine cloud areas/volumes, trajectory linking and a range of analysis methods. This enables the extension of tobac by other algorithms and workflows in a single framework. The package makes use of modern capabilities of Python libraries for data reading, memory usage and specific calculations. Furthermore, an existing Python library initially developed for microscopic analysis in biophysical applications, trackpy (Allan et al., 2018), was successfully adapted for linking the identified cloud features. Two example applications of the framework for studying deep convective clouds based on different data types were presented. This included the assessment of the required time resolution for a successful tracking result. In the first application, isolated deep convective cells were tracked in CRM simulations based on the vertical velocity and condensate mixing ratio field. It was shown that input data with a 5-minute time resolution is sufficient for the tracking of deep convective clouds in this type of simulations, while 1-minute data output is beneficial for a more robust tracking result. In the second application, deep convective clouds were tracked based on the outgoing longwave radiation (OLR) field both

from convection-permitting model simulations and derived from geostationary satellite retrievals (GOES-13). For this application, the temporal resolution of 15 minutes available from the GOES-13 satellite retrievals was shown to be sufficient for a successful tracking, while a coarser time resolution would be detrimental to the tracking performance.

In Chap. 5, the pathway analysis developed in Chap. 3 and the tracking framework tobac established in Chap. 4 were combined to provide a detailed analysis of microphysical effects for individually tracked clouds in simulations of a large freely evolving population of convective clouds. The CRM simulations with the WRF and RAMS (Regional Atmospheric Modelling System, Saleeby and van den Heever, 2013) used for this analysis are part of a model intercomparison that was performed with several current CRMs in the deep convection case study of the Aerosols, Clouds, Precipitation and Climate (ACPC) initiative (van den Heever et al., 2017). The case study was performed for scattered deep convection over the area around Houston, Texas, for two cases representing clean and polluted aerosol conditions. The study aims to understand the differences in the response of the models to aerosol perturbations and the contribution of individual physical processes to these uncertainties. Preliminary analyses of all models in the intercomparison study have shown large discrepancies both in the simulated deep convection and the response of clouds and precipitation to changes in aerosols. WRF and RAMS were used to further investigate these differences in using both traditional domain-wide analyses and the newly developed Lagrangian analysis framework. The two models show a large difference in the total accumulated surface precipitation over the entire simulation period and marked differences in the domain-averaged properties, especially concerning the evolution of the ice phase. The RAMS simulations show substantially more frozen hydrometeors and mixed- and ice-phase processes than in WRF for both aerosol conditions. However, the two models show a consistent response to increases in aerosols, with both models showing a decrease of warm rain formation and suppression of surface precipitation with increased aerosols. The tracked clouds were separated into different categories for a more detailed

assessment based on composites of their time evolution. This revealed important differences in the distribution of cloud types between the models, e.g. more shallow convective cells with only liquid-phase microphysics in WRF and more cells transitioning into deep convections in RAMS. However, there was no clear effect of changes in aerosol conditions on these cloud categories. The detailed analyses of the cloud composites for specific cloud types showed that the two models agree well in how they simulate shallow convective clouds. The analysis of the composites for the clouds that are tracked through the transition from warm-phase dominated to deep convective clouds shows much more substantial differences between the two models. This includes much stronger mixed-phase processes like freezing, riming and melting in RAMS than in WRF. Further analyses confirmed that the cold rain formation from melting frozen hydrometeors after the onset of mixed-phase processes contributes substantially to the warm rain formation. The resulting efficient accretion of cloud droplets partially buffers the response of the precipitation formation to changes in aerosols and CDNC. This agrees with the results obtained from the analyses of the idealised simulations in Chap. 3.

The analyses developed in this thesis enabled a detailed investigation of the microphysical processes and pathways of the effects of aerosol changes in numerical models simulations of deep convective clouds. The results from both the idealised simulations (Chap.3) and the analysis of the case study simulation (Chap. 5) confirmed the substantial uncertainties resulting from differences in the representation of the physical processes in numerical models that have been discussed in previous studies (Khain et al., 2008; Tao et al., 2012; Khain et al., 2015; White et al., 2017). The differences between the individual models or model configurations with different microphysics schemes were often larger than the cloud response to changes in aerosols or aerosol proxies. This shows that the differences in the CRMs result from a combination of differences in the microphysics schemes themselves and the coupling of the microphysical evolution to the representation of other physical processes in the models. The detailed analysis of process rates and the focus on individually tracked cells, however, allowed for a more detailed insight into the mi-

crophysical pathways in the clouds. This enabled an investigation of the responses of individual processes to changes in aerosols or aerosol proxies in the model, where usual analysis methods would often break down due to cancellations between the responses or the dominance of other impacts in a bulk analysis. The different types of simulations in this thesis do not show clear signs of convective invigoration due to additional latent heat release from increased freezing as hypothesised, e.g. by Rosenfeld et al. (2008). This includes the idealised supercell simulations studied in Chap. 3 that revealed clear changes to the freezing processes with shifts in the altitude but no substantial increase in integrated latent heating. Furthermore, a suppression of convective activity and surface precipitation was observed as the primary response to an increase in aerosols for the large cloud field simulations in Chap. 5. This result might be related to the specific types of deep convective clouds studied here, as the range of responses to aerosols previously reported is strongly dependent on the specific types of clouds and the conditions under which they evolve (Khain et al., 2008; Kalina et al., 2014). However, the results show that convective invigoration due to additional freezing cannot be assumed to be the default response of deep convective clouds to an increased CCN concentration, even when changes in the freezing processes occur. Previous investigations on the effects of aerosols on deep convection mainly relied on domain-wide statistical analyses of cloud properties (Tao et al., 2012; Altaratz et al., 2014). These analyses are inherently not able to resolve the important time evolution of individual clouds over their lifecycle (Altaratz et al., 2014). Here, we use tobac to extend the detailed pathway analysis to individual clouds in entire large case study simulations based on tobac as a flexible analysis tool for the tracking of individual clouds. The creation of cloud composites with a relative time axis for specific types of tracked clouds enabled a novel way of resolving the time evolution of the microphysical evolution for the clouds in a large cloud field simulation. The separation of the cloud field into different types of clouds revealed differences between cloud types in simulations with the two different models, which partially explains the differences observed between simulations with different CRMs. Additionally, this time-resolved perspective

revealed important microphysical pathways, such as the critical role of melting processes in mediating and buffering the response of warm rain formation to changes in aerosols.

The results from the analyses in this thesis give rise to new research questions, both with regards to the type of analyses developed here and for the general research on convective clouds and aerosol–cloud interactions. There are several aspects of the analyses performed in the individual chapters that could be extended further to provide a more detailed insight into individual aspects of the chain of processes or address a broader range of research questions. The analyses of the time evolution of precipitation and the analysis of microphysical process rates in Chap. 5 have shown that the 3-hour period chosen for the tracking-based analysis is affected by differences in the timing of the convective activity, e.g. in the form of shifts in the convective evolution at the time scale of a few hours. Extending the tracking-based analysis to the 12-hour period with 5-minute data output will allow to include a full diurnal cycle of convective activity and provide a larger number of tracked cells for improved statistics. To asses the response of deep convection to changes in aerosols with a more representative coverage of different meteorological conditions, additional cases could be simulated for case study simulations for ACPC case study setup. It is planned to extend the detailed analysis developed for WRF and RAMS in Chap. 5 to the other models in the ACPC intercomparison project based on the high-frequency output and detailed microphysical diagnostics.

The analyses presented in Chap.5 will be important for the field campaign TRACER 2021 as the focused observations of individual deep convective clouds require detailed counterparts on the side of the modelling community. The extended analysis of the ACPC case will include extensive comparisons of radar measurements with model forward-simulated radar properties in the CRMs, e.g. following the methods developed in (Fridlind et al., 2019). The use of dual-polar radar measurements makes it possible to obtain a range of detailed microphysical insights on the microphysical evolution of the convective clouds (Fridlind et al., 2012; van Lier-Walqui et al., 2016). These analyses can be combined with the detailed analysis of the model microphysical process rates presented in this thesis to

allow for increased observational constraints in the assessment of the variation of the simulated convective clouds and their aerosol response in different models.

The tracking framework tobac presented in Chap. 4 is currently evolving into continuous development as a community project (https://github.com/climate-processes/tobac). Scientists in research groups currently involved in the development of the package (University of Oxford, TROPOS Leipzig, Colorado State University) have started to use tobac for other analyses, including studies on the vertical momentum budget to accompany the microphysical process rate analysis presented in Chap. 5 or investigations of shallow trade wind cumulus clouds. Several contributors are currently working on adding new tracking and analysis routines, which involves the development of new detailed analyses based on geostationary satellite retrieval that go beyond the use of OLR as presented in Chap. 4 and the implementation of existing analyses from previous studies like Senf et al. (2018). This will enable a convenient comparison between different approaches and for different datasets within a single framework. This could be used to derive more robust observational constraints for studies based on high-resolution models simulations such as the ones presented in this thesis.The newest generation of geostationary satellites (Himawari-8, GOES-16/17 and the future Meteosat 3G (Stuhlmann et al., 2005; Bessho et al., 2016; Schmit et al., 2016)) with routinely recorded high time resolution of at least 5 minutes offers the opportunity to perform more detailed analyses based on satellite data.

Current work on the implementation of lightweight prognostic aerosols with advection, activation and removal in the WRF simulations based on a simplified version of the HAM aerosol model (Stier et al., 2005) will enable the extension of the analysis of aerosol microphysical effects on clouds by allowing for more complex interactions between the clouds and the aerosol distribution. A fully interactive coupling between aerosols and clouds in models allows the use of the analytical framework developed here to investigate several interesting questions for our understanding of aerosol–cloud interactions. The concurrent impact of aerosols on convective clouds through aerosol microphysical effects and semi-direct effects via the radiative impact of aerosols in the atmosphere has been in-

vestigated intensively based on different approaches (Koren et al., 2008; Rosenfeld et al., 2008), but also poses significant challenges for the attribution of aerosol effects on convective clouds. Detailed analyses focusing on the microphysical evolution of individual convective clouds and the radiative processes in the surrounding air masses based on the methods presented in this thesis could improve our understanding of the role of these interacting pathways in aerosol–convection interactions.

Furthermore, the tracking-based analysis developed in this thesis is suited for an assessment of the time scales of cloud effects on the aerosol field due to removal processes such as activation and precipitation scavenging, e.g. by assessing aerosol concentrations around individual clouds or composites of clouds over the cloud life cycle.

In addition to the effects of aerosols acting as CCN discussed in this thesis, aerosol can have an impact on deep convective clouds due to their role as ice nucleating particles (IN) (Lohmann, 2006; Fan et al., 2016). Although the effect of changes in IN on the evolution of deep convection has not been assessed in this thesis, the analysis framework developed here could be used investigate IN-based pathways of aerosol effects on deep convection, too.

Box closure experiments (Rosenfeld et al., 2014a) such as the one planned as part of the ACPC case study over Houston (van den Heever et al., 2017) can be used to extend the understanding gained through detailed analyses of the physical processes in high-resolution modelling studies the scale relevant for the effects of aerosols on deep convection in the global climate system. The detailed understanding of the propagation of the aerosol effects through the microphysics of deep convective clouds can be useful for the ongoing work on representing convective cloud microphysics and aerosol effects on convective clouds in global climate models (Zhang and Song, 2016). Furthermore, global model simulations at grid spacings approaching those of the CRMs used in this study are going to become more common over the coming decade (Neumann et al., 2019), which can specifically profit from analysis methods as the ones developed here. Therefore, detailed process studies as presented in this thesis are crucial to advance our understanding of the

role of specific types of aerosol–cloud interactions in anthropogenic radiative forcing and thus contribute to an improved understanding of the current and future evolution of the climate.

7. Appendix

7.1. Analysis software developed as part of the thesis

The analyses in this thesis involved the development of a wide range of analysis software. The data processing is based on Iris cubes (Met Office, 2018) as the underlying data structure, which allows for a convenient way of writing flexible analysis methods that are not strictly fixed to the detailed structure of the specific model output. This was particularly important to allow for a consistent analysis of the results of simulations with different models and microphysics schemes.

Several aspects of the analyses developed for the different studies in this thesis are distributed as individual Python modules to allow for continued use of the analysis methods. The source code for all these analysis packages is publicly available on GitHub.

tobac

The tracking and analysis framework tobac is described in detail in Chap. 4. The module is hosted on GitHub at https://github.com/climate-processes/tobac.

mpdiag

Comparing detailed microphysical output from different models or microphysics schemes requires to load them into a consistent data structure that allows for meaningful comparisons between equivalent processes or quantities in the different schemes. The module currently includes routines for the different microphysics schemes used in this thesis, which includes the Morrison and Thompson bulk microphysics schemes (Morrison et al., 2005; Thompson et al., 2008) as well as the full and fast SBM scheme (Lynn et al., 2005a; Khain et al., 2009) in WRF and the microphysics scheme of the RAMS model

(Saleeby and van den Heever, 2013). It is planned to extend the analysis to the microphysics schemes in additional models to make the basic analyses presented in this thesis conveniently available for additional cloud-resolving models.
The module is hosted on GitHub at https://github.com/mheikenfeld/mpdiag.

mpanalysis

This package provides the analysis routines creating the detailed visualisations of the cloud microphysics used in Chap. 3 and Chap. 5. This includes both slices through individual clouds showing the cloud morphology, the time evolution of hydrometeor mass and microphysical process rates as well as the creation and visualisation of the cloud composites. The data structure is based on the mpdiag and tobac modules. Thus, these analyses are available for any model or microphysics scheme that has been implemented in mpdiag.
The module is hosted on GitHub at https://github.com/mheikenfeld/mpanalysis.

piecharts

The visualisation of hydrometeor mixing ratios and microphysical process rates with coloured pie chart diagrams in the analyses in this thesis allowed for a novel way of presenting a two-dimensionally resolved picture of the complete microphysical evolution of clouds. The creation of these diagrams from arbitrary input data has been packaged as a Python module and is available on GitHub at https://github.com/mheikenfeld/piecharts.

wrfcube

Although the WRF model outputs its data in NetCDF format, the output can be problematic to read with most software that has not been developed with a direct focus on WRF at the Centre for NCAR. This includes definitions of dimensions and variables that do not conform to the CF standards and a range of variables that are stored as a combination of a base field and a variation, e.g. potential air temperature or air pressure. The wrfcube module provides a convenient way to load WRF output into Iris cubes

with meaningful metadata. Furthermore, the module contains routines to calculate a wide range of properties based on the model output. The module is available on GitHub at https://github.com/mheikenfeld/wrfcube.

ramscube

This module provides a convenient way of loading the RAMS-specific HDF5 files into consistent Iris cubes including metadata based on the header files provided with the model output. Furthermore, the package contains various routines to calculate a wide range of properties based on the model output. This includes integrated properties such as the liquid and ice water paths. The module is available on GitHub at https://github.com/mheikenfeld/ramscube.

8. References

Abdul-Razzak, H. and Ghan, S. J. (2000). "A Parameterization of Aerosol Activation: 2. Multiple Aerosol Types". In: *Journal of Geophysical Research: Atmospheres* 105.D5, pp. 6837–6844. DOI: 10.1029/1999JD901161.

Abdul-Razzak, H., Ghan, S. J. and Rivera-Carpio, C. (1998). "A Parameterization of Aerosol Activation: 1. Single Aerosol Type". In: *Journal of Geophysical Research: Atmospheres* 103.D6, pp. 6123–6131. DOI: 10.1029/97JD03735.

Ackerman, A. S., Toon, O. B., Stevens, D. E., Heymsfield, A. J., Ramanathan, V. and Welton, E. J. (2000). "Reduction of Tropical Cloudiness by Soot". In: *Science* 288.5468, pp. 1042–1047. DOI: 10.1126/science.288.5468.1042.

Albrecht, B. A. (1989). "Aerosols, Cloud Microphysics, and Fractional Cloudiness". In: *Science* 245.4923, pp. 1227–1230. DOI: 10.1126/science.245.4923.1227.

Allan, D. B., Caswell, T., Keim, N. C. and van der Wel, C. M. (2018). *Trackpy: Trackpy v0.4*. Zenodo. DOI: 10.5281/zenodo.1213241. (Visited on 24/02/2019).

Allan, D., Caswell, T., Keim, N. and van der Wel, C. (2016). *Trackpy: Trackpy v0.3.2*. Zenodo. DOI: 10.5281/zenodo.60550. (Visited on 31/12/2018).

Altaratz, O., Bar-Or, R. Z., Wollner, U. and Koren, I. (2013). "Relative Humidity and Its Effect on Aerosol Optical Depth in the Vicinity of Convective Clouds". In: *Environmental Research Letters* 8.3, p. 034025. DOI: 10.1088/1748-9326/8/3/034025.

Altaratz, O., Koren, I., Remer, L. A. and Hirsch, E. (2014). "Review: Cloud Invigoration by Aerosols - Coupling between Microphysics and Dynamics". In: *Atmospheric Research* 140–141, pp. 38–60. DOI: 10.1016/j.atmosres.2014.01.009.

Anderson, T. L., Charlson, R. J., Winker, D. M., Ogren, J. A. and Holmén, K. (2003). "Mesoscale Variations of Tropospheric Aerosols". In: *Journal of the Atmospheric Sciences* 60.1, pp. 119–136. DOI: 10.1175/1520-0469(2003)060⟨0119:MVOTA⟩2.0.CO;2.

Andreae, M. O. and Rosenfeld, D. (2008). "Aerosol–Cloud–Precipitation Interactions. Part 1. The Nature and Sources of Cloud-Active Aerosols". In: *Earth-Science Reviews* 89.1–2, pp. 13–41. DOI: 10.1016/j.earscirev.2008.03.001.

Andreae, M. O., Rosenfeld, D., Artaxo, P., Costa, A. A., Frank, G. P., Longo, K. M. and Silva-Dias, M. a. F. (2004). "Smoking Rain Clouds over the Amazon". In: *Science* 303.5662, pp. 1337–1342. DOI: 10.1126/science.1092779.

Andreae, M. O. (2007). "Aerosols Before Pollution". In: *Science* 315.5808, pp. 50–51. DOI: 10.1126/science.1136529.

Andrews, D. G. (2010). *An Introduction to Atmospheric Physics*. Cambridge University Press. 249 pp.

Arakawa, A. (2004). "The Cumulus Parameterization Problem: Past, Present, and Future". In: *Journal of Climate* 17.13, pp. 2493–2525. DOI: 10.1175/1520-0442(2004)017⟨2493:RATCPP⟩2.0.CO;2.

ARM (2019). *Tracer Field Campaign 2021*. URL: https://www.arm.gov/research/campaigns/amf2021tracer (visited on 29/03/2019).

Autonès, F. and Moisselin, J. M. (2013). *Algorithm Theoretical Basis Document for "Rapid Development Thunderstorms" (RDT-PGE11 v3.0)*. SAF/NWC/CDOP/MFT/SCI/ATBD/11. URL: http://www.%20nwcsaf.%20org/AemetWebContents/ScientificDocumentation/Documentation/MSG/SAF-NWC-CDOP2-MFT-SCI-VR-11_%20v3.%200.%20pdf.

Ban, N., Schmidli, J. and Schär, C. (2014). "Evaluation of the Convection-Resolving Regional Climate Modeling Approach in Decade-Long Simulations". In: *Journal of Geophysical Research: Atmospheres* 119.13, pp. 7889–7907. DOI: 10.1002/2014JD021478.

Beheng, K. D. (1994). "A Parameterization of Warm Cloud Microphysical Conversion Processes". In: *Atmospheric Research*. 11th International Conference on Clouds and Precipitation, Part II 33.1–4, pp. 193–206. DOI: 10.1016/0169-8095(94)90020-5.

– (2012). "From Size Distributions to Bulk Microphysical Parameterizations". In: COST Workshop, COST-ES0905 - WG4 Meeting Jerusalem, 12–16 Nov.

Berry, E. X. and Reinhardt, R. L. (1974a). "An Analysis of Cloud Drop Growth by Collection Part II. Single Initial Distributions". In: *Journal of the Atmospheric Sciences* 31.7, pp. 1825–1831. DOI: 10.1175/1520-0469(1974)031⟨1825:AAOCDG⟩2.0.CO;2.

– (1974b). "An Analysis of Cloud Drop Growth by Collection: Part I. Double Distributions". In: *Journal of the Atmospheric Sciences* 31.7, pp. 1814–1824. DOI: 10.1175/1520-0469(1974)031⟨1814:AAOCDG⟩2.0.CO;2.

– (1974c). "An Analysis of Cloud Drop Growth by Collection: Part III. Accretion and Self-Collection". In: *Journal of the Atmospheric Sciences* 31.8, pp. 2118–2126. DOI: 10.1175/1520-0469(1974)031⟨2118:AAOCDG⟩2.0.CO;2.

Bessho, K., Date, K., Hayashi, M., Ikeda, A., Imai, T. et al. (2016). "An Introduction to Himawari-8/9— Japan's New-Generation Geostationary Meteorological Satellites". In: *Journal of the Meteorological Society of Japan. Ser. II* 94.2, pp. 151–183. DOI: 10.2151/jmsj.2016-009.

Betts, A. K. (1997). "The Parameterization of Deep Convection". In: *The Physics and Parameterization of Moist Atmospheric Convection*. Ed. by R. K. Smith. NATO ASI Series 505. Springer Netherlands, pp. 255–279. DOI: 10.1007/978-94-015-8828-7_10. (Visited on 28/03/2016).

Bigg, E. K. (1953). "The Supercooling of Water". In: *Proceedings of the Physical Society. Section B* 66.8, p. 688. DOI: 10.1088/0370-1301/66/8/309.

Bond, T. C., Doherty, S. J., Fahey, D. W., Forster, P. M., Berntsen, T. et al. (2013). "Bounding the Role of Black Carbon in the Climate System: A Scientific Assessment". In: *Journal of Geophysical Research: Atmospheres* 118.11, pp. 5380–5552. DOI: 10.1002/jgrd.50171.

Bony, S., Colman, R., Kattsov, V. M., Allan, R. P., Bretherton, C. S. et al. (2006). "How Well Do We Understand and Evaluate Climate Change Feedback Processes?" In: *Journal of Climate* 19.15, pp. 3445–3482. DOI: 10.1175/JCLI3819.1.

Bony, S., Stevens, B., Frierson, D. M. W., Jakob, C., Kageyama, M. et al. (2015). "Clouds, Circulation and Climate Sensitivity". In: *Nature Geoscience* 8.4, pp. 261–268. DOI: 10.1038/ngeo2398.

Boucher, O., Randall, D., Artaxo, P., Bretherton, C., Feingold, G. et al. (2013). "Clouds and Aerosols". In: *Climate Change 2013: The Physical Science Basis. Contribution of Working Group I to the Fifth Assessment Report of the Intergovernmental Panel on Climate Change*. Ed. by T. Stocker, D. Qin, G.-K. Plattner, M. Tignor, S. Allen, J. Boschung, A. Nauels, Y. Xia, V. Bex and P. Midgley. Cambridge, United Kingdom and New York, NY, USA: Cambridge University Press, pp. 571–658. DOI: 0.1017/CBO9781107415324.016.

Boucher, O. and Quaas, J. (2013). "Water Vapour Affects Both Rain and Aerosol Optical Depth". In: *Nature Geoscience* 6.1, pp. 4–5. DOI: 10.1038/ngeo1692.

Bouwman, A. F., Lee, D. S., Asman, W. a. H., Dentener, F. J., Hoek, K. W. V. D. and Olivier, J. G. J. (1997). "A Global High-Resolution Emission Inventory for Ammonia". In: *Global Biogeochemical Cycles* 11.4, pp. 561–587. DOI: 10.1029/97GB02266.

Bryan, G. H., Wyngaard, J. C. and Fritsch, J. M. (2003). "Resolution Requirements for the Simulation of Deep Moist Convection". In: *Monthly Weather Review* 131.10, pp. 2394–2416. DOI: 10.1175/1520-0493(2003)131⟨2394:RRFTSO⟩2.0.CO;2.

Byers, H. R. and Braham, R. R. (1948). "Thunderstorm Structure and Circulation". In: *Journal of Meteorology* 5.3, pp. 71–86. DOI: 10.1175/1520-0469(1948)005⟨0071:TSAC⟩2.0.CO;2.

Cao, Y., Tan, W. and Wu, Z. (2018). "Aircraft Icing: An Ongoing Threat to Aviation Safety". In: *Aerospace Science and Technology* 75, pp. 353–385. DOI: 10.1016/j.ast.2017.12.028.

Carrió, G. G. and Cotton, W. R. (2011). "Urban Growth and Aerosol Effects on Convection over Houston. Part II: Dependence of Aerosol Effects on Instability". In: *Atmospheric Research* 102.1, pp. 167–174. DOI: 10.1016/j.atmosres.2011.06.022.

Carrió, G. G., Cotton, W. R. and Cheng, W. Y. Y. (2010). "Urban Growth and Aerosol Effects on Convection over Houston: Part I: The August 2000 Case". In: *Atmospheric Research* 96.4, pp. 560–574. DOI: 10.1016/j.atmosres.2010.01.005.

Carslaw, K. S., Lee, L. A., Reddington, C. L., Pringle, K. J., Rap, A. et al. (2013). "Large Contribution of Natural Aerosols to Uncertainty in Indirect Forcing". In: *Nature* 503.7474, pp. 67–71. DOI: 10.1038/nature12674.

Cecil, D. J., Buechler, D. E. and Blakeslee, R. J. (2015). "TRMM LIS Climatology of Thunderstorm Occurrence and Conditional Lightning Flash Rates". In: *Journal of Climate* 28.16, pp. 6536–6547. DOI: 10.1175/JCLI-D-15-0124.1.

Chang, D., Cheng, Y., Reutter, P., Trentmann, J., Burrows, S. M., Spichtinger, P., Nordmann, S., Andreae, M. O., Pöschl, U. and Su, H. (2015). "Comprehensive Mapping and Characteristic Regimes of Aerosol Effects on the Formation and Evolution of Pyro-

Convective Clouds". In: *Atmos. Chem. Phys.* 15.18, pp. 10325–10348. DOI: 10.5194/acp-15-10325-2015.

Charlson, R. J., Schwartz, S. E., Hales, J. M., Cess, R. D., Coakley, J. A., Hansen, J. E. and Hofmann, D. J. (1992). "Climate Forcing by Anthropogenic Aerosols". In: *Science* 255.5043, pp. 423–430. DOI: 10.1126/science.255.5043.423.

Chen, F. and Dudhia, J. (2001). "Coupling an Advanced Land Surface–Hydrology Model with the Penn State–NCAR MM5 Modeling System. Part I: Model Implementation and Sensitivity". In: *Monthly Weather Review* 129.4, pp. 569–585. DOI: 10.1175/1520-0493(2001)129⟨0569:CAALSH⟩2.0.CO;2.

Chen, Q., Koren, I., Altaratz, O., Heiblum, R. H., Dagan, G. and Pinto, L. (2017). "How Do Changes in Warm-Phase Microphysics Affect Deep Convective Clouds?" In: *Atmos. Chem. Phys.* 17.15, pp. 9585–9598. DOI: 10.5194/acp-17-9585-2017.

Choularton, T. W., Latham, J. and Mason, B. J. (1978). "A Possible Mechanism of Ice Splinter Production during Riming". In: *Nature* 274.5673, p. 791. DOI: 10.1038/274791a0.

Collins, M., Knutti, R., Arblaster, J., Dufresne, J.-L., Fichefet, T. et al. (2013). "Long-Term Climate Change: Projections, Commitments and Irreversibility". In: *Climate Change 2013: The Physical Science Basis. Contribution of Working Group I to the Fifth Assessment Report of the Intergovernmental Panel on Climate Change*. Ed. by T. Stocker, D. Qin, G.-K. Plattner, M. Tignor, S. Allen, J. Boschung, A. Nauels, Y. Xia, V. Bex and P. Midgley. Cambridge, United Kingdom and New York, NY, USA: Cambridge University Press. Chap. 12, pp. 1029–1136. DOI: 10.1017/CBO9781107415324.024.

Cooper, W. A. (1986). "Ice Initiation in Natural Clouds". In: *Precipitation Enhancement—A Scientific Challenge*. Meteorological Monographs. American Meteorological Society, Boston, MA, pp. 29–32. DOI: 10.1007/978-1-935704-17-1_4. (Visited on 01/05/2018).

Cotton, W. R., Bryan, G. and Heever, S. C. van den (2010). *Storm and Cloud Dynamics*. Academic Press. 826 pp.

Couvreux, F., Hourdin, F. and Rio, C. (2010). "Resolved Versus Parametrized Boundary-Layer Plumes. Part I: A Parametrization-Oriented Conditional Sampling in Large-Eddy Simulations". In: *Boundary-Layer Meteorology* 134.3, pp. 441–458. DOI: 10.1007/s10546-009-9456-5.

Crane, R. (1979). "Automatic Cell Detection and Tracking". In: *IEEE Transactions on Geoscience Electronics* 17.4, pp. 250–262. DOI: 10.1109/TGE.1979.294654.

Crocker, J. C. and Grier, D. G. (1996). "Methods of Digital Video Microscopy for Colloidal Studies". In: *Journal of Colloid and Interface Science* 179.1, pp. 298–310. DOI: 10.1006/jcis.1996.0217.

Cui, Z. and Carslaw, K. S. (2006). "Enhanced Vertical Transport Efficiency of Aerosol in Convective Clouds Due to Increases in Tropospheric Aerosol Abundance". In: *Journal of Geophysical Research: Atmospheres* 111.D15, p. D15212. DOI: 10.1029/2005JD006781.

Dagan, G., Koren, I. and Altaratz, O. (2018). "Quantifying the Effect of Aerosol on Vertical Velocity and Effective Terminal Velocity in Warm Convective Clouds". In: *Atmos. Chem. Phys.* 18.9, pp. 6761–6769. DOI: 10.5194/acp-18-6761-2018.

Dagan, G., Koren, I., Altaratz, O. and Heiblum, R. H. (2017). "Time-Dependent, Non-Monotonic Response of Warm Convective Cloud Fields to Changes in Aerosol Loading". In: *Atmos. Chem. Phys.* 17.12, pp. 7435–7444. DOI: 10.5194/acp-17-7435-2017.

Dagan, G., Koren, I. and Altaratz, O. (2015). "Aerosol Effects on the Timing of Warm Rain Processes". In: *Geophysical Research Letters* 42.11, pp. 4590–4598. DOI: 10.1002/2015GL063839.

Dask Development Team (2016). *Dask: Library for Dynamic Task Scheduling*. URL: http://dask.pydata.org.

Dauhut, T., Chaboureau, J.-P., Haynes, P. H. and Lane, T. P. (2018). "The Mechanisms Leading to a Stratospheric Hydration by Overshooting Convection". In: *Journal of the Atmospheric Sciences* 75.12, pp. 4383–4398. DOI: 10.1175/JAS-D-18-0176.1.

Davis, C. A., Brown, B. G., Bullock, R. and Halley-Gotway, J. (2009). "The Method for Object-Based Diagnostic Evaluation (MODE) Applied to Numerical Forecasts from the 2005 NSSL/SPC Spring Program". In: *Weather and Forecasting* 24.5, pp. 1252–1267. DOI: 10.1175/2009WAF2222241.1.

Davis, C., Brown, B. and Bullock, R. (2006). "Object-Based Verification of Precipitation Forecasts. Part II: Application to Convective Rain Systems". In: *Monthly Weather Review* 134.7, pp. 1785–1795. DOI: 10.1175/MWR3146.1.

Dawe, J. T. and Austin, P. H. (2012). "Statistical Analysis of an LES Shallow Cumulus Cloud Ensemble Using a Cloud Tracking Algorithm". In: *Atmos. Chem. Phys.* 12.2, pp. 1101–1119. DOI: 10.5194/acp-12-1101-2012.

Dawson, D. T., Mansell, E. R., Jung, Y., Wicker, L. J., Kumjian, M. R. and Xue, M. (2013). "Low-Level ZDR Signatures in Supercell Forward Flanks: The Role of Size Sorting and Melting of Hail". In: *Journal of the Atmospheric Sciences* 71.1, pp. 276–299. DOI: 10.1175/JAS-D-13-0118.1.

DeMott, P. J., Prenni, A. J., Liu, X., Kreidenweis, S. M., Petters, M. D., Twohy, C. H., Richardson, M. S., Eidhammer, T. and Rogers, D. C. (2010). "Predicting Global Atmospheric Ice Nuclei Distributions and Their Impacts on Climate". In: *Proceedings of the National Academy of Sciences* 107.25, pp. 11217–11222. DOI: 10.1073/pnas.0910818107.

Dixon, M. and Wiener, G. (1993). "TITAN: Thunderstorm Identification, Tracking, Analysis, and Nowcasting—A Radar-Based Methodology". In: *Journal of Atmospheric and Oceanic Technology* 10.6, pp. 785–797. DOI: 10.1175/1520-0426(1993)010⟨0785:TTITAA⟩2.0.CO;2.

Doswell, C. A. (2001). "Severe Convective Storms—An Overview". In: *Severe Convective Storms*. Ed. by C. A. Doswell. Meteorological Monographs. Boston, MA: American Meteorological Society, pp. 1–26. DOI: 10.1007/978-1-935704-06-5_1. (Visited on 08/04/2019).

Dowling, D. R. and Radke, L. F. (1990). "A Summary of the Physical Properties of Cirrus Clouds". In: *Journal of Applied Meteorology* 29.9, pp. 970–978. DOI: 10.1175/1520-0450(1990)029⟨0970:ASOTPP⟩2.0.CO;2.

Ekman, A. M. L., Engström, A. and Wang, C. (2007). "The Effect of Aerosol Composition and Concentration on the Development and Anvil Properties of a Continental Deep Convective Cloud". In: *Quarterly Journal of the Royal Meteorological Society* 133.627, pp. 1439–1452. DOI: 10.1002/qj.108.

Ekman, A. M. L., Engström, A. and Söderberg, A. (2011). "Impact of Two-Way Aerosol–Cloud Interaction and Changes in Aerosol Size Distribution on Simulated Aerosol-Induced Deep Convective Cloud Sensitivity". In: *Journal of the Atmospheric Sciences* 68.4, pp. 685–698. DOI: 10.1175/2010JAS3651.1.

Emanuel, K. A. (1994). *Atmospheric Convection*. New York: Oxford University Press. 598 pp.

Engström, A. and Ekman, A. M. L. (2010). "Impact of Meteorological Factors on the Correlation between Aerosol Optical Depth and Cloud Fraction". In: *Geophysical Research Letters* 37.18, p. L18814. DOI: 10.1029/2010GL044361.

Fan, J., Comstock, J. M. and Ovchinnikov, M. (2010). "The Cloud Condensation Nuclei and Ice Nuclei Effects on Tropical Anvil Characteristics and Water Vapor of the Tropical Tropopause Layer". In: *Environmental Research Letters* 5.4, p. 044005. DOI: 10.1088/1748-9326/5/4/044005.

Fan, J., Han, B., Varble, A., Morrison, H., North, K. et al. (2017). "Cloud-Resolving Model Intercomparison of an MC3E Squall Line Case: Part I—Convective Updrafts". In: *Journal of Geophysical Research: Atmospheres* 122.17, pp. 9351–9378. DOI: 10.1002/2017JD026622.

Fan, J., Leung, L. R., Rosenfeld, D., Chen, Q., Li, Z., Zhang, J. and Yan, H. (2013). "Microphysical Effects Determine Macrophysical Response for Aerosol Impacts on Deep Convective Clouds". In: *Proceedings of the National Academy of Sciences of the United States of America* 110.48, E4581–E4590. DOI: 10.1073/pnas.1316830110.

Fan, J., Rosenfeld, D., Ding, Y., Leung, L. R. and Li, Z. (2012). "Potential Aerosol Indirect Effects on Atmospheric Circulation and Radiative Forcing through Deep Convection". In: *Geophysical Research Letters* 39.9, p. L09806. DOI: 10.1029/2012GL051851.

Fan, J., Rosenfeld, D., Zhang, Y., Giangrande, S. E., Li, Z. et al. (2018). "Substantial Convection and Precipitation Enhancements by Ultrafine Aerosol Particles". In: *Science* 359.6374, pp. 411–418. DOI: 10.1126/science.aan8461.

Fan, J., Wang, Y., Rosenfeld, D. and Liu, X. (2016). "Review of Aerosol–Cloud Interactions: Mechanisms, Significance, and Challenges". In: *Journal of the Atmospheric Sciences* 73.11, pp. 4221–4252. DOI: 10.1175/JAS-D-16-0037.1.

Fan, J., Yuan, T., Comstock, J. M., Ghan, S., Khain, A., Leung, L. R., Li, Z., Martins, V. J. and Ovchinnikov, M. (2009). "Dominant Role by Vertical Wind Shear in Regulating Aerosol Effects on Deep Convective Clouds". In: *Journal of Geophysical Research: Atmospheres* 114.D22, p. D04201. DOI: 10.1029/2009JD012352.

Fan, J., Zhang, R., Li, G., Tao, W.-K. and Li, X. (2007). "Simulations of Cumulus Clouds Using a Spectral Microphysics Cloud-Resolving Model". In: *Journal of Geophysical Research: Atmospheres* 112.D4, p. D04201. DOI: 10.1029/2006JD007688.

Fan, J., Zhang, R., Tao, W.-K. and Mohr, K. I. (2008). "Effects of Aerosol Optical Properties on Deep Convective Clouds and Radiative Forcing". In: *Journal of Geophysical Research: Atmospheres* 113.D8, p. D08209. DOI: 10.1029/2007JD009257.

Feingold, G., Jiang, H. and Harrington, J. Y. (2005). "On Smoke Suppression of Clouds in Amazonia". In: *Geophysical Research Letters* 32.2, p. L02804. DOI: 10.1029/2004GL021369.

Feingold, G., McComiskey, A., Yamaguchi, T., Johnson, J. S., Carslaw, K. S. and Schmidt, K. S. (2016). "New Approaches to Quantifying Aerosol Influence on the Cloud Radiative Effect". In: *Proceedings of the National Academy of Sciences*, p. 201514035. DOI: 10.1073/pnas.1514035112.

Feng, Z., Dong, X., Xi, B., McFarlane, S. A., Kennedy, A., Lin, B. and Minnis, P. (2012). "Life Cycle of Midlatitude Deep Convective Systems in a Lagrangian Framework". In: *Journal of Geophysical Research: Atmospheres* 117.D23, p. D23201. DOI: 10.1029/2012JD018362.

Feng, Z., Leung, L. R., Houze Jr., R. A., Hagos, S., Hardin, J., Yang, Q., Han, B. and Fan, J. (2018). "Structure and Evolution of Mesoscale Convective Systems: Sensitivity to Cloud Microphysics in Convection-Permitting Simulations Over the United States". In: *Journal of Advances in Modeling Earth Systems* 10.7, pp. 1470–1494. DOI: 10.1029/2018MS001305.

Field, P. R., Hogan, R. J., Brown, P. R. A., Illingworth, A. J., Choularton, T. W. and Cotton, R. J. (2005). "Parametrization of Ice-Particle Size Distributions for Mid-Latitude Stratiform Cloud". In: *Quarterly Journal of the Royal Meteorological Society* 131.609, pp. 1997–2017. DOI: 10.1256/qj.04.134.

Findeisen, W. (1938). "Kolloid-Meteorologische Vorgänge Bei Niederschlags-Bildung". In: *Meteor. Z* 55, pp. 121–133.

Findeisen, W., Volken, E., Giesche, A. M. and Brönnimann, S. (2015). "Colloidal Meteorological Processes in the Formation of Precipitation". In: *Meteorologische Zeitschrift* 24.4, pp. 443–454.

Fiolleau, T. and Roca, R. (2013). "An Algorithm for the Detection and Tracking of Tropical Mesoscale Convective Systems Using Infrared Images From Geostationary Satellite". In: *IEEE Transactions on Geoscience and Remote Sensing* 51.7, pp. 4302–4315. DOI: 10.1109/TGRS.2012.2227762.

Fridlind, A. M., Ackerman, A. S., Chaboureau, J.-P., Fan, J., Grabowski, W. W. et al. (2012). "A Comparison of TWP-ICE Observational Data with Cloud-Resolving Model Results". In: *Journal of Geophysical Research: Atmospheres* 117.D5, p. D05204. DOI: 10.1029/2011JD016595.

Fridlind, A. M., Lier-Walqui, M. van, Collis, S., Giangrande, S. E., Jackson, R. C. et al. (2019). "Use of Polarimetric Radar Measurements to Constrain Simulated Convective Cell Evolution: A Pilot Study with Lagrangian Tracking". In: *Atmospheric Measurement Techniques Discussions*, pp. 1–36. DOI: https://doi.org/10.5194/amt-2018-454.

Fritsch, J. M. and Forbes, G. S. (2001). "Mesoscale Convective Systems". In: *Severe Convective Storms*. Ed. by C. A. Doswell. Meteorological Monographs. Boston, MA: American Meteorological Society, pp. 323–357. DOI: 10.1007/978-1-935704-06-5_9. (Visited on 08/04/2019).

Gensini, V. A. and Mote, T. L. (2014). "Estimations of Hazardous Convective Weather in the United States Using Dynamical Downscaling". In: *Journal of Climate* 27.17, pp. 6581–6589. DOI: 10.1175/JCLI-D-13-00777.1.

Gettelman, A. (2015). "Putting the Clouds Back in Aerosol–Cloud Interactions". In: *Atmos. Chem. Phys.* 15.21, pp. 12397–12411. DOI: 10.5194/acp-15-12397-2015.

Gettelman, A., Salby, M. L. and Sassi, F. (2002). "Distribution and Influence of Convection in the Tropical Tropopause Region". In: *Journal of Geophysical Research: Atmospheres* 107.D10, ACL 6-1-ACL 6–12. DOI: 10.1029/2001JD001048.

Gettelman, A., Schmidt, A. and Egill Kristjánsson, J. (2015). "Icelandic Volcanic Emissions and Climate". In: *Nature Geoscience* 8.4, pp. 243–243. DOI: 10.1038/ngeo2376.

Ghan, S. J., Abdul-Razzak, H., Nenes, A., Ming, Y., Liu, X., Ovchinnikov, M., Shipway, B., Meskhidze, N., Xu, J. and Shi, X. (2011a). "Correction to "Droplet Nucleation: Physically-Based Parameterizations and Comparative Evaluation"". In: *Journal of Advances in Modeling Earth Systems* 3.4, p. M12006. DOI: 10.1029/2011MS000107.

– (2011b). "Droplet Nucleation: Physically-Based Parameterizations and Comparative Evaluation". In: *Journal of Advances in Modeling Earth Systems* 3.4, p. M10001. DOI: 10.1029/2011MS000074.

Glassmeier, F. and Lohmann, U. (2016). "Constraining Precipitation Susceptibility of Warm-, Ice-, and Mixed-Phase Clouds with Microphysical Equations". In: *Journal of the Atmospheric Sciences* 73.12, pp. 5003–5023. DOI: 10.1175/JAS-D-16-0008.1.

Grabowski, W. W. (2001). "Coupling Cloud Processes with the Large-Scale Dynamics Using the Cloud-Resolving Convection Parameterization (CRCP)". In: *Journal of the Atmospheric Sciences* 58.9, pp. 978–997. DOI: 10.1175/1520-0469(2001)058⟨0978:CCPWTL⟩2.0.CO;2.

– (2006). "Indirect Impact of Atmospheric Aerosols in Idealized Simulations of Convective–Radiative Quasi Equilibrium". In: *Journal of Climate* 19.18, pp. 4664–4682. DOI: 10.1175/JCLI3857.1.

– (2015). "Untangling Microphysical Impacts on Deep Convection Applying a Novel Modeling Methodology". In: *Journal of the Atmospheric Sciences* 72.6, pp. 2446–2464. DOI: 10.1175/JAS-D-14-0307.1.

Grabowski, W. W. and Morrison, H. (2011). "Indirect Impact of Atmospheric Aerosols in Idealized Simulations of Convective–Radiative Quasi Equilibrium. Part II: Double-Moment Microphysics". In: *Journal of Climate* 24.7, pp. 1897–1912. DOI: 10.1175/2010JCLI3647.1.

– (2016). "Untangling Microphysical Impacts on Deep Convection Applying a Novel Modeling Methodology. Part II: Double-Moment Microphysics". In: *Journal of the Atmospheric Sciences* 73.9, pp. 3749–3770. DOI: 10.1175/JAS-D-15-0367.1.

Grady, L. (2006). "Random Walks for Image Segmentation". In: *IEEE Transactions on Pattern Analysis and Machine Intelligence* 28.11, pp. 1768–1783. DOI: 10.1109/TPAMI.2006.233.

Grant, L. D. and van den Heever, S. C. (2014). "Aerosol-Cloud-Land Surface Interactions within Tropical Sea Breeze Convection". In: *Journal of Geophysical Research: Atmospheres* 119.13, 2014JD021912. DOI: 10.1002/2014JD021912.

Gryspeerdt, E., Stier, P. and Grandey, B. S. (2014). "Cloud Fraction Mediates the Aerosol Optical Depth-Cloud Top Height Relationship". In: *Geophysical Research Letters* 41.10, pp. 3622–3627. DOI: 10.1002/2014GL059524.

Gryspeerdt, E., Goren, T., Sourdeval, O., Quaas, J., Mülmenstädt, J., Dipu, S., Unglaub, C., Gettelman, A. and Christensen, M. (2018). "Constraining the Aerosol Influence on Cloud Liquid Water Path". In: *Atmospheric Chemistry and Physics Discussions*, pp. 1–25. DOI: 10.5194/acp-2018-885.

Gryspeerdt, E., Quaas, J., Ferrachat, S., Gettelman, A., Ghan, S. et al. (2017). "Constraining the Instantaneous Aerosol Influence on Cloud Albedo". In: *Proceedings of the National Academy of Sciences* 114.19, pp. 4899–4904. DOI: 10.1073/pnas.1617765114.

Guichard, F. and Couvreux, F. (2017). "A Short Review of Numerical Cloud-Resolving Models". In: *Tellus A: Dynamic Meteorology and Oceanography* 69.1, p. 1373578. DOI: 10.1080/16000870.2017.1373578.

Guo, H., Golaz, J.-C., Donner, L. J., Wyman, B., Zhao, M. and Ginoux, P. (2015). "CLUBB as a Unified Cloud Parameterization: Opportunities and Challenges". In: *Geophysical Research Letters* 42.11, pp. 4540–4547. DOI: 10.1002/2015GL063672.

Hagos, S., Feng, Z., McFarlane, S. and Leung, L. R. (2013). "Environment and the Lifetime of Tropical Deep Convection in a Cloud-Permitting Regional Model Simulation". In: *Journal of the Atmospheric Sciences* 70.8, pp. 2409–2425. DOI: 10.1175/JAS-D-12-0260.1.

Hallett, J. and Mossop, S. C. (1974). "Production of Secondary Ice Particles during the Riming Process". In: *Nature* 249.5452, pp. 26–28. DOI: 10.1038/249026a0.

Hamilton, D. S., Hantson, S., Scott, C. E., Kaplan, J. O., Pringle, K. J., Nieradzik, L. P., Rap, A., Folberth, G. A., Spracklen, D. V. and Carslaw, K. S. (2018). "Reassessment of Pre-Industrial Fire Emissions Strongly Affects Anthropogenic Aerosol Forcing". In: *Nature Communications* 9.1, p. 3182. DOI: 10.1038/s41467-018-05592-9.

Hane, C. E. (1973). "The Squall Line Thunderstorm: Numerical Experimentation". In: *Journal of the Atmospheric Sciences* 30.8, pp. 1672–1690. DOI: 10.1175/1520-0469(1973)030⟨1672:TSLTNE⟩2.0.CO;2.

Hansen, J., Sato, M. and Ruedy, R. (1997). "Radiative Forcing and Climate Response". In: *Journal of Geophysical Research: Atmospheres* 102.D6, pp. 6831–6864. DOI: 10.1029/96JD03436.

Harrington, J. Y. (1997). "The Effects of Radiative and Microphysical Processes on Simulated Warm and Transition Season Arctic Stratus". PhD Thesis. Colorado State University.

Harrington, J. Y., Reisin, T., Cotton, W. R. and Kreidenweis, S. M. (1999). "Cloud Resolving Simulations of Arctic Stratus: Part II: Transition-Season Clouds". In: *Atmospheric Research* 51.1, pp. 45–75. DOI: 10.1016/S0169-8095(98)00098-2.

Harrington, J. Y., Sulia, K. and Morrison, H. (2013a). "A Method for Adaptive Habit Prediction in Bulk Microphysical Models. Part I: Theoretical Development". In: *Journal of the Atmospheric Sciences* 70.2, pp. 349–364. DOI: 10.1175/JAS-D-12-040.1.

– (2013b). "A Method for Adaptive Habit Prediction in Bulk Microphysical Models. Part II: Parcel Model Corroboration". In: *Journal of the Atmospheric Sciences* 70.2, pp. 365–376. DOI: 10.1175/JAS-D-12-0152.1.

Hauglustaine, D. A., Balkanski, Y. and Schulz, M. (2014). "A Global Model Simulation of Present and Future Nitrate Aerosols and Their Direct Radiative Forcing of Climate". In: *Atmos. Chem. Phys.* 14.20, pp. 11031–11063. DOI: 10.5194/acp-14-11031-2014.

Heath, N. K., Fuelberg, H. E., Tanelli, S., Turk, F. J., Lawson, R. P., Woods, S. and Freeman, S. (2017). "WRF Nested Large-Eddy Simulations of Deep Convection during SEAC4RS". In: *Journal of Geophysical Research: Atmospheres* 122.7, pp. 3953–3974. DOI: 10.1002/2016JD025465.

Heiblum, R. H., Altaratz, O., Koren, I., Feingold, G., Kostinski, A. B. et al. (2016a). "Characterization of Cumulus Cloud Fields Using Trajectories in the Center of Gravity versus Water Mass Phase Space: 1. Cloud Tracking and Phase Space Description". In: *Journal of Geophysical Research: Atmospheres* 121.11, 2015JD024186. DOI: 10.1002/2015JD024186.

– (2016b). "Characterization of Cumulus Cloud Fields Using Trajectories in the Center of Gravity versus Water Mass Phase Space: 2. Aerosol Effects on Warm Convective Clouds". In: *Journal of Geophysical Research: Atmospheres* 121.11, 2015JD024193. DOI: 10.1002/2015JD024193.

Heikenfeld, M., Marinescu, P. J., Christensen, M., Watson-Parris, D., Senf, F., Heever, S. C. van den and Stier, P. (2019a). "Tobac v1.0: Towards a Flexible Framework for Tracking and Analysis of Clouds in Diverse Datasets". In: *Geoscientific Model Development Discussions*, pp. 1–31. DOI: https://doi.org/10.5194/gmd-2019-105.

Heikenfeld, M., White, B., Labbouz, L. and Stier, P. (2019b). "Aerosol Effects on Deep Convection: The Propagation of Aerosol Perturbations through Convective Cloud Microphysics". In: *Atmospheric Chemistry and Physics* 19.4, pp. 2601–2627. DOI: https://doi.org/10.5194/acp-19-2601-2019.

Heintzenberg, J. (1994). "Properties of the Log-Normal Particle Size Distribution". In: *Aerosol Science and Technology* 21.1, pp. 46–48. DOI: 10.1080/02786829408959695.

Hernandez-Deckers, D. and Sherwood, S. C. (2016). "A Numerical Investigation of Cumulus Thermals". In: *Journal of the Atmospheric Sciences* 73.10, pp. 4117–4136. DOI: 10.1175/JAS-D-15-0385.1.

Heus, T. and Seifert, A. (2013). "Automated Tracking of Shallow Cumulus Clouds in Large Domain, Long Duration Large Eddy Simulations". In: *Geosci. Model Dev.* 6.4, pp. 1261–1273. DOI: 10.5194/gmd-6-1261-2013.

Heus, T., Jonker, H. J. J., Van den Akker, H. E. A., Griffith, E. J., Koutek, M. and Post, F. H. (2009). "A Statistical Approach to the Life Cycle Analysis of Cumulus Clouds Selected in a Virtual Reality Environment". In: *Journal of Geophysical Research: Atmospheres* 114.D6, p. D06208. DOI: 10.1029/2008JD010917.

Heymsfield, J. and Hjelmfelt, M. (1984). "Measurements inside Oklahoma Thunderstorms during Project SESAME". In: DOI: 10.5065/D6PZ56SG.

Hill, A. A., Shipway, B. J. and Boutle, I. A. (2015). "How Sensitive Are Aerosol-Precipitation Interactions to the Warm Rain Representation?" In: *Journal of Advances in Modeling Earth Systems* 7.3, pp. 987–1004. DOI: 10.1002/2014MS000422.

Hillger, D. W. and Schmit, T. J. (2007). "The GOES-13 Science Test: Imager and Sounder Radiance and Product Validations. NOAA". In: *Environ. Satell. Data Inf. Serv., Silver Spring, MD, NOAA Tech. Rep* 141.

Hitschfeld, W. F. (1986). "The Invention of Radar Meteorology". In: *Bulletin of the American Meteorological Society* 67.1, pp. 33–37. DOI: 10.1175/1520-0477(1986)067⟨0033:TIORM⟩2.0.CO;2.

Hobbs, P. V. and Biswas, K. R. (1979). "The Cellular Structure of Narrow Cold-Frontal Rainbands". In: *Quarterly Journal of the Royal Meteorological Society* 105.445, pp. 723–727. DOI: 10.1002/qj.49710544516.

Hoesly, R. M., Smith, S. J., Feng, L., Klimont, Z., Janssens-Maenhout, G. et al. (2018). "Historical (1750–2014) Anthropogenic Emissions of Reactive Gases and Aerosols from the Community Emissions Data System (CEDS)". In: *Geoscientific Model Development* 11.1, pp. 369–408. DOI: https://doi.org/10.5194/gmd-11-369-2018.

Hong, S.-Y., Noh, Y. and Dudhia, J. (2006). "A New Vertical Diffusion Package with an Explicit Treatment of Entrainment Processes". In: *Monthly Weather Review* 134.9, pp. 2318–2341. DOI: 10.1175/MWR3199.1.

Höpfner, M., Ungermann, J., Borrmann, S., Wagner, R., Spang, R. et al. (2019). "Ammonium Nitrate Particles Formed in Upper Troposphere from Ground Ammonia Sources during Asian Monsoons". In: *Nature Geoscience*, p. 1. DOI: 10.1038/s41561-019-0385-8.

Houze Jr., R. A. (2004). "Mesoscale Convective Systems". In: *Reviews of Geophysics* 42.4, 2004RG000150. DOI: 10.1029/2004RG000150.

Houze, R. A. (2014). *Cloud Dynamics*. Academic Press. 457 pp.

– (2018). "100 Years of Research on Mesoscale Convective Systems". In: *Meteorological Monographs* 59, pp. 17.1–17.54. DOI: 10.1175/AMSMONOGRAPHS-D-18-0001.1.

Howard, L. (1803). "On the Modifications of Clouds, and on the Principles of Their Production, Suspension, and Destruction". In: *The Philosophical Magazine* 16.64, pp. 344–357. DOI: 10.1080/14786440308676358.

Hoyer, S. and Hamman, J. (2017). "Xarray: N-D Labeled Arrays and Datasets in Python". In: *Journal of Open Research Software* 5.1, p. 10. DOI: 10.5334/jors.148.

Humphreys, W. J. (1914). "The Thunderstorm and Its Phenomena". In: *Journal of the Franklin Institute* 178.5, pp. 517–560. DOI: 10.1016/S0016-0032(14)90264-2.

Hunter, J. D. (2007). “Matplotlib: A 2D Graphics Environment”. In: *Computing in Science Engineering* 9.3, pp. 90–95. DOI: 10.1109/MCSE.2007.55.

Iacono, M. J., Delamere, J. S., Mlawer, E. J., Shephard, M. W., Clough, S. A. and Collins, W. D. (2008). “Radiative Forcing by Long-Lived Greenhouse Gases: Calculations with the AER Radiative Transfer Models”. In: *Journal of Geophysical Research: Atmospheres* 113.D13, p. D13103. DOI: 10.1029/2008JD009944.

Igel, A. L., Igel, M. R. and van den Heever, S. C. (2014). “Make It a Double? Sobering Results from Simulations Using Single-Moment Microphysics Schemes”. In: *Journal of the Atmospheric Sciences* 72.2, pp. 910–925. DOI: 10.1175/JAS-D-14-0107.1.

IPCC (2013a). *Climate Change 2013: The Physical Science Basis. Contribution of Working Group I to the Fifth Assessment Report of the Intergovernmental Panel on Climate Change*. Cambridge, United Kingdom and New York, NY, USA: Cambridge University Press. 1535 pp. DOI: 10.1017/CBO9781107415324.

– (2013b). “Summary for Policymakers”. In: *Climate Change 2013: The Physical Science Basis. Contribution of Working Group I to the Fifth Assessment Report of the Intergovernmental Panel on Climate Change*. Ed. by T. Stocker, D. Qin, G.-K. Plattner, M. Tignor, S. Allen, J. Boschung, A. Nauels, Y. Xia, V. Bex and P. Midgley. Cambridge, United Kingdom and New York, NY, USA: Cambridge University Press. Chap. SPM, pp. 1–30. DOI: 10.1017/CBO9781107415324.004.

– (2014). “Summary for Policymakers”. In: *Climate Change 2014: Impacts, Adaptation, and Vulnerability. Part A: Global and Sectoral Aspects. Contribution of Working Group II to the Fifth Assessment Report of the Intergovernmental Panel on Climate Change*. Ed. by C. B. Field, V. R. Barros, D. J. Dokken, K. J. Mach, M. D. Mastrandrea et al. Cambridge, United Kingdom, and New York, NY, USA: Cambridge University Press, pp. 1–32.

Isaac, G. A. (1986). “Summer Cumulus Cloud Lifetime—Importance to Static Mode Seeding”. In: *Precipitation Enhancement—A Scientific Challenge*. Ed. by R. R. Braham, W. A. Cooper, W. R. Cotton, R. D. Elliot, J. A. Flueck et al. Meteorological Monographs. Boston, MA: American Meteorological Society, pp. 25–28. DOI: 10.1007/978-1-935704-17-1_3. (Visited on 16/07/2019).

Jiang, H., Xue, H., Teller, A., Feingold, G. and Levin, Z. (2006). “Aerosol Effects on the Lifetime of Shallow Cumulus”. In: *Geophysical Research Letters* 33.14. DOI: 10.1029/2006GL026024.

Jiang, J. H., Su, H., Huang, L., Wang, Y., Massie, S., Zhao, B., Omar, A. and Wang, Z. (2018). “Contrasting Effects on Deep Convective Clouds by Different Types of Aerosols”. In: *Nature Communications* 9.1, p. 3874. DOI: 10.1038/s41467-018-06280-4.

Johnson, B. T., Shine, K. P. and Forster, P. M. (2004). “The Semi-Direct Aerosol Effect: Impact of Absorbing Aerosols on Marine Stratocumulus”. In: *Quarterly Journal of the Royal Meteorological Society* 130.599, pp. 1407–1422. DOI: 10.1256/qj.03.61.

Kalina, E. A., Friedrich, K., Morrison, H. and Bryan, G. H. (2014). “Aerosol Effects on Idealized Supercell Thunderstorms in Different Environments”. In: *Journal of the Atmospheric Sciences* 71.12, pp. 4558–4580. DOI: 10.1175/JAS-D-14-0037.1.

Kanji, Z. A., Ladino, L. A., Wex, H., Boose, Y., Burkert-Kohn, M., Cziczo, D. J. and Krämer, M. (2017). "Overview of Ice Nucleating Particles". In: *Meteorological Monographs* 58, pp. 1.1–1.33. DOI: 10.1175/AMSMONOGRAPHS-D-16-0006.1.

Kessler, E. (1969). "On the Distribution and Continuity of Water Substance in Atmospheric Circulations". In: *On the Distribution and Continuity of Water Substance in Atmospheric Circulations*, pp. 1–84. DOI: 10.1007/978-1-935704-36-2_1.

Khain, A. P., Beheng, K. D., Heymsfield, A., Korolev, A., Krichak, S. O. et al. (2015). "Representation of Microphysical Processes in Cloud-Resolving Models: Spectral (Bin) Microphysics versus Bulk Parameterization". In: *Reviews of Geophysics* 53.2, pp. 247–322. DOI: 10.1002/2014RG000468.

Khain, A. P., BenMoshe, N. and Pokrovsky, A. (2008). "Factors Determining the Impact of Aerosols on Surface Precipitation from Clouds: An Attempt at Classification". In: *Journal of the Atmospheric Sciences* 65.6, pp. 1721–1748. DOI: 10.1175/2007JAS2515.1.

Khain, A. P., Leung, L. R., Lynn, B. and Ghan, S. (2009). "Effects of Aerosols on the Dynamics and Microphysics of Squall Lines Simulated by Spectral Bin and Bulk Parameterization Schemes". In: *Journal of Geophysical Research: Atmospheres* 114.D22, p. D22203. DOI: 10.1029/2009JD011902.

Khain, A. P., Phillips, V., Benmoshe, N. and Pokrovsky, A. (2012). "The Role of Small Soluble Aerosols in the Microphysics of Deep Maritime Clouds". In: *Journal of the Atmospheric Sciences* 69.9, pp. 2787–2807. DOI: 10.1175/2011JAS3649.1.

Khain, A., Pokrovsky, A., Pinsky, M., Seifert, A. and Phillips, V. (2004). "Simulation of Effects of Atmospheric Aerosols on Deep Turbulent Convective Clouds Using a Spectral Microphysics Mixed-Phase Cumulus Cloud Model. Part I: Model Description and Possible Applications". In: *Journal of the Atmospheric Sciences* 61.24, pp. 2963–2982. DOI: 10.1175/JAS-3350.1.

Khain, A., Rosenfeld, D. and Pokrovsky, A. (2005). "Aerosol Impact on the Dynamics and Microphysics of Deep Convective Clouds". In: *Quarterly Journal of the Royal Meteorological Society* 131.611, pp. 2639–2663. DOI: 10.1256/qj.04.62.

Khain, A., Rosenfeld, D., Pokrovsky, A., Blahak, U. and Ryzhkov, A. (2011). "The Role of CCN in Precipitation and Hail in a Mid-Latitude Storm as Seen in Simulations Using a Spectral (Bin) Microphysics Model in a 2D Dynamic Frame". In: *Atmospheric Research* 99.1, pp. 129–146. DOI: 10.1016/j.atmosres.2010.09.015.

Khain, A. P. and Pinsky, M. (2018). *Physical Processes in Clouds and Cloud Modeling*. 1 edition. Cambridge, United Kingdom ; New York, NY: Cambridge University Press. 640 pp.

Khain, A. and Lynn, B. (2009). "Simulation of a Supercell Storm in Clean and Dirty Atmosphere Using Weather Research and Forecast Model with Spectral Bin Microphysics". In: *Journal of Geophysical Research: Atmospheres* 114.D19, p. D19209. DOI: 10.1029/2009JD011827.

Khairoutdinov, M. F., Krueger, S. K., Moeng, C.-H., Bogenschutz, P. A. and Randall, D. A. (2009). "Large-Eddy Simulation of Maritime Deep Tropical Convection". In:

Journal of Advances in Modeling Earth Systems 1.4, p. 15. DOI: 10.3894/JAMES.2009.1.15.

Khairoutdinov, M. F. and Randall, D. A. (2001). "A Cloud Resolving Model as a Cloud Parameterization in the NCAR Community Climate System Model: Preliminary Results". In: *Geophysical Research Letters* 28.18, pp. 3617–3620. DOI: 10.1029/2001GL013552.

Khairoutdinov, M. and Kogan, Y. (2000). "A New Cloud Physics Parameterization in a Large-Eddy Simulation Model of Marine Stratocumulus". In: *Monthly Weather Review* 128.1, pp. 229–243. DOI: 10.1175/1520-0493(2000)128⟨0229:ANCPPI⟩2.0.CO;2.

Khairoutdinov, M., Randall, D. and DeMott, C. (2005). "Simulations of the Atmospheric General Circulation Using a Cloud-Resolving Model as a Superparameterization of Physical Processes". In: *Journal of the Atmospheric Sciences* 62.7, pp. 2136–2154. DOI: 10.1175/JAS3453.1.

King, M. D., Platnick, S., Menzel, W. P., Ackerman, S. A. and Hubanks, P. A. (2013). "Spatial and Temporal Distribution of Clouds Observed by MODIS Onboard the Terra and Aqua Satellites". In: *IEEE Transactions on Geoscience and Remote Sensing* 51.7, pp. 3826–3852. DOI: 10.1109/TGRS.2012.2227333.

Kipling, Z., Stier, P., Labbouz, L. and Wagner, T. (2017). "Dynamic Subgrid Heterogeneity of Convective Cloud in a Global Model: Description and Evaluation of the Convective Cloud Field Model (CCFM) in ECHAM6–HAM2". In: *Atmos. Chem. Phys.* 17.1, pp. 327–342. DOI: 10.5194/acp-17-327-2017.

Klimont, Z., Smith, S. J. and Cofala, J. (2013). "The Last Decade of Global Anthropogenic Sulfur Dioxide: 2000–2011 Emissions". In: *Environmental Research Letters* 8.1, p. 014003. DOI: 10.1088/1748-9326/8/1/014003.

Kluyver, T., Ragan-Kelley, B., Pérez, F., Granger, B. E., Bussonnier, M., Frederic, J., Kelley, K., Hamrick, J. B., Grout, J. and Corlay, S. (2016). "Jupyter Notebooks-a Publishing Format for Reproducible Computational Workflows." In: *ELPUB*, pp. 87–90.

Knupp, K. R. and Cotton, W. R. (1985). "Convective Cloud Downdraft Structure: An Interpretive Survey". In: *Reviews of Geophysics* 23.2, pp. 183–215. DOI: 10.1029/RG023i002p00183.

Köhler, H. (1936). "The Nucleus in and the Growth of Hygroscopic Droplets". In: *Transactions of the Faraday Society* 32.0, pp. 1152–1161. DOI: 10.1039/TF9363201152.

Koop, T., Luo, B., Tsias, A. and Peter, T. (2000). "Water Activity as the Determinant for Homogeneous Ice Nucleation in Aqueous Solutions". In: *Nature* 406.6796, pp. 611–614. DOI: 10.1038/35020537.

Koren, I., Altaratz, O., Feingold, G., Levin, Z. and Reisin, T. (2009). "Cloud's Center of Gravity – a Compact Approach to Analyze Convective Cloud Development". In: *Atmos. Chem. Phys.* 9.1, pp. 155–161. DOI: 10.5194/acp-9-155-2009.

Koren, I., Feingold, G. and Remer, L. A. (2010a). "The Invigoration of Deep Convective Clouds over the Atlantic: Aerosol Effect, Meteorology or Retrieval Artifact?" In: *Atmos. Chem. Phys.* 10.18, pp. 8855–8872. DOI: 10.5194/acp-10-8855-2010.

Koren, I., Remer, L. A., Altaratz, O., Martins, J. V. and Davidi, A. (2010b). "Aerosol-Induced Changes of Convective Cloud Anvils Produce Strong Climate Warming". In: *Atmos. Chem. Phys.* 10.10, pp. 5001–5010. DOI: 10.5194/acp-10-5001-2010.

Koren, I., Altaratz, O., Remer, L. A., Feingold, G., Martins, J. V. and Heiblum, R. H. (2012). "Aerosol-Induced Intensification of Rain from the Tropics to the Mid-Latitudes". In: *Nature Geoscience* 5.2, pp. 118–122. DOI: 10.1038/ngeo1364.

Koren, I., Dagan, G. and Altaratz, O. (2014). "From Aerosol-Limited to Invigoration of Warm Convective Clouds". In: *Science* 344.6188, pp. 1143–1146. DOI: 10.1126/science.1252595.

Koren, I., Kaufman, Y. J., Remer, L. A. and Martins, J. V. (2004). "Measurement of the Effect of Amazon Smoke on Inhibition of Cloud Formation". In: *Science* 303.5662, pp. 1342–1345. DOI: 10.1126/science.1089424.

Koren, I., Martins, J. V., Remer, L. A. and Afargan, H. (2008). "Smoke Invigoration Versus Inhibition of Clouds over the Amazon". In: *Science* 321.5891, pp. 946–949. DOI: 10.1126/science.1159185.

Korolev, A. (2007). "Limitations of the Wegener–Bergeron–Findeisen Mechanism in the Evolution of Mixed-Phase Clouds". In: *Journal of the Atmospheric Sciences* 64.9, pp. 3372–3375. DOI: 10.1175/JAS4035.1.

Kumjian, M. R., Ryzhkov, A. V., Melnikov, V. M. and Schuur, T. J. (2010). "Rapid-Scan Super-Resolution Observations of a Cyclic Supercell with a Dual-Polarization WSR-88D". In: *Monthly Weather Review* 138.10, pp. 3762–3786. DOI: 10.1175/2010MWR3322.1.

Kunkel, K. E., Easterling, D. R., Kristovich, D. A. R., Gleason, B., Stoecker, L. and Smith, R. (2012). "Meteorological Causes of the Secular Variations in Observed Extreme Precipitation Events for the Conterminous United States". In: *Journal of Hydrometeorology* 13.3, pp. 1131–1141. DOI: 10.1175/JHM-D-11-0108.1.

Labbouz, L., Kipling, Z., Stier, P. and Protat, A. (2018). "How Well Can We Represent the Spectrum of Convective Clouds in a Climate Model? Comparisons between Internal Parameterization Variables and Radar Observations". In: *Journal of the Atmospheric Sciences* 75.5, pp. 1509–1524. DOI: 10.1175/JAS-D-17-0191.1.

Laing, A. G. and Fritsch, J. M. (1997). "The Global Population of Mesoscale Convective Complexes". In: *Quarterly Journal of the Royal Meteorological Society* 123.538, pp. 389–405. DOI: 10.1002/qj.49712353807.

Lakshmanan, V. and Smith, T. (2009a). "An Objective Method of Evaluating and Devising Storm-Tracking Algorithms". In: *Weather and Forecasting* 25.2, pp. 701–709. DOI: 10.1175/2009WAF2222330.1.

– (2009b). "Data Mining Storm Attributes from Spatial Grids". In: *Journal of Atmospheric and Oceanic Technology* 26.11, pp. 2353–2365. DOI: 10.1175/2009JTECHA1257.1.

Lamarck, J. B. (1802). "Sur La Forme Des Nuages". In: *Annuaire Météorologique pour l'an X de la République Française* 3.

Lamarque, J.-F., Bond, T. C., Eyring, V., Granier, C., Heil, A. et al. (2010). "Historical (1850–2000) Gridded Anthropogenic and Biomass Burning Emissions of Reactive Gases and Aerosols: Methodology and Application". In: *Atmospheric Chemistry and Physics* 10.15, pp. 7017–7039. DOI: https://doi.org/10.5194/acp-10-7017-2010.

Langhans, W., Schmidli, J. and Schär, C. (2012). "Bulk Convergence of Cloud-Resolving Simulations of Moist Convection over Complex Terrain". In: *Journal of the Atmospheric Sciences* 69.7, pp. 2207–2228. DOI: 10.1175/JAS-D-11-0252.1.

Lebo, Z. J., Morrison, H. and Seinfeld, J. H. (2012). "Are Simulated Aerosol-Induced Effects on Deep Convective Clouds Strongly Dependent on Saturation Adjustment?" In: *Atmos. Chem. Phys.* 12.20, pp. 9941–9964. DOI: 10.5194/acp-12-9941-2012.

Lebo, Z. J. and Seinfeld, J. H. (2011). "Theoretical Basis for Convective Invigoration Due to Increased Aerosol Concentration". In: *Atmos. Chem. Phys.* 11.11, pp. 5407–5429. DOI: 10.5194/acp-11-5407-2011.

Lebo, Z. (2018). "A Numerical Investigation of the Potential Effects of Aerosol-Induced Warming and Updraft Width and Slope on Updraft Intensity in Deep Convective Clouds". In: *Journal of the Atmospheric Sciences* 75.2, pp. 535–554. DOI: 10.1175/JAS-D-16-0368.1.

Lebo, Z. J. (2014). "The Sensitivity of a Numerically Simulated Idealized Squall Line to the Vertical Distribution of Aerosols". In: *Journal of the Atmospheric Sciences* 71.12, pp. 4581–4596. DOI: 10.1175/JAS-D-14-0068.1.

Lebo, Z. J. and Morrison, H. (2014). "Dynamical Effects of Aerosol Perturbations on Simulated Idealized Squall Lines". In: *Monthly Weather Review* 142.3, pp. 991–1009. DOI: 10.1175/MWR-D-13-00156.1.

Li, G., Wang, Y. and Zhang, R. (2008). "Implementation of a Two-Moment Bulk Microphysics Scheme to the WRF Model to Investigate Aerosol-Cloud Interaction". In: *Journal of Geophysical Research: Atmospheres* 113.D15. DOI: 10.1029/2007JD009361.

Li, Z., Niu, F., Fan, J., Liu, Y., Rosenfeld, D. and Ding, Y. (2011). "Long-Term Impacts of Aerosols on the Vertical Development of Clouds and Precipitation". In: *Nature Geoscience* 4.12, pp. 888–894. DOI: 10.1038/ngeo1313.

Lilly, D. K. (1975). "Severe Storms and Storm Systems: Scientific Background, Methods, and Critical Questions". In: *pure and applied geophysics* 113.1, pp. 713–734. DOI: 10.1007/BF01592955.

Lin, J. C., Matsui, T., Pielke Sr., R. A. and Kummerow, C. (2006). "Effects of Biomass-Burning-Derived Aerosols on Precipitation and Clouds in the Amazon Basin: A Satellite-Based Empirical Study". In: *Journal of Geophysical Research: Atmospheres* 111.D19. DOI: 10.1029/2005JD006884.

Lin, J. W.-B. (2012). "Why Python Is the Next Wave in Earth Sciences Computing". In: *Bulletin of the American Meteorological Society* 93.12, pp. 1823–1824. DOI: 10.1175/BAMS-D-12-00148.1.

Liu, C. and Zipser, E. J. (2005). "Global Distribution of Convection Penetrating the Tropical Tropopause". In: *Journal of Geophysical Research: Atmospheres* 110.D23. DOI: 10.1029/2005JD006063.

Loeb, N. G., Wielicki, B. A., Doelling, D. R., Smith, G. L., Keyes, D. F., Kato, S., Manalo-Smith, N. and Wong, T. (2009). "Toward Optimal Closure of the Earth's Top-of-Atmosphere Radiation Budget". In: *Journal of Climate* 22.3, pp. 748–766. DOI: 10.1175/2008JCLI2637.1.

Lohmann, U. (2006). "Aerosol Effects on Clouds and Climate". In: *Space Science Reviews* 125.1-4, pp. 129–137. DOI: 10.1007/s11214-006-9051-8.

– (2008). "Global Anthropogenic Aerosol Effects on Convective Clouds in ECHAM5-HAM". In: *Atmos. Chem. Phys.* 8.7, pp. 2115–2131. DOI: 10.5194/acp-8-2115-2008.

Lohmann, U. and Feichter, J. (2005). "Global Indirect Aerosol Effects: A Review". In: *Atmos. Chem. Phys.* 5.3, pp. 715–737. DOI: 10.5194/acp-5-715-2005.

Lohmann, U., Rotstayn, L., Storelvmo, T., Jones, A., Menon, S., Quaas, J., Ekman, A. M. L., Koch, D. and Ruedy, R. (2010). "Total Aerosol Effect: Radiative Forcing or Radiative Flux Perturbation?" In: *Atmospheric Chemistry and Physics* 10.7, pp. 3235–3246. DOI: https://doi.org/10.5194/acp-10-3235-2010.

Lohmann, U. and Feichter, J. (2001). "Can the Direct and Semi-Direct Aerosol Effect Compete with the Indirect Effect on a Global Scale?" In: *Geophysical Research Letters* 28.1, pp. 159–161. DOI: 10.1029/2000GL012051.

Lohmann, U., Lüönd, F. and Mahrt, F. (2016). *An Introduction to Clouds: From the Microscale to Climate*. Cambridge University Press. DOI: 10.1017/CBO9781139087513.

Lynn, B. H., Khain, A. P., Dudhia, J., Rosenfeld, D., Pokrovsky, A. and Seifert, A. (2005a). "Spectral (Bin) Microphysics Coupled with a Mesoscale Model (MM5). Part I: Model Description and First Results". In: *Monthly Weather Review* 133.1, pp. 44–58. DOI: 10.1175/MWR-2840.1.

– (2005b). "Spectral (Bin) Microphysics Coupled with a Mesoscale Model (MM5). Part II: Simulation of a CaPE Rain Event with a Squall Line". In: *Monthly Weather Review* 133.1, pp. 59–71. DOI: 10.1175/MWR-2841.1.

Mace, G. G., Deng, M., Soden, B. and Zipser, E. (2006). "Association of Tropical Cirrus in the 10–15-Km Layer with Deep Convective Sources: An Observational Study Combining Millimeter Radar Data and Satellite-Derived Trajectories". In: *Journal of the Atmospheric Sciences* 63.2, pp. 480–503. DOI: 10.1175/JAS3627.1.

Machado, L. a. T., Rossow, W. B., Guedes, R. L. and Walker, A. W. (1998). "Life Cycle Variations of Mesoscale Convective Systems over the Americas". In: *Monthly Weather Review* 126.6, pp. 1630–1654. DOI: 10.1175/1520-0493(1998)126⟨1630:LCVOMC⟩2.0.CO;2.

Malavelle, F. F., Haywood, J. M., Jones, A., Gettelman, A., Clarisse, L. et al. (2017). "Strong Constraints on Aerosol–Cloud Interactions from Volcanic Eruptions". In: *Nature* 546.7659, pp. 485–491. DOI: 10.1038/nature22974.

Mann, G. W., Carslaw, K. S., Ridley, D. A., Spracklen, D. V., Pringle, K. J. et al. (2012). "Intercomparison of Modal and Sectional Aerosol Microphysics Representations within the Same 3-D Global Chemical Transport Model". In: *Atmos. Chem. Phys.* 12.10, pp. 4449–4476. DOI: 10.5194/acp-12-4449-2012.

Mason, P. J. (1989). “Large-Eddy Simulation of the Convective Atmospheric Boundary Layer”. In: *Journal of the Atmospheric Sciences* 46.11, pp. 1492–1516. DOI: 10.1175/1520-0469(1989)046⟨1492:LESOTC⟩2.0.CO;2.

– (1994). “Large-Eddy Simulation: A Critical Review of the Technique”. In: *Quarterly Journal of the Royal Meteorological Society* 120.515, pp. 1–26. DOI: 10.1002/qj.49712051503.

McCoy, D. T. and Hartmann, D. L. (2015). “Observations of a Substantial Cloud-aerosol Indirect Effect during the 2014–2015 Bárðarbunga-Veiðivötn Fissure Eruption in Iceland”. In: *Geophysical Research Letters* 42.23, pp. 10, 409–10, 414. DOI: 10.1002/2015GL067070.

McGarragh, G. R., Poulsen, C. A., Thomas, G. E., Povey, A. C., Sus, O. et al. (2018). “The Community Cloud Retrieval for CLimate (CC4CL); Part 2: The Optimal Estimation Approach”. In: *Atmospheric Measurement Techniques* 11.6, pp. 3397–3431. DOI: https://doi.org/10.5194/amt-11-3397-2018.

McGee, C. J. and van den Heever, S. C. (2013). “Latent Heating and Mixing Due to Entrainment in Tropical Deep Convection”. In: *Journal of the Atmospheric Sciences* 71.2, pp. 816–832. DOI: 10.1175/JAS-D-13-0140.1.

McKinney, W. (2010). “Data Structures for Statistical Computing in Python”. In: Proceedings of the 9th Python in Science Conference, pp. 51–56. URL: http://conference.scipy.org/proceedings/scipy2010/mckinney.html (visited on 24/08/2018).

Mecikalski, J. R. and Bedka, K. M. (2006). “Forecasting Convective Initiation by Monitoring the Evolution of Moving Cumulus in Daytime GOES Imagery”. In: *Monthly Weather Review* 134.1, pp. 49–78. DOI: 10.1175/MWR3062.1.

Mecikalski, J. R., Watts, P. D. and Koenig, M. (2011). “Use of Meteosat Second Generation Optimal Cloud Analysis Fields for Understanding Physical Attributes of Growing Cumulus Clouds”. In: *Atmospheric Research* 102.1, pp. 175–190. DOI: 10.1016/j.atmosres.2011.06.023.

Menzel, W. P., Smith, W. L. and Stewart, T. R. (1983). “Improved Cloud Motion Wind Vector and Altitude Assignment Using VAS”. In: *Journal of Climate and Applied Meteorology* 22.3, pp. 377–384. DOI: 10.1175/1520-0450(1983)022⟨0377:ICMWVA⟩2.0.CO;2.

Menzel, W. P. (2001). “Cloud Tracking with Satellite Imagery: From the Pioneering Work of Ted Fujita to the Present”. In: *Bulletin of the American Meteorological Society* 82.1, pp. 33–48. DOI: 10.1175/1520-0477(2001)082⟨0033:CTWSIF⟩2.3.CO;2.

Met Office (2018). *Iris: A Python Library for Analysing and Visualising Meteorological and Oceanographic Data Sets*.

Meyer, F. (1994). “Topographic Distance and Watershed Lines”. In: *Signal Processing*. Mathematical Morphology and Its Applications to Signal Processing 38.1, pp. 113–125. DOI: 10.1016/0165-1684(94)90060-4.

Meyers, M. P., Walko, R. L., Harrington, J. Y. and Cotton, W. R. (1997). “New RAMS Cloud Microphysics Parameterization. Part II: The Two-Moment Scheme”. In: *Atmospheric Research* 45.1, pp. 3–39. DOI: 10.1016/S0169-8095(97)00018-5.

Milbrandt, J. A. and Yau, M. K. (2005a). "A Multimoment Bulk Microphysics Parameterization. Part I: Analysis of the Role of the Spectral Shape Parameter". In: *Journal of the Atmospheric Sciences* 62.9, pp. 3051–3064. DOI: 10.1175/JAS3534.1.

– (2005b). "A Multimoment Bulk Microphysics Parameterization. Part II: A Proposed Three-Moment Closure and Scheme Description". In: *Journal of the Atmospheric Sciences* 62.9, pp. 3065–3081. DOI: 10.1175/JAS3535.1.

Miller, L. J., Tuttle, J. D. and Knight, C. A. (1988). "Airflow and Hail Growth in a Severe Northern High Plains Supercell". In: *Journal of the Atmospheric Sciences* 45.4, pp. 736–762. DOI: 10.1175/1520-0469(1988)045⟨0736:AAHGIA⟩2.0.CO;2.

Miller, S. W. and Bodhaine, B. A. (1982). "Supersaturation and Expansion Ratios in Condensation Nuclei Counters: An Historical Perspective". In: *Journal of Aerosol Science* 13.6, pp. 481–490. DOI: 10.1016/0021-8502(82)90014-3.

Miltenberger, A. K., Field, P. R., Hill, A. A., Rosenberg, P., Shipway, B. J., Wilkinson, J. M., Scovell, R. and Blyth, A. M. (2018a). "Aerosol–Cloud Interactions in Mixed-Phase Convective Clouds – Part 1: Aerosol Perturbations". In: *Atmospheric Chemistry and Physics* 18.5, pp. 3119–3145. DOI: https://doi.org/10.5194/acp-18-3119-2018.

Miltenberger, A. K., Field, P. R., Hill, A. A., Shipway, B. J. and Wilkinson, J. M. (2018b). "Aerosol–Cloud Interactions in Mixed-Phase Convective Clouds – Part 2: Meteorological Ensemble". In: *Atmospheric Chemistry and Physics* 18.14, pp. 10593–10613. DOI: https://doi.org/10.5194/acp-18-10593-2018.

Morrison, H. (2012). "On the Robustness of Aerosol Effects on an Idealized Supercell Storm Simulated with a Cloud System-Resolving Model". In: *Atmospheric Chemistry and Physics* 12.16, pp. 7689–7705. DOI: https://doi.org/10.5194/acp-12-7689-2012.

Morrison, H., Curry, J. A. and Khvorostyanov, V. I. (2005). "A New Double-Moment Microphysics Parameterization for Application in Cloud and Climate Models. Part I: Description". In: *Journal of the Atmospheric Sciences* 62.6, pp. 1665–1677. DOI: 10.1175/JAS3446.1.

Morrison, H. and Grabowski, W. W. (2011). "Cloud-System Resolving Model Simulations of Aerosol Indirect Effects on Tropical Deep Convection and Its Thermodynamic Environment". In: *Atmos. Chem. Phys.* 11.20, pp. 10503–10523. DOI: 10.5194/acp-11-10503-2011.

Morrison, H., Thompson, G. and Tatarskii, V. (2009). "Impact of Cloud Microphysics on the Development of Trailing Stratiform Precipitation in a Simulated Squall Line: Comparison of One- and Two-Moment Schemes". In: *Monthly Weather Review* 137.3, pp. 991–1007. DOI: 10.1175/2008MWR2556.1.

Morrison, H. and Grabowski, W. W. (2008). "Modeling Supersaturation and Subgrid-Scale Mixing with Two-Moment Bulk Warm Microphysics". In: *Journal of the Atmospheric Sciences* 65.3, pp. 792–812. DOI: 10.1175/2007JAS2374.1.

Morrison, H. and Milbrandt, J. (2010). "Comparison of Two-Moment Bulk Microphysics Schemes in Idealized Supercell Thunderstorm Simulations". In: *Monthly Weather Review* 139.4, pp. 1103–1130. DOI: 10.1175/2010MWR3433.1.

Morrison, H. and Milbrandt, J. A. (2014). "Parameterization of Cloud Microphysics Based on the Prediction of Bulk Ice Particle Properties. Part I: Scheme Description and Idealized Tests". In: *Journal of the Atmospheric Sciences* 72.1, pp. 287–311. DOI: 10.1175/JAS-D-14-0065.1.

Morrison, H., Milbrandt, J. A., Bryan, G. H., Ikeda, K., Tessendorf, S. A. and Thompson, G. (2015). "Parameterization of Cloud Microphysics Based on the Prediction of Bulk Ice Particle Properties. Part II: Case Study Comparisons with Observations and Other Schemes". In: *Journal of the Atmospheric Sciences* 72.1, pp. 312–339. DOI: 10.1175/JAS-D-14-0066.1.

Moseley, C., Berg, P. and Haerter, J. O. (2013). "Probing the Precipitation Life Cycle by Iterative Rain Cell Tracking". In: *Journal of Geophysical Research: Atmospheres* 118.24, pp. 13, 361–13, 370. DOI: 10.1002/2013JD020868.

Moseley, C., Hohenegger, C., Berg, P. and Haerter, J. O. (2016). "Intensification of Convective Extremes Driven by Cloud-Cloud Interaction". In: *Nature Geoscience* 9.10, pp. 748–752. DOI: 10.1038/ngeo2789.

Mossop, S. C., Cottis, R. E. and Bartlett, B. M. (1972). "Ice Crystal Concentrations in Cumulus and Stratocumulus Clouds". In: *Quarterly Journal of the Royal Meteorological Society* 98.415, pp. 105–123. DOI: 10.1002/qj.49709841509.

Myhre, G., Samset, B. H., Schulz, M., Balkanski, Y., Bauer, S. et al. (2013a). "Radiative Forcing of the Direct Aerosol Effect from AeroCom Phase II Simulations". In: *Atmospheric Chemistry and Physics* 13.4, pp. 1853–1877. DOI: https://doi.org/10.5194/acp-13-1853-2013.

Myhre, G., Shindell, D., Bréon, F.-M., Collins, W., Fuglestvedt, J. et al. (2013b). "Anthropogenic and Natural Radiative Forcing". In: *Climate Change 2013: The Physical Science Basis. Contribution of Working Group I to the Fifth Assessment Report of the Intergovernmental Panel on Climate Change*. Ed. by T. Stocker, D. Qin, G.-K. Plattner, M. Tignor, S. Allen, J. Boschung, A. Nauels, Y. Xia, V. Bex and P. Midgley. Cambridge, United Kingdom and New York, NY, USA: Cambridge University Press, pp. 659–740. DOI: 0.1017/CBO9781107415324.018.

NASA (2013). *DISCOVER-AQ Aerosol-Trace Gas Measurements*. DOI: 10.5067/Aircraft/DISCOVER-AQ/Aerosol-TraceGas.

National Climatic Data Center, NESDIS, NOAA (2019). *NOAA Weather and Climate Toolkit (WCT)*. URL: https://www.ncdc.noaa.gov/wct/ (visited on 09/04/2019).

Naylor, J. and Gilmore, M. S. (2012). "Convective Initiation in an Idealized Cloud Model Using an Updraft Nudging Technique". In: *Monthly Weather Review* 140.11, pp. 3699–3705. DOI: 10.1175/MWR-D-12-00163.1.

NCEP (2015). *NCEP GDAS/FNL 0.25 Degree Global Tropospheric Analyses and Forecast Grids*. DOI: 10.5065/D65Q4T4Z. (Visited on 29/10/2018).

Nesbitt, S. W., Cifelli, R. and Rutledge, S. A. (2006). "Storm Morphology and Rainfall Characteristics of TRMM Precipitation Features". In: *Monthly Weather Review* 134.10, pp. 2702–2721.

Neumann, P., Düben, P., Adamidis, P., Bauer, P., Brück, M., Kornblueh, L., Klocke, D., Stevens, B., Wedi, N. and Biercamp, J. (2019). "Assessing the Scales in Numerical Weather and Climate Predictions: Will Exascale Be the Rescue?" In: *Philosophical Transactions of the Royal Society A: Mathematical, Physical and Engineering Sciences* 377.2142, p. 20180148. DOI: 10.1098/rsta.2018.0148.

Nieman, S. J., Menzei, W. P., Hayden, C. M., Gray, D., Wanzong, S. T., Velden, C. S. and Daniels, J. (1997). "Fully Automated Cloud-Drift Winds in NESDIS Operations". In: *Bulletin of the American Meteorological Society* 78.6, pp. 1121–1134. DOI: 10.1175/1520-0477(1997)078⟨1121:FACDWI⟩2.0.CO;2.

Nishant, N. and Sherwood, S. C. (2017). "A Cloud-Resolving Model Study of Aerosol-Cloud Correlation in a Pristine Maritime Environment". In: *Geophysical Research Letters* 44.11, pp. 5774–5781. DOI: 10.1002/2017GL073267.

NOAA (2019). *NOAA's Comprehensive Large Array-Data Stewardship System - GOES Satellite Data - Imager (GVAR_IMG)*. URL: https://www.avl.class.noaa.gov/saa/products/search?datatype_family=GVAR_IMG (visited on 09/04/2019).

Orlanski, I. (1975). "A Rational Subdivision of Scales for Atmospheric Processes". In: *Bulletin of the American Meteorological Society* 56.5, pp. 527–530. URL: https://www.jstor.org/stable/26216020 (visited on 09/04/2019).

Orville, R. E., Huffines, G., Nielsen-Gammon, J., Zhang, R., Ely, B., Steiger, S., Phillips, S., Allen, S. and Read, W. (2001). "Enhancement of Cloud-to-Ground Lightning over Houston, Texas". In: *Geophysical Research Letters* 28.13, pp. 2597–2600. DOI: 10.1029/2001GL012990.

Ovchinnikov, M., Ackerman, A. S., Avramov, A., Cheng, A., Fan, J. et al. (2014). "Intercomparison of Large-Eddy Simulations of Arctic Mixed-Phase Clouds: Importance of Ice Size Distribution Assumptions". In: *Journal of Advances in Modeling Earth Systems* 6.1, pp. 223–248. DOI: 10.1002/2013MS000282.

Pearson, K. J., Hogan, R. J., Allan, R. P., Lister, G. M. S. and Holloway, C. E. (2010). "Evaluation of the Model Representation of the Evolution of Convective Systems Using Satellite Observations of Outgoing Longwave Radiation". In: *Journal of Geophysical Research: Atmospheres* 115.D20, p. D20206. DOI: 10.1029/2010JD014265.

Penner, J. E., Quaas, J., Storelvmo, T., Takemura, T., Boucher, O., Guo, H., Kirkevg, A., Kristjánsson, J. E. and Seland, Ø. (2006). "Model Intercomparison of Indirect Aerosol Effects". In: *Atmospheric Chemistry and Physics* 6.11, pp. 3391–3405. DOI: https://doi.org/10.5194/acp-6-3391-2006.

Penner, J. E., Xu, L. and Wang, M. (2011). "Satellite Methods Underestimate Indirect Climate Forcing by Aerosols". In: *Proceedings of the National Academy of Sciences* 108.33, pp. 13404–13408. DOI: 10.1073/pnas.1018526108.

Perez, F. and Granger, B. E. (2007). "IPython: A System for Interactive Scientific Computing". In: *Computing in Science Engineering* 9.3, pp. 21–29. DOI: 10.1109/MCSE.2007.53.

Perkel, J. M. (2015). "Programming: Pick up Python". In: *Nature News* 518.7537, p. 125. DOI: 10.1038/518125a.

Petters, M. D. and Kreidenweis, S. M. (2007). "A Single Parameter Representation of Hygroscopic Growth and Cloud Condensation Nucleus Activity". In: *Atmospheric Chemistry and Physics* 7.8, pp. 1961–1971. DOI: https://doi.org/10.5194/acp-7-1961-2007.

Plant, R. S. (2009). "Statistical Properties of Cloud Lifecycles in Cloud-Resolving Models". In: *Atmos. Chem. Phys.* 9.6, pp. 2195–2205. DOI: 10.5194/acp-9-2195-2009.

Porter, J. N. and Clarke, A. D. (1997). "Aerosol Size Distribution Models Based on in Situ Measurements". In: *Journal of Geophysical Research: Atmospheres* 102.D5, pp. 6035–6045. DOI: 10.1029/96JD03403.

Pöschl, U., Martin, S. T., Sinha, B., Chen, Q., Gunthe, S. S. et al. (2010). "Rainforest Aerosols as Biogenic Nuclei of Clouds and Precipitation in the Amazon". In: *Science* 329.5998, pp. 1513–1516. DOI: 10.1126/science.1191056.

Pruppacher, H. R. and Klett, J. D. (2010). *Microphysics of Clouds and Precipitation*. Springer Science & Business Media. 975 pp.

Quaas, J., Ming, Y., Menon, S., Takemura, T., Wang, M. et al. (2009). "Aerosol Indirect Effects – General Circulation Model Intercomparison and Evaluation with Satellite Data". In: *Atmospheric Chemistry and Physics* 9.22, pp. 8697–8717. DOI: https://doi.org/10.5194/acp-9-8697-2009.

Rangno, A. L. (2015). "CLOUDS AND FOG — Classification of Clouds". In: *Encyclopedia of Atmospheric Sciences (Second Edition)*. Ed. by G. R. North, J. Pyle and F. Zhang. Oxford: Academic Press, pp. 141–160. DOI: 10.1016/B978-0-12-382225-3.00112-2. (Visited on 19/02/2019).

Rasmussen, R. M., Geresdi, I., Thompson, G., Manning, K. and Karplus, E. (2002). "Freezing Drizzle Formation in Stably Stratified Layer Clouds: The Role of Radiative Cooling of Cloud Droplets, Cloud Condensation Nuclei, and Ice Initiation". In: *Journal of the Atmospheric Sciences* 59.4, pp. 837–860. DOI: 10.1175/1520-0469(2002)059⟨0837:FDFISS⟩2.0.CO;2.

Reed, J. L., Lanterman, A. D. and Trostel, J. M. (2017). "Weather Radar: Operation and Phenomenology". In: *IEEE Aerospace and Electronic Systems Magazine* 32.7, pp. 46–62. DOI: 10.1109/MAES.2017.150178.

Reisin, T., Levin, Z. and Tzivion, S. (1996a). "Rain Production in Convective Clouds as Simulated in an Axisymmetric Model with Detailed Microphysics. Part II: Effects of Varying Drops and Ice Initiation". In: *Journal of the Atmospheric Sciences* 53.13, pp. 1815–1837. DOI: 10.1175/1520-0469(1996)053⟨1815:RPICCA⟩2.0.CO;2.

Reisin, T., Tzivion, S. and Levin, Z. (1996b). "Seeding Convective Clouds with Ice Nuclei or Hygroscopic Particles: A Numerical Study Using a Model with Detailed Microphysics". In: *Journal of Applied Meteorology* 35.9, pp. 1416–1434. DOI: 10.1175/1520-0450(1996)035⟨1416:SCCWIN⟩2.0.CO;2.

Rocklin, M. (2015). "Dask: Parallel Computation with Blocked Algorithms and Task Scheduling". In: *Proceedings of the 14th Python in Science Conference*. Ed. by K. Huff and J. Bergstra, pp. 130–136.

Rosenfeld, D. (1987). "Objective Method for Analysis and Tracking of Convective Cells as Seen by Radar". In: *Journal of Atmospheric and Oceanic Technology* 4.3, pp. 422–434. DOI: 10.1175/1520-0426(1987)004⟨0422:OMFAAT⟩2.0.CO;2.

Rosenfeld, D., Andreae, M. O., Asmi, A., Chin, M., de Leeuw, G. et al. (2014a). "Global Observations of Aerosol-Cloud-Precipitation-Climate Interactions". In: *Reviews of Geophysics*, 2013RG000441. DOI: 10.1002/2013RG000441.

Rosenfeld, D., Lohmann, U., Raga, G. B., O'Dowd, C. D., Kulmala, M., Fuzzi, S., Reissell, A. and Andreae, M. O. (2008). "Flood or Drought: How Do Aerosols Affect Precipitation?" In: *Science* 321.5894, pp. 1309–1313. DOI: 10.1126/science.1160606.

Rosenfeld, D., Sherwood, S., Wood, R. and Donner, L. (2014b). "Climate Effects of Aerosol-Cloud Interactions". In: *Science* 343.6169, pp. 379–380. DOI: 10.1126/science.1247490.

Rosenfeld, D., Zheng, Y., Hashimshoni, E., Pöhlker, M. L., Jefferson, A. et al. (2016). "Satellite Retrieval of Cloud Condensation Nuclei Concentrations by Using Clouds as CCN Chambers". In: *Proceedings of the National Academy of Sciences* 113.21, pp. 5828–5834. DOI: 10.1073/pnas.1514044113.

Rothenberg, D., Avramov, A. and Wang, C. (2018). "On the Representation of Aerosol Activation and Its Influence on Model-Derived Estimates of the Aerosol Indirect Effect". In: *Atmospheric Chemistry and Physics* 18.11, pp. 7961–7983. DOI: https://doi.org/10.5194/acp-18-7961-2018.

Russo, M. R., Marécal, V., Hoyle, C. R., Arteta, J., Chemel, C. et al. (2011). "Representation of Tropical Deep Convection in Atmospheric Models – Part 1: Meteorology and Comparison with Satellite Observations". In: *Atmospheric Chemistry and Physics* 11.6, pp. 2765–2786. DOI: https://doi.org/10.5194/acp-11-2765-2011.

Saleeby, S. M. and Cotton, W. R. (2004). "A Large-Droplet Mode and Prognostic Number Concentration of Cloud Droplets in the Colorado State University Regional Atmospheric Modeling System (RAMS). Part I: Module Descriptions and Supercell Test Simulations". In: *Journal of Applied Meteorology* 43.1, pp. 182–195. DOI: 10.1175/1520-0450(2004)043⟨0182:ALMAPN⟩2.0.CO;2.

– (2005). "A Large-Droplet Mode and Prognostic Number Concentration of Cloud Droplets in the Colorado State University Regional Atmospheric Modeling System (RAMS). Part II: Sensitivity to a Colorado Winter Snowfall Event". In: *Journal of Applied Meteorology* 44.12, pp. 1912–1929. DOI: 10.1175/JAM2312.1.

Saleeby, S. M. and van den Heever, S. C. (2013). "Developments in the CSU-RAMS Aerosol Model: Emissions, Nucleation, Regeneration, Deposition, and Radiation". In: *Journal of Applied Meteorology and Climatology* 52.12, pp. 2601–2622. DOI: 10.1175/JAMC-D-12-0312.1.

Sassen, K., Wang, Z. and Liu, D. (2008). "Global Distribution of Cirrus Clouds from CloudSat/Cloud-Aerosol Lidar and Infrared Pathfinder Satellite Observations (CALIPSO) Measurements". In: *Journal of Geophysical Research: Atmospheres* 113.D8. DOI: 10.1029/2008JD009972.

Sato, Y., Goto, D., Michibata, T., Suzuki, K., Takemura, T., Tomita, H. and Nakajima, T. (2018). "Aerosol Effects on Cloud Water Amounts Were Successfully Simulated by a

Global Cloud-System Resolving Model". In: *Nature Communications* 9.1, p. 985. DOI: 10.1038/s41467-018-03379-6.

Satoh, M., Tomita, H., Yashiro, H., Kajikawa, Y., Miyamoto, Y. et al. (2017). "Outcomes and Challenges of Global High-Resolution Non-Hydrostatic Atmospheric Simulations Using the K Computer". In: *Progress in Earth and Planetary Science* 4.1, p. 13. DOI: 10.1186/s40645-017-0127-8.

Savre, J., Ekman, A. M. L., Svensson, G. and Tjernström, M. (2015). "Large-Eddy Simulations of an Arctic Mixed-Phase Stratiform Cloud Observed during ISDAC: Sensitivity to Moisture Aloft, Surface Fluxes and Large-Scale Forcing". In: *Quarterly Journal of the Royal Meteorological Society* 141.689, pp. 1177–1190. DOI: 10.1002/qj.2425.

Schmale, J., Henning, S., Henzing, B., Keskinen, H., Sellegri, K. et al. (2017). "Collocated Observations of Cloud Condensation Nuclei, Particle Size Distributions, and Chemical Composition". In: *Scientific Data* 4, p. 170003. DOI: 10.1038/sdata.2017.3.

Schmetz, J., Holmlund, K., Hoffman, J., Strauss, B., Mason, B., Gaertner, V., Koch, A. and Van De Berg, L. (1993). "Operational Cloud-Motion Winds from Meteosat Infrared Images". In: *Journal of Applied Meteorology* 32.7, pp. 1206–1225. DOI: 10.1175/1520-0450(1993)032⟨1206:OCMWFM⟩2.0.CO;2.

Schmit, T. J., Griffith, P., Gunshor, M. M., Daniels, J. M., Goodman, S. J. and Lebair, W. J. (2016). "A Closer Look at the ABI on the GOES-R Series". In: *Bulletin of the American Meteorological Society* 98.4, pp. 681–698. DOI: 10.1175/BAMS-D-15-00230.1.

Schutgens, N. A. J. and Stier, P. (2014). "A Pathway Analysis of Global Aerosol Processes". In: *Atmos. Chem. Phys.* 14.21, pp. 11657–11686. DOI: 10.5194/acp-14-11657-2014.

Schutgens, N., Tsyro, S., Gryspeerdt, E., Goto, D., Weigum, N., Schulz, M. and Stier, P. (2017). "On the Spatio-Temporal Representativeness of Observations". In: *Atmos. Chem. Phys. Discuss.* 2017, pp. 1–40. DOI: 10.5194/acp-2017-149.

Schwarz, J. P., Spackman, J. R., Fahey, D. W., Gao, R. S., Lohmann, U. et al. (2008). "Coatings and Their Enhancement of Black Carbon Light Absorption in the Tropical Atmosphere". In: *Journal of Geophysical Research: Atmospheres* 113.D3, p. D03203. DOI: 10.1029/2007JD009042.

Seifert, A. and Beheng, K. D. (2006). "A Two-Moment Cloud Microphysics Parameterization for Mixed-Phase Clouds. Part 2: Maritime vs. Continental Deep Convective Storms". In: *Meteorology and Atmospheric Physics* 92.1, pp. 67–82. DOI: 10.1007/s00703-005-0113-3.

Seifert, A., Köhler, C. and Beheng, K. D. (2012). "Aerosol-Cloud-Precipitation Effects over Germany as Simulated by a Convective-Scale Numerical Weather Prediction Model". In: *Atmospheric Chemistry and Physics* 12.2, pp. 709–725. DOI: https://doi.org/10.5194/acp-12-709-2012.

Seifert, A. and Beheng, K. D. (2001). "A Double-Moment Parameterization for Simulating Autoconversion, Accretion and Selfcollection". In: *Atmospheric Research*. 13th International Conference on Clouds and Precipitation 59-60, pp. 265–281. DOI: 10.1016/S0169-8095(01)00126-0.

Seifert, A., Khain, A., Pokrovsky, A. and Beheng, K. D. (2006). "A Comparison of Spectral Bin and Two-Moment Bulk Mixed-Phase Cloud Microphysics". In: *Atmospheric Research* 80.1, pp. 46–66. DOI: 10.1016/j.atmosres.2005.06.009.

Seiki, T., Kodama, C., Noda, A. T. and Satoh, M. (2014). "Improvement in Global Cloud-System-Resolving Simulations by Using a Double-Moment Bulk Cloud Microphysics Scheme". In: *Journal of Climate* 28.6, pp. 2405–2419. DOI: 10.1175/JCLI-D-14-00241.1.

Seinfeld, J. H. and Pandis, S. N. (2016). *Atmospheric Chemistry and Physics: From Air Pollution to Climate Change*. New York, UNITED STATES: John Wiley & Sons, Incorporated.

Senf, F. and Deneke, H. (2017). "Satellite-Based Characterization of Convective Growth and Glaciation and Its Relationship to Precipitation Formation over Central Europe". In: *Journal of Applied Meteorology and Climatology* 56.7, pp. 1827–1845. DOI: 10.1175/JAMC-D-16-0293.1.

Senf, F., Dietzsch, F., Hünerbein, A. and Deneke, H. (2015). "Characterization of Initiation and Growth of Selected Severe Convective Storms over Central Europe with MSG-SEVIRI". In: *Journal of Applied Meteorology and Climatology* 54.1, pp. 207–224. DOI: 10.1175/JAMC-D-14-0144.1.

Senf, F., Klocke, D. and Brueck, M. (2018). "Size-Resolved Evaluation of Simulated Deep Tropical Convection". In: *Monthly Weather Review* 146.7, pp. 2161–2182. DOI: 10.1175/MWR-D-17-0378.1.

Sheffield, A. M., Saleeby, S. M. and Heever, S. C. van den (2015). "Aerosol-Induced Mechanisms for Cumulus Congestus Growth". In: *Journal of Geophysical Research: Atmospheres* 120.17, pp. 8941–8952. DOI: 10.1002/2015JD023743.

Shepherd, J. M. (2005). "A Review of Current Investigations of Urban-Induced Rainfall and Recommendations for the Future". In: *Earth Interactions* 9.12, pp. 1–27. DOI: 10.1175/EI156.1.

Shepherd, J. M. and Burian, S. J. (2003). "Detection of Urban-Induced Rainfall Anomalies in a Major Coastal City". In: *Earth Interactions* 7.4, pp. 1–17. DOI: 10.1175/1087-3562(2003)007⟨0001:DOUIRA⟩2.0.CO;2.

Sherwood, S. C., Hernández-Deckers, D., Colin, M. and Robinson, F. (2013). "Slippery Thermals and the Cumulus Entrainment Paradox". In: *Journal of the Atmospheric Sciences* 70.8, pp. 2426–2442. DOI: 10.1175/JAS-D-12-0220.1.

Shinozuka, Y., Clarke, A. D., Nenes, A., Jefferson, A., Wood, R. et al. (2015). "The Relationship between Cloud Condensation Nuclei (CCN) Concentration and Light Extinction of Dried Particles: Indications of Underlying Aerosol Processes and Implications for Satellite-Based CCN Estimates". In: *Atmospheric Chemistry and Physics* 15.13, pp. 7585–7604. DOI: https://doi.org/10.5194/acp-15-7585-2015.

Sieglaff, J. M., Hartung, D. C., Feltz, W. F., Cronce, L. M. and Lakshmanan, V. (2012). "A Satellite-Based Convective Cloud Object Tracking and Multipurpose Data Fusion Tool with Application to Developing Convection". In: *Journal of Atmospheric and Oceanic Technology* 30.3, pp. 510–525. DOI: 10.1175/JTECH-D-12-00114.1.

Simpson, E., Connolly, P. and McFiggans, G. (2014). "An Investigation into the Performance of Four Cloud Droplet Activation Parameterisations". In: *Geoscientific Model Development* 7.4, pp. 1535–1542. DOI: https://doi.org/10.5194/gmd-7-1535-2014.

Singh, R., Thapliyal, P. K., Kishtawal, C. M., Pal, P. K. and Joshi, P. C. (2007). "A New Technique for Estimating Outgoing Longwave Radiation Using Infrared Window and Water Vapor Radiances from Kalpana Very High Resolution Radiometer". In: *Geophysical Research Letters* 34.23, p. L23815. DOI: 10.1029/2007GL031715.

Skamarock, C., Klemp, B., Dudhia, J., Gill, O., Barker, D., Duda, G., Huang, X.-y., Wang, W. and Powers, G. (2008). *A Description of the Advanced Research WRF Version 3*. URL: https://opensky.ucar.edu:/islandora/object/technotes%3A500/ (visited on 25/02/2019).

Skamarock, C., Klemp, B., Dudhia, J., Gill, O., Barker, M., Wang, W. and Powers, G. (2005). *A Description of the Advanced Research WRF Version 2*. DOI: 10.5065/D6DZ069T. (Visited on 29/01/2019).

Soille, P. J. and Ansoult, M. M. (1990). "Automated Basin Delineation from Digital Elevation Models Using Mathematical Morphology". In: *Signal Processing* 20.2, pp. 171–182. DOI: 10.1016/0165-1684(90)90127-K.

Song, X. and Zhang, G. J. (2011). "Microphysics Parameterization for Convective Clouds in a Global Climate Model: Description and Single-Column Model Tests". In: *Journal of Geophysical Research: Atmospheres* 116.D2, p. D02201. DOI: 10.1029/2010JD014833.

Srivastava, R. C. (1987). "A Model of Intense Downdrafts Driven by the Melting and Evaporation of Precipitation". In: *Journal of the Atmospheric Sciences* 44.13, pp. 1752–1774. DOI: 10.1175/1520-0469(1987)044⟨1752:AMOIDD⟩2.0.CO;2.

Steiger, S. M., Orville, R. E. and Huffines, G. (2002). "Cloud-to-Ground Lightning Characteristics over Houston, Texas: 1989–2000". In: *Journal of Geophysical Research: Atmospheres* 107.D11, ACL 2. DOI: 10.1029/2001JD001142.

Stephens, G. L., Li, J., Wild, M., Clayson, C. A., Loeb, N., Kato, S., L'Ecuyer, T., Jr, P. W. S., Lebsock, M. and Andrews, T. (2012). "An Update on Earth's Energy Balance in Light of the Latest Global Observations". In: *Nature Geoscience* 5.10, p. 691. DOI: 10.1038/ngeo1580.

Stevens, B. and Feingold, G. (2009). "Untangling Aerosol Effects on Clouds and Precipitation in a Buffered System". In: *Nature* 461.7264, pp. 607–613. DOI: 10.1038/nature08281.

Stier, P., Feichter, J., Kinne, S., Kloster, S., Vignati, E. et al. (2005). "The Aerosol-Climate Model ECHAM5-HAM". In: *Atmospheric Chemistry and Physics* 5.4, pp. 1125–1156. DOI: 10.5194/acp-5-1125-2005.

Stith, J. L., Baumgardner, D., Haggerty, J., Hardesty, R. M., Lee, W.-C., Lenschow, D., Pilewskie, P., Smith, P. L., Steiner, M. and Vömel, H. (2018). "100 Years of Progress in Atmospheric Observing Systems". In: *Meteorological Monographs* 59, pp. 2.1–2.55. DOI: 10.1175/AMSMONOGRAPHS-D-18-0006.1.

Stocker, T., Qin, D., Plattner, G.-K., Alexander, L., Allen, S. et al. (2013). "Technical Summary". In: *Climate Change 2013: The Physical Science Basis. Contribution of*

Working Group I to the Fifth Assessment Report of the Intergovernmental Panel on Climate Change. Ed. by T. Stocker, D. Qin, G.-K. Plattner, M. Tignor, S. Allen, J. Boschung, A. Nauels, Y. Xia, V. Bex and P. Midgley. Cambridge, United Kingdom and New York, NY, USA: Cambridge University Press. Chap. TS, pp. 33–115. DOI: 10.1017/CBO9781107415324.005.

Storelvmo, T., Hoose, C. and Eriksson, P. (2011). "Global Modeling of Mixed-Phase Clouds: The Albedo and Lifetime Effects of Aerosols". In: *Journal of Geophysical Research: Atmospheres* 116.D5, p. D05207. DOI: 10.1029/2010JD014724.

Storelvmo, T. and Tan, I. (2015). "The Wegener-Bergeron-Findeisen Process – Its Discovery and Vital Importance for Weather and Climate". In: *Meteorologische Zeitschrift* 24.4, pp. 455–461. DOI: 10.1127/metz/2015/0626.

Storer, R. L., van den Heever, S. C. and L'Ecuyer, T. S. (2014). "Observations of Aerosol-Induced Convective Invigoration in the Tropical East Atlantic". In: *Journal of Geophysical Research: Atmospheres* 119.7, pp. 3963–3975. DOI: 10.1002/2013JD020272.

Storer, R. L. and van den Heever, S. C. (2013). "Microphysical Processes Evident in Aerosol Forcing of Tropical Deep Convective Clouds". In: *Journal of the Atmospheric Sciences* 70.2, pp. 430–446. DOI: 10.1175/JAS-D-12-076.1.

Storer, R. L., van den Heever, S. C. and Stephens, G. L. (2010). "Modeling Aerosol Impacts on Convective Storms in Different Environments". In: *Journal of the Atmospheric Sciences* 67.12, pp. 3904–3915. DOI: 10.1175/2010JAS3363.1.

Stuhlmann, R., Rodriguez, A., Tjemkes, S., Grandell, J., Arriaga, A., Bézy, J. .-.-L., Aminou, D. and Bensi, P. (2005). "Plans for EUMETSAT's Third Generation Meteosat Geostationary Satellite Programme". In: *Advances in Space Research*. Atmospheric Remote Sensing: Earth's Surface, Troposphere, Stratosphere and Mesosphere- I 36.5, pp. 975–981. DOI: 10.1016/j.asr.2005.03.091.

Sullivan, S. C., Lee, D., Oreopoulos, L. and Nenes, A. (2016). "Role of Updraft Velocity in Temporal Variability of Global Cloud Hydrometeor Number". In: *Proceedings of the National Academy of Sciences* 113.21, pp. 5791–5796. DOI: 10.1073/pnas.1514039113.

Tao, W.-K., Chen, J.-P., Li, Z., Wang, C. and Zhang, C. (2012). "Impact of Aerosols on Convective Clouds and Precipitation". In: *Reviews of Geophysics* 50.2, RG2001. DOI: 10.1029/2011RG000369.

Tao, W.-K., Li, X., Khain, A., Matsui, T., Lang, S. and Simpson, J. (2007). "Role of Atmospheric Aerosol Concentration on Deep Convective Precipitation: Cloud-Resolving Model Simulations". In: *Journal of Geophysical Research: Atmospheres* 112.D24, D24S18. DOI: 10.1029/2007JD008728.

Tegen, I., Werner, M., Harrison, S. P. and Kohfeld, K. E. (2004). "Relative Importance of Climate and Land Use in Determining Present and Future Global Soil Dust Emission". In: *Geophysical Research Letters* 31.5. DOI: 10.1029/2003GL019216.

Terwey, W. D. and Rozoff, C. M. (2014). "Objective Convective Updraft Identification and Tracking: Part 1. Structure and Thermodynamics of Convection in the Rainband Regions of Two Hurricane Simulations". In: *Journal of Geophysical Research: Atmospheres* 119.11, pp. 6470–6496. DOI: 10.1002/2013JD020904.

Thompson, G. and Eidhammer, T. (2014). "A Study of Aerosol Impacts on Clouds and Precipitation Development in a Large Winter Cyclone". In: *Journal of the Atmospheric Sciences* 71.10, pp. 3636–3658. DOI: 10.1175/JAS-D-13-0305.1.

Thompson, G., Field, P. R., Rasmussen, R. M. and Hall, W. D. (2008). "Explicit Forecasts of Winter Precipitation Using an Improved Bulk Microphysics Scheme. Part II: Implementation of a New Snow Parameterization". In: *Monthly Weather Review* 136.12, pp. 5095–5115. DOI: 10.1175/2008MWR2387.1.

Thompson, G., Rasmussen, R. M. and Manning, K. (2004). "Explicit Forecasts of Winter Precipitation Using an Improved Bulk Microphysics Scheme. Part I: Description and Sensitivity Analysis". In: *Monthly Weather Review* 132.2, pp. 519–542. DOI: 10.1175/1520-0493(2004)132⟨0519:EFOWPU⟩2.0.CO;2.

Thorpe, A. J., Miller, M. J. and Moncrieff, M. W. (1982). "Two-Dimensional Convection in Non-Constant Shear: A Model of Mid-Latitude Squall Lines". In: *Quarterly Journal of the Royal Meteorological Society* 108.458, pp. 739–762. DOI: 10.1002/qj.49710845802.

Tiedtke, M. (1989). "A Comprehensive Mass Flux Scheme for Cumulus Parameterization in Large-Scale Models". In: *Monthly Weather Review* 117.8, pp. 1779–1800. DOI: 10.1175/1520-0493(1989)117⟨1779:ACMFSF⟩2.0.CO;2.

Tompkins, A. M. (2001). "Organization of Tropical Convection in Low Vertical Wind Shears: The Role of Cold Pools". In: *Journal of the Atmospheric Sciences* 58.13, pp. 1650–1672. DOI: 10.1175/1520-0469(2001)058⟨1650:OOTCIL⟩2.0.CO;2.

Tory, K. J., Montgomery, M. T. and Davidson, N. E. (2006). "Prediction and Diagnosis of Tropical Cyclone Formation in an NWP System. Part I: The Critical Role of Vortex Enhancement in Deep Convection". In: *Journal of the Atmospheric Sciences* 63.12, pp. 3077–3090. DOI: 10.1175/JAS3764.1.

Trenberth, K. E., Fasullo, J. T. and Kiehl, J. (2009). "Earth's Global Energy Budget". In: *Bulletin of the American Meteorological Society* 90.3, pp. 311–324. DOI: 10.1175/2008BAMS2634.1.

Twomey, S. (1974). "Pollution and the Planetary Albedo". In: *Atmospheric Environment (1967)* 8.12, pp. 1251–1256. DOI: 10.1016/0004-6981(74)90004-3.

– (1977a). *Atmospheric Aerosols*. Elsevier Scientific Pub. Co. 324 pp.

– (1977b). "The Influence of Pollution on the Shortwave Albedo of Clouds". In: *Journal of the Atmospheric Sciences* 34.7, pp. 1149–1152. DOI: 10.1175/1520-0469(1977)034⟨1149:TIOPOT⟩2.0.CO;2.

Vali, G., DeMott, P. J., Möhler, O. and Whale, T. F. (2015). "Technical Note: A Proposal for Ice Nucleation Terminology". In: *Atmospheric Chemistry and Physics* 15.18, pp. 10263–10270. DOI: https://doi.org/10.5194/acp-15-10263-2015.

Vali, G. (1996). "Ice Nucleation-a Review". In: *Nucleation and Atmospheric Aerosols*, pp. 271–279. DOI: 10.1016/B978-008042030-1/50066-4.

Van den Heever, S. C., Fridlind, A. M., Marinescu, P. J., Heikenfeld, M., White, B. and Stier, P. (2017). *Aerosol-Cloud-Precipitation-Climate (ACPC) Initiative:Deep Convect-*

ive Cloud Group Roadmap. URL: http://acpcinitiative.org/Docs/ACPC_DCC_Roadmap_171019.pdf (visited on 08/04/2019).

Van den Heever, S. C., Carrió, G. G., Cotton, W. R., DeMott, P. J. and Prenni, A. J. (2006). "Impacts of Nucleating Aerosol on Florida Storms. Part I: Mesoscale Simulations". In: *Journal of the Atmospheric Sciences* 63.7, pp. 1752–1775. DOI: 10.1175/JAS3713.1.

Van den Heever, S. C. and Cotton, W. R. (2007). "Urban Aerosol Impacts on Downwind Convective Storms". In: *Journal of Applied Meteorology and Climatology* 46.6, pp. 828–850. DOI: 10.1175/JAM2492.1.

Van den Heever, S. C., Stephens, G. L. and Wood, N. B. (2011). "Aerosol Indirect Effects on Tropical Convection Characteristics under Conditions of Radiative–Convective Equilibrium". In: *Journal of the Atmospheric Sciences* 68.4, pp. 699–718. DOI: 10.1175/2010JAS3603.1.

Van Lier-Walqui, M., Fridlind, A. M., Ackerman, A. S., Collis, S., Helmus, J., MacGorman, D. R., North, K., Kollias, P. and Posselt, D. J. (2016). "On Polarimetric Radar Signatures of Deep Convection for Model Evaluation: Columns of Specific Differential Phase Observed during MC3E". In: *Monthly Weather Review* 144.2, pp. 737–758. DOI: 10.1175/MWR-D-15-0100.1.

Varble, A. (2018). "Erroneous Attribution of Deep Convective Invigoration to Aerosol Concentration". In: *Journal of the Atmospheric Sciences* 75.4, pp. 1351–1368. DOI: 10.1175/JAS-D-17-0217.1.

Varble, A., Fridlind, A. M., Zipser, E. J., Ackerman, A. S., Chaboureau, J.-P., Fan, J., Hill, A., McFarlane, S. A., Pinty, J.-P. and Shipway, B. (2011). "Evaluation of Cloud-Resolving Model Intercomparison Simulations Using TWP-ICE Observations: Precipitation and Cloud Structure". In: *Journal of Geophysical Research: Atmospheres* 116.D12, p. D12206. DOI: 10.1029/2010JD015180.

Varble, A., Zipser, E. J., Fridlind, A. M., Zhu, P., Ackerman, A. S., Chaboureau, J.-P., Collis, S., Fan, J., Hill, A. and Shipway, B. (2014a). "Evaluation of Cloud-Resolving and Limited Area Model Intercomparison Simulations Using TWP-ICE Observations: 1. Deep Convective Updraft Properties". In: *Journal of Geophysical Research: Atmospheres* 119.24, pp. 13, 891–13, 918. DOI: 10.1002/2013JD021371.

Varble, A., Zipser, E. J., Fridlind, A. M., Zhu, P., Ackerman, A. S., Chaboureau, J.-P., Fan, J., Hill, A., Shipway, B. and Williams, C. (2014b). "Evaluation of Cloud-Resolving and Limited Area Model Intercomparison Simulations Using TWP-ICE Observations: 2. Precipitation Microphysics". In: *Journal of Geophysical Research: Atmospheres* 119.24, pp. 13, 919–13, 945. DOI: 10.1002/2013JD021372.

Wagner, T. M. and Graf, H.-F. (2010). "An Ensemble Cumulus Convection Parameterization with Explicit Cloud Treatment". In: *Journal of the Atmospheric Sciences* 67.12, pp. 3854–3869. DOI: 10.1175/2010JAS3485.1.

Walko, R. L., Cotton, W. R., Meyers, M. P. and Harrington, J. Y. (1995). "New RAMS Cloud Microphysics Parameterization Part I: The Single-Moment Scheme". In: *Atmospheric Research* 38.1, pp. 29–62. DOI: 10.1016/0169-8095(94)00087-T.

Walko, R. L., Band, L. E., Baron, J., Kittel, T. G. F., Lammers, R. et al. (2000). "Coupled Atmosphere–Biophysics–Hydrology Models for Environmental Modeling". In: *Journal*

of Applied Meteorology 39.6, pp. 931–944. DOI: 10.1175/1520-0450(2000)039⟨0931:CABHMF⟩2.0.CO;2.

Wall, C., Zipser, E. and Liu, C. (2013). "An Investigation of the Aerosol Indirect Effect on Convective Intensity Using Satellite Observations". In: *Journal of the Atmospheric Sciences* 71.1, pp. 430–447. DOI: 10.1175/JAS-D-13-0158.1.

Walt, S. van der, Colbert, S. C. and Varoquaux, G. (2011). "The NumPy Array: A Structure for Efficient Numerical Computation". In: *Computing in Science Engineering* 13.2, pp. 22–30. DOI: 10.1109/MCSE.2011.37.

Walt, S. van der, Schönberger, J. L., Nunez-Iglesias, J., Boulogne, F., Warner, J. D., Yager, N., Gouillart, E. and Yu, T. (2014). "Scikit-Image: Image Processing in Python". In: *PeerJ* 2, e453. DOI: 10.7717/peerj.453.

Wang, S., Sobel, A. H., Fridlind, A., Feng, Z., Comstock, J. M., Minnis, P. and Nordeen, M. L. (2015). "Simulations of Cloud-Radiation Interaction Using Large-Scale Forcing Derived from the CINDY/DYNAMO Northern Sounding Array". In: *Journal of Advances in Modeling Earth Systems* 7.3, pp. 1472–1498. DOI: 10.1002/2015MS000461.

Wang, Y., Fan, J., Zhang, R., Leung, L. R. and Franklin, C. (2013). "Improving Bulk Microphysics Parameterizations in Simulations of Aerosol Effects". In: *Journal of Geophysical Research: Atmospheres* 118.11, pp. 5361–5379. DOI: 10.1002/jgrd.50432.

Wang, Z., Guo, L., Wang, S., Chen, L. and Wang, H. (2019). "Review of Random Walk in Image Processing". In: *Archives of Computational Methods in Engineering* 26.1, pp. 17–34. DOI: 10.1007/s11831-017-9225-4.

Warren, S., Eastman, R. and Hahn, C. J. (2015). "CLOUDS AND FOG — Climatology". In: *Encyclopedia of Atmospheric Sciences (Second Edition)*. Ed. by G. R. North, J. Pyle and F. Zhang. Oxford: Academic Press, pp. 161–169. DOI: 10.1016/B978-0-12-382225-3.00113-4. (Visited on 19/02/2019).

Watson-Parris, D., Schutgens, N., Cook, N., Kipling, Z., Kershaw, P., Gryspeerdt, E., Lawrence, B. and Stier, P. (2016). "Community Intercomparison Suite (CIS) v1.4.0: A Tool for Intercomparing Models and Observations". In: *Geosci. Model Dev.* 9.9, pp. 3093–3110. DOI: 10.5194/gmd-9-3093-2016.

Wegener, A. (1911). *Thermodynamik der Atmosphäre.* Leipzig: J.A. Barth.

Weigum, N., Schutgens, N. and Stier, P. (2016). "Effect of Aerosol Subgrid Variability on Aerosol Optical Depth and Cloud Condensation Nuclei: Implications for Global Aerosol Modelling". In: *Atmospheric Chemistry and Physics* 16.21, pp. 13619–13639. DOI: https://doi.org/10.5194/acp-16-13619-2016.

Weisman, M. L. and Klemp, J. B. (1982). "The Dependence of Numerically Simulated Convective Storms on Vertical Wind Shear and Buoyancy". In: *Monthly Weather Review* 110.6, pp. 504–520. DOI: 10.1175/1520-0493(1982)110⟨0504:TDONSC⟩2.0.CO;2.

Weisman, M. L. and Klemp, J. B. (1984). "The Structure and Classification of Numerically Simulated Convective Stormsin Directionally Varying Wind Shears". In: *Monthly Weather Review* 112.12, pp. 2479–2498. DOI: 10.1175/1520-0493(1984)112⟨2479:TSACON⟩2.0.CO;2.

Weisman, M. L. and Rotunno, R. (2000). "The Use of Vertical Wind Shear versus Helicity in Interpreting Supercell Dynamics". In: *Journal of the Atmospheric Sciences* 57.9, pp. 1452–1472. DOI: 10.1175/1520-0469(2000)057⟨1452:TUOVWS⟩2.0.CO;2.

Wendisch, M., Pöschl, U., Andreae, M. O., Machado, L. A. T., Albrecht, R. et al. (2016). "ACRIDICON–CHUVA Campaign: Studying Tropical Deep Convective Clouds and Precipitation over Amazonia Using the New German Research Aircraft HALO". In: *Bulletin of the American Meteorological Society* 97.10, pp. 1885–1908. DOI: 10.1175/BAMS-D-14-00255.1.

Werf, G. R. van der, Randerson, J. T., Giglio, L., Collatz, G. J., Mu, M., Kasibhatla, P. S., Morton, D. C., DeFries, R. S., Jin, Y. and Leeuwen, T. T. van (2010). "Global Fire Emissions and the Contribution of Deforestation, Savanna, Forest, Agricultural, and Peat Fires (1997–2009)". In: *Atmospheric Chemistry and Physics* 10.23, pp. 11707–11735. DOI: https://doi.org/10.5194/acp-10-11707-2010.

Whitby, K. T. (1978). "The Physical Characteristics of Sulfur Aerosols". In: *Atmospheric Environment (1967)*. Proceedings of the International Symposium 12.1, pp. 135–159. DOI: 10.1016/0004-6981(78)90196-8.

White, B., Gryspeerdt, E., Stier, P., Morrison, H., Thompson, G. and Kipling, Z. (2017). "Uncertainty from the Choice of Microphysics Scheme in Convection-Permitting Models Significantly Exceeds Aerosol Effects". In: *Atmospheric Chemistry and Physics* 17.19, pp. 12145–12175. DOI: https://doi.org/10.5194/acp-17-12145-2017.

Wilcox, E. M. (2010). "Stratocumulus Cloud Thickening beneath Layers of Absorbing Smoke Aerosol". In: *Atmospheric Chemistry and Physics* 10.23, pp. 11769–11777. DOI: https://doi.org/10.5194/acp-10-11769-2010.

Williams, E., Rosenfeld, D., Madden, N., Gerlach, J., Gears, N. et al. (2002). "Contrasting Convective Regimes over the Amazon: Implications for Cloud Electrification". In: *Journal of Geophysical Research: Atmospheres* 107.D20, LBA 50. DOI: 10.1029/2001JD000380.

Wood, R. (2015). "CLOUDS AND FOG — Stratus and Stratocumulus". In: *Encyclopedia of Atmospheric Sciences (Second Edition)*. Ed. by G. R. North, J. Pyle and F. Zhang. Oxford: Academic Press, pp. 196–200. DOI: 10.1016/B978-0-12-382225-3.00396-0. (Visited on 19/02/2019).

Wood, R. (2012). "Stratocumulus Clouds". In: *Monthly Weather Review* 140.8, pp. 2373–2423. DOI: 10.1175/MWR-D-11-00121.1.

World Meteorological Organization (1956). *International Cloud Atlas*. World Meteorological Organization. book.

– (2017). *International Cloud Atlas*. URL: https://cloudatlas.wmo.int (visited on 18/02/2019).

Yan, H., Li, Z., Huang, J., Cribb, M. and Liu, J. (2014). "Long-Term Aerosol-Mediated Changes in Cloud Radiative Forcing of Deep Clouds at the Top and Bottom of the Atmosphere over the Southern Great Plains". In: *Atmospheric Chemistry and Physics* 14.14, pp. 7113–7124. DOI: https://doi.org/10.5194/acp-14-7113-2014.

Yang, S. and Smith, E. A. (2008). "Convective–Stratiform Precipitation Variability at Seasonal Scale from 8 Yr of TRMM Observations: Implications for Multiple Modes

of Diurnal Variability". In: *Journal of Climate* 21.16, pp. 4087–4114. DOI: 10.1175/2008JCLI2096.1.

Yau, M. K. and Rogers, R. R. (1989). *A Short Course in Cloud Physics*. 3 edition. Oxford: Butterworth-Heinemann. 304 pp.

Zhang, G. J. and Song, X. (2016). "Parameterization of Microphysical Processes in Convective Clouds in Global Climate Models". In: *Meteorological Monographs* 56, pp. 12.1–12.18. DOI: 10.1175/AMSMONOGRAPHS-D-15-0015.1.

Zhang, K., Fu, R., Shaikh, M. J., Ghan, S., Wang, M., Leung, L. R., Dickinson, R. E. and Marengo, J. (2017). "Influence of Superparameterization and a Higher-Order Turbulence Closure on Rainfall Bias Over Amazonia in Community Atmosphere Model Version 5". In: *Journal of Geophysical Research: Atmospheres* 122.18, pp. 9879–9902. DOI: 10.1002/2017JD026576.

Zhao, M. and Austin, P. H. (2005a). "Life Cycle of Numerically Simulated Shallow Cumulus Clouds. Part I: Transport". In: *Journal of the Atmospheric Sciences* 62.5, pp. 1269–1290. DOI: 10.1175/JAS3414.1.

– (2005b). "Life Cycle of Numerically Simulated Shallow Cumulus Clouds. Part II: Mixing Dynamics". In: *Journal of the Atmospheric Sciences* 62.5, pp. 1291–1310. DOI: 10.1175/JAS3415.1.

Zinner, T., Forster, C., Coning, E. de and Betz, H.-D. (2013). "Validation of the Meteosat Storm Detection and Nowcasting System Cb-TRAM with Lightning Network Data – Europe and South Africa". In: *Atmospheric Measurement Techniques* 6.6, pp. 1567–1583. DOI: https://doi.org/10.5194/amt-6-1567-2013.

Zinner, T., Mannstein, H. and Tafferner, A. (2008). "Cb-TRAM: Tracking and Monitoring Severe Convection from Onset over Rapid Development to Mature Phase Using Multi-Channel Meteosat-8 SEVIRI Data". In: *Meteorology and Atmospheric Physics* 101.3, pp. 191–210. DOI: 10.1007/s00703-008-0290-y.